

Demonstrating the Applicability of Chemical Looping Combustion for Fluid Catalytic Cracking Unit as a Novel CO_2 Capture Technology

A Thesis Submitted to

The University of Nottingham

By

Mr Fatih Güleç

MSc, BSc Chemical Engineering

For the degree of

Doctor of Philosophy (PhD) in Chemical Engineering

Supervisors

Professor Colin E. Snape, Dr Will Meredith, Dr Cheng-gong Sun

Faculty of Engineering
Department of Chemical Engineering
The University of Nottingham
United Kingdom

June 2020

Abstract

Fluid Catalytic Cracking (FCC) units are responsible for ~25% of CO_2 emissions released from the oil refineries, which themselves account for 4-6% of total global CO_2 emissions. Although post- and oxy-combustion technologies have been suggested to capture the CO_2 released from the regenerator of FCC, Chemical Looping Combustion (CLC) may also be a potential approach to capture the CO_2 released from the regenerators in FCC units with lower energy consumption.

In this study, the applicability of CLC for the FCC unit was investigated as a novel approach for CO_2 capture. In order to demonstrate the applicability of CLC, four main aspects were studied. A refinery FCC catalyst (Equilibrium Catalyst–ECat) was firstly modified with reduced oxygen carriers e.g. Copper (Cu), Copper (I) oxide (Cu_2O), Cobalt (II) oxide (CoO), and Manganese (II, III) oxide (Mn_3O_4) and oxidised oxygen carriers e.g. Copper (II) oxide (CuO), Cobalt (II, III) oxide (Co_3O_4), and Manganese (II) oxide (Mn_2O_3) using mechanical mixing and wet-impregnation methods. Secondly, to identify any detrimental effects of the oxygen carriers on cracking, both reduced and oxidised oxygen carrier modified ECat formulations were tested for n-hexadecane cracking using the standard test method of FCC catalysts. Then, to investigate the CLC behaviour of coke with oxidised oxygen carriers (CuO, Co_3O_4 and Mn_2O_3), thermogravimetric analyses (TGA) were conducted on a low volatile semi-anthracite Welsh coal, which has a similar elemental composition to actual FCC coke. Finally, the CLC of coke deposited on the reduced oxygen carrier impregnated ECat was investigated with the stoichiometrically required amount of oxidised oxygen carrier impregnated ECat. The CLC tests were investigated in a fixed-bed and a fluidised-bed reactors equipped with an online mass spectrometer to monitor CO_2 release.

The results demonstrated that mechanical mixing of Cu with ECat was shown to have a negative impact on the cracking of n-hexadecane. However, the mixing of Cu_2O, CoO, and Mn_3O_4 with ECat had no significant effect on gas, liquid and coke yields on product selectivity. Additionally, wet-impregnation of Cu, MnO, and Mn_3O_4 had a negligible impact on the cracking of n-hexadecane in terms of conversion, yields and product selectivity. In terms of the CLC tests of coke, complete combustion of the model coke

was achieved with bulk CuO, Co_3O_4, and Mn_2O_3 when the stoichiometric ratio of oxygen carrier to coke was maintained higher than 1.0 and sufficient time was provided. Furthermore, although 90 vol.% combustion efficiency of the coke deposited on ECat was reached with bulk CuO and Mn_2O_3, the regeneration temperature required (800 °C) was not realistic in terms of commercial regenerator conditions. However, a relatively high combustion efficiency, (> 94 vol.%) of the coke deposited on reduced Cu and Mn_3O_4 impregnated ECat was achieved with the stoichiometrically required amount of CuO and Mn_2O_3 impregnated ECat at the conditions used in conventional FCC regenerators, 750 °C for 45 min. According to these results, CLC is a promising technology to incorporate into the next generation of FCC units to optimise CO_2 capture.

In addition to the application of CLC for FCC, the selective low temperature CLC of higher hydrocarbons was discovered during the cracking tests of n-hexadecane over oxidised oxygen carriers mixed ECat. Therefore, CLC of n-hexadecane and n-heptane with CuO and Mn_2O_3 was investigated in a fixed bed reactor to reveal the extent to which low temperature CLC can potentially apply to hydrocarbons. The effects of fuel to oxygen carrier ratio, fuel feed flow rate and fuel residence time on the extent of combustion were reported. Methane did not combust, while near complete conversion was achieved for both n-hexadecane and n-heptane with excess oxygen carrier for CuO. For Mn_2O_3, total reduction to Mn_3O_4 occurred, but the slower reduction step to MnO controlled the extent of combustion. Although the extent of cracking is negligible in the absence of cracking catalysts, for the mechanism to be selective for higher hydrocarbons suggests that the reaction with oxygen involves radicals or carbocations arising from bond scission. Sintering of bulk CuO occurred after repeated cycles, but this can easily be avoided using alumina support. The fact that higher hydrocarbons can be combusted selectively at 500 °C and below, offers the possibility of using CLC to remove these hydrocarbons and potentially other organics from hot gas streams.

Acknowledgements

I would like to express my sincere gratitude to God for giving me the strength and wisdom to persevere and complete this accomplishment satisfactorily.

It is a great pleasure to acknowledge my sincerest thanks and gratitude to my supervisors; Professor Colin E. Snape, Dr Will Meredith, and Dr Cheng-gong Sun for their help, encouragement, guidance and advice of this work.

I would like to express my extreme sincere Dr Lee Stevens and Dr Clement Uguna, who have provided me with their time, support and advice towards the successful progression of this research. I would also like to acknowledge the technicians, particularly Mr Adrian Quinn in Energy Technologies Building at the University of Nottingham.

I would like to present my deepest thanks to my friends, Alejandro Pineda (MSc), Dr Andrew Gill, Dr Eduardo Garcia, Dr Gary Newbolt, and Dr Khalil Al Hanashi, who have always been a major source of academic and social support. To that special person, I also want to thank you for your continuous encouragement, sympathy and love.

I also express my sincerest thanks to the Republic of Turkey, Ministry of National Education for the financial support to undertake my PhD at the University of Nottingham, United Kingdom.

Last but not least, I am incredibly thankful to my family for their infinitive support, love, and great words of encouragement.

"Dedicated to my beloved parents; Mr and Mrs Güleç"

For their love, endless support, encouragement and sacrifices

Contents

Abstract i
Acknowledgements iii
Dedication iv
Contents v
List of Figures ix
List of Tables xvi
List of Abbreviations xviii
List of Publications xx

1 Introduction 1
1.1 Background on global CO_2 emissions and capture technologies 1
1.2 Aims and objectives 2
1.3 Thesis structure 4

2 Literature Review 6
2.1 Fundamentals of CO_2 emissions 6
2.2 Fundamentals of CO_2 capture 8
2.3 Introduction to fluid catalytic cracking (FCC) 11
2.4 CO_2 capture technologies from an FCC unit 15
2.4.1 Application of post-combustion for FCC units 16
2.4.2 Application of oxy-combustion for FCC units 19
2.4.3 Comparison of post- and oxy-combustion technologies for FCC 23
2.5 Fundamentals of chemical looping combustion (CLC) 25
2.5.1 CLC mechanisms for gas and solid fuels 27
2.5.2 CLC for gas and solid fuels 32
2.5.3 CLC for liquid fuels 38

3 Proposed Application of CLC to FCC Units 40

4 Materials and Experimental Methods 43
4.1 FCC catalyst formulations 43
4.1.1 Mechanical mixing of oxygen carriers with FCC catalysts 44
4.1.2 Impregnation of oxidised and reduced oxygen carriers into FCC catalyst 45
4.2 Catalytic cracking tests with the microactivity test (MAT) unit 48
4.2.1 Baseline cracking experiments 48

4.2.2 Cracking of n-hexadecane over oxygen carriers modified FCC catalyst 51
4.2.3 Characterisation of cracking products 51
4.2.4 Data evaluation of the catalytic cracking tests.....52
4.3 Chemical looping combustion tests of coke with oxygen carriers 53
4.3.1 Chemical looping combustion tests in TGA.....54
4.3.2 CLC tests of FCC coke with oxygen carriers in FxB-MS unit.....56
4.3.3 CLC test of coke deposited on reduced oxygen carriers impregnated ECat with oxidised oxygen carriers impregnated ECat in FxB-MS and FsB-MS units.....58
4.4 Characterisation of fresh and used oxygen carriers modified ECat.....61
4.4.1 X-ray powder diffraction (XRD) analysis 62
4.4.2 Scanning electron microscope (SEM) and Energy-dispersive X-ray spectroscopy (EDS) analysis 62
4.4.3 Energy-dispersive X-ray fluorescence (XRF) analysis 63
4.4.4 Analysis of textural properties with N_2 sorption.....63
4.4.5 True density analysis 64
4.4.6 Fourier-transform infrared spectroscopy-pyridine (IR-Py) analysis.....64
4.4.7 Elemental analysis of coke deposited on prepared catalysts 65
4.5 Chemical looping combustion of hydrocarbons with Cu- and Mn-Oxidises.....66
4.5.1 Liquid fuels and oxygen carriers 66
4.5.2 Baseline thermal cracking tests of liquid fuels 66
4.5.3 Combustion of model liquid fuels with oxygen carriers.....67
4.5.4 Data evaluation 69
4.5.5 Characterisation of used oxygen carriers.....70

5 Cracking Activity Test of Modified FCC Catalysts.....72
5.1 Baseline cracking tests with commercial FCC catalysts 72
5.2 Cracking of n-hexadecane over oxygen carrier modified ECat prepared by mechanical mixing.....78
5.2.1 The effect of oxidised oxygen carriers mixed ECat 79
5.2.2 The effects of reduced oxygen carriers mixed ECat.....86
5.3 Cracking of n-hexadecane over oxygen carrier modified ECat prepared by wet-impregnation.....93
5.3.1 The effects of oxidised oxygen carriers impregnated ECat 93
5.3.2 The effect of the reduced oxygen carriers impregnated ECat.....111
5.4 Summary.....130

6 Chemical Looping Combustion of FCC Coke 131
6.1 CLC of model coke with oxygen carriers in TA instrument 131
6.1.1 Oxygen carriers and model coke behaviours in TGA conditions 131
6.1.2 Chemical looping with oxygen uncoupling for the combustion of model coke with CuO 133
6.1.3 Chemical looping with oxygen uncoupling for the combustion of model coke with Co_3O_4 137
6.1.4 Chemical looping with oxygen uncoupling for the combustion of model coke with Mn_2O_3 140
6.2 CLC of MAT coke with oxygen carriers in a fixed-bed mass spectroscopy (FxB-MS) unit 143
6.2.1 Baseline experiments of the model and MAT coke in FxB-MS unit 143
6.2.2 CLC of MAT coke deposited on ECat with bulk oxygen carriers in FxB-MS unit 150
6.3 CLC of coke deposited on reduced oxygen carrier impregnated ECat with oxidised oxygen carrier impregnated ECat in FxB-MS and FsB-MS units 152
6.3.1 CLOU properties of oxidised oxygen carriers impregnated ECat 153
6.3.2 CLC of MAT coke deposited on I-Cu/ECat with I-CuO/ECat 154
6.3.3 CLC of MAT coke deposited on I-Mn_3O_4/ECat with I-Mn_2O_3/ECat 155
6.3.4 Combustion behaviour of MAT coke with air, bulk-CuO and I-CuO/ECat 157
6.4 Summary 158

7 Selective Low Temperature CLC of Higher Alkanes with Cu- and Mn-Oxides 159
7.1 Baseline experiments 160
7.2 The effects of fuel to oxygen carrier equivalence ratio (ϕ) 160
7.3 Definition of gas and liquid products after combustion 164
7.4 Liquid fuel feed rate and residence time 165
7.5 The effect of temperature 166
7.6 Multiple cycles of n-hexadecane combustion with CuO 167
7.7 Characterisation of fresh and used oxygen carriers 168
7.8 Possible reaction pathways and potential applications 171
7.9 A simple kinetic analysis of n-hexadecane combustion with CuO 173
7.10 Summary 175

8 Conclusions and Future Work 176
8.1 Conclusions 176
8.1.1 Catalytic cracking tests over modified commercial FCC catalyst 176

8.1.2 CLC tests of coke deposited on FCC catalyst....177
8.1.3 Low temperature CLC of hydrocarbons with Cu- and Mn- oxidises....178
8.2 Future work....179
8.2.1 Suggestions for the CLC-FCC concept....179
8.2.2 Suggestions for the applicability of CLC for other processes....180
8.2.3 Suggestions for the applicability of low temperature CLC....180

References....181
Appendix A — GC chromatograms for the liquid and gas products....199
Appendix B — Effects of temperature and oxygen carriers on the CLC products of coke....203
Appendix C — Kinetic analysis of n-hexadecane combustion with CuO....204

List of Figures

Figure 2.1. Trends in CO_2 emissions from 1960 to 2019. 6
Figure 2.2. CO_2 emissions by region in 1960 and 2018 7
Figure 2.3. Global CO_2 emissions by sector in 2018. 7
Figure 2.4. CO_2 capture approaches (post-, pre-, oxy-combustion). 9
Figure 2.5. State of global CCS projects in 2019. 10
Figure 2.6. Future goals of CCS in the power and industrial sectors. 11
Figure 2.7. Percentage distribution of total refinery CO_2 emissions. 12
Figure 2.8. A typical FCC unit. 12
Figure 2.9. a) FCC products from the refinery feedstock and b) consecutive cracking reactions of complex FCC feedstock leading to the final FCC products. 13
Figure 2.10. Typical chemical and structural composition of an FCC particle 14
Figure 2.11. Catalyst properties required for the FCC unit 14
Figure 2.12. Post-combustion capture in an FCC unit 17
Figure 2.13. Simplified process flow diagram of HiCapt$^+$ process 17
Figure 2.14. Process flow diagram presenting three different heat integration options with post-combustion capture for the flue gas released from the regenerator of the FCC unit. 19
Figure 2.15. Oxy-combustion capture in an FCC unit 20
Figure 2.16. Process schematic of oxy-combustion-FCC operation. 20
Figure 2.17. Comparison of oxy-combustion and air operation. 21
Figure 2.18. Two-stages FCC regeneration with diathermy wall provides heat transfer. 22
Figure 2.19. Chemical looping combustion process 26
Figure 2.20. Combustion mechanisms of gas fuels and solid fuels in the fuel reactor. 28
Figure 2.21. Reduction of an oxygen carrier particle during the CLC. 29
Figure 2.22. Scheme of the reduction mechanism of Fe20γAl with CH_4. 29
Figure 2.23. Combustion mechanism of syngas species over Ni-based oxygen carrier. 30
Figure 3.1. Schematic diagram of the proposed CLC-FCC process. 41
Figure 4.1. The mechanically mixing procedure of both reduced and oxidised oxygen carriers with ECat. 45
Figure 4.2. Flowchart of wet-impregnation method used for the preparation of oxidised and reduced oxygen carrier modified ECat. 46
Figure 4.3. Commercial hydropyrolysis rig used for the reduction of oxidised oxygen carriers impregnated ECat (hydrogen reduction). 47
Figure 4.4. The experimental set-up of MAT unit, a) Flowchart and b) Picture. 49
Figure 4.5. Details of the MAT unit experimental set-up 50

Figure 4.6. Discovery TGA from TA Instruments. 53
Figure 4.7. The experimental set-up of FxB-MS unit, a) Flowchart and b) Picture 57
Figure 4.8. a) Schematic diagram and b) picture of FsB-MS experimental set-up (Rd: reduced oxygen carrier, Ox: Oxidised oxygen carrier) 59
Figure 4.9. Schematic diagram of AccuPyc II 1340 pycnometer 64
Figure 4.10. An elemental analysis instrument with vertical combustion furnace 65
Figure 5.1. Gas chromatograms of the liquid products obtained from the cracking of n-hexadecane over ECat, a) scale to nC_6 b) scale to nC_8. The numbers on the chromatograms represent the presence of n-alkanes. 73
Figure 5.2. Gas chromatogram of the gas products obtained from the cracking of n-hexadecane over ECat at 482 ºC 74
Figure 5.3. Overall conversion of n-hexadecane with the commercial FCC catalysts, FCC76, FCC75, and ECat. 75
Figure 5.4. Coke, gas, and liquid yields from n-hexadecane cracking over FCC76, FCC75 and ECat. 76
Figure 5.5. Product selectivity for C_{1-2} (light gases), C_{3-4} (LPG), C_{5-15} (gasoline) and coke from n-hexadecane cracking over FCC76, FCC75 and ECat. 77
Figure 5.6. XRD patterns of a) fresh ECat and b) used M-Mn_2O_3/Cat, c) used M-Co_3O_4/ECat and d) used M-CuO/ECat 80
Figure 5.7. Conversion (overall and excluding CLC) of n-hexadecane over the commercial ECat and oxidised oxygen carriers mixed ECat; M-CuO/ECat, M-Co_3O_4/ECat, and M-Mn_2O_3/ECat. 82
Figure 5.8. Coke, gas, and liquid yields from the cracking of n-hexadecane over commercial ECat and oxidised form oxygen carrier mixed ECat; M-CuO/ECat, M-Co_3O_4/ECat, and M-Mn_2O_3/ECat. 84
Figure 5.9. Product selectivity of C_{1-2} (light gases), C_{3-4} (LPG), C_{5-15} (gasoline), C_{16+} (higher hydrocarbons) and coke from the cracking of n-hexadecane over commercial ECat and reduced form oxygen carrier mixed ECat; M-CuO/ECat, M-Co_3O_4/ECat, and M-Mn_2O_3/ECat. 85
Figure 5.10. XRD patterns of the prepared reduced oxygen carriers; a) Mn_3O_4, b) CoO, c) Cu_2O 87
Figure 5.11. Colour of both oxidised oxygen carriers (CuO, Co_3O_4, Mn_2O_3) and reduced oxygen carriers (Cu_2O, CoO, Mn_3O_4) 87
Figure 5.12. XRD patterns of a) fresh ECat and b) used M-Mn_3O_4/ECat c) used M-CoO/ECat d) used M-Cu_2O/ECat 88

Figure 5.13. Conversion (both overall and excluding CLC) of n-hexadecane over ECat and reduced oxygen carriers mixed ECat, M-Cu/ECat, M-Cu_2O/ECat, M-CoO/ECat, and M-Mn_3O_4/ECat. 90
Figure 5.14. Coke, gas, and liquid yields from the cracking of n-hexadecane over ECat and reduced oxygen carriers mixed ECat; M-Cu/ECat, M-Cu_2O/ECat, M-CoO/ECat, and M-Mn_3O_4/ECat. 91
Figure 5.15. Product selectivity of C_{1-2} (light gases), C_{3-4} (LPG), C_{5-15} (gasoline), C_{16+} (higher hydrocarbons) and coke from the cracking of n-hexadecane over commercial ECat and reduced oxygen carriers mixed ECat; M-Cu/ECat, M-Cu_2O/ECat, M-CoO/ECat, and M-Mn_3O_4/ECat. 92
Figure 5.16. XRD patterns of a) ECat, b) fresh I-CuO/ECat, and c) used I-CuO/ECat. 94
Figure 5.17. XRD patterns of a) ECat, b) fresh I-Co_3O_4/ECat, and c) used I-Co_3O_4/ECat. 94
Figure 5.18. XRD patterns of a) ECat, b) fresh I-Mn_2O_3/ECat., and c) used I-Mn_2O_3/ECat. 95
Figure 5.19. SEM images of fresh ECat surface. 96
Figure 5.20. SEM images of a) fresh I-CuO/ECat and b) used I-CuO/ECat. 97
Figure 5.21. SEM images of a) fresh I-Co_3O_4/ECat and b) used I-Co_3O_4/ECat. 97
Figure 5.22. SEM images of a) fresh I-Mn_2O_3/ECat and b) used I-Mn_2O_3/ECat..... 98
Figure 5.23. SEM image and EDS spectrum of agglomerated part of fresh I-Mn_2O_3/ECat. 99
Figure 5.24. EDS mapping for Cu and element spectrums of a) fresh I-CuO/ECat and b) used I-CuO/ECat. 101
Figure 5.25. EDS mapping for Co and element spectrums of a) fresh I-Co_3O_4/ECat and b) used I-Co_3O_4/ECat. 101
Figure 5.26. EDS mapping for Mn and element spectrums of a) fresh I-Mn_2O_3/ECat and b) used I-Mn_2O_3/ECat. 102
Figure 5.27. Nitrogen adsorption-desorption isotherms of fresh oxidised oxygen carriers impregnated ECat; ECat, I-CuO/ECat, I-Co_3O_4/ECat, I-Mn_2O_3/ECat. 103
Figure 5.28. IR-Py spectra of parent and oxidised oxygen carriers impregnated ECat 105
Figure 5.29. Conversion of n-hexadecane over the control ECat and oxidised oxygen carriers impregnated ECat; I-CuO/ECat, I-Co_3O_4/ECat, and I-Mn_2O_3/ECat. 108
Figure 5.30. Coke, gas, and liquid yields from the cracking of n-hexadecane over ECat and oxidise oxygen carriers impregnated ECat; I-CuO/ECat, I-Co_3O_4/ECat, and I-Mn_2O_3/ECat... 109
Figure 5.31. Product selectivity of C_{1-2} (light gases), C_{3-4} (LPG), C_{5-15} (gasoline), C_{16+} (higher hydrocarbons) and coke from the cracking of n-hexadecane over control ECat and oxidise oxygen carriers impregnated ECat; I-CuO/ECat, I-Co_3O_4/ECat, and I-Mn_2O_3/ECat. 110
Figure 5.32. XRD patterns of the I-CuO/ECat and reduced I-CuO/ECat by hydrogen at 200, 300, 450 °C. 111

Figure 5.33. XRD patterns of I-Co_3O_4/ECat and reduced I-Co_3O_4/ECat by hydrogen at 250, 300, 350, 450 °C. 112
Figure 5.34. XRD patterns of I-Mn_2O_3/ECat and reduced I-Mn_2O_3/ECat by hydrogen at 250, 300, 350, 450 °C. 112
Figure 5.35. XRD patterns of a) ECat, b) fresh I-Cu/ECat, and c) used I-Cu/ECat..... 114
Figure 5.36. XRD patterns of a) ECat, b) fresh I-MnO/ECat, and c) used I-MnO/ECat. 114
Figure 5.37. XRD patterns of a) ECat, b) fresh I-CoO/ECat, and c) used I-CoO/ECat. 115
Figure 5.38. XRD patterns of a) ECat, b) fresh I-Mn_3O_4/ECat, and c) used I-Mn_3O_4/ECat.... 115
Figure 5.39. SEM images of a) fresh I-Cu/ECat and b) used I-Cu/ECat. 117
Figure 5.40. SEM images of a) fresh I-CoO/ECat and b) used I-CoO/ECat. 117
Figure 5.41. SEM images of a) fresh I-MnO/ECat and b) used I-MnO/ECat..... 118
Figure 5.42. SEM images of a) fresh I-Mn_3O_4/ECat and b) used I- Mn_3O_4/ECat..... 118
Figure 5.43. EDS element spectrums of a) fresh I-Cu/ECat and b) used I-Cu/ECat. 120
Figure 5.44. EDS element spectrums of a) fresh I-CoO/ECat and b) used I-CoO/ECat..... 120
Figure 5.45. EDS element spectrums of a) fresh I-MnO/ECat and b) used I-MnO/ECat..... 121
Figure 5.46. EDS element spectrums of a) fresh I-Mn_3O_4/ECat and b) used I- Mn_3O_4/ECat.. 122
Figure 5.47. Nitrogen adsorption-desorption isotherms of fresh reduced oxygen carriers impregnated ECat; ECat, I-Cu/ECat, I-CoO/ECat, I-Mn_3O_4/ECat, I-MnO/ECat. 123
Figure 5.48. IR-Py spectra of parent and reduced oxygen carriers impregnated ECat 125
Figure 5.49. Conversion (overall and excluding CLC) of n-hexadecane over the control ECat and reduced form oxygen carrier impregnated ECat; I-Cu/ECat, I-CoO/ECat, I-Mn_3O_4/ECat, and I-MnO/ECat..... 127
Figure 5.50. Coke, gas, and liquid yields from the cracking of n-hexadecane over control ECat and reduced form oxygen carrier impregnated ECat; I-Cu/ECat, I-CoO/ECat, I-Mn_3O_4/ECat, and I-MnO/ECat..... 128
Figure 5.51. Product selectivity of C_{1-2} (light gases), C_{3-4} (LPG), C_{5-15} (gasoline), C_{16+} (higher hydrocarbons) and coke from the cracking of n-hexadecane over control ECat and reduced form oxygen carrier impregnated ECat; I-Cu/ECat, I-CoO/ECat, I-Mn_3O_4/ECat, and I-MnO/ECat. 129
Figure 6.1. TGA profile of the model coke under nitrogen and air atmosphere at 1000 °C.... 132
Figure 6.2. TGA profiles of oxygen carriers under N_2 atmosphere 133
Figure 6.3. Combustion (wt.%) of model coke with CuO in various oxygen excess numbers (R = 0.5, 1.0, and 2.0) at various isothermal temperatures (750-900 °C). 134
Figure 6.4. Fractional reduction of model coke with CuO for various oxygen excess numbers (R = 0.5, 1.0, 2.0) at various isotherm temperatures a) 900, b) 850, c) 800, d) 750 °C. 135

Figure 6.5. Weight loss rate of model coke (hard coke part) with CuO for various oxygen excess numbers (R=0.5, 1.0, and 2.0) at various isothermal temperatures a) 900 °C, b) 850 °C, c) 800 °C, d) 750 °C (line dashes represent the temperature profile). 136
Figure 6.6. Combustion (wt.%) of model coke with Co_3O_4 in various oxygen excess numbers (R = 0.5, 1.0, and 2.0) at various isothermal temperatures (750-900 °C). 137
Figure 6.7. Fractional reduction of model coke with Co_3O_4 for various oxygen excess numbers (R = 0.5, 1.0, and 2.0) at various isothermal temperatures a) 900 °C, b) 850 °C, c) 800 °C, d) 750 °C. 138
Figure 6.8. Weight loss rate of model coke (hard coke part) with Co_3O_4 for various oxygen excess numbers (R=0.5, 1.0, and 2.0) at various isothermal temperatures a) 900 °C, b) 850 °C, c) 800 °C, d)750 °C (line dashes represent the temperature profile). 139
Figure 6.9. Combustion (wt.%) of model coke with Mn_2O_3 in various oxygen excess numbers (R = 0.5, 1.0, and 1.5) at various isothermal temperatures (750-900 °C). 140
Figure 6.10. Fractional reduction of model coke with Mn_2O_3 for various oxygen excess numbers (R = 0.5, 1.0, and 1.5) at various isothermal temperatures a) 900 °C, b) 850 °C, c) 800 °C, d) 750 °C..... 141
Figure 6.11. Weight loss rate of model coke (hard coke part) with Mn_2O_3 for various oxygen excess numbers (R=0.5, 1.0, and 1.5) at various isothermal temperatures a) 900 °C, b) 850 °C, c) 800 °C, d)750 °C (line dashes represent the temperature profile). 142
Figure 6.12. Comparison of TGA and FxB-MS combustion profiles of model coke with CuO at 850 °C under N_2 atmosphere, a) TGA results, b) comparison of TGA and FxB-MS results ("IC" refers to Ion Current measured by MS). 144
Figure 6.13. Comparison of the combustion products of a) model coke, which is a semi-anthracite, and b) MAT coke (MC), which was deposited on ECat during the cracking of n-hexadecane at 482 °C, using stoichiometrically required amount CuO in FxB-MS unit at 850 °C under N_2 atmosphere ("1 and 2" refers to repeating tests). The ratio of m/z was 44 for CO_2, 15 for CH_4, 2 for H_2 and 28 for N_2..... 146
Figure 6.14. Calibration graph for the ion current to the a) percentage of CO_2 and b) percentage of N_2 in combustion gases..... 148
Figure 6.15. Comparison of the combustion behaviour of model and MAT coke with CuO in FxB-MS unit at 850 °C under N_2 atmosphere ("WC" refers to model coke, which is low volatile semi-anthracite Welsh coal, "MC-C16 and MC-VGO" refer to MAT coke which was deposited on ECat during the cracking of n-hexadecane (C16) and vacuum gas oil (VGO) at 482 °C). . 149
Figure 6.16. Effects of temperatures (700-850 °C) on the combustion of MAT coke with CuO in FxB-MS unit under N_2 atmosphere..... 150

Figure 6.17. Effects of oxygen carriers, CuO, Co_3O_4, and Mn_2O_3, on the combustion of MAT coke in FxB-MS unit at 800 °C under N_2 atmosphere (SC: soft coke and HC: hard coke)..... 152
Figure 6.18. Comparison of chemical looping oxygen uncoupling (CLOU) properties of a) bulk CuO and I-CuO/ECat, b) bulk Mn_2O_3 and I- Mn_2O_3/ECat, at 800 °C under N_2 atmosphere in FxB-MS unit. 153
Figure 6.19. Combustion results of coke deposited on I-Cu/ECat with I-CuO/ECat at 800 and 750 °C under N_2 atmosphere in FxB-MS and FsB-MS units and the comparison with the combustion of coke deposited ECat with bulk CuO at 800 °C in FxB-MS unit (FxB: Fixed bed, FsB: Fluidised bed, MS: Mass spectroscopy). 154
Figure 6.20. The combustion results of coke deposited I-Mn_3O_4/ECat with I-Mn_2O_3/ECat at 800 and 750 °C under N_2 atmosphere in FxB-MS and FsB-MS units, and the comparison with the combustion of coke deposited ECat with bulk Mn_2O_3 at 800 °C in FxB-MS unit (FxB: Fixed bed, FsB: Fluidised bed, MS: Mass spectroscopy). 156
Figure 6.21. Combustion behaviour of coke using air, bulk-CuO, and CuO impregnated ECat (I-CuO/ECat) at 750 °C. 157
Figure 7.1. Combustion % of a) n-hexadecane; b) n-heptane over CuO and Mn_2O_3 for different fuel to oxygen carrier equivalence ratios (ϕ: 0.7, 1.0, 1.3, and 2.0) for 0.03 ml/min feed flow rate at 482 °C (the error bars represents the standard deviation calculated by triple experiments). 161
Figure 7.2. Oxygen carrier bed after the combustion of n-hexadecane at an oxygen carrier equivalence ratio of 1.0 for 0.03 ml/min feed flow rate at 482 °C. 161
Figure 7.3. The volumetric ratio of CO/CO_2 for a) n–hexadecane; b) n-heptane combustion with CuO and Mn_2O_3 for 0.03 ml/min fuel feed flow rate at ϕ: 0.7, 1.0, 1.3, and 2.0 fuel to oxygen carrier equivalence ratios, 482 °C. 163
Figure 7.4. The yield of $C_{1\text{-}6}$ for a) n–hexadecane and b) n-heptane combustion, with CuO and Mn_2O_3 for 0.03 ml/min feed flow rate at ϕ: 0.7, 1.0, 1.3, and 2.0 fuel to oxygen carrier equivalence ratios, 482 °C. 163
Figure 7.5. Gas chromatograms of the a) liquid products; b) hydrocarbon gas products obtained after n-hexadecane combustion with CuO for 0.03 ml/min at ϕ: 2.0 at 482 °C. 164
Figure 7.6. Combustion % of n-hexadecane over CuO and SaCuO a) at different volumetric feed flow rates (0.03, 0.1, 0.2, and 1.4 ml/min) for ϕ: 0.7 at 482 °C; b) Combustion % of n-hexadecane over CuO for ϕ: 0.7 at 0.2 ml/min, 482 °C using different carrier gas flow rates (0.5, 1.0, 2.0 ml/min). 165
Figure 7.7. Combustion % of n-hexadecane over CuO for ϕ: 0.7 at 0.2 ml/min at eight different temperatures; 320, 360, 380, 400, 440, 480, 520, 560 °C. 166
Figure 7.8. Combustion % of n-hexadecane over CuO for ϕ: 1.3 at 0.03 ml/min at 482 °C for seven cycles. 167

Figure 7.9. Ion Current for the CO_2 evolution by the combustion of n-hexadecane over CuO/Al_2O_3 for ϕ: 1.3 with an n-hexadecane flowrate of 0.03 ml/min at 482 °C for cycles. 168
Figure 7.10. Wide-angle XRD patterns of a) CuO; b) Mn_2O_3 before and after n-hexadecane combustion experiments; a-1) fresh CuO, a-2) used CuO at ϕ: 1.0, a-3) used CuO at ϕ: 2.0, b-1) fresh Mn_2O_3, b-2) used Mn_2O_3 at ϕ: 1.0, b-3) used Mn_2O_3 at ϕ: 2.0 for 0.03 ml/min n-hexadecane feed flow rate at 482 °C. 169
Figure 7.11. SEM images of fresh CuO (a), CuO/Al_2O_3 (c) and used CuO (b), CuO/Al_2O_3 (d) after 7 cycles at ϕ: 1.3 (7 cycles) under a 0.03 ml/min n-hexadecane at 482 °C. 170
Figure 7.12. SEM images of fresh CuO (a), CuO/Al_2O_3 (d) and used CuO (b, c), CuO/Al_2O_3 (e, f) after 1st and 7th cycles at ϕ: 1.3 under a 0.03 ml/min n-hexadecane at 482 °C. 171
Figure 7.13. Possible reaction figure of CLC of liquid fuel with oxygen carriers at low temperature. 172
Figure 7.14. Elementary slice of solid oxygen carrier plug flow reactor (A represents n-hexadecane)..... 174
Figure 7.15. a) Reaction order (n) and reaction rate coefficient (k) calculation for n-hexadecane combustion with CuO at different volumetric feed flow rates (0.03, 0.1, 0.2, and 1.4 ml/min) for ϕ: 0.7 at 482 °C; b) Arrhenius plot for the combustion reaction rate constant of n-hexadecane with CuO for ϕ: 0.7 at 0.2 ml/min at different temperatures; 380-560 °C. 174
Figure A.1. GC chromatogram of the liquid products obtained from the cracking of n-hexadecane over oxidised and reduced oxygen carriers modified ECat by mechanically mixing. The numbers on the chromatograms represent the presence of n-alkanes. 199
Figure A.2. GC chromatogram of the liquid products obtained from the cracking of n-hexadecane over oxidised and reduced oxygen carriers modified ECat by impregnation. The numbers on the chromatograms represent the presence of n-alkanes. 200
Figure A.3. GC chromatogram of the gas products obtained from the cracking of n-hexadecane over oxidised and reduced oxygen carriers modified ECat by mechanically mixing. 201
Figure A.4. GC chromatogram of the gas products obtained from the cracking of n-hexadecane over oxidised and reduced oxygen carriers modified ECat by impregnation. 202
Figure B.1. CLC products from the combustion of coke deposited on ECat with CuO at 700-850 °C in FxB-MS unit. 203
Figure B.2. CLC products from the combustion of coke deposited on ECat with CuO, Co_3O_4 and Mn_2O_3 at 800 °C in FxB-MS unit. 203

List of Tables

Table 2.1. CO_2 capture in industrial processes and estimated year of maturity 10
Table 2.2. Summary of continuous CLC tests of gas fuels with a variety of oxygen carriers. .. 33
Table 5.1. Coke tests for fresh and used commercial catalysts, FCC76, FCC75 and ECat. 78
Table 5.2. Coke percentage on the catalysts and normalized coke composition of fresh ECat, used ECat, M-CuOECat, M-Co_3O_4ECat, and M-Mn_2O_3ECat. 81
Table 5.3. Coke percentage on the catalysts and normalized coke composition of fresh ECat, used ECat, M-Mn_3O_4/ECat, M-CoO/ECat, and M-Cu_2O/ECat. 89
Table 5.4. Amount of oxygen carrier impregnated on ECat. 100
Table 5.5. Surface properties of ECat, I-CuO/ECat, I-Co_3O_4/ECat, I-Mn_2O_3/ECat..... 104
Table 5.6. Integrated area of IR-Py peaks for parent and oxidised oxygen carriers impregnated ECat. 106
Table 5.7. Coke percentage and normalized coke composition of used catalysts, ECat, I-CuO/ECat, I-Co_3O_4/ECat, I-Mn_2O_3/ECat. 107
Table 5.8. Semi-quantification of Cu-, Co- and Mn-states after reduction of I-CuO/ECat, I-Co_3O_4/ECat, and I-Mn_2O_3/ECat at different temperatures by Hydrogen. 113
Table 5.9. Proportion of reduced oxygen carriers impregnated with ECat. 119
Table 5.10. Surface properties of the catalysts; ECat, I-Cu/ECat, I-CoO/ECat, I-Mn_3O_4/ECat, I-MnO/ECat. 124
Table 5.11. Integrated area of IR-Py peaks for parent and reduced oxygen carriers impregnated ECat. 125
Table 5.12. Coke percentage and normalized coke composition of used catalysts; ECat, I-Cu/ECat, I-CoO/ECat, I-Mn_3O_4/ECat, I-MnO/ECat..... 126
Table 6.1. Ultimate and proximate analysis of the semi-anthracite model coke and normalized elemental analyses of the model and FCC cokes. 131
Table 6.2. Combustion % of the model and MAT cokes with CuO in FxB-MS unit at 850 °C under N_2 atmosphere. 149
Table 6.3. Combustion % of MAT coke with CuO in FxB-MS unit at a temperature ranges 850-700 °C under N_2 atmosphere..... 151
Table 6.4. Combustion % of MAT coke with CuO, Co_3O_4, and Mn_2O_3 in FxB-MS unit at a temperature of 800 °C under N_2 atmosphere. 151
Table 6.5. Combustion % of coke deposited on I-Cu/ECat with I-CuO/ECat at 800 and 750 °C under N_2 atmosphere in FxB-MS and FsB-MS units, and the comparison with the combustion of coke deposited ECat with bulk CuO at 800 °C in FxB-MS unit..... 155

Table 6.6. Combustion % of coke deposited on I-Mn_3O_4/ECat with I-Mn_2O_3/ECat at 800 and 750 °C under N_2 atmosphere in FxB-MS and FsB-MS units and the comparison with the combustion of coke deposited ECat with bulk Mn_2O_3 at 800 °C in FxB-MS unit. 155
Table 7.1. Preliminary results for n-hexadecane cracking using a CuO mixed FCC catalyst.. 159
Table 7.2. Thermal cracking results for n-hexadecane and n-heptane. 160
Table 7.3. Combustion products from methane with CuO at 482 °C..... 160
Table 7.4. The main characteristics of the oxygen carriers before and after combustion tests. 169
Table 7.5. XRD of fresh and used Mn_2O_3 in CLC for n-hexadecane at ϕ: 1.0-2.0 at 482 °C. . 170
Table 7.6. Possible reactions of liquid fuels with and without oxygen carriers and oxygen transport capacities of CuO and Mn_2O_3. 172
Table C.1. Concentration of n-hexadecane (A) in reactor inlet (C_{A0}) and outlet (C_A)..... 205
Table C.2. Reaction rate values for four different flowrates of n-hexadecane (Q_A). 206
Table C.3. Reaction rate values at different temperatures from 380 to 560 °C. 208

List of Abbreviations

Air Separation Unit – ASU

American Society for Testing and Materials – ASTM

Brunauer Emmett Teller – BET

Barrett Joyner Halenda – BJH

Carbon Capture and Storage – CCS

Chemical Looping Combustion – CLC

Circa – ca.

CLC with oxygen uncoupling – CLOU

Commercial BASF Catalyst #7075 – FCC75

Commercial BASF Catalyst #7076 – FCC76

Coprecipitation – COP

Carbon dioxide – CO_2

Cobalt (II, III) oxide – Co_3O_4

Cobalt (II) oxide – CoO

Cobalt – Co

Copper (II) oxide – CuO

Copper (I) oxide – Cu_2O

Copper – Cu

Dry Gas – C_{1-2}

Energy-Dispersive X-ray Spectroscopy – EDS

Equilibrium catalyst – ECat

Equivalence ratio of fuel to oxygen carrier – ϕ

Fluid Catalytic Cracking – FCC

Fixed Bed reactor equipped with Mass Spectroscopy – FxB-MS

Fluidised Bed reactor equipped with Mass Spectroscopy – FsB-MS

Fourier-transform infrared spectroscopy – FTIR

Flame ionization detector – FID

Freeze granulation – FG

Fractional reduction – X_R

Greenhouse gases – GHG

Gas chromatography – GC

Gasoline – C_{5-15}

Higher hydrocarbons – C_{16+}

Hard coke – HC

International Energy Agency – IEA

Intergovernmental Panel on Climate Change – ICCP

In-situ gasification CLC – iG-CLC

Impregnation – IMP

Joint Committee on Powder Diffraction Standards – JCPDS

Liquefied petroleum gas – LPG – C_{3-4}

Mass spectrometer (MS)

Microactivity Test – MAT

Monoethanolamine – MEA

Metal oxide – Me_nO_m

Model coke – WC; low volatile semi-anthracite Welsh coal

MAT coke – MC; coke deposited on ECat during the MAT test

Methane – CH_4

Manganese (III) oxide – Mn_2O_3

Manganese (II,III) oxide – Mn_3O_4

Manganese (II) oxide – MnO

Nitrogen – N_2

n-hexadecane – $C_{16}H_{34}$

n-heptane – C_7H_{16}

Operation and Maintenance – O&M

Oxygen excess numbers – R

Oxygen – O_2

Pyridine adsorbed Fourier transform infrared spectroscopy – IR-Py

Reduced metal oxide – Me_nO_{m-1}

Scanning Electron Microscopy – SEM

Spray drying – SD

Soft coke – SC

Thermal conductivity detector – TCD

Vacuum gas oil – VGO

Volumetric Parts per Million – vppm

Waste heat steam generator – WHSG

X-ray diffraction – XRD

X-ray Fluorescence – XRF

List of Publications

Journal Publications (published)

1. **Güleç Fatih**, Meredith Will, Snape E. Colin, "Progress in the CO_2 Capture Technologies for Fluid Catalytic Cracking (FCC) Units – A Review", Frontiers in Energy Research, 8, 62, **2020**.

2. **Güleç Fatih**, Meredith Will, Sun Cheng-Gong, Snape E. Colin, "Demonstrating the applicability of chemical looping combustion for the regeneration of fluid catalytic cracking catalysts", Chemical Engineering Journal, 389, 124492, **2020**.

3. **Güleç Fatih**, Meredith Will, Sun Cheng-Gong, Snape E. Colin, "A Novel Approach to CO_2 Capture in the Fluid Catalytic Cracking – Chemical Looping Combustion", Fuel, 244, 140-150, **2019.**

4. **Güleç Fatih**, Meredith Will, Sun Cheng-Gong, Snape E. Colin, "Selective low temperature chemical looping combustion of higher alkanes with Cu- and Mn-oxides", Energy, 173, 658-666, **2019**.

Conference Presentations

1. **Güleç Fatih**, Meredith Will, Snape E. Colin, "Reducing CO_2 Emissions from Fluid Catalytic Cracking Units in Oil Refineries by Integration with Chemical Looping Combustion", 1st The European Conference on Fuel and Energy Research and its Application, Nottingham, UK, 2021 (Oral-accepted).

2. **Güleç Fatih**, Meredith Will, Snape E. Colin, "Capturing CO_2 Emissions from Oil Refineries – The Integration of Chemical Looping Combustion (CLC) into Fluid Catalytic Cracking (FCC) Units", ACS National Meeting, Philadelphia, USA, 2020 (Online).

3. **Güleç Fatih**, Meredith Will, Sun Cheng-Gong, Snape E. Colin, "Utilisation of Chemical Looping Strategy in Fluid Catalytic Cracking Unit", CCUS Network Conference by UKCCS Research Centre, Cardiff, UK, 2019 (Poster).

4. **Güleç Fatih**, Meredith Will, Sun Chen-Gong, Snape E. Colin, "Assessing the CO_2 Capture Technologies in the Fluid Catalytic Cracking Unit: Integration of Chemical Looping Combustion", Energy For Life Conference, Energy Technologies Research Institute, Nottingham, UK, 2019 (Poster).

5. **Güleç Fatih**, Meredith Will, Sun Chen-Gong, Snape E. Colin, "A Novel Approach to CO_2 Capture in the Fluid Catalytic Cracking Unit: Chemical Looping Combustion", 12th European Conference on Coal Research and Its Applications, Cardiff, UK, 2018 (Oral).

Chapter 1
Introduction

1.1 Background on global CO_2 emissions and capture technologies

The increase in greenhouse gas (GHG) emissions in the atmosphere has escalated global warming [1], which is the most critical environmental issue faced by the civilisation. Fossil fuels, namely coal, oil, and natural gas, are the primary source of carbon dioxide (CO_2) emissions, which is the primary GHG [2, 3]. Atmospheric CO_2 concentration considerably increased over the past century up to 416 ppm at the beginning of 2020 [2]. An atmospheric CO_2 concentration higher than 750 ppm is predicted by 2100 unless sustained mitigation efforts are implemented in the next decades [3].

The upward trend of CO_2 emissions has been associated with the use of fossil fuels for energy production [2, 4]. In the industrial sector, power plants and a variety of industrial facilities such as cement, iron-steel, petrochemical, and refineries are the primary sources of CO_2 emissions [5]. In these processes, fuel is fired with air in a combustion chamber as this is the most economical technology to exploit the energy in the fuels [6]. Power plants have the highest CO_2 emissions, roughly 78%, and the heavy industries are responsible for much of the rest, approximately 22% [1, 2, 6-10]. Among these industries, oil refineries account for 4-6% of the global CO_2 emissions [11, 12], mainly because they are the second-highest energy consumers. Industrial units such as process heaters and boilers, sulphur recovery, hydrogen production, and fluid catalytic cracking (FCC) are the main sources of CO_2 in industrial applications [13].

Owing to the negative environmental impacts of CO_2, technological options including Carbon Capture and Storage (CCS) have been proposed to meet the increasing energy demand and reducing net CO_2 emissions into the atmosphere [14]. CCS technologies

(post-combustion, pre-combustion, and oxy-combustion) can capture the CO_2 released from these industries.

Based on the characteristics of the FCC process, it is possible to capture the CO_2 from flue gas released from an FCC regenerator equipped with post-combustion methods such as amine scrubbing [15, 16]. Despite post-combustion is a mature technology for CO_2 capture from FCC, thanks to its wide applications in industrial scales, other processes, notably oxy-combustion and chemical looping combustion (CLC), offer lower energy penalties [17, 18]. In FCC-oxy-combustion, oxygen mixed with recycled CO_2 is used rather than air to oxidise the coke which deposited on the FCC catalyst. While oxy-combustion is a promising technology for CO_2 capture from the regenerator of FCC, the process conditions and effect of CO_2 on coke regeneration are needed to be improved before commercial applications [19].

The CLC process, where metal oxides are used as an oxygen supplier rather than air to combust the fuel stream [20], is an alternative CO_2 capture method for FCC. CLC has been indicated as an energy saving alternative process compare to post- and oxy-combustion capture technologies [21]. In CLC, air and fuel are never mixed [22]. Therefore, the technique does not require a separation process [20, 23], unlike the CO_2 separation unit for both post-combustion and pre-combustion methods [24], or the air separation unit for oxy-combustion methods [25].

Even though CLC has shown as an alternative energy saving CO_2 capture technology, there was no technical report or economic evaluation about the feasibility of CLC for the regenerator of FCC units. Therefore, this thesis is the first research assessing the applicability of CLC for FCC as an innovative approach for CO_2 capture from the regenerator by modifying conventional FCC units and FCC catalysts.

1.2 Aims and objectives

This study aims to assess the applicability of CLC as an innovative approach for CO_2 capture from the regenerator of an FCC unit. This new CLC-FCC concept aims to develop

the next generation of FCC units to optimise CO_2 capture with the addition of reactor, a metal oxidiser (air reactor).

The objectives of this study were;

- To develop the new generation FCC catalysts modified by oxygen carriers such as Cu-, Co-, and Mn-based to use in the novel CLC-FCC concept. Mechanical mixing and impregnation methods were employed to prepare the new generation of CLC-FCC catalysts to investigate in both cracking and combustion sections.

- To characterise the chemical and physical properties of the oxygen carrier modified FCC catalysts developed in this research. X-ray diffraction (XRD), Scanning Electron Microscopy/Energy-Dispersive X-ray Spectroscopy (SEM-EDS), X-ray Fluorescence (XRF), N_2 adsorption-desorption, Elemental analysis, and Pyridine adsorbed Fourier transform infrared spectroscopy (IR-Py) were employed to characterise the new generation of CLC-FCC catalysts and the results compared with the commercial FCC catalysts.

- To demonstrate the effects of the oxygen carrier modified with FCC catalysts (mechanically mixing and impregnation) on the cracking reaction. The cracking activity of new generation CLC-FCC catalysts were tested in a fixed bed microactivity test unit suggested by ASTM D3907, "Standard test method for testing FCC catalysts by microactivity test" to demonstrate which kind of oxygen carriers have no adverse effect on the cracking reaction as required for the application of the novel CLC-FCC concept.

- To demonstrate the combustion activity of the coke (or regeneration activity of FCC catalysts) with oxygen carriers. The CLC tests of coke deposited on FCC catalysts were investigated with oxygen carriers (both bulk and impregnated on FCC catalyst) in a), thermogravimetric analyses (TGA), a fixed-bed reactor, and a fluidised-bed reactor to identify the combustion profiles of the cokes with different oxygen carriers and conditions.

1.3 Thesis structure

Following the introduction section, seven further chapters have been presented in this thesis as follows,

Chapter 2 – Literature review: This chapter reviews the literature on the fundamentals of CO_2 emissions and capture technologies, and future scenarios for the CO_2 emissions. Further, it informs the contribution of industries to the CO_2 emissions and suggests capture technologies. It also presents an introduction of a FCC unit and detail studies on the current CO_2 capture opportunities from FCC. Additionally, it highlights the research on the fundamentals of CLC, which is a novel CO_2 capture technology. Part of this literature review has been published in *Frontiers in Energy Research, 2020 (8, 62)[26]*.

Chapter 3 – Proposed application of CLC to FCC units: This chapter presents the information about the proposed application of CLC to FCC units. The working principles of the new generation of CLC-FCC units are clarified and demonstrated, and the advantages of the suggested process described in this chapter.

Chapter 4 – Material and experimental methods: This chapter highlights the description of the materials and experimental methods within the scope of the research project. First, the catalyst modification methods (mechanically mixing and impregnation) and conditions are presented. Then the equipment and conditions for the catalytic cracking activity test of the prepared catalysts are described. Following that the CLC conditions and material for the combustion of coke deposited on FCC catalysts with oxygen carriers are presented. Then the techniques used to characterise the prepared catalysts before and after cracking tests are stated.

Chapter 5 – Cracking activity test of modified FCC catalysts: This chapter presents the results and discussion from the catalytic cracking activity tests of the prepared catalysts (oxygen carriers modified FCC catalysts) with n-hexadecane cracking in fixed-bed microactivity test (MAT) reactor. This chapter also presents the characterisation results of the prepared catalysts before and after testing in the cracking. These results

were published in the first parts of the papers in *Chemical Engineering Journal, 2020 (389, 4124492) [27] and Fuel, 2019 (244, 140-150) [28]*.

Chapter 6 – Chemical looping combustion tests of FCC coke: The chapter demonstrates the results and discussion about the combustion of FCC coke with oxygen carriers. In the first part, the TGA tests of model coke combustion with oxidised oxygen carriers (bulk) are presented. Following that the fixed-bed and fluidised-bed tests for the combustion of coke deposited on FCC catalysts (and reduced oxygen carriers modified FCC catalysts) with the oxidised oxygen carriers (both bulk and impregnated on FCC catalysts) are presented. These results were also published in the second parts of the papers in *Chemical Engineering Journal, 2020 (389, 4124492) and Fuel, 2019 (244, 140-150).*

Chapter 7 – Selective low temperature CLC of higher alkanes with Cu- and Mn-oxides: The chapter presents the results and discussion about how a higher hydrocarbon (alkanes) can be selectively combusted with oxygen carriers (and Mn-based oxides) in a fixed bed MAT reactor at relatively low temperatures. This phenomenon was discovered during the tests; cracking of n-hexadecane over oxidised oxygen carriers modified FCC catalysts. The results were also published in *Energy, 2019 (173, 658-666) [29]*.

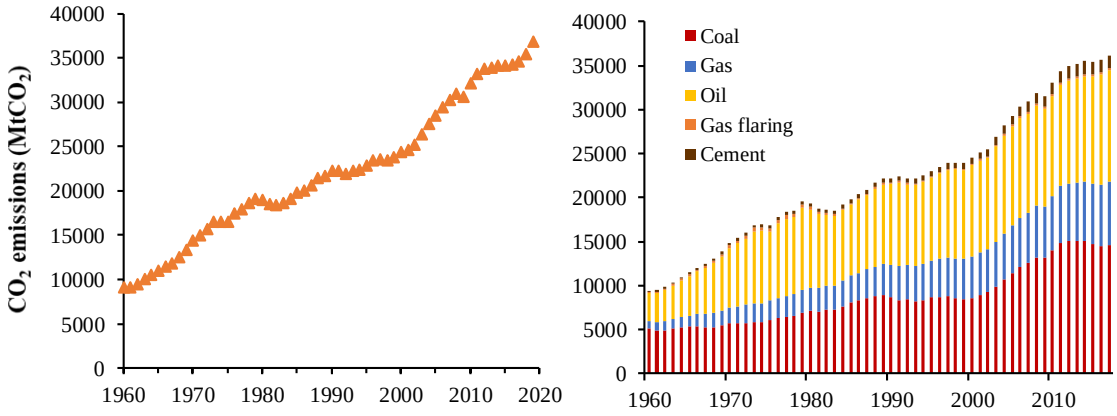
Chapter 8 – Conclusions and future work: This chapter summarises the main conclusions regarding the applicability of CLC to FCC as a novel CO_2 capture technology. Additionally, it concludes the selective low temperature combustion of higher hydrocarbons using CLC technology. The outline recommendations for future work are also included in this chapter.

Chapter 2

Literature Review

2.1 Fundamentals of CO_2 emissions

The concentration of CO_2 in the atmosphere has risen dramatically throughout the 1900s. According to the International Energy Agency (IEA) report [1], the annual CO_2 emissions have significantly increased to over 14 $GtCO_2$ in 1970 [1] and reached over 37 $GtCO_2$ in the following 50 years, in 2019 (Figure 2.1) [4].



a) Trend in CO_2 emissions **b)** CO_2 emissions by source

Figure 2.1. Trends in CO_2 emissions from 1960 to 2019 [4].

In 1960, the top three countries with the highest CO_2 emission rates were the United States of America (2.8 $GtCO_2$), Russia (0.89 $GtCO_2$) and Germany (0.81 $GtCO_2$). However, in 2018, China emitted the highest amount of CO_2 (approximately 10.1 $GtCO_2$), followed by the United States of America (5.4 $GtCO_2$) and India (2.6 $GtCO_2$) (Figure 2.2) [4, 9, 30, 31].

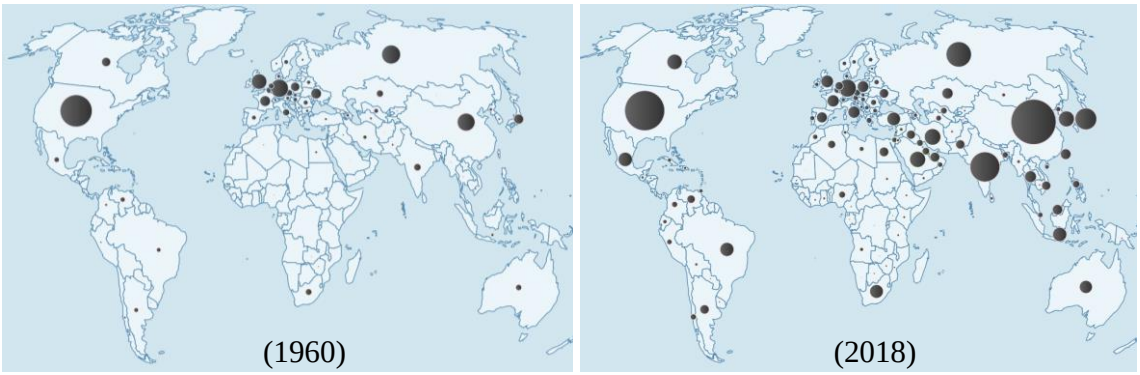


Figure 2.2. CO_2 emissions by region in 1960 and 2018 [32].

Combustion processes such as power plants, furnace in industries, cement kilns, and iron and steel production plants result in the most considerable CO_2 emissions. In this type of large-scale processes, fuel is mostly combusted using air since this is the most economical way to exploit the energy in the fuels [6]. However, using air during the combustion increases the CO_2 emissions and complicate the separation process of CO_2 from flue gases i.e. CO_2, N_2, O_2, CO, NO_X, SO_X. In 2018, electricity and heat production had the highest CO_2 emissions (42%, almost half of it for industrial requirements [2]), transportation (25%) and industrial activities (19%) followed as the second and the third largest global CO_2 emissions caused by fuel combustion (Figure 2.3).

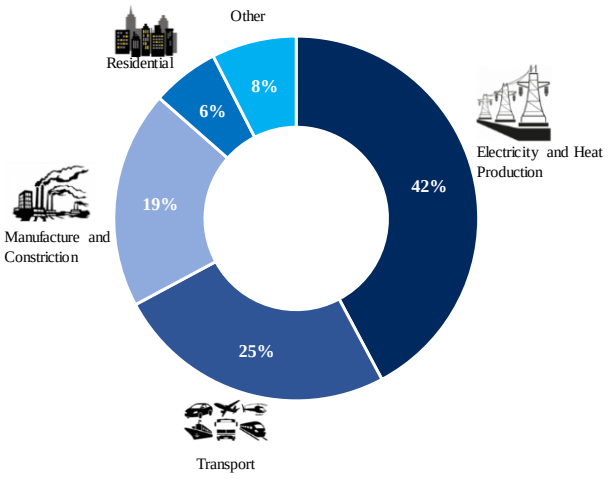


Figure 2.3. Global CO_2 emissions by sector in 2018 [33].

Consequently, the industries such as power plants, cement production, oil refining, iron-steel production, hydrogen/ammonia production and natural gas processing have the highest CO_2 emissions worldwide [1, 2, 6, 8-10]. Globally, the power sector ranks first

among the stationary CO_2 producers, heavy industries including cement, iron-steel, oil refining, are responsible for approximately 20% of global CO_2 emissions [7], of which oil refineries account for 4-6% [7, 12, 34].

2.2 Fundamentals of CO_2 capture

In the last few decades, several studies have focused on CO_2 capture as a possible solution to tackle the adverse effects of CO_2 emissions in the atmosphere [1, 2, 6, 8-10, 35-44]. The results have shown that CO_2 can be captured from the industrial processes using post-combustion [45-50], pre-combustion [24, 51-55], and oxy-combustion [35, 38, 56-58] technologies. Figure 2.4 illustrates the flow chart of these CO_2 capture processes.

The post-combustion process acts as the removal of CO_2 from the flue gas released through biomass or fossil fuels combustion. In this system, CO_2 is separated from the flue gas using absorption (amines, advanced amines, aqueous ammonia and ionic liquids), adsorption (metal-organic frameworks, activated carbon, zeolites), and membrane-amine hybrid technologies. Subsequently, the captured CO_2 can then be stored in a reservoir, and the flue gas (without CO_2) vents into the atmosphere [6].

In the pre-combustion method, the fuel reacts with oxygen or air and/or steam to create a synthesis gas or fuel gas, including carbon monoxide and hydrogen. The carbon monoxide produced also reacts with steam to produce more hydrogen and CO_2. This reaction occurs in a shift reactor, a type of catalytic reactor. After that, CO_2 might be separated using a chemical or a physical absorption process. At the end of the separation, hydrogen fuel may be used in energy production [6]. Pre-combustion capture technologies are more efficient than post-combustion technologies owing to an enhanced concentration of CO_2. The release of CO_2 may be decreased by more than 90% in the pre-combustion system [39].

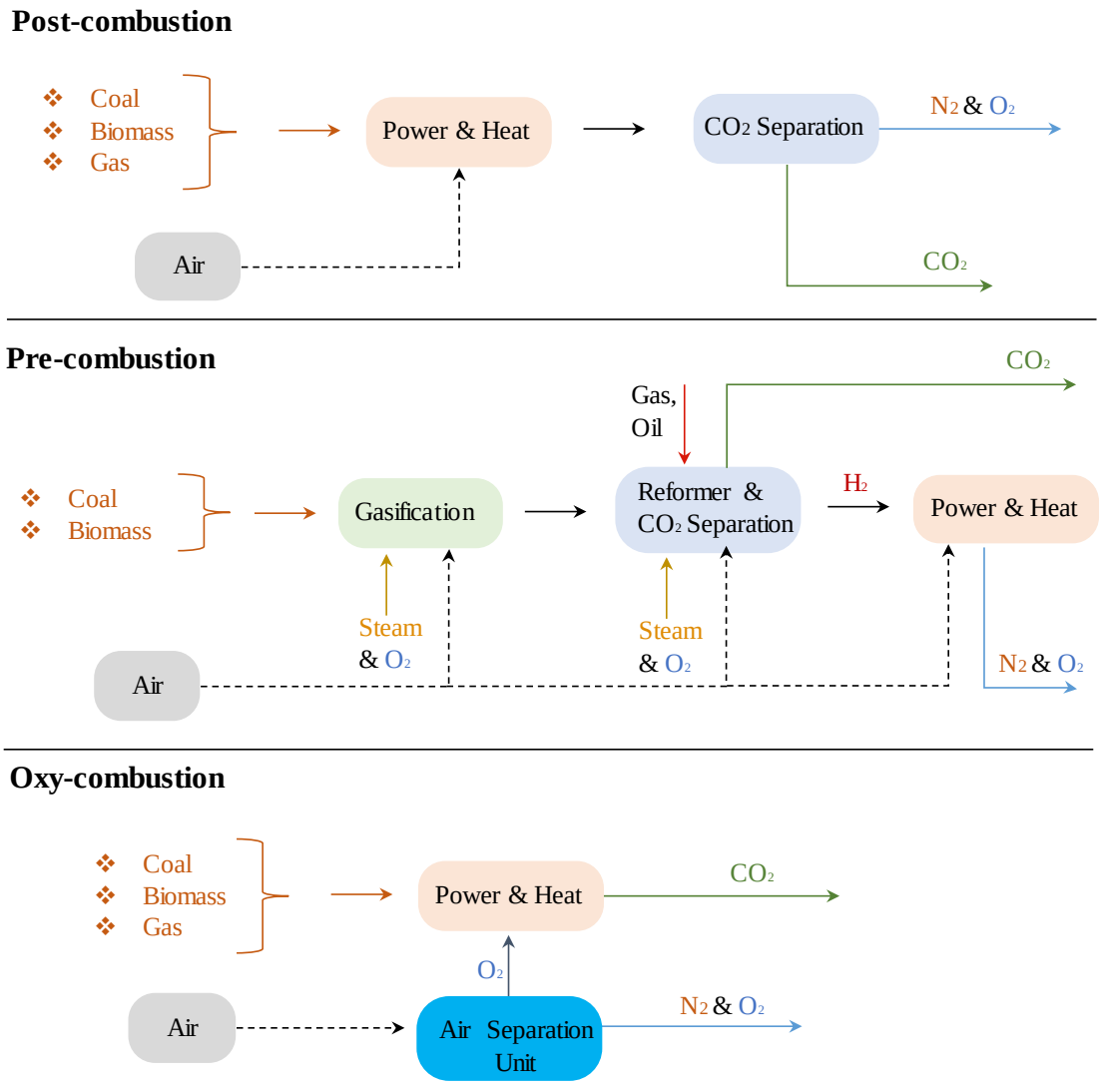


Figure 2.4. CO_2 capture approaches (post-, pre-, oxy-combustion) [14].

The other approach for CO_2 capture is oxy-combustion, in which a combustion reaction occurs with pure oxygen (95% - 99.9%) instead of air, and a mixture of CO_2 and water is formed as flue gases. The method may help to release highly pure CO_2 (90% <) in flue gases. However, an Air Separation Unit (ASU), which is needed to get pure oxygen from the air, increases the cost of the process [59]. Although elements of oxy-combustion technologies are in use in some industries such as iron and steel, FCC, and glass melting industries, the commercial scale of oxy-combustion has not yet been deployed [6].

In 2019, the Institute of global CCS identified 51 large-scale Carbon Capture and Storage (CCS) projects in the report of "The Global Status of CCS 2019" [60]. Twenty-three of these CCS facilities are either in commercial operation or under construction (Figure 2.5),

while ten of them are in advanced development using a dedicated front end engineering design and last eighteen are at early stages of development. Additionally, there are many other facilities defined as “smaller scale in operation”, “smaller scale in completed” and “test centre” as shown in Figure 2.5. The CCS projects, which are in operation and under construction, captured about 40 Mtpa (Million tonnes per annum) of CO_2 in 2019 [60].

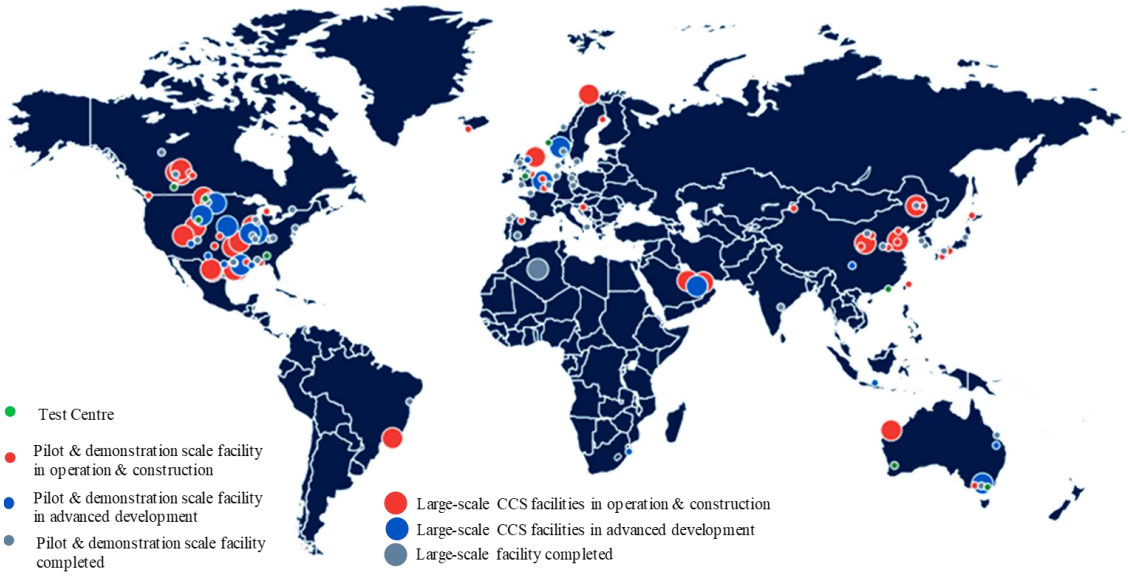


Figure 2.5. State of global CCS projects in 2019 [60].

Table 2.1. CO_2 capture in industrial processes and estimated year of maturity [61].

Sector	Technology	Estimated date
Refineries	Fluid Catalytic Cracker (FCC)	2020-2030
	Hydrogen gasification residues	2015-2020
	Hydrogen from synthetic gas reforming	Currently mature
Iron and steel	Post-combustion blast furnace	2020
	Oxy-combustion blast furnace	2020-2030
	Gas DRI	2020
	FINEX steelmaking process	2020-30
Cement	Chemical absorption	2015-2020
	Oxy-combustion	2030
	Carbonate looping	2030
High purity	Ammonia	Currently mature
	Gas processing	Currently mature
	Liquefied natural gas (LNG) production	Currently mature
	Fischer-Tropsch (FT) – synthesis coal	Currently mature
Hydrogen from fossil fuels/biomass	Coal/Biomass gasification	Currently mature
	Steam methane reforming	Currently mature

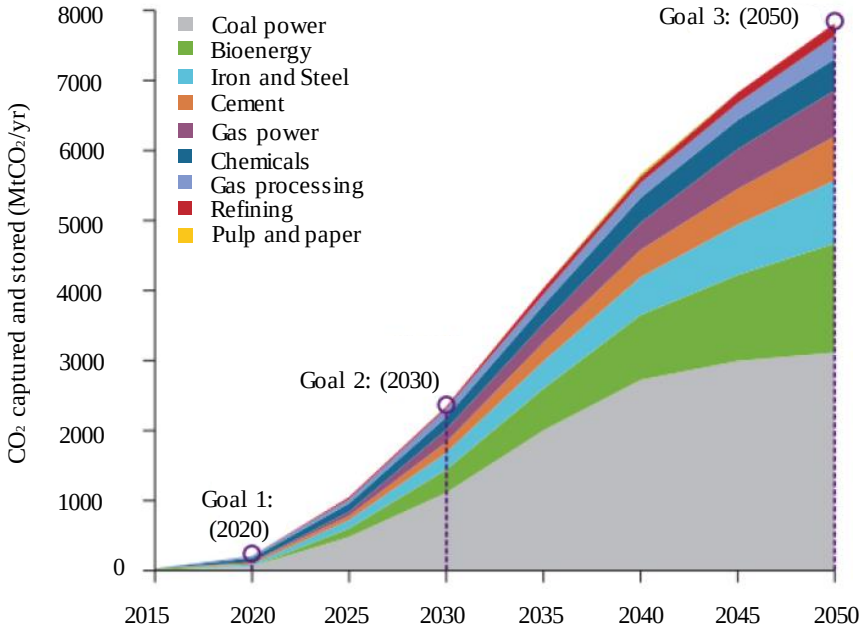


Figure 2.6. Future goals of CCS in the power and industrial sectors [62].

Table 2.1 shows the primary industrial processes emitting high amount of CO_2 and estimated years of the maturity of CCS technologies for these industries. Figure 2.6 presents the future goals for the CCS in the power and industrial sectors published by IEA [62]. It is worth noting that the IEA predicts a rapid increase in CO_2 capture and storage from 2020, reaching at least 2000 million tonnes in 2030, with a considerable jump of over 7000 million tonnes by 2050.

2.3 Introduction to fluid catalytic cracking (FCC)

CO_2 emissions in oil refining arise from a number of different processes, including Fluid Catalytic Cracking (FCC), hydrogen production, and sulphur recovery units in addition to the combustion-related sources (e.g. heaters and boilers) [13, 63]. The regenerator part of the FCC unit is one of the largest CO_2 emitters, about 20-35%, from a standard refinery [7, 63, 64]. The distribution of CO_2 emissions from the refineries is shown in Figure 2.7. In an oil refinery, FCC is one of the essential processes for the conversion of gas oils and petroleum residues into more valuable gasoline and distillate fuel products. The main aim of the process is to decrease the molecular weight of the feedstock to light cycle oil (LCO; C_{13}-C_{20}), gasoline (C_5-C_{12}), and LPG (C_3-C_4), but the production of light gases (H_2, C_1-C_2) should be minimised [65].

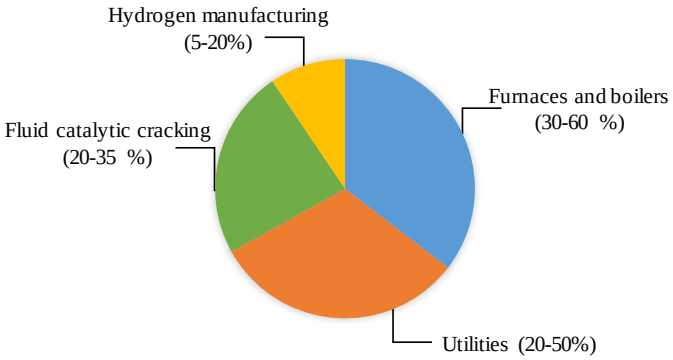


Figure 2.7. Percentage distribution of total refinery CO_2 emissions [7].

A commercial FCC unit, presented in Figure 2.8, consists of a catalytic reactor (a riser reactor) and a regenerator [66, 67]. The reactor is a riser in which the preheated feedstock is injected, vaporised, and mixed with hot catalyst and steam, with cracking temperatures of 480-600 °C which decrease up to the riser as the endothermic cracking reactions proceed. The consecutive reactions of complex FCC feedstock leading to the final FCC products (Figure 2.9) were presented by Vogt and Weckhuysen [68].

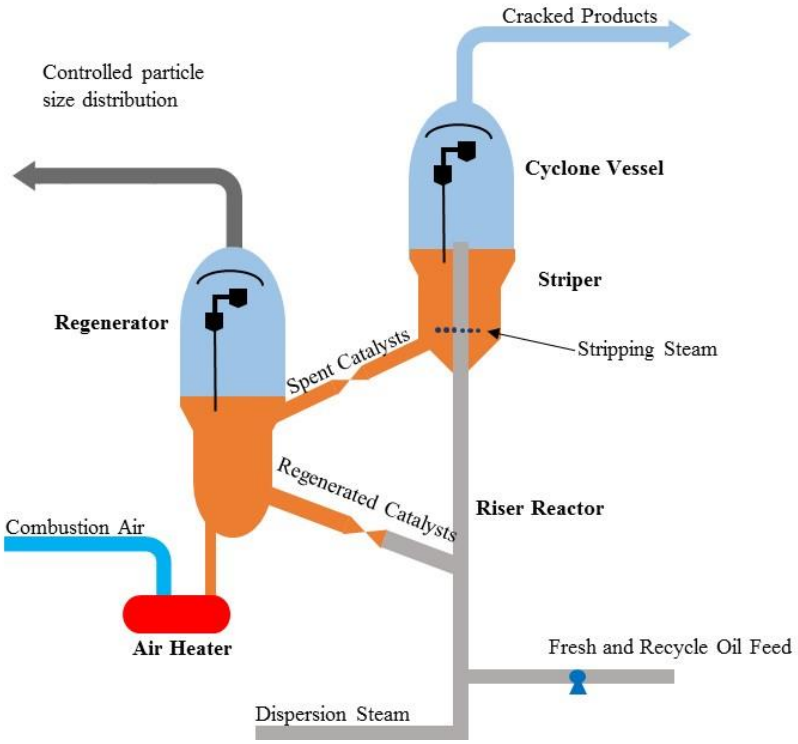


Figure 2.8. A typical FCC unit [65, 69].

After the riser reactor, the gas-phase cracked products and catalysts powders are separated in the disengagement zone, a cyclone. The gas-phase products are then sent to a fractional column while the coke deposited catalysts are stripped with steam to remove volatiles and then sent to the regenerator where the coke is combusted with air in a controlled manner at temperatures typically close to 750 °C. After regeneration, coke free catalysts are sent back to the riser; thereby, the cycle is completed. Combustion of the coke generates heat to sustain the endothermic cracking reactions in the riser, so the system is thermally balanced. The concentration of CO_2 in the flue gas is 10-20 vol.% with a low concentration of CO (0-5%) in the full combustion mode. Additionally, the flue gas contains 50-200 vppm of NO_x and 300-600 vppm of SO_x [65, 69].

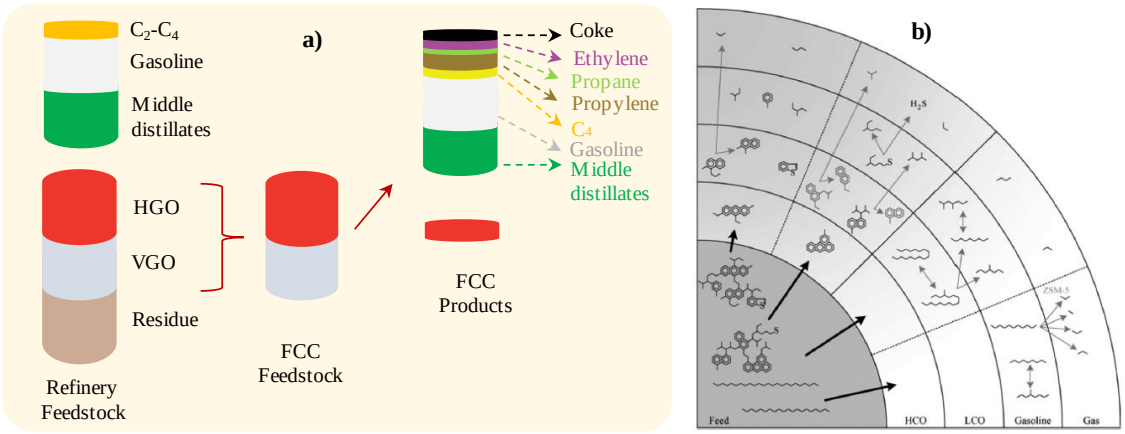


Figure 2.9. a) FCC products from the refinery feedstock and b) consecutive cracking reactions of complex FCC feedstock leading to the final FCC products [68].

The chemical and structural composition of an FCC catalyst was presented by Vogt and Weckhuysen [68], as demonstrated in Figure 2.10. Generally, type Y zeolite-based catalysts are the primary catalyst used for the cracking reaction in FCC units. The zeolites can be modified with rare earth metals to increase acidity and improve thermal stability and dealuminated to provide even greater stability. Type Y zeolite catalysts also comprise an aluminosilicate matrix with mesoporosity and some acidity to crack larger molecules, clay to improve physical strength and a binder [65]. FCC units have been faced with increasingly stringent quality emission standards that require lower emissions of CO, NOx and SOx, and this together with the trend to heavier residue feedstock containing Nickel (Ni) and Vanadium (V) has resulted in many innovations in catalyst formulations

both maximise product selectivity and control these pollutants [65]. An FCC catalyst should have the critical properties, shown in Figure 2.11.



Figure 2.10. Typical chemical and structural composition of an FCC particle [68].

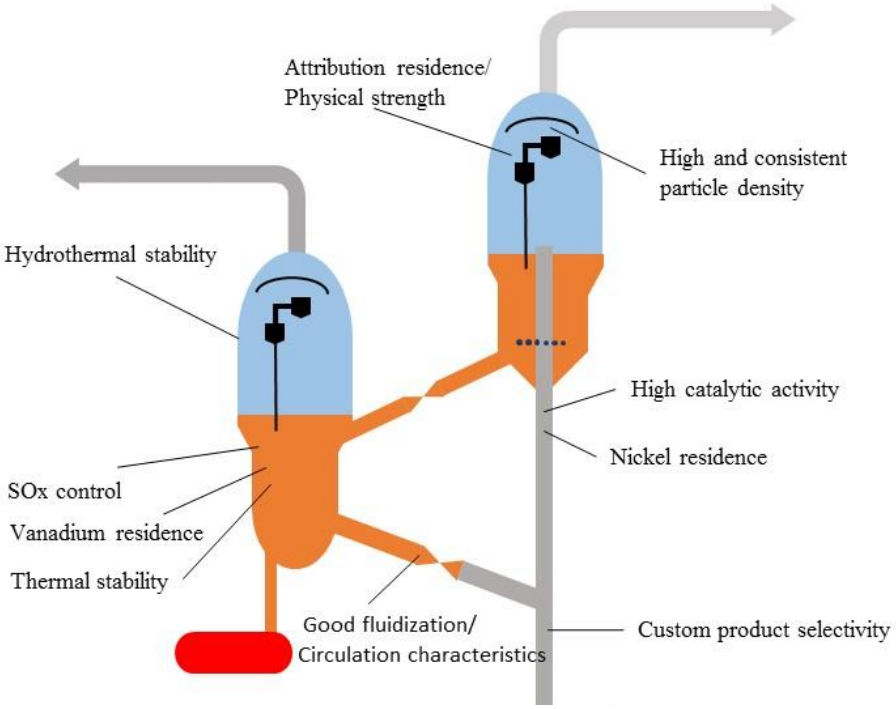


Figure 2.11. Catalyst properties required for the FCC unit [65].

Similar to the other industrial catalysts, selectivity, activity, attrition resistance, and durability are the key performance attributes of FCC catalysts. Laboratory scale fixed-bed, fixed-fluid bed or fluid transport of riser reactors have been ordinarily used to evaluate activity and product selectivity of an FCC catalyst [65, 70-75]. The micro activity fixed bed reactor system is described in ASTM D3907 [76].

2.4 CO_2 capture technologies from an FCC unit

As described in the introduction, oil refineries are the third-highest CO_2 emitter after power plants and cement industries [7, 34]. N_2O (0.08%) and CH_4 (2.25%) are the other greenhouse gases which are emitted by refineries besides CO_2 (97.67%) [63]. The CO_2 produced in the refineries come from several units such as FCC, hydrogen production, sulphur recovery plants in addition to boilers and process heaters (combustion-related CO_2 sources) [16, 77]. Although the FCC system is one of the most important units for a refinery, the regenerator part of FCC is responsible for roughly a quarter of standard refinery CO_2 emissions at the refinery [13]. For instance, a medium-size FCC unit, which has been fed 60,000 barrels per day (bpd), emits almost 0.5 million tonnes of CO_2 per year to the atmosphere [78]. Therefore deploying CO_2 capture to FCC can play a crucial role in fully decarbonising oil refinery operations.

Based on the characteristics of the FCC process, post-combustion capture and oxyfuel combustion have already been suggested to capture the CO_2, released from the regenerator of FCC units. In FCC-post combustion capture, the CO_2 in the flue gas can be captured using an amine scrubbing method. In FCC-oxyfuel combustion capture, oxygen mixed with recycled CO_2 is used instead of air to oxidise the coke that deposited on the FCC catalyst during cracking reaction. In addition to these technologies, Mace et al. [79] suggested changing the regenerator in a FCC unit from a combustor to a steam gasifier to produce syngas (CO and H_2) rather than H_2O and CO_2 with gasification of coke, in which the oxygen ratio may be reduced by increasing the ratio of CO_2/O_2 or H_2O/O_2 in the regenerator feed. However, Mace et al. [79] also highlighted some serious questions about the regeneration of catalysts, the reverse Boudouard reaction without poisoning the catalysts, maintaining the heat balance on FCC unit, additional combustion source to provide all of the process heat, required partial pressure of H_2O and CO_2 etc.

Although gasification of the coke deposited on FCC catalyst is an alternative way to CO_2 capture, the uncertainty of the process conditions and lack of experimental study make it difficult to compare this process with other suggested technologies. On the other hand, the coke deposition on FCC catalyst, pre-combustion cannot be applied to FCC [80].

2.4.1 Application of post-combustion for FCC units

Post-combustion is one of the CO_2 capture technologies suggested for the FCC regenerator [16, 19, 81-87] where studies demonstrate that the technology can be retrofitted to the regenerator flue gas line containing 10-20% CO_2 [86, 87]. Straelen et al. [5] reported a case study on the deployment of post-combustion CO_2 capture at a complex, large-scale refinery, consisting of a hydrogen production unit, a fluid catalytic cracker, and a group of smaller and larger utility plants, handling in the range of 400,000-500,000 bpd. The results demonstrated that application of post-combustion to refineries is technically feasible. Miracca and Butler [19] described a system for an FCC unit with CO_2 capture modifications established downstream from the FCC unit, as presented in Figure 2.12. In this system, the flue gas, which is released from the regenerator, is fed to an amine scrubbing system by a flue gas blower. The CO_2 is chemically absorbed by an aqueous amine solution and then a very high purity (99.5% vol.) CO_2 is desorbed in the stripper unit. The results of the study illustrated that 85% of the CO_2 can be captured from flue gas using an industrial post-combustion capture technology with a suitable amine solvent [19].

Digne et al. [16] undertook a techno-economic evaluation of a commercial post-combustion CO_2 capture technology, named HiCapt$^+$ (Figure 2.13) developed by *IFP Energies Nouvelles* and *PROSERNAT*, for FCC flue gas. The commercial HiCapt$^+$ post-combustion CO_2 capture process consists of three main part; absorber, stripper, and CO_2 compression units, as presented in Figure 2.13. A case study for a capacity of 60,000 bpd was considered to evaluate HiCapt$^+$. As for any amines scrubbing operation, HiCapt$^+$ process consists of three central units; the absorber, stripper, and CO_2 compressors. The process was described as follows; flue gas, which is cooled down to 50 °C by a water quench tower, is introduced at the bottom of the absorber at atmospheric pressure.

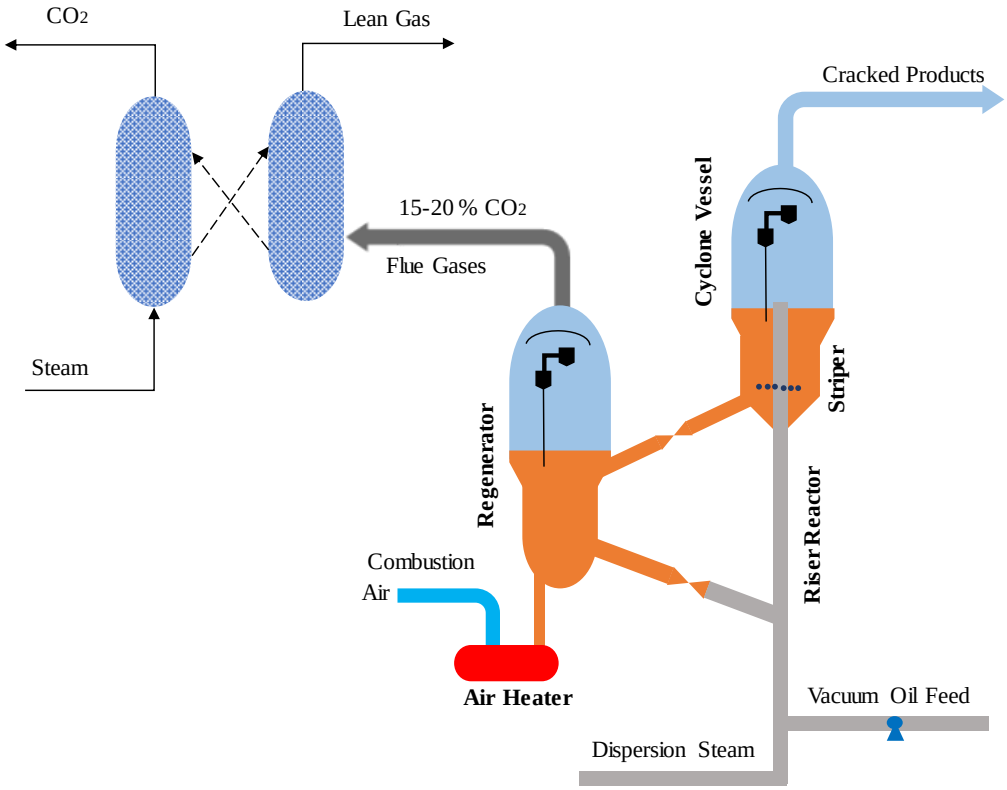


Figure 2.12. Post-combustion capture in an FCC unit [19].

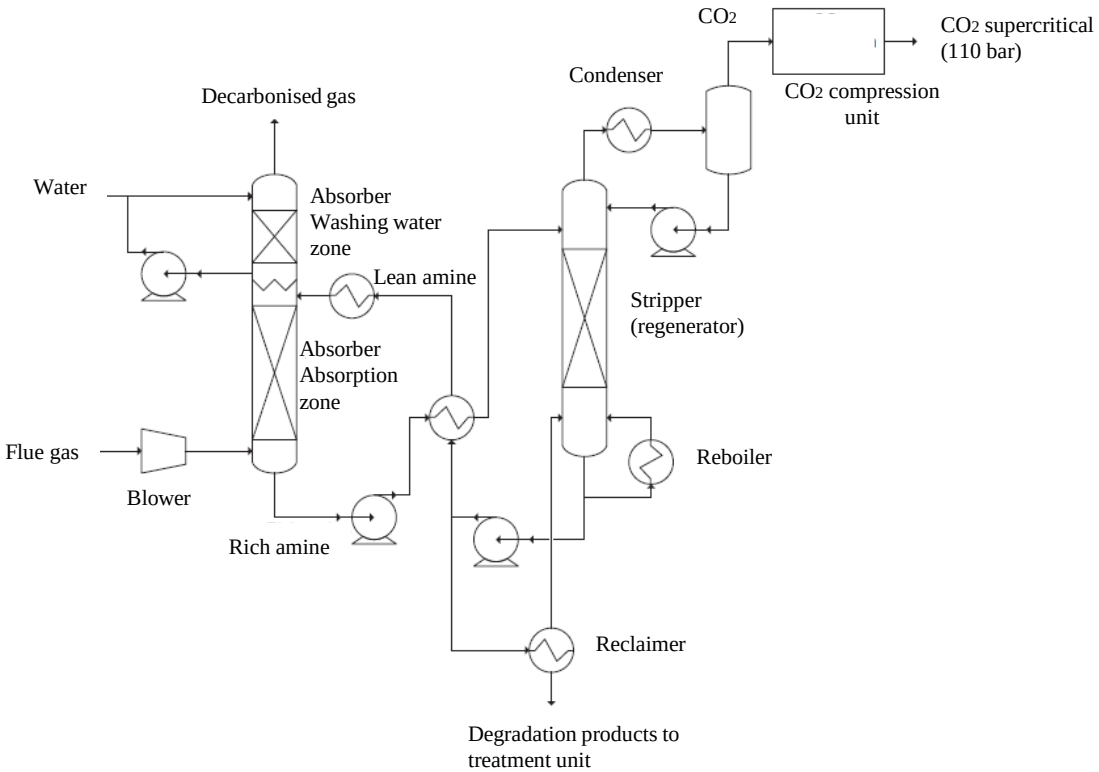


Figure 2.13. Simplified process flow diagram of HiCapt^{+} process [16, 88].

The lean solvent is an aqueous solution containing 40 wt.% of monoethanolamine (MEA) also enters at the top of the absorber. The CO_2 in flue gas diffuses to the solvent and react with MEA. The gas described as a decarbonised is then sent to the washing section zone of the absorber. In this section, MEA in the vapour is recovered by water washing. Decarbonised flue gas is, then, released to the atmosphere from the top of the absorber. After a heat recovery exchanger, the solvent highly loaded with CO_2 is introduced to the regenerator (also called the stripper) at a pressure approximately 1-2 bar. The heated solvent is pumped through the packed stripper column. The solvent recovered from the stripper column is sent to the absorber from the bottom of the regenerator, and after a condensation unit, the high purity (99.9 mol%) CO_2 separated from the solvent is delivered to the CO_2 compression unit. Here, the CO_2 compressed at 110 barg in several stages of compression and condensation [16]. From a technical point of view, because of the HiCapt$^+$ inlet specifications, 74% of CO_2 emitted from the FCC unit can be captured, approximately 14% of total CO_2 emitted from the refinery under consideration.

Wei et al. [89] have also demonstrated the integration of solvent-based carbon capture with FCC through process simulation. An industrial-scale FCC unit (1.4 million tons VGO per year) was modelled in which different heat integration options were considered to reduce the energy penalty. Further, the model was validated through industrial operating data. As demonstrated in Figure 2.14, three cases were suggested to provide the energy required for the carbon capture plant after the regenerator. In case-1, the heat required by the CO_2 capture plant was completely supplied by the excess heat of the FCC unit coming from the waste heat steam generator (WHSG) and the heat exchanger located after the chimney, which was calculated as 11.52 MWth. In case 2, 90% CO_2 capture from the regenerator was ensured using the only excess heat of the FCC unit, which was calculated as 14.67 MWth. The additional 3.15 MWth in case-2 came from the energy produced in the flue gas turbine. In case 3, 90% CO_2 capture was also secured using an additional heat supply. The results indicated that a proper design of heat integration would significantly decrease the energy penalties for CO_2 capture in FCC units.

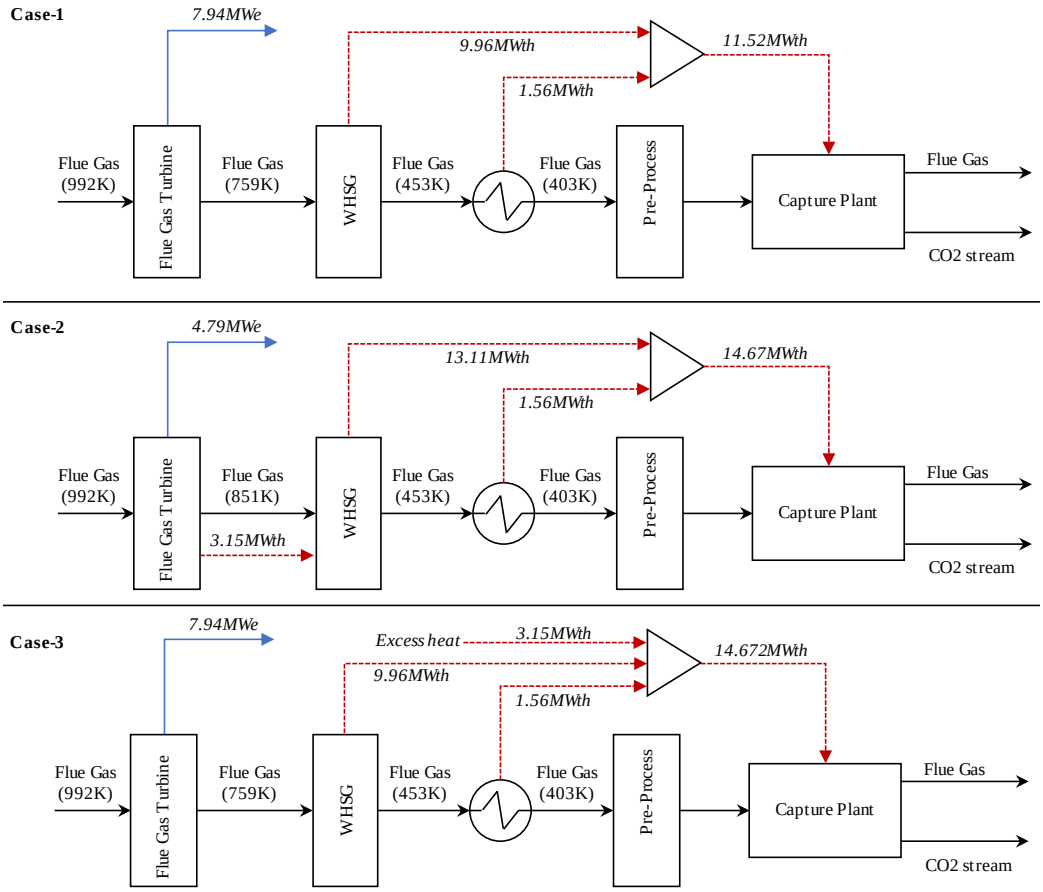


Figure 2.14. Process flow diagram presenting three different heat integration options with post-combustion capture for the flue gas released from the regenerator of the FCC unit [89].

2.4.2 Application of oxy-combustion for FCC units

Oxyfuel combustion is another technology proposed to capture CO_2 from the FCC regenerator [17, 18, 25, 77, 78, 85, 90-92]. High purity oxygen is used in the regenerator to produce a flue gas consisting of mainly CO_2 and H_2O. The application of oxyfuel combustion to the regenerator is illustrated in Figure 2.15 [18, 19]. An air separation unit (ASU) produces the pure oxygen for use in the regenerator, which is then mixed with CO_2 recycled from the dehydration unit. This mixture is then sent to the regenerator for the combustion of coke deposited on FCC catalyst. Thanks to the pure oxygen used in the combustion, the flue gas released from the regenerator consist of 85-93% of CO_2 by volume [18, 19, 78] balanced moisture which can be separated by dehydration unit. Before transportation and injection of CO_2, one more purification unit may be needed depending on the presence of other impurities such as oxygen and nitrogen in the flue

gas. Due to the flue gas compression, partial bypass to the stack is not required, which gives oxyfuel combustion an inherent boost on CO_2 recovery compared to post-combustion capture [19].

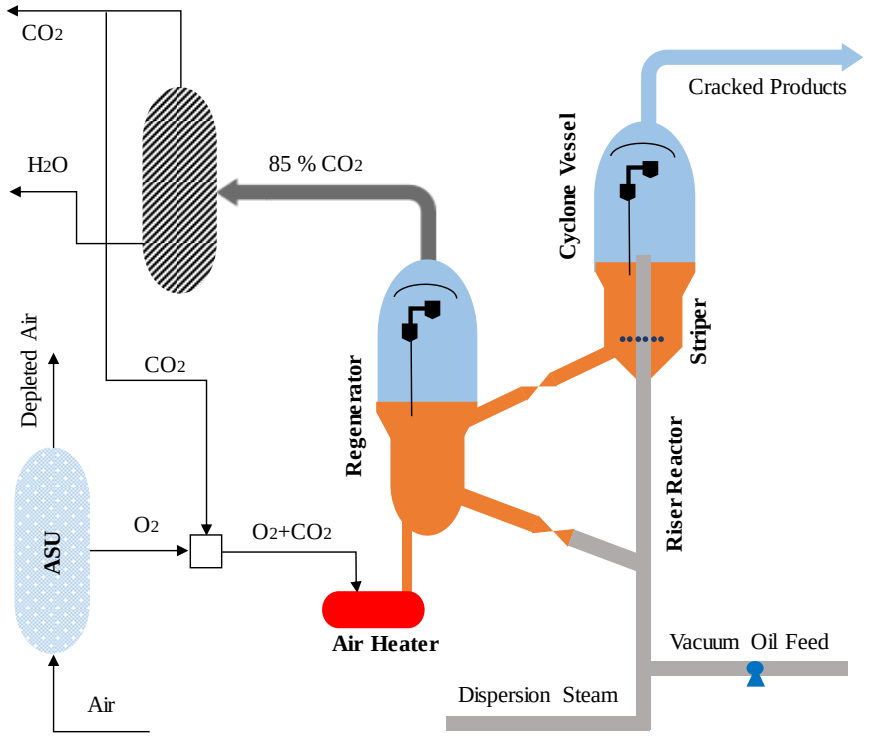


Figure 2.15. Oxy-combustion capture in an FCC unit [18, 19].

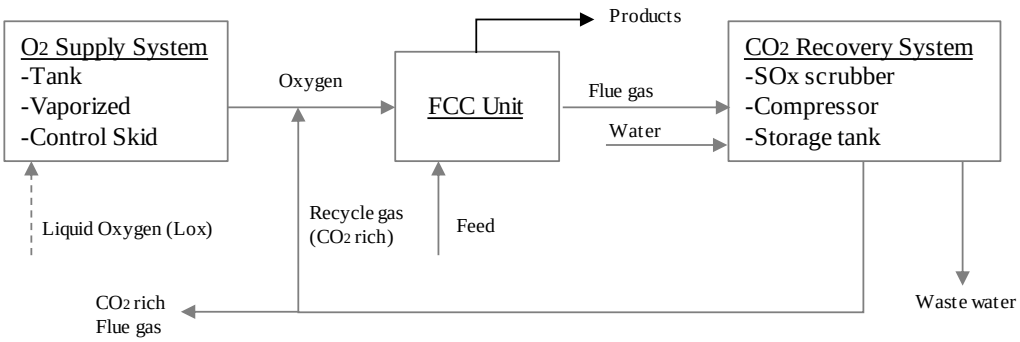


Figure 2.16. Process schematic of oxy-combustion-FCC operation [18].

Mello et al. [18, 78] also demonstrated the technical viability of oxyfuel combustion for a pilot-scale retrofitted FCC unit operated by Petrobras (Brazil). An oxygen supply system and a CO_2 recycling system was retrofitted to a pilot-scale FCC unit, as demonstrated by Mello et al. [18]. The major equipment for the oxygen supply system is a liquid O_2 tank, vaporiser system, flow and pressure control skid, gaseous O_2 injector,

and piping (Figure 2.16). Heat balance and volumetric flow rate tests were carried out with two different FCC feeds; an Atmospheric Residue (ATR) and a conventional vacuum gas oil (VGO) to define the technical feasibility of oxyfuel combustion [85]. Furthermore, catalyst balance and catalyst deactivation tests were performed using VGO.

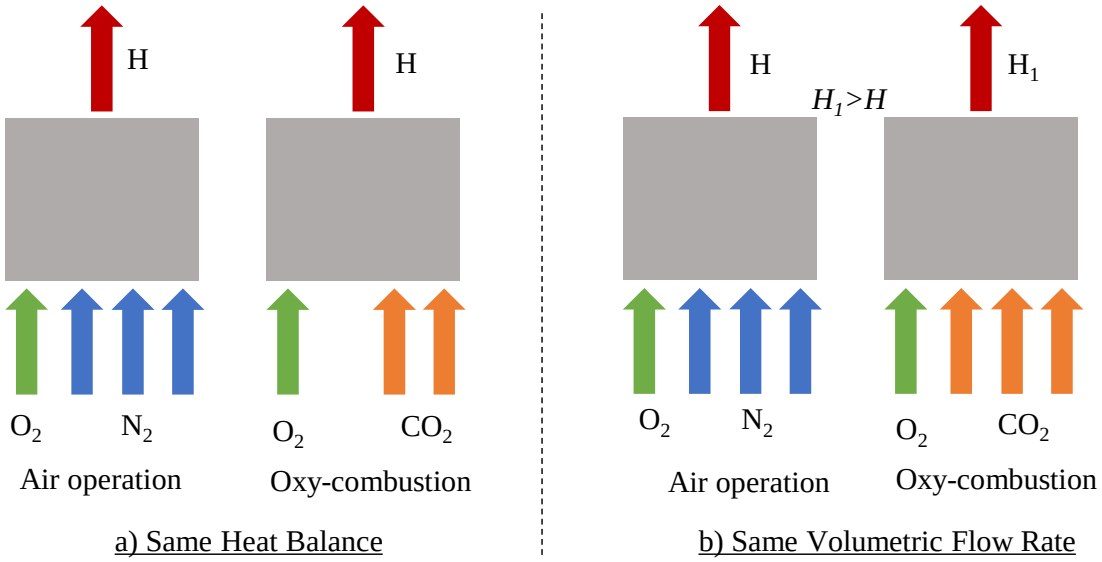


Figure 2.17. Comparison of oxy-combustion and air operation [18, 78].

Due to the properties of CO_2 and N_2, including density and heat capacity, it is essential to evaluate the same heat balance and volumetric flow rate conditions (Figure 2.17) [85]. The results demonstrated that an oxyfuel combustion FCC unit might be run in the same heat balance conditions as air operation once the CO_2 flow rate in the regenerator is kept lower than the N_2 flowrate with an air combustion. Moreover, there is no impact on the thermal balance of the unit, and very few changes occurred in the product yields. The retrofitted system may also be run with the same inert volumetric flow rate, but the thermal balance of the unit and product distributions are affected because of the heat capacity of CO_2, compared with the nitrogen, as demonstrated in Figure 2.17. The effects of using the same heat balance as for air are the temperature decrease, higher catalyst circulation and feed conversion. For the same volumetric flowrate are an increase in the distribution of gasoline and LPG because of the decreasing bottom products [78]. The catalysts did not show a significant deactivation by increasing the partial pressure of oxygen in the regenerator [18, 78].

Miracca and Butler [19] also summarised technical and economic evaluation of oxy-combustion using two different oxygen purity cases; case 1 with 97% oxygen purity and case 2 with 99.5%. The overall capture rate was 90% of CO_2 for case 1 and 99.98% for case 2 [19]. In both instances, the ASU is responsible for the highest power consumption, 11.4 and 15.9 MW, respectively. Because of the higher oxygen purity in case 2, power consumptions for flue gas recycle compression (7.5 MW), and CO_2 purification and compression (6.4 MW) are lower than those of Case-1 (9.8 and 9.1 MW, respectively). Although ASU consumes more power in case 2, the total power consumption (32.5 MW) is slightly lower than in case 1 (34.2 MW) [19].

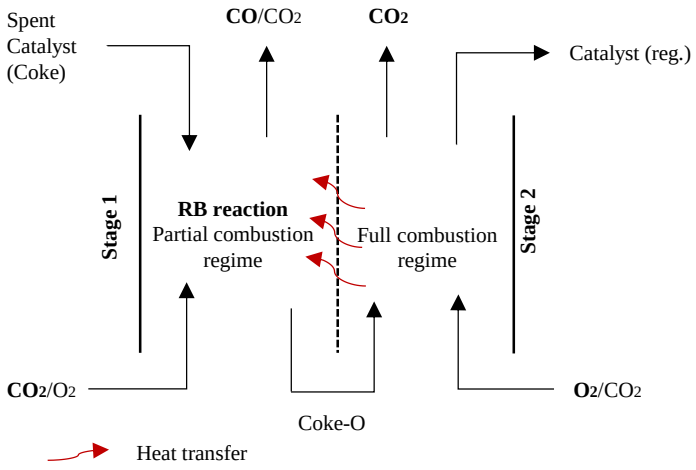


Figure 2.18. Two-stages FCC regeneration with diathermy wall provides heat transfer [92].

In addition to the feasibility studies of oxyfuel combustion for FCC, Santos et al. [91] and Silva et al. [92], focused on the reactions occurred in the regenerator. Santos et al. [91] reported mechanistic insights of coke-CO_2 reactions in the regenerator. Coke functionality, especially aliphatic carbon, having much more influence on the CO_2-coke reaction than O_2-coke reaction. Furthermore, Silva et al. [92] have explained the reverse Boudouard reaction over vanadium, lithium, magnesium, potassium, calcium and sodium modified alumina, which occurs for the coke deposited FCC catalyst. Potassium (K) and vanadium (V) modified alumina showed a synergism for the CO_2 coke reaction, which released ^{13}CO followed by ^{12}CO and $^{12}CO_2$. In reverse Boudouard reaction, ^{12}CO and $^{12}CO_2$ are affected by catalyst types and reaction temperatures. During regeneration, besides CO_2 capture, the FCC process may have an important role to supply CO for other processes [91, 92]. A two-stage regenerator system was suggested, as presented in Figure

2.18 [92]. In the first step, the Reverse Boudouard reaction would be favoured using high CO_2 and low O_2. In the second stage, residual coke would be combusted by highly pure O_2. The second stage would also provide energy to the first stage and the overall FCC process [92].

2.4.3 Comparison of post- and oxy-combustion technologies for FCC

Although post-combustion and oxy combustion are applicable for CO_2 capture, technical and economic evaluation have an important role in establishing pilot or commercial scale FCC units with low CO_2 emissions. While there is no need for any modification to the FCC regenerator under for post-combustion capture, the regenerator and its operating conditions must be modified for the application of oxy combustion.

From a technical point of view, 74% of CO_2 released from the regenerator of the FCC unit flue was captured thanks to the HiCapt$^+$ inlet specifications, presented by Digne et al. [16]. Miracca and Butler [19] and Mello et al. [18] demonstrated 85 and 90% CO_2 capture levels, respectively. Bench-scale tests for oxy combustion demonstrated the regeneration of coke with O_2 mixed CO_2 [17-19, 48, 91]. Moreover, larger-scale tests showed that oxy combustion is also technically feasible for the FCC regenerator [18, 91]. Compare to post-combustion, oxy-combustion offers much higher CO_2 capture levels depending on the oxygen purity used in the regenerator; when oxygen purity increases from 95% to 99.5%, the CO_2 capture increases from about 90.2% to 99.99%. Additionally, there are no significant changes in the stability of operation, the product profile, and effectiveness of coke burn [18]. The operation of the FCC unit with oxy-combustion is considered to be more flexible than post-combustion capture, and also it requires less area [19].

A result of the economic analysis is to the high ASU cost, the total installed cost for the oxy-combustion unit is calculated to be approximately two times higher than for a post-combustion capture unit [18]. Similarly, the total capital investment for oxy-combustion (193.3M$ - for 99.5% of O_2 purity) is estimated at ~1.5 times higher than post-combustion (133.1 M$ - amine) based on medium size of FCC unit (60,000-62,000 bpd) [17, 19, 25]. However, the total Operation and Maintenance (O&M) costs for post-combustion capture

(77.3 M$) was much higher than that for oxy-combustion (29.1 M$). The high utility cost for post-combustion capture was attributed to demand for low-pressure (LP) steam required for the amine regeneration and extra cooling tower water [25]. Additionally, the higher chemical cost for post-combustion capture was also attributed to the requirements of MEA, corrosion inhibitor, particulate filters, activated carbon to remove hydrocarbons, sodium carbonate to reclaim MEA, plus disposal costs. Such chemical costs are not required for oxy-combustion applications.

Although it is possible to decrease the total capital cost for oxy-combustion by decreasing the oxygen purity used in the regenerator, the requirement of the propane refrigeration system and larger recycling compressors resulted in an overall higher investment as noted by Mello et al. [25]. On the other hand, Digne et al. [16] and Lemaire et al. [88] indicated that the HiCapt$^+$ process using 40% MEA solution gives a 15% reduction in the cost of an amine scrubbing plant compared to using only 30% MEA. Although post-combustion capture for a FCC regenerator has a lower capital cost [83], oxy combustion indicated a lower CO_2 capture and avoided cost than post-combustion capture [17, 18]. In another study, the Inside Battery Limit cost, which is the cost of purchasing and installing all process equipment, for an FCC unit with CO_2 capture was determined to be 1.25 times higher than that of an FCC unit without capture [16].

Most of the energy consumption in post-combustion capture is due to solvent regeneration in the boiler [93]. Additionally, besides the capture solvent and technology, the concentration of CO_2 in flue gas also influences the capture cost [5]. The energy penalty (specific duty) for the application of post-combustion capture to an industrial scale FCC unit was reported as 4.2 GJ/t CO_2 (for CO_2 capture level of 90%), and this decreased to 3.8 GJ/t CO_2 with the modification of heat integration option case 1 having a CO_2 capture level of 78% (Figure 2.14, [89]). Furthermore, the novel post-combustion capture technology, HiCapt$^+$, developed explicitly for FCC units by Digne et al. [16] resulted in an energy consumption of 3.1–3.3 GJ/t CO_2, for 74% CO_2 capture. The CO_2 avoided cost was 75–110 €/t CO_2 for the application of post-combustion to a medium-sized FCC unit [17, 19]. It was also determined between 90-120 €/t CO_2 if the current amine capture technology is modified to the refineries [5]. The application of oxy-combustion to FCC was demonstrated to have a lower energy penalty than post-combustion capture of 1.8-

2.5 GJ/t CO_2 depending on oxygen purities of 95 to 99.5% [17, 19, 94]. The energy penalty for oxy-combustion arises from the ASU, oxygen and flue gas recycle compression. Further, oxy-combustion provides lower CO_2 avoided costs of 55-85 €/t CO_2 compared to post-combustion capture [17, 19].

In summary, even though post-combustion CO_2 capture for FCC is a mature technology, the overall cost per tonne of CO_2 capture appears to be significantly higher than for oxy combustion. Therefore, breakthrough technological developments, such as improved solvents, are required to make post-combustion couture more competitive [5]. Although the studies to date demonstrate that the oxy combustion can be a promising technology for CO_2 capture from the FCC regenerator, the technology still requires further improvements before commercial applications [19, 78, 85]. A high-energy penalty and extra equipment requirements are apparent with both these technologies. CLC may well be a technology that provides a unique potential for avoiding the high costs and energy penalties inherent in gas separation and CO_2 capture [17, 18]. This technology can separate the oxygen from the air without an ASU. Moreover, it has excellent potential to be competitive with post-combustion and oxy-combustion in CO_2 capturing technology. Fundamentals of CLC and its possible application method on the FCC unit are mentioned in the following two sections.

2.5 Fundamentals of chemical looping combustion (CLC)

The chemical looping combustion concept was firstly described by Richter and Knoche [95]. Figure 2.9 shows the CLC process, which is based on oxygen transfer from the air reactor to the fuel reactor via a solid oxygen carrier. In this process, air does not need to mix with fuel for combustion. Firstly, the fuel either solid or gas is introduced to the fuel reactor and oxidised to CO_2 and H_2O (as described in Reaction 2.1.) by a metal oxide (Me_nO_m) [96] which is reduced to metal (Me_n) or any other reduced form (Me_nO_{m-1}) during this reaction. After a condensation and purification step, the pure CO_2 is ready for transport and storage [97]. Subsequently, in the air reactor, the reduced oxygen carrier (Me_nO_{m-1}) is oxidised (as described in Reaction 2.2.) by oxygen in the air stream. The re-oxidised oxygen carrier (Me_nO_m) gets ready for a new combustion cycle. The flue gas

from the air reactor contains nitrogen and excess oxygen gases [97, 98]. The net reaction is illustrated in Reaction 2.3.

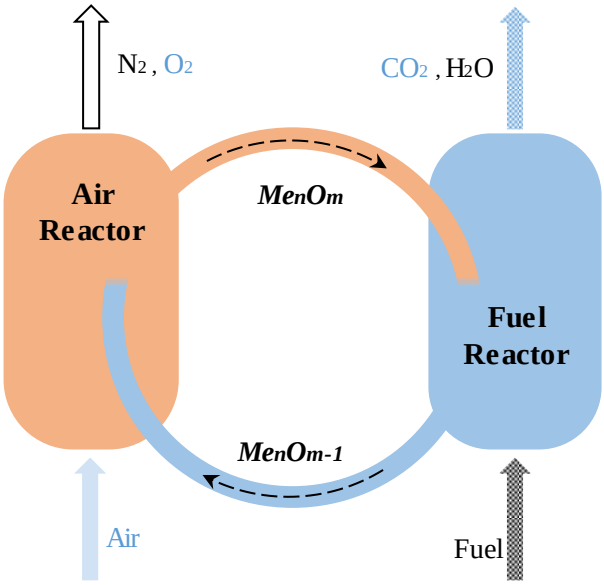


Figure 2.19. Chemical looping combustion process [22, 98, 99].

Fuel reactor : $C_xH_y + Me_nO_m \rightarrow CO_2 + H_2O + Me_nO_{m-1}$ (2.1)

Air reactor : $Me_nO_m + O_2 \rightarrow Me_nO_m$ (2.2)

Net reaction : $C_xH_y + O_2 \rightarrow CO_2 + H_2O$ (2.3)

CLC technology has been investigated with various fuels such as methane, natural gas, syngas, coal, biomass, and petroleum coke, in various size pilot-scale reactors [23, 96, 99-103]. The first application of CLC as a CO_2 capture technology was investigated in 2001 [104], and after five years, in 2006, the first CLC study with solid fuel was published [105].

The CLC studies focus on the development of oxygen carriers, reactor design, and application of CLC for fuels (solid, liquid and gas). The studies bring out that the CLC is a promising technology to generate high concentration of CO_2 in combustion and hydrogen production processes [99, 106, 107], especially when a suitable metal oxide is used as an oxygen carrier [22]. As a result of these studies, the CLC process, where metal oxides can be used as an oxygen supplier instead of air to combust the fuel stream [20], have been proposed as a potential alternative process to decrease CO_2 capture costs [21]

and energy penalties. Additionally, according to the Intergovernmental Panel on Climate Change (ICCP) report on CO_2 capture and storage, CLC is defined as one of the cheapest methods for CO_2 capture [6]. CLC is a method of indirect combustion, where air and fuel are never mixed [22]; thus, the technique does not need an additional separation process [20, 23] as the CLC method may allow for natural separation of CO_2 and H_2O from other non-condensable gases; N_2 and excess O_2 [23]. The fact that the other three techniques required a gas separation process; either CO_2 separation unit in both post-combustion and pre-combustion methods [24] or O_2 separation unit in oxy-combustion method [25]. In order to demonstrate industrial feasibility of CLC in an economic and technical perspective, suitable oxygen carriers are the critical issues for specific fuels and reactor systems.

Synthetic oxygen carriers usually arise from metal oxide (either single or combined form of metal oxides) such as Fe_2O_3, CuO, NiO, Mn_2O_3, Co_3O_4 etc. and inert binders, for instance, Al_2O_3, $MgAl_2O_4$, SiO_2, ZrO_2 [20, 96, 108, 109]. Moreover, natural minerals such as iron ore, manganese ore, and copper ore can be used as an oxygen carrier [110-112], but the natural mineral oxygen carriers generally show less reactivity compared to the synthetic oxygen carriers [96]. The oxygen carriers should accomplish the following characteristics to be feasible for industrial applications of CLC [96-98, 113];

- Sufficient oxygen transport capacity
- High reduction-oxidation reactivity
- Resistance to fragmentation and attrition
- Complete fuel conversion to CO_2 and H_2O
- Negligible carbon deposition
- Low tendency for agglomeration
- Easy preparation method and low cost
- Environmentally friendly

2.5.1 CLC mechanisms for gas and solid fuels

In the CLC technology, the gas fuels (i.e. natural gas, refinery gas or syngas) derived from gasification of solid fuels (i.e. coal, petroleum coke, biomass and solid wastes) can be

directly combusted with the oxygen carrier in the fuel reactor. According to the gas fuel combustion mechanism, the gas fuels give a reaction with oxygen carrier (MeO), and the flue gas is expected to mainly consist of CO_2 and H_2O [99] as demonstrated in Figure 2.20.

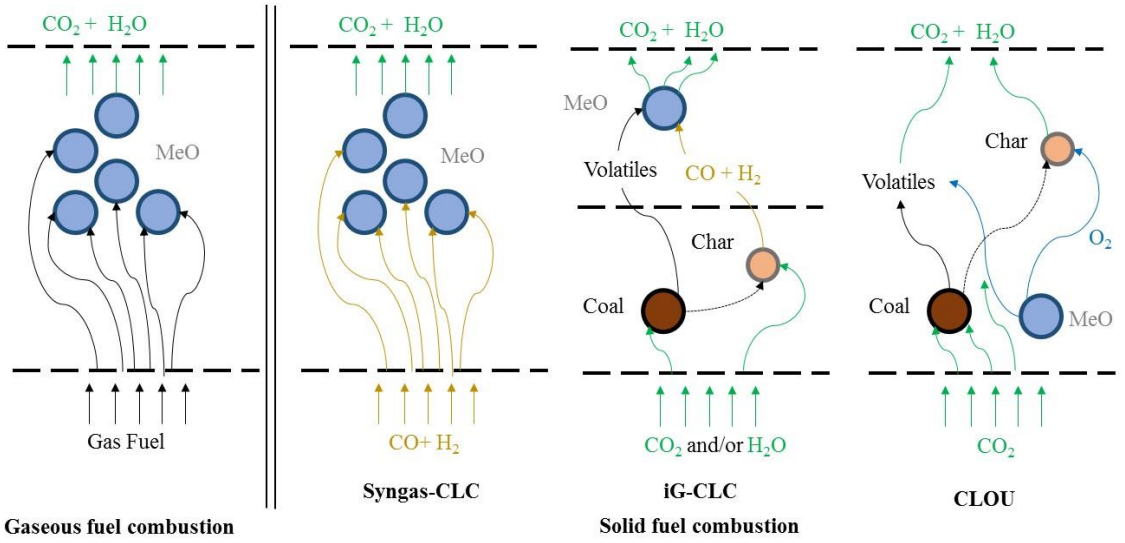


Figure 2.20. Combustion mechanisms of gas fuels and solid fuels in the fuel reactor [97, 99].

Furthermore, Figure 2.20 illustrates the CLC mechanism of solid fuels with oxygen carriers presented by Adanez et al. [97], in which the combustion of solid fuels drives by syngas-CLC, in-situ gasification CLC (iG-CLC) and/or CLC with oxygen uncoupling (CLOU), [99]. Because of the difficulties in solid-solid reactions, the solid fuel-CLC processes have been fluidised with CO_2 and H_2O, which are also gasifying agents [23]. In this way, the solid fuel tends to be gasified, and thus, the combustion ratio might increase. If the CLC concept were successful with solid fuels, it would be quite attractive with restrictions in CO_2 emissions, as there are plenty of solid fuels which are less expensive than gas fuels [23].

CLC of gas fuels: The reduction of oxygen carriers due to the combustion of gas fuels starts outside of the oxygen carriers and goes through into particles as non-catalytic gas-solid reaction systems; both oxygen carrier and gas fuel are the reactants. Mendiara et al. [114] demonstrated the reduction stages of an oxygen carrier particle, as shown in Figure 2.21.

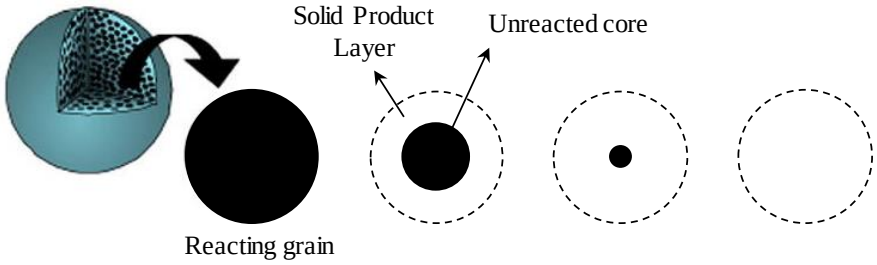


Figure 2.21. Reduction of an oxygen carrier particle during the CLC [114].

However, the reduction steps may demonstrate slight differences depending on the oxygen carriers, supports, and fuels. For instance, Cabello et al. [115] have investigated the kinetic parameters for the reduction of Fe-based oxygen carriers supported by alumina using CLC of CH_4. The reduction mechanism of Fe-based oxygen carriers, supported by alumina with CH_4 was shown in two steps. The first step is the kinetic control step by the chemical reaction in the grain surface, where a product layer of $FeAl_2O_4$ is formed. The second step is the diffusion control step through the product layer of $FeAl_2O_4$ around the grains (Figure 2.22). They reported that the reduction rate was independent of the concentration of CH_4 in the second step [115]. After the reduction of oxygen carriers, the reduced state oxygen carriers are then re-oxidised by oxygen in the air stream in the air reactor, ready for a new combustion cycle [113].



Figure 2.22. Scheme of the reduction mechanism of Fe20γAl with CH_4 [115].

Syngas-CLC of solid fuels: In the syngas-CLC process, the solid fuel is, firstly, pyrolyzed to volatile matter and char, which is then, gasified inside a gasifier (Reaction 2.4). The syngas, which is released from the gasifier, is fed to the fuel reactor [96]. After this step, the CLC works similar to gas fuel-CLC process [97]. Ahmed and Lasa [116] demonstrated the kinetic model for CLC of syngas with a Ni-based oxygen carrier, as shown in Figure 2.23. The combustion of CH_4 with Ni-based oxygen carriers loads to the

formation of H_2 and CO. Following this reaction, the high reactive species such as H_2 and CO are directly converted into H_2O and CO_2, respectively.

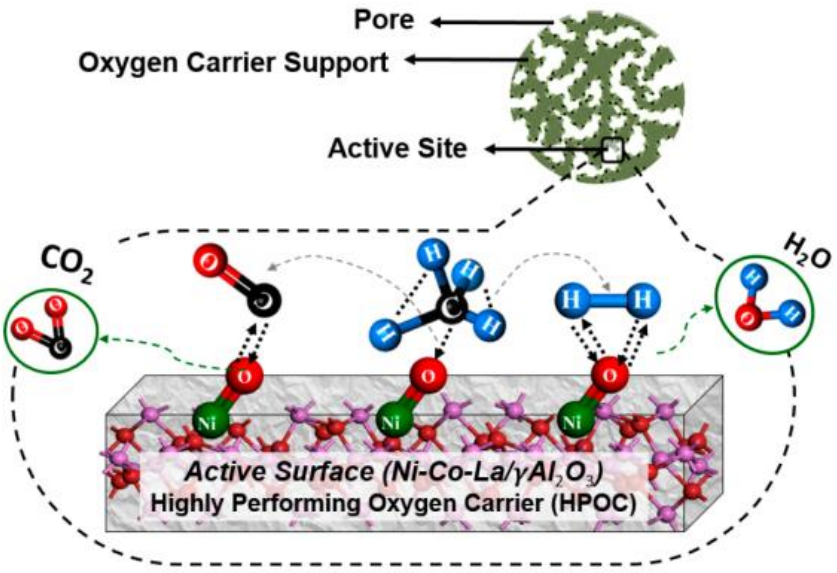


Figure 2.23. Combustion mechanism of syngas species over Ni-based oxygen carrier [116].

Other synthetic oxygen carriers such as Cu-, Mn- and Fe-based, have shown combustion reactivity with syngas components at atmospheric and pressurised conditions [96, 117-120]. Moreover, the syngas-CLC system has been accomplished in the 300-1000 W continuous process using various oxygen carriers; Ni-, Cu-, Co-based [121, 122]. The pilot-scale studies demonstrated that the CO_2 capture efficiency has reached in 95-99%, depending on the oxygen carriers used.

In-situ gasification-CLC of solid fuels: In the iG-CLC process, solid fuel is directly introduced into the fuel reactor and physically mixed with an oxygen carrier. The coal is pyrolysed to volatile matters and char in the fuel reactor (Reaction 2.4) before the combustion with oxygen carrier. The char is gasified in situ by fluidising agents H_2O and/or CO_2 in the fuel reactor, described in Reaction 2.5 and 2.6 [96]. The in situ gasification products (CO and H_2) and the volatile matters rapidly react with oxygen carriers as demonstrated in Reaction 2.8.

$$Coal \rightarrow Volatiles + Char \quad (2.4)$$

$$C_{(s)} + H_2O_{(g)} \rightarrow CO_{(g)} + H_{2(g)} \quad (2.5)$$

$$C_{(s)} + CO_{2(g)} \rightarrow 2CO_{(g)} \quad (2.6)$$

Chemical looping oxygen uncoupling (CLOU) of solid fuels: The third approach for the use of solid fuels in CLC is oxygen uncoupling (CLOU) process, where the oxygen carriers release their oxygen (Reaction 2.7). In the fuel reactor, coal is firstly pyrolysed to volatile matter and char (Reaction 2.4) as in conventional combustion. The volatile matter and char are directly combusted by gaseous oxygen (Reaction 2.8 and 2.9), released from oxygen carriers. The CLOU process is a promising technology for the solid fuel-CLC system thanks to the oxygen released from oxygen carriers.

$$2Me_nO_m \rightarrow 2Me_nO_{m-1} + O_{2(g)} \quad (2.7)$$

$$Volatiles + O_2 \rightarrow CO_{2(g)} + H_2O_{(g)} \quad (2.8)$$

$$Char + O_2 \rightarrow CO_{2(g)} + H_2O_{(g)} \quad (2.9)$$

CLOU studies have mainly focused on CuO, Mn_2O_3, and Co_3O_4 as oxygen carriers, which can release oxygen with the decomposition under temperature [97]. The oxygen uncoupling reactions of these metal oxides are given by Reactions 2.10-2.12. While the overall reaction between carbon (volatile matter and char) and oxygen carrier is exothermic for copper oxide and manganese oxide (Reaction 2.13 and 2.14), it is endothermic for cobalt oxide (Reaction 2.15) [96].

$$4CuO \leftrightarrow 2Cu_2O + O_{2(g)} \qquad \Delta H^o_{900} = 262.1\ kj/mol\ O_2 \quad (2.10)$$

$$6Mn_2O_3 \leftrightarrow 4Mn_3O_4 + O_{2(g)} \qquad \Delta H^o_{900} = 193.1\ kj/mol\ O_2 \quad (2.11)$$

$$2Co_3O_4 \leftrightarrow 6CoO + O_{2(g)} \qquad \Delta H^o_{900} = 406.7\ kj/mol\ O_2 \quad (2.12)$$

$$4CuO + C \leftrightarrow 2Cu_2O + CO_{2(g)} \qquad \Delta H^o_{900} = -132.9\ kj/mol\ O_2 \quad (2.13)$$

$$6Mn_2O_3 + C \leftrightarrow 4Mn_3O_4 + CO_{2(g)} \qquad \Delta H^o_{900} = -201.9\ kj/mol\ O_2 \quad (2.14)$$

$$2Co_3O_4 + C \leftrightarrow 6CoO + CO_{2(g)} \qquad \Delta H^o_{900} = 11.7\ kj/mol\ O_2 \quad (2.15)$$

CLC is one of the most promising technologies to CO_2 capture from industries where solid fuels are used as an energy source. CLC may also be applicable in coke cleaning technologies such as regenerator part of FCC as the coke on the FCC catalysts has quite

similar properties to solid fuels. Therefore, a novel CLC-FCC concept is described in Chapter 3.

2.5.2 CLC for gas and solid fuels

CLC of gas fuels (both natural gas and syngas produced by solid fuels gasification) have been investigated over a variety of oxygen carriers in both lab-scale units such as TGA, fixed-bed and fluidised-bed reactors and pilot-scale units. Some of the literature about the combustion of gas over oxygen carriers in continuously operated CLC units are presented in Table 2.2.

The effects of CLC operational conditions on methane combustion with Ni-, Cu- and Fe-based oxygen carriers (modified by a support such as γAl_2O_3, αAl_2O_3, $MgAl_2O_4$, and Bentonite) were investigated using pilot-scale continuous units operating at 500 W – 120 kW [113, 121, 123-131]. Adanez et al. [121] demonstrated that the CLC of methane over Ni-based oxygen carriers was successfully operated for 70 h of combustion conditions and the combustion efficiency reached 99% at temperatures in the range of 800-880 °C. It is possible to achieve the maximum combustion efficiency allowed by thermodynamic constraints using optimum conditions at 880 °C, for an oxygen carrier to fuel ratio of greater than 1.5 [121]. Kim and Son [125] also highlighted that the combustion efficiency increases with increasing temperature, and the optimum reaction temperature was reported as 850 °C in which CO and H_2 emissions from the fuel reactor were shown to be negligible. Furthermore, Kolbitsch et al. [123, 124] presented the high methane conversion over Ni-based oxygen carriers in addition to the thermodynamic maximum H_2 and CO conversion. Ryu et al. [126] also concluded that inherent CO_2 separation is possible with CLC of methane in addition to NOx free combustion.

No sign of carbon formation [121, 123, 124, 126] and agglomeration [121] were detected on Ni-based oxygen carriers used for the combustion of methane. Furthermore, no physical deformation was observed on the oxygen carrier particles [121]. The Ni-based oxygen carriers supported by Al_2O_3 consisted of two phases; NiO and $NiAl_2O_4$. The former (NiO) is more reactive than the later ($NiAl_2O_4$), although both of them are defined as active phases for oxygen transfer from the air reactor to the fuel reactor. Thus, Ni-

based oxygen carriers prepared by impregnation was concluded as a suitable oxygen carrier for the combustion of methane in a continuously operated CLC system [121].

Table 2.2. Summary of continuous CLC tests of gas fuels with a variety of oxygen carriers.

Oxygen carrier	Support	Preparation*	Facility	References
CLC of CH_4				
NiO (18%)	αAl_2O_3	IMP	500 W	Adanez et al. [121]
NiO (40%)	$NiAl_2O_4$	SD	120 kW	Kolbitsch et al. [123, 124]
NiO (60%)	Bentonite	MM	1.5 kW	Kim and Son [125]
NiO (60%)	Bentonite	MM	50 kW	Ryu et al. [126]
CuO (15%)	αAl_2O_3	IMP	500 W	Gayan et al. [127]
CuO (14%)	γAl_2O_3	IMP	10kW	Adanez et al. [113]
CuO (14%)	γAl_2O_3	IMP	10kW	Abad et al. [130]
CuO (14%)	γAl_2O_3	IMP	500 W	Gayan et al. [127]
CuO (14%)	γAl_2O_3	IMP	500 W	Forero et al. [131]
CuO (12%)	$MgAl_2O_4$	IMP	500 W	Gayan et al. [127]
Fe_2O_3 (60%)	Bentonite	MM	1 kW	Kim and Son [125]
CLC of Syngas ($CO+H_2$)				
NiO (18%)	αAl_2O_3	IMP	500 W	Dueso et al. [132]
NiO (60%)	$MgAl_2O_4$	FG	170 W	Mattisson et al. [117]
NiO (60%)	$MgAl_2O_4$	FG	170 W	Johansson et al. [133]
NiO (40%)	$NiAl_2O_4$	SD	65 kW	Kolbitsch et al. [123, 124]
CuO (14%)	γAl_2O_3	IMP	500 W	Forero et al. [134]
Fe_2O_3 (60%)	Al_2O_4	FG	300 W	Mattisson et al. [117]
Fe_2O_3 (60%)	Al_2O_4	FG	300 W	Abad et al. [135]
Mn_3O_4 (40%)	$MgZrO_2$	FG	300 W	Abad et al. [136]
CLC of (CH_4 + H_2S) or (Syngas+H_2S)				
NiO (18%)	αAl_2O_3	IMP	500 W	Labiano et al. [137]
CuO (14%)	γAl_2O_3	IMP	500 W	Forero et al. [138]
NiO (35%)	Al_2O_4	COP	1 kW	Shen et al. [139]
CLC of light hydrocarbons (C_2-C_3)				
NiO (18%)	αAl_2O_3	IMP	500 W	Adanez et al. [140]

*The oxygen carriers prepared by impregnation (IMP), coprecipitation (COP), freeze granulation (FG), and spray drying (SD).

The activity of Cu- based oxygen carriers supported by γAl_2O_3, αAl_2O_3, and NiO/γAl_2O_3 was investigated in a 500 W – 10 kW CLC unit operating continuously using methane as fuel at 800–900 °C [113, 127, 130, 131]. A complete methane combustion was achieved at 900 °C for the oxygen carrier to fuel ratio of greater than 1.2 with all Cu- based oxygen carriers [127, 131]. However, when the temperature decreased to 800 °C, an oxygen carrier to fuel ratio higher than 1.4 was required for the complete methane combustion

over a Cu-based oxygen carrier [113, 131]. Furthermore, neither agglomeration nor deactivation over the Cu-based oxygen carrier was observed [113, 127, 131] although it was suggested a low operating temperature (<800 °C) due to its likely agglomeration problem. Additionally, even if the attrition rate was high at the beginning of the experiments, it was low and constant after 40 h of operation [113]. It was concluded that high reactivity, together with high mechanical durability and absence of agglomeration, Cu-based oxygen carriers with γAl_2O_3 modified with NiO addition as support [127]. Thus, Cu-based oxygen carriers are suitable for CLC processes [113, 127, 131].

Syngas derived from the gasification of solid fuels such as coal and biomass is another type of gas fuel which can be used in the CLC process [132]. A high combustion efficiency (about 99%) for the syngas is possible with Ni-based [132, 133], Cu-based [134], Fe-based [135], and Mn-based [136] oxygen carriers in a CLC unit continuously operating at 800-950 °C. Furthermore, the combustion efficiency was hardly affected by the composition of syngas [132, 134]. The optimum oxygen carriers to fuel ratio for the combustion of syngas required greater than 5.0 for Ni-based oxygen carriers [132] and greater than 1.5 for Cu-based oxygen carriers [134]. The CLC tests with pure H_2 and CO demonstrated that the efficiency for H_2 is higher than that for CO due to the low reactivity of oxygen carriers with CO [134], which indicates that the water gas shift reaction may act as an intermediate step in the continuous CLC plant [132, 134]. Fe-based and Mn-based oxygen carriers demonstrated a better combustion efficiency (about 99%) for syngas compared with methane [135, 136]. The oxygen carriers, Ni-based [132], Cu-based [134], Fe-based [135], and Mn-based [136] demonstrated adequate behaviour in terms of agglomeration, carbon deposition, and attrition in the continuously operated CLC of syngas. Therefore, they could be used in a continuously operating CLC unit for the combustion of syngas [132, 134-136], which is produced in an integrated gasification process [132].

Gas fuels such as natural gas, refinery gas or syngas from coal gasification may contain different amount of sulphur compounds such as H_2S. Labiano et al. [137] and Forero et al. [138] have investigated the CLC of methane mixed H_2S in a continuous CLC unit of 500 W. Furthermore, the effect of H_2S on the combustion of syngas over Ni-based oxygen carriers was investigated by Shen et al. [139] in a 1 kW CLC unit. It was found that during

the combustion reaction, sulphide can react with Ni-based oxygen carriers and produce nickel sulphide (Ni_3S_2) at all the operating conditions used in the fuel reactor [137]. After the combustion of syngas, the Ni-based oxygen carriers reduced to Ni and Ni_3S_2 phases, but no evidence of other phases such as NiS or NiS_2 was observed [139]. Although the formation of Ni_3S_2 decreased the activity of oxygen carriers and combustion efficiency [137], it is completely reversible in the air reactor where oxidation occurs [139]. However, SO_2 was produced as flue gas, once the produced sulphides were circulated to the air reactor [137]. Due to the low melting point of Ni_3S_2 in the Ni-based oxygen carriers, a liquid phase sintering was observed over the reduced Ni-based oxygen carriers tested in the combustion of syngas (including H_2S) [139]. Labiano et al. [137] noticed that gas fuels containing low H_2S (<100 ppm) could be applicable in industrial CLC operations, once operational and environmental aspects taking into consideration.

The presence of light hydrocarbons such as C_2H_6 and C_3H_8 in the feeding gas of a CLC system were investigated over Ni-based oxygen carriers by Adanez et al. [140]. The study demonstrated that the light hydrocarbons are entirely combusted in the CLC process at temperatures higher than 900 °C. Furthermore, no carbon formation, nor agglomeration was detected under any experimental conditions [140].

In addition to the high-temperature CLC processes (higher than 800 °C), low-temperature CLC may have potential applications in a wide range of industries. For example, it could be used to eliminate uncombusted hydrocarbon gases, non-methane volatile organic compounds and CO released from incomplete biofuel and coal combustion, which have been defined as toxic wastes polluting to the environment [141-144]. Moreover, these incomplete combustion gases decrease combustion efficiency [143, 145]. A two-stage CLC process, which is a combination of the normal CLC with the low-temperature CLC (300 °C for fuel reactor and 400 °C for air reactor), have been suggested to eliminate the unburnt gases and improve CO_2 purity in the fuel combustion gases by Xu et al. [146]. The cement supported Cu-based oxygen carrier demonstrated relatively fast oxidation and reduction rates with air and carbon monoxide, respectively, at low temperatures, approximately 300 °C, in TGA. Moreover, low temperature gas-solid kinetics of an active Ni-based oxygen carrier has been investigated with H_2, CO, CH_4 as reducing agents at temperatures between 500 °C and 800 °C by Medrano et al. [147]. A good description

was obtained for gas-solid kinetics of redox reactions with H_2, CO and O_2 at 500-800 °C and atmospheric pressure.

Oxygen carriers used in the CLC of solid fuels: Iron (Fe-) based oxygen carriers mostly have a lower cost, lower environmental impact, better mechanical strength, and higher melting point than other oxygen carriers [20, 98, 108, 110]. The reactivity of Fe-based oxygen carriers is enough at atmospheric and pressurised conditions [35, 98, 110]. The Fe-based oxygen carriers react rapidly with intermediate gasification products; CO and H_2, produced from coal gasification [148]. Additionally, the combustion of coal with Fe_2O_3 may be improved when the coal is blended with biomaterials such as straws [149]. Furthermore, the alkali carbonate (K_2CO_3, Li_2CO_3, Na_2CO_3) treatment on Fe_2O_3 oxygen carriers can enhance the combustion rate of coal char direct CLC [150]. In addition to synthetic Fe-based oxygen carriers, some natural Fe-based oxygen carriers were also investigated as oxygen carriers. Both hematite and Fe-based synthetic oxygen carriers showed high combustion efficiency with the lowest amount of oxygen carrier in the reactor bed [111]. As for the carbon formation, while there is no or minimal carbon deposition on Fe-based synthetic oxygen carriers [110, 151, 152], carbon formation of natural Fe-based oxygen carriers is associated with reduction time [112]. Most investigations have been agreed that Fe-based oxygen carriers remain durable through multiple reduction-oxidation cycles [110, 153]. Therefore, the direct combustion of carbon produced by char without prior gasification with Fe_2O_3 encouraged for the application of CLC to the combustion of solid fuels [153].

Although Copper (Cu-) based oxygen carriers mostly demonstrate higher costs (~7860 $/t) than Fe-based oxygen carriers (~100 $/t) and lower melting point (1084-1326 °C) than other oxygen carriers, the properties such as high oxygen carrier capacity, high durability and low environmental impact of Cu-based oxygen carriers increase the interest for them in CLC studies [113, 154]. Based on the thermodynamic analysis, Cu-based oxygen carriers strongly support the feasibility of the CLC process for solid fuels such as coal, biomass, solid wastes [155]. Studies into the reactivity of Cu-based oxygen carriers verified that both gas and solid combustion process with Cu-based oxygen carriers should be possible [23, 98] because of their high reactivity, more extensive oxygen transfer and releasing capacities [156]. For example, the primary Cu-based synthetic oxygen carrier,

CuO, demonstrated high reduction and oxidation so it can be described as an excellent oxygen carrier for solid fuel CLC [102]. It has also been claimed that CuO can be fully converted into Cu in a reduction process, either combustion of solid fuels or indirect combustion of pyrolysis and gasification products of solid fuel [155]. The combustion and oxidation performance of Cu-based natural ores as an oxygen carrier is worse than synthetic CuO oxygen carrier due to the low active species concentration in ores [112]. Despite the higher oxygen capacity of Fe-based natural ores, Cu-based natural ores showed faster reaction rates than Fe-based natural ores in methane CLC process [112]. No carbon deposition [113, 155], little or no agglomeration [98, 113] and no surface sintering [102] after combustion and oxidation of Cu-based oxygen carriers.

Nickel (Ni-) and Manganese (Mn-) based oxygen carriers are also suitable for CLC applications since both demonstrate relatively high melting points, high oxygen capacity and low agglomeration [99, 157]. Though lower oxygen transfer capacities than Cu-based oxygen carrier [155], they show high reactivity [98, 99]. On the other hand, Mn_2O_3 and NiO showed a lower combustion rate for solid fuels compared to Cu-, Fe- and Co-based oxygen carriers. Moreover, carbon deposition, cost and toxicity of the carriers are still a significant problem to be solved [99, 151, 158]. Carbon deposition of Ni-based oxygen carriers may be addressed using correct Ni concentration on oxygen carrier [151, 153, 159].

Cobalt (Co-) based oxygen carriers showed an excellent performance in chemical looping biomass gasification thanks to its superior properties such as high oxygen capacity, mechanical strength, high melting point, and thermal stability [155]. Oxygen release capacity and thermal stability make Co a preferred oxygen carrier compared to Mn and Cu [160], while the high cost and toxicity reduce its application in CLC [160]. In addition to CoO oxygen carrier, both CuO and NiO based oxygen carriers were illustrated to be the optimal oxygen carriers for development of the CLC of solid fuels in terms of thermodynamic analysis and physical properties of the oxygen carriers [155].

In contrast to these oxygen carriers, combined oxygen carriers such as $CoFe_2O_4$, $CuFe_2O_4$, Fe-Cu/Mg showed better reaction activity [101, 149, 161]. Wang et al. [101] described a new combined oxygen carrier, Fe45Cu15M40, which consists of 45% of

Fe_2O_3, 15% of CuO and 40% of $MgAl_2O_4$. The activity of the oxygen carrier remained high and stable for long reduction-oxidation cycles. This also showed high reactivity in a pressurised CLC unit for 15 h and provided for the high conversion of the fuel. Furthermore, catalyst showed a resistance towards agglomeration and fragmentation. Wang et al. [149] showed that the desired reaction superiority of $CoFe_2O_4$ over single reference oxides Fe_2O_3 and CoO. The principal reduction of $CoFe_2O_4$ is to Fe_3O_4 and Co, which was also verified by thermodynamic simulations. Wang et al. [161] have investigated the solid reaction activity of $CuFe_2O_4$ oxygen carrier. The reactivity of $CuFe_2O_4$ in coal combustion reaction was found much closer to that of CuO.

2.5.3 CLC for liquid fuels

The recent applications of CLC for both gas and solid fuels were widely summarised in reviews [23, 162-164], while CLC for liquid fuels requires further experiments. Cao et al. [165] investigated the gasification of bitumen and asphalt in an upstream process, and then the synthesis gases were combusted over lanthanum promoted copper-based oxygen carrier in a laboratory-scale batch fluidized bed reactor. Hoteit et al. [166] carried out chemical looping combustion experiments with dodecane as liquid fuel over nickel-based oxygen carrier, $NiAl_{0.44}O_{1.67}$, at 800 and 900 °C in a batch fluidized bed reactor. They showed that full combustion of dodecane to CO_2 and H_2O is possible if enough time is provided to all hydrocarbon in a batch fluidized bed. Bao et al. [167] investigated combustion of n-heptane in a saturated nitrogen flow as fuel over Fe-based oxygen carrier in a laboratory-scale fluidised bed reactor. Both Cao et al. [165] and Hoteit et al. [166] agreed that at the end of the reduction step, there were no carbon or sulphur decomposition on Ni-based and Cu-based oxygen carriers on the contrary of the Fe_2O_3 oxygen carriers [167]. Serrano et al. [168] also investigated the combustion of liquid fuels such as diesel, mineral and synthetic lubricant oils with Fe-based oxygen carriers at different oxygen carrier to fuel ratios. The results demonstrated that it is possible to reach higher than 90% combustion efficiency when using a greater than 3.0 oxygen carrier to fuel ratio at 900 °C.

Additionally, studies on CLC-liquid fuels have been published by Moldenhauer et al. [169-174], on the combustion of kerosene (sulphur-free and with sulphur), fuel oil, and

vacuum residue with using oxygen carriers; Ni-, Mn-, and Cu- based zirconium oxide, ilmenite, and calcium manganite in a 300 W circulating fluidized bed laboratory reactor at the temperatures of 750-900 °C. These studies revealed high CO_2 yields for kerosene combustion; higher than 95% over NiO based oxygen carrier [170], between 83% and 99.3% over a Mn_3O_4 based oxygen carrier [169], and between 95% and 99% over a CuO based oxygen carrier [169]. They also demonstrated that it was possible to reach above 99% CO_2 yield with sulphur-free kerosene and sulphurous kerosene over ilmenite at 950 °C [173].

Moldenhauer et al. [170] also mentioned that although the fuel conversion at the lowest temperatures (650-700 °C) is high enough, these temperatures are probably not very realistic, especially for commercial applications. As oxygen release at such temperatures is so low that CLOU properties, which are an essential benefit of this material, can be neglected. However, for using CLOU properties of oxygen carriers, very high temperatures are required such as higher than 800 °C for CuO to reduce Cu_2O, higher than 700 °C for Mn_2O_3 to reduce Mn_3O_4 and higher than 750 °C for Co_3O_4 to reduce CoO [23]. On the other hand, although CuO decomposition is not thermodynamically favourable below 700 °C according to the Positive Gibbs free energy, the reaction between CuO and C can be occurred between 200-1000 °C as mentioned by Siriwardane et al. [175].

Chapter 3
Proposed Application of CLC to FCC Units

CLC technology has been employed for the combustion of various fuels such as natural gas, syngas, coal, biomass, petroleum coke, and hydrocarbon-based liquid fuels, with a wide range of oxygen carriers including Fe_2O_3, CuO, NiO, Mn_2O_3, and Co_3O_4, [20, 97, 108, 109], using lab and pilot scale reactors [23, 97, 98, 100, 103]. In addition to producing CO_2 abundant flue gas, CLC serves to decrease NOx emissions as no direct interaction between the air and fuel occurs. Compared to oxy-combustion and post-combustion, CLC does not require capital-intensive air separation and generates flue gas richer in CO_2 (virtually no excess O_2 present). In principle, commercial FCC catalysts can be modified with an oxygen carrier. Since deactivated FCC catalysts typically contain only 1-2 wt.% coke, relatively small amounts of oxygen carriers would be required for the combustion (or oxidation) of the coke. Furthermore, there is the possibility of incorporating oxygen carriers into the binders and fillers used in FCC catalyst formulations.

The proposed CLC-FCC concept is presented in Figure 3.1. The oxygen carrier in the fresh catalyst would be in a reduced state (designated Me_nO_{m-1}/Cat) as it enters the FCC reactor. The spent or deactivated catalyst with deposited coke assigned as Coke/Me_nO_{m-1}/Cat is then transferred to the regenerator. The Me_nO_{m-1}/Cat catalyst would also be circulated to the air reactor via another fluidised bed, where the reduced state is oxidised, and so designated as Me_nO_m/Cat. By the mixing of Coke/Me_nO_{m-1}/Cat and Me_nO_m/Cat in the regenerator, the coke would be oxidised to CO_2 + H_2O while the oxidised oxygen carrier reduced to Me_nO_{m-1}/Cat. The concentrated CO_2 is then captured from the regenerator. The Me_nO_{m-1}/Cat is then circulated back to both the FCC reactor and the air reactor. Given that the cracking and metal oxidation reactions are fast in relation to the oxidized metal coke combustion, the average coke content of the catalyst in the

regenerator would be low meaning that little CO2 would be lost through combustion in the air reactor where the residence time would be short. The reactions for CLC of carbon indicate that all heat is generated in the air reactor, and this needs to balance the heat required for the combustion and cracking reactions. The net CLC reaction and the reactions in the regenerator and air reactor for CuO, Co_3O_4 and Mn_2O_3, are given in reactions 3.1-.3.7.

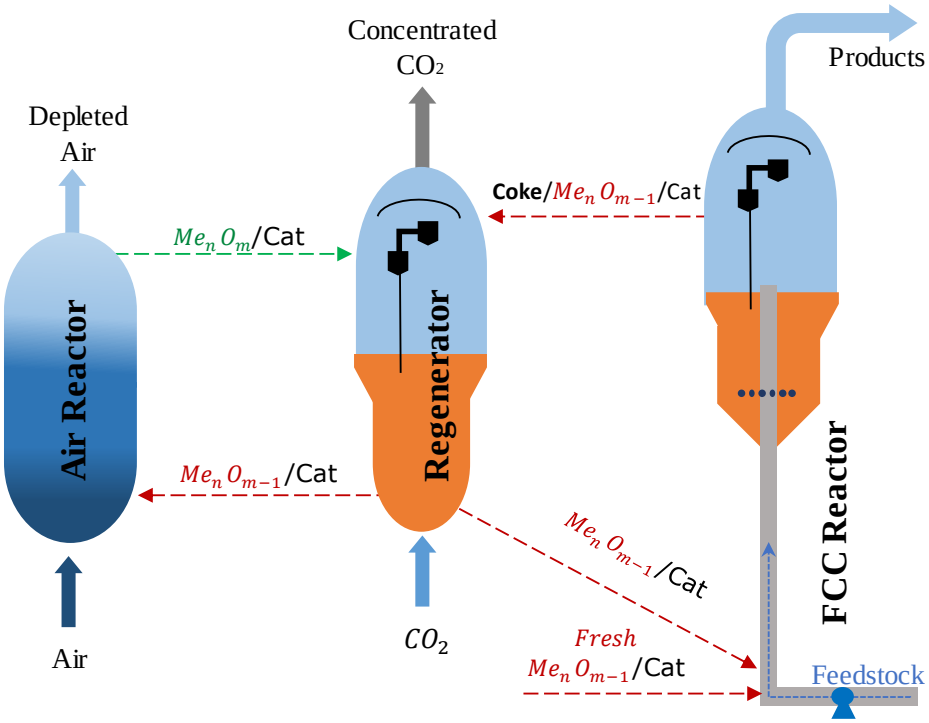


Figure 3.1. Schematic diagram of the proposed CLC-FCC process.

For coke combustion with CuO;

Regenerator: $4CuO_{(s)}+C_{(s)} \longrightarrow 2Cu_2O_{(s)}+ CO_{2(g)}$ ΔH_r^0= -101.5 kJ/mol (3.1)

Air reactor: $2Cu_2O_{(s)}+O_{2(g)} \longrightarrow 4CuO_{(s)}$ ΔH_0^0= -292.0 kJ/mol (3.2)

For coke combustion with Co_3O_4;

Regenerator: $2Co_3O_{4(s)}+C_{(s)} \longrightarrow 6CoO_{(s)}+ CO_{2(g)}$ ΔH_r^0= -38.9 kJ/mol (3.3)

Air reactor: $6CoO_{(s)}+O_{2(g)} \longrightarrow 2Co_3O_{4(s)}$ ΔH_0^0= -237.9 kJ/mol (3.4)

For coke combustion with Mn_2O_3;

Regenerator: $6Mn_2O_{3(s)}+C_{(s)} \longrightarrow 4Mn_3O_{4(s)}+ CO_{2(g)}$ ΔH_r^0= -190.7 kJ/mol (3.5)

Air reactor: $4Mn_3O_{4(s)} + O_{2(g)} \rightarrow 6Mn_2O_{3(s)}$ ΔH_0^0= -202.8 kJ/mol (3.6)

The net reaction from the regenerator and air reactors;

Net reaction: $C_{(s)} + O_{2(g)} \rightarrow CO_{2(g)}$ ΔH_C^0= -393.5 kJ/mol (3.7)

ΔH_r^0 and ΔH_0^0 are the standard heats of reaction for the reduction and oxidation at 298K and 1 atm.

Coke combustion with oxygen carriers may occur through a couple of mechanisms. Firstly, the soft coke released from the coke deposited catalyst can combust with the solid oxygen carriers. Secondly, hard coke can be combusted with the solid phase oxygen carriers via solid-solid interactions between coke and oxygen carriers. Hard coke combustion may occur with gas phase oxygen released from the oxygen carriers thanks to their chemical looping with oxygen uncoupling (CLOU) properties. Finally, the combustion of coke may occur by the gasification of coke thanks to CO_2-Coke and H_2O-Coke interactions. NOx emission is another issue in conventional FCC that demands a control strategy [48], and CLC may be advantageous in that NOx emissions would be lower than for normal combustion [96, 155].

Chapter 4
Materials and Experimental Methods

4.1 FCC catalyst formulations

In order to assess the feasibility of the CLC-FCC concept, the FCC catalyst must first be modified with reduced oxygen carriers, as illustrated in Figure 3.1. However, some oxidised oxygen carriers modified FCC catalyst may pass through the regenerator without full reduction, and so the cracking reaction may then occur on the oxidised oxygen carriers modified FCC catalyst. Therefore, the FCC catalyst was modified with an oxygen carrier (both oxidised and reduced) and prepared catalysts were tested in the cracking reaction to demonstrate the effect of oxygen carrier modification.

According to the novel CLC-FCC concept, the oxygen carrier modified FCC catalyst should have no significant effect on the cracking reaction in terms of conversion, yield, and product selectivity. Moreover, these oxygen carrier modified FCC catalysts must perform well in the regenerator to remove the coke deposited on FCC catalyst. A variety of modification methods for the oxygen carriers into the binders of supports have been presented in the literature such as mechanical mixing, impregnation, co-precipitation, deposition precipitation, freeze granulation, hydrothermal synthesis, and sol-gel [20, 37, 38, 101, 103, 108, 113, 119, 125, 127, 129, 158, 176-187].

The mechanical mixing is one of the quick and easy processes to indicate which kind of oxygen carrier has no significant effect on the cracking reaction, while density differences between oxygen carriers and FCC catalyst, and inhomogeneity in the regenerator may change the results. Impregnation is another process, which enables the preparation a novel FCC catalyst combined with oxygen carriers. However, the physical and chemical properties of the FCC catalyst such as surface area, pore volume, pore diameter, acidity

etc. may show differences. Both mechanically mixing and impregnation methods were employed for the preparation of new generation oxygen carriers modified FCC catalyst.

4.1.1 Mechanical mixing of oxygen carriers with FCC catalysts

4.1.1.1 Preparation of reduced oxygen carriers

The reduction procedure for the oxidised oxygen carriers, CuO (98.0%), Co_3O_4 (99.0%), and Mn_2O_3 (99.0%), supplied by Sigma Aldrich is as follows: Firstly, 20 g of oxidised oxygen carriers (CuO, Co_3O_4, Mn_2O_3) was placed into a porcelain crucible within the central zone of a horizontal tubular furnace. The furnace temperature was then increased from room temperature to 900 °C, at a heating rate of 20 °C/min, and kept at this temperature for 3 h under an N_2 flow of 2 L/min. As demonstrated by reactions R2.10 – R2.12 [23], at this temperature, the oxidised oxygen carriers; CuO, Co_3O_4, and Mn_2O_3, are reduced to Cu_2O, CoO, and Mn_3O_4, respectively, thanks to CLOU properties. The furnace was then switched off and allowed to cool to room temperature under N_2 flow.

4.1.1.2 Preparation of oxidised and reduced oxygen carriers mixed ECat

For modifying the FCC catalyst, a refinery equilibrium catalyst (ECat, supplied by Chemical Process and Energy Resources Institute (CPERI), Greece), a mechanical mixing method was employed as shown in Figure 4.1. The required amount of oxygen carrier; CuO, Co_3O_4, and Mn_2O_3, was determined by considering the amount of coke on the FCC catalyst [74, 188-193] and the oxygen release capacity of oxygen carriers. The reduced oxygen carriers, 0.23g of Cu, 0.51 g of Cu_2O, 0.81 g of CoO, and 1.64 g of Mn_3O_4, were mechanically mixed with 4.0 g of ECat using a vertical angle rotator (PTR-35, Grant-bio) for 20 min, and designated as M-Cu/ECat (5.4% of Cu), M-Cu_2O/ECat (11.3% of Cu_2O), M-CoO/ECat (16.8% of CoO) and M-Mn_3O_4/ECat (29.0% of Mn_3O_4). Additionally, the oxidised oxygen carriers, 0.57 g of CuO, 0.87 g of Co_3O_4, and 1.70 g of Mn_2O_3, were mechanically mixed with 4.0 g of ECat by the same rotator for 20 min, and designated as M-CuO/ECat (12.5% of CuO), M-Co_3O_4/ECat (17.8% of Co_3O_4) and M-Mn_2O_3/ECat (29.8% of Mn_2O_3).

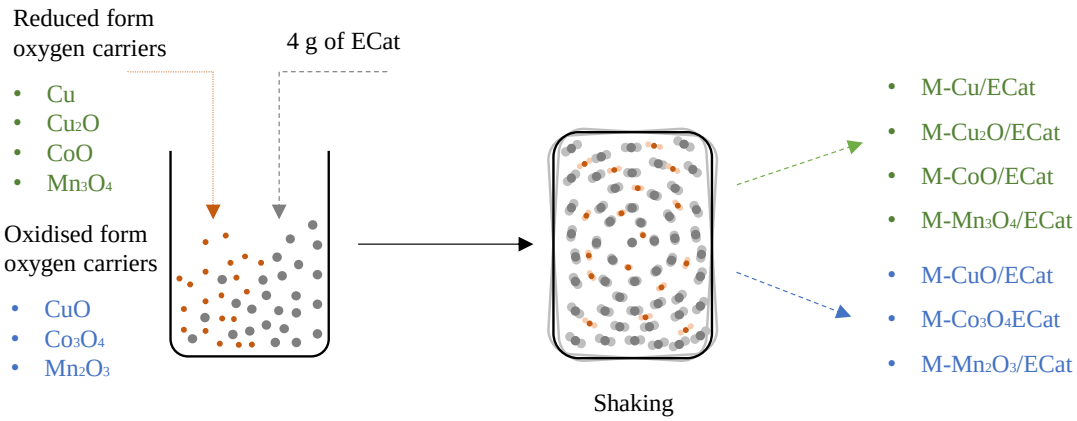


Figure 4.1. The mechanically mixing procedure of both reduced and oxidised oxygen carriers with ECat.

4.1.2 Impregnation of oxidised and reduced oxygen carriers into FCC catalyst

Wet-impregnation was employed for the preparation of oxidised oxygen carrier modified ECat, as demonstrated in Figure 4.2 [184, 194-196]. Firstly, a 25 ml aqueous solutions of the required amount of metal nitrate salts, $Cu(NO_3)_2.3H_2O$ (Acros Organics, 99%), $Co(NO_3)_2.6H_2O$ (Acros Organics, 99%), and $Mn(NO_3)_2.4H_2O$ (Alfa Aesar, 98%), were prepared. The amount of oxygen carriers were calculated according to the stoichiometrically required amount of oxidised oxygen carriers for the combustion of coke deposited on the catalyst. The prepared nitrate solutions were then slowly added to 20 g of ECat, with thorough stirring at room temperature for 18 h. The impregnated samples were then slowly dried at 60 °C for 24 h and 100 °C for 4 h. The dried samples were then calcined at 550 °C for 30 min in an air atmosphere to decompose the impregnated copper nitrate into cupric oxide (CuO), cobalt nitrate into cobalt oxide (Co_3O_4 – $CoO.Co_2O_3$), and manganese nitrate into manganic oxide (Mn_2O_3). The oxidised oxygen carrier impregnated FCC catalysts were then designated as I-CuO/ECat (12.5 wt.% of CuO), I-Co_3O_4/ECat (17.8 wt.% of Co_3O_4), and I-Mn_2O_3/ECat (29.8 wt.% of Mn_2O_3). “I” represents the preparation method – Impregnation.

In order to prepare the reduced oxygen carrier impregnated ECat, the oxidised oxygen carrier impregnated ECat were reduced using hydrogen in a commercial hydropyrolysis rig [197] as shown in Figure 4.3. Firstly, 5 g of I-CuO/ECat, I-Co_3O_4/ECat, and I-Mn_2O_3/ECat was placed into a stainless steel reactor (9 mm by 25 cm). The reactor was

then heated from room temperature to 300 °C (for the reduction of $Mn_2O_3 \rightarrow Mn_3O_4$), 350 °C (for the reduction of $Co_3O_4 \rightarrow CoO$ and $CuO \rightarrow Cu$), and 450 °C (for the reduction of $Mn_2O_3 \rightarrow MnO$) with a heating rate of 20 °C/min and maintained at the target temperature for 1 h under hydrogen flow (30 ml/min) and at 5 bar. Then the reduced oxygen carrier impregnated ECat were then designated as I-Cu/ECat, I-CoO/ECat, I-Mn_3O_4/ECat, and I-MnO/ECat.

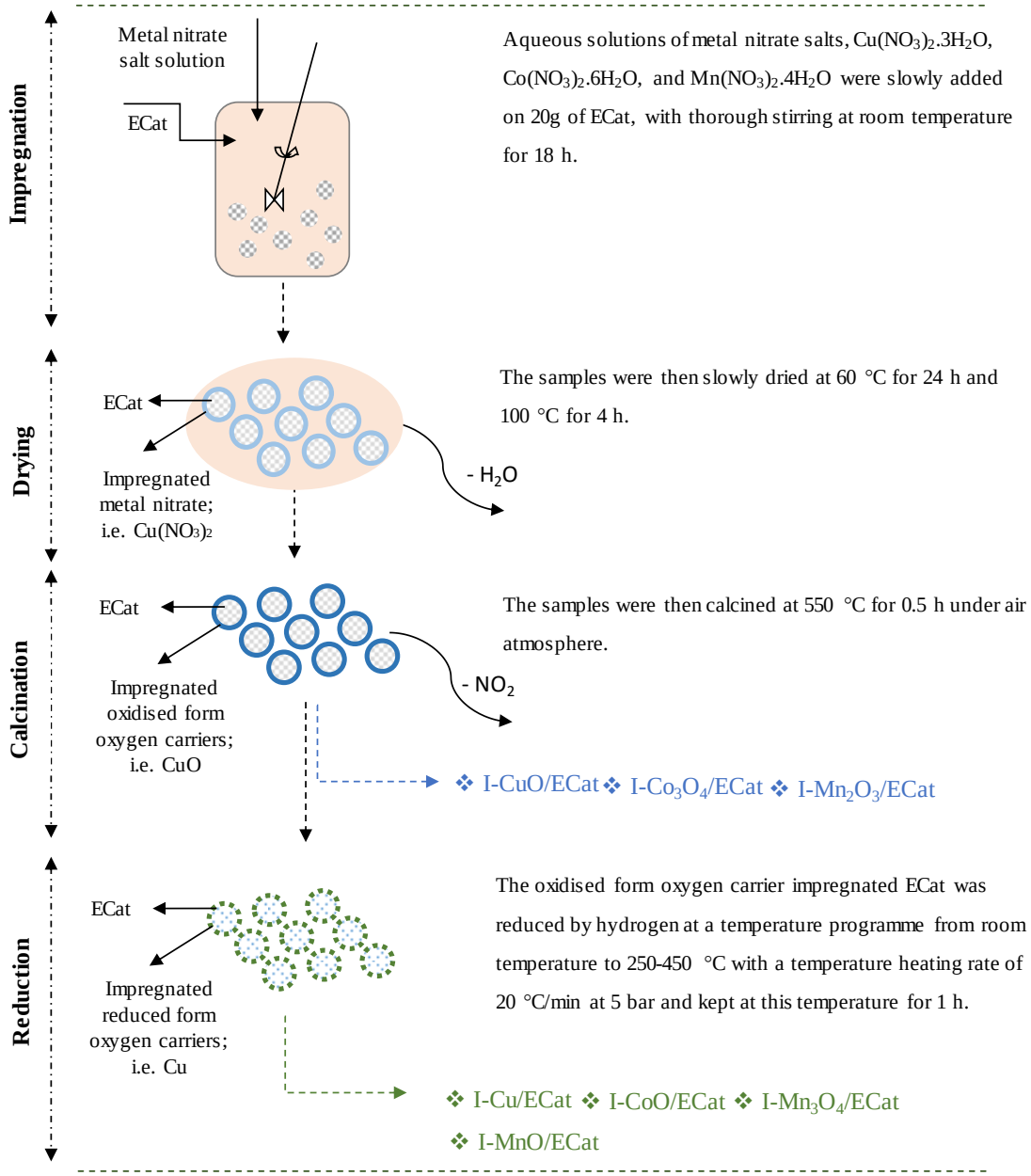


Figure 4.2. Flowchart of wet-impregnation method used for the preparation of oxidised and reduced oxygen carrier modified ECat.

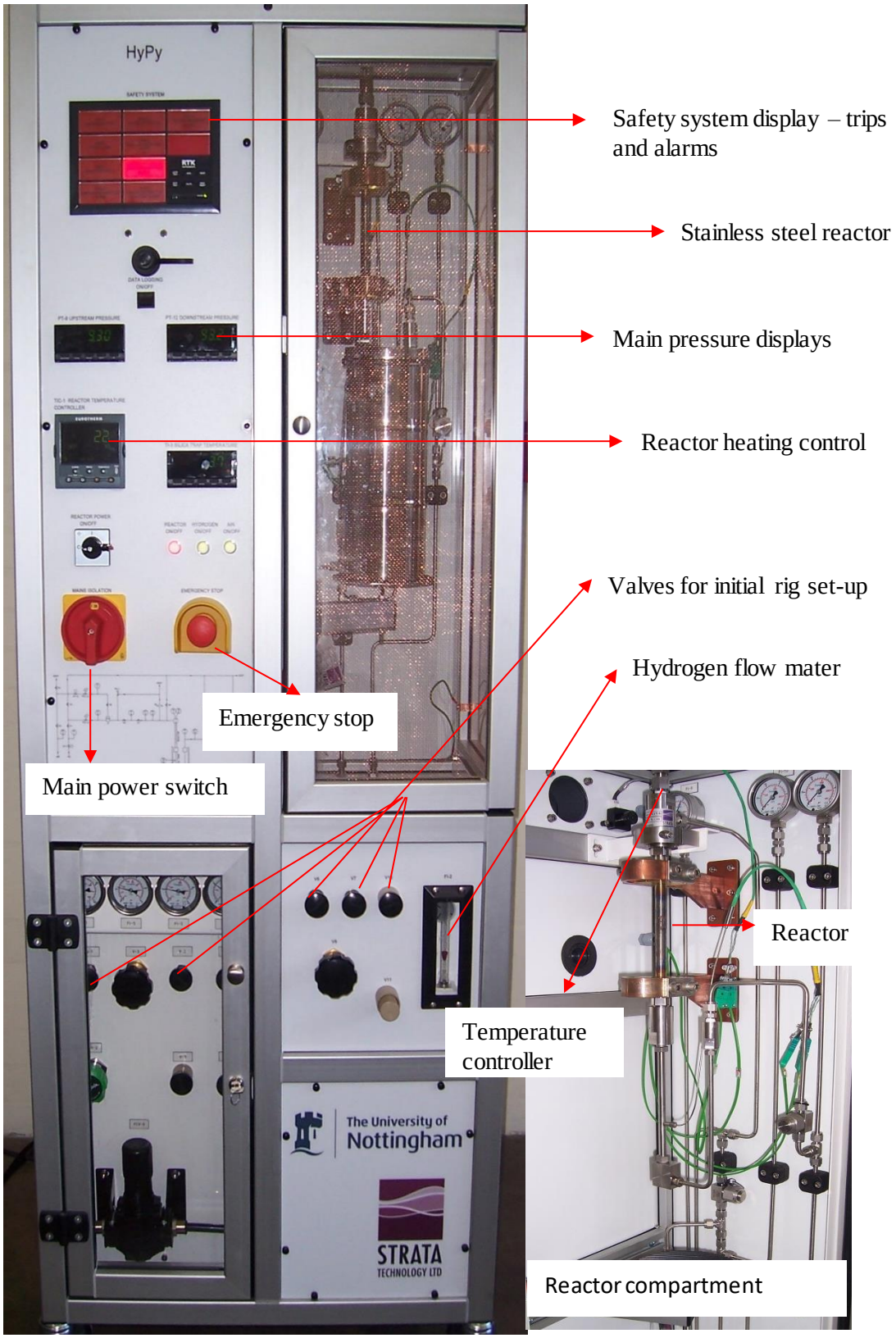


Figure 4.3. Commercial hydropyrolysis rig used for the reduction of oxidised oxygen carriers impregnated ECat (hydrogen reduction).

4.2 Catalytic cracking tests with the microactivity test (MAT) unit

4.2.1 Baseline cracking experiments

The catalytic cracking activity of prepared FCC catalyst, which was modified with both oxidised and reduced oxygen carriers using mechanically mixing and wet-impregnation, were investigated in a microactivity test (MAT) unit described in ASTM D3907-13 [76], a standard test method for testing of FCC catalysts. This standard test (and experimental set-up) is one of the most widely used systems for the testing activity of new cracking catalysts [198-201]. As a standard test, it has some advantages such as requires only gram quantities of catalysts, and this ideal for rapid screening of the candidate oxygen carriers. However, it has received criticism that the results obtained do not always correlate with those in the FCC reactors riser [69]. This arises from the much longer catalyst time of 75 s compared to 2-10 s in a riser, meaning much of the cracking in the MAT reactor occurs on the deactivated catalyst. The lower reaction temperatures compared to those for oil catalyst mixing in a riser leads to diffusion limitations due to incomplete vaporisation. Nevertheless, the test would be highly satisfactory for screening the influence of the oxygen carriers and understanding the impact of them on catalyst performance. The MAT experimental set-up, illustrated in Figure 4.4 and Figure 4.5, consists of a Pyrex glass tubular reactor with an internal diameter of 1.9 cm and length of 27 cm, temperature-controlled tubular furnace, syringe pump, liquid product receiver and gas sampling bag. The reactor is located in a cylindrical furnace whose temperature measured by a vertically located thermocouple in contact with the glass wool just over the catalyst bed.

In the cracking experiments, n-hexadecane ($C_{16}H_{34}$, Purity: 99%, Alfa Aesar) was selected as a model cracking feed, and the experimental conditions reported in the ASTM D3907-13 standard were accordingly. Thermal cracking of n-hexadecane (without catalyst) and catalytic cracking of n-hexadecane over commercial FCC catalysts (BASF-FCC75, BASF-FCC76 and CPERI-ECat) were firstly carried out as baseline experiments in the MAT unit.

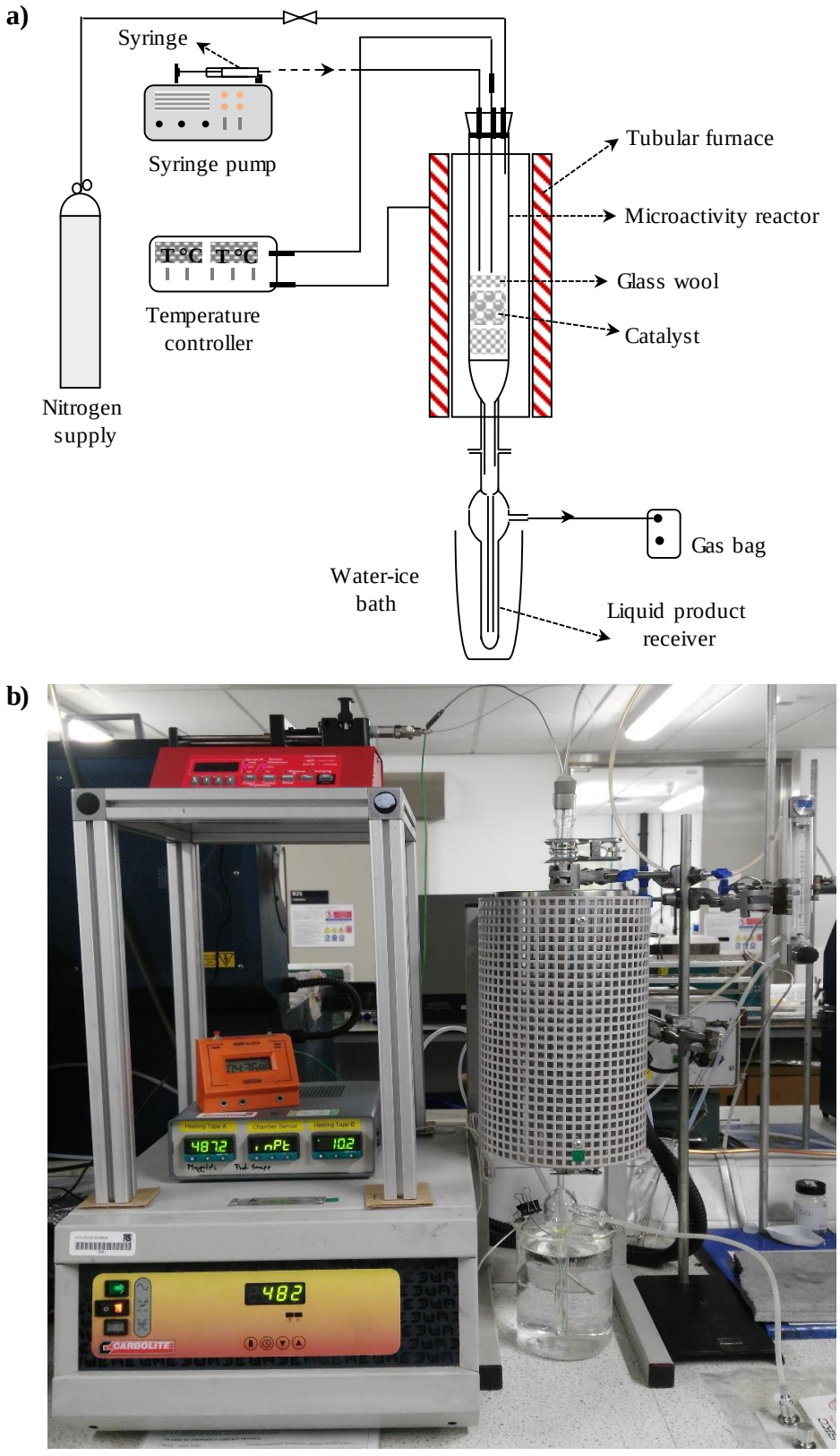
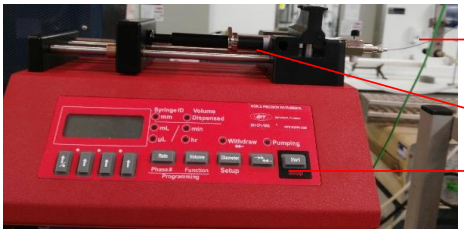


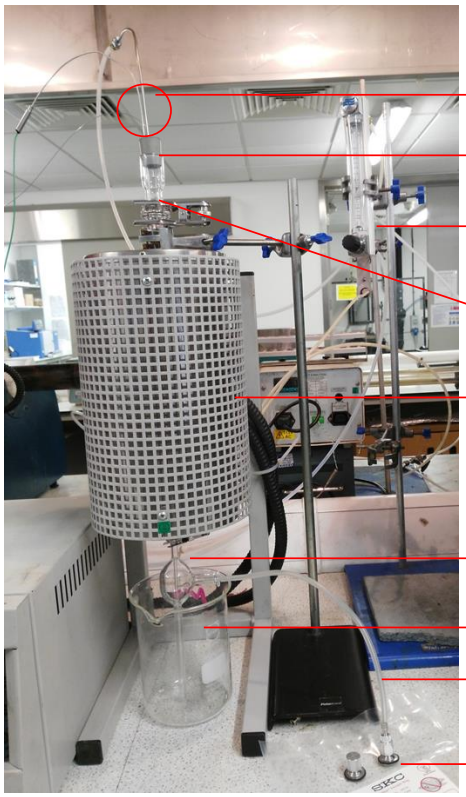
Figure 4.4. The experimental set-up of MAT unit, a) Flowchart and b) Picture [202].



Temperature controllers



Syringe pump



Reactor and product receivers

Figure 4.5. Details of the MAT unit experimental set-up [202].

For the baseline cracking tests, firstly, a piece of glass wool (for thermal cracking) and then 4 g of commercial catalysts (FCC75, FCC76 and ECat) were placed between two

pieces of glass wool in MAT reactor located in the tubular furnace. The reactor temperature was then increased to 482 °C (± 5 °C) with a heating rate of 20 °C/min, under a N_2 flow of 20 ml/min. Once the reaction temperature had been attained, the system was purged with N_2 for 30 min. The feed, n-hexadecane, was then introduced to the MAT reactor at a rate of 1.38 ml/min for 75 s. During this injection period, the N_2 flow was switched off, and the feed injection temperature was controlled by a vertically located thermocouple in contact with the glass wool bed. After injection, the reactor and the product recovery system were purged with an N_2 flow of 20 ml/min for 15 min. The liquid products were condensed in the liquid product receiver using a water-ice bath, and the cracked gases were collected in a 1 L gas sampling bag. In order to eliminate experimental error, the tests were repeated three times, and the conversion, yield, and product selectivity are presented with error bars representing one standard deviation.

4.2.2 Cracking of n-hexadecane over oxygen carriers modified FCC catalyst

The cracking activity of 4 g of ECat (modified with reduced/oxidised oxygen carriers) was also investigated in the same experimental set-up using the same procedure as described for baseline cracking experiments. Over 50 screening tests were conducted with the catalysts;

- Prepared by **mechanically mixing**; M-Cu/ECat, M-Cu_2O/ECat, M-CoO/ECat and M-Mn_3O_4/ECat as reduced oxygen carriers mixed ECat, M-CuO/ECat, M-Co_3O_4/ECat and M-Mn_2O_3/ECat as oxidised oxygen carriers mixed ECat.

- Prepared by **wet-impregnation**; I-Cu/ECat, I-CoO/ECat, I-Mn_3O_4/ECat and I-MnO/ECat as reduced oxygen carriers impregnated ECat, I-CuO/ECat, I-Co_3O_4/ECat and I-Mn_2O_3/ECat as oxidised oxygen carriers impregnated ECat.

4.2.3 Characterisation of cracking products

The liquid products were analysed using a Clarus 580 GC (Perkin Elmer Elite-1 phase 60 m x 0.25 mm x 0.25 µm capillary column) fitted with an FID detector. An aliquot, 1 µl, of the liquid sample (diluted in dichloromethane) was injected at 250 °C with helium as

the carrier gas. The gas products were immediately analysed after collection in the gas sampling bag using a Clarus 580 GC fitted with an FID and TCD detectors for the hydrocarbon and non-hydrocarbon gases respectively, operating at 200 °C. 5 ml of gas samples were injected (split ratio 10:1) at 250 °C with separation performed on an alumina plot fused silica 30 m x 0.32 mm x 10 µm column, with helium as the carrier gas. The oven temperature was programmed from 60 °C (13 min hold) to 160 °C (10 min hold) at 10 °C/min. In addition to the liquid and gaseous products, the carbon (coke) contents of the used catalysts were determined by elemental analysis using a Leco CHN-628 analyser. Further details presented in "*4.4.7. Elemental analysis of coke deposited on prepared catalysts*".

4.2.4 Data evaluation of the catalytic cracking tests

Conversion of n-hexadecane (Equation 4.1 and 4.2) to coke, liquid, and gas (Equation 4.3–4.5) and product selectivities (Equation 4.6) to $C_{1\text{-}2}$ (dry gas), $C_{3\text{-}4}$ (LPG), $C_{5\text{-}15}$ (gasoline), C_{16+} (higher hydrocarbons), and coke were determined as;

$$\text{Conversion (overall) wt.\%} = \frac{W_{C16,0} - W_{C16,f}}{W_{C16,0}} * 100 \quad (4.1)$$

$$\text{Conversion (excluding CLC) wt.\%} = \frac{W_{C16,0} - (W_{C16,f} + W_{CO_2})}{W_{C16,0}} * 100 \quad (4.2)$$

$W_{C16,0}$: Weight of n-hexadecane feed (g)

$W_{C16,f}$: Weight of uncracked n-hexadecane in the products (g)

W_{CO2}: Total weight of carbon in carbon dioxide in the products (g)

$$\text{Gas yield (wt.\%)} = \frac{W_g}{W_{C16,0}} * 100 \quad (4.3)$$

$$\text{Coke yield (wt.\%)} = \frac{W_C}{W_{C16,0}} * 100 \quad (4.4)$$

$$\text{Liquid yield (wt.\%)} = \frac{(W_{C16,0} - W_{C16,f} - W_g - W_C)}{W_{C16,0}} * 100 \quad (4.5)$$

$W_{C16,0}$: Weight of n-hexadecane feed (g)

$W_{C16,f}$: Weight of uncracked n-hexadecane in the products (g)

W_g: Total weight of gas products (g)

W_C: Total weight of coke (g)

$$\text{Selectivity (wt.\%)} = \frac{W_i}{\sum W_{products}} * 100 \qquad (4.6)$$

W_i: Weight of the product; C_{1-2} (dry gas), C_{3-4} (LPG), C_{5-15} (gasoline), C_{16+} (higher hydrocarbons) and coke, (g)

$\sum W_{products}$: Total weight of the products C_{1-2}, C_{3-4}, C_{5-15}, C_{16+}, and coke (g)

4.3 Chemical looping combustion tests of coke with oxygen carriers

To investigate the combustion of coke deposited on FCC catalyst with the oxygen carriers, CLC tests were carried out using a thermogravimetric analyser (TGA-Discovery, Figure 4.6), which can operate with fast heating rates. During the TGA experiments, because of the low carbon contents (ca. 1%) of the used ECat and the weight limitation of TGA pans, a low volatile semi-anthracite Welsh coal having a similar chemical composition (presented in Table 6.1) to FCC coke was selected as a model FCC coke. While the TGA tests of model coke combustion with bulk oxygen carriers provided insight to the CLC possibility of FCC coke, the results were limited by the low amount of model coke (approximately 5-10 mg) able to be combusted in the TGA pan. A lab-scale fixed-bed and fluidised-bed reactors equipped with an online gas analyser (ThermoStar TM GSD 301 T) (FxB-MS and FsB-MS) were therefore employed to obtain more accurate and realistic data for the combustion of coke deposited on the prepared catalysts with oxygen carriers impregnated ECat.

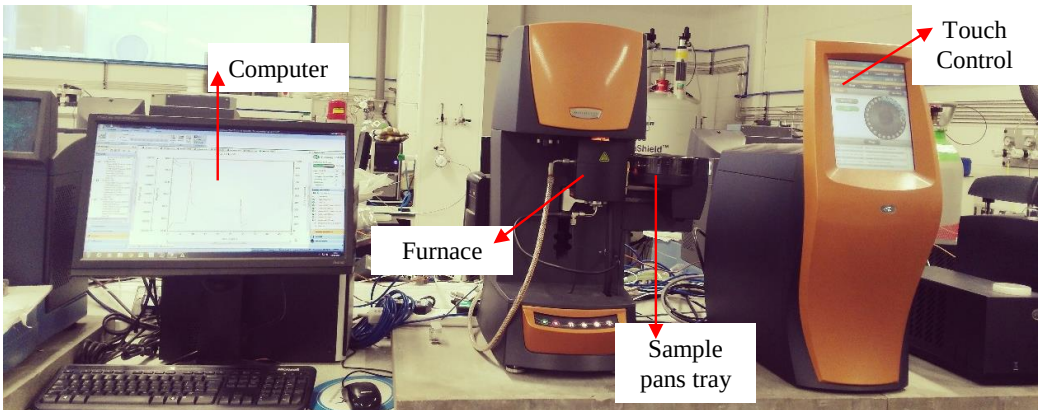


Figure 4.6. Discovery TGA from TA Instruments.

4.3.1 Chemical looping combustion tests in TGA

Before the TGA experiments of model coke combustion with bulk oxygen carriers (CuO, Co_3O_4, and Mn_2O_3), characterisation of model coke and behaviour of bulk oxygen carriers were employed using the Discovery TGA. The TGA tests were then employed to screen the combustion behaviour of model coke with bulk oxygen carriers.

4.3.1.1 Characterisation of model coke (low volatile semi-anthracite)

The model coke (WC, low volatile semi-anthracite Welsh coal) was characterised by proximate and ultimate analyses. The model coke was firstly dried at 105 °C for 24 h and then to collect the samples in 53-75 µm, grinded and sieved. The proximate analyses were performed in the Discovery TGA using the following procedure. Approximately 30 mg of model coke was loaded in a platinum pan (4 mm in depth and 10 mm in diameter) and heated from ambient temperature to 110 °C with a heating rate of 50 °C/min and kept at this temperature for about 10 min under N_2 (100 ml/min) to remove the moisture. After the moisture was removed, the mixture was heated to 1000 °C with a heating rate of 50 °C/min under the same N_2 flow rate and kept about 20 min to remove the volatile matter. Finally, to combust the fixed carbon, N_2 flow was replaced by air with a flow rate of 100 ml/min at 1000 °C for 15 min. The ultimate analysis of model coke was determined using Leco CHN 628 for the amount of carbon, hydrogen, nitrogen and Leco 628-S for the amount of sulphur content. (Further details about ultimate analysis are presented in the following section "*4.4.7 Elemental analysis of coke deposited on prepared catalysts*").

In order to clarify the reduction steps of oxygen carriers, approximately 50 mg of oxidised oxygen carriers CuO, Co_3O_4 and Mn_2O_3 was loaded in the platinum TGA pan. The sample was heated from ambient temperature to 110 °C with a heating rate of 50 °C/min and kept at 110 °C for 10 min under N_2 (100 ml/min) to remove the moisture. After the moisture was removed, the sample was heated from 110 °C to 900 °C with a heating rate of 500 °C/min under the N_2 flow for 20 min to demonstrate the weight loss, due to the CLOU properties of oxygen carriers (oxygen releasing during the reductions from CuO to Cu_2O, Co_3O_4 to CoO and M_2O_3 to Mn_3O_4).

4.3.1.2 CLC tests of model coke with oxygen carriers

The model coke was physically mixed with the oxygen carriers, CuO, Co_3O_4, and Mn_2O_3, at three oxygen excess numbers including R = 0.5, 1.0, and 2.0, which is defined as the molar ratio of oxygen to fuel. For example, each gram of model coke stoichiometrically required 22.74 g of CuO, 34.50 g of Co_3O_4, and 67.87 g of Mn_2O_3 for the combustion under the oxygen excess number of R = 1.0. After mixing of oxygen carrier and model coke, the mixture was loaded in the platinum pan. The mixture was then heated from ambient temperature to 110 °C with a heating rate of 50 °C/min and kept at this temperature for 5 min to remove all the moisture. It was then rapidly heated from this temperature to combustion temperature, 700-900 °C, with a heating rate of 500 °C/min under a N_2 flow rate of 100 ml/min and held at the final temperature isothermally, under same N_2 flow rate, until combustion either was completed or had reached a limiting value. Finally, to burn off any remaining fixed carbon, the N_2 flow was replaced by air at the same temperature for 15 min. The TGA tests were repeated three times in order to reduce systematic errors.

4.3.1.3 Data evaluation of CLC tests in TGA

The combustion of fixed carbon in the model coke and fractional reduction (X_R) were calculated using Equations 4.7 and 4.8, respectively [102, 112, 160].

$$\text{Combustion (of model coke) wt.\%} = \frac{M_{HC,f}}{M_{HC,0}} * 100 \qquad (4.7)$$

$M_{HC,f}$: Actual mass loss of fixed carbon (hard coke) from TGA graph (g)

$M_{HC,0}$: Theoretical mass of fixed carbon (hard coke) determined from carbon content (g)

$$X_R = \frac{M_0 - M_t}{M_0 - M_f} \qquad (4.8)$$

X_R: Fractional reduction of coke + oxygen carrier mixture

M_0: Mass of model coke + oxygen carrier mixture before combustion (g)

M_f: Mass of completely combusted model coke + oxygen carrier mixture (reduced oxygen carrier + ash), (g)
M_t: Instantaneous mass of model coke + oxygen carrier mixture (g)

4.3.2 CLC tests of FCC coke with oxygen carriers in FxB-MS unit

The validity of the experimental results obtained from TGA was investigated using a lab-scale fixed-bed reactor, equipped with an online mass spectroscopy (FxB-MS). The products (CO_2, CH_4, and H_2) from the combustion of model coke with CuO were determined using the ratios of m/z (44, 15, and 2) in MS. The effects of temperature and oxygen carriers on the combustion of MAT coke (MC; deposited on ECat during the MAT tests) were investigated using the FxB-MS unit.

4.3.2.1 Comparison of combustion profiles of model coke in TGA and FxB-MS units

The combustion of model coke with bulk CuO was investigated with the FxB-MS unit (Figure 4.7) using the following experimental conditions; 0.054 g of model coke (low volatile semi-anthracite, consisting of 77.4 wt.% of C and 3.77 wt.% of H) were physically mixed with stoichiometrically required amount of CuO (~1.27 g). The mixture was then placed in a quartz reactor, heated from ambient temperature to the combustion temperature (850 °C) with a heating rate of 20 °C/min under an N_2 flow rate of 35 ml/min and the temperature was maintained at this level until the combustion finished. The combustion products were simultaneously analysed in the online MS integrated with fixed-bed.

4.3.2.2 Identification of combustion products of the model and MAT cokes with CuO

The CLC tests were repeated using ~0.92 g of MAT coke (consisting of 4.55 wt.% of C and 0.37 wt.% of H) deposited on ECat during the cracking of n-hexadecane with ~1.38 g of bulk CuO at the same conditions mentioned above using the FxB-MS unit. In the CLC tests of MAT and model cokes, the amount of carbon was kept the same to get an easy comparison on the combustion behaviours and products. The combustion gases such as CO_2, H_2, and CH_4 were screened by the online MS.

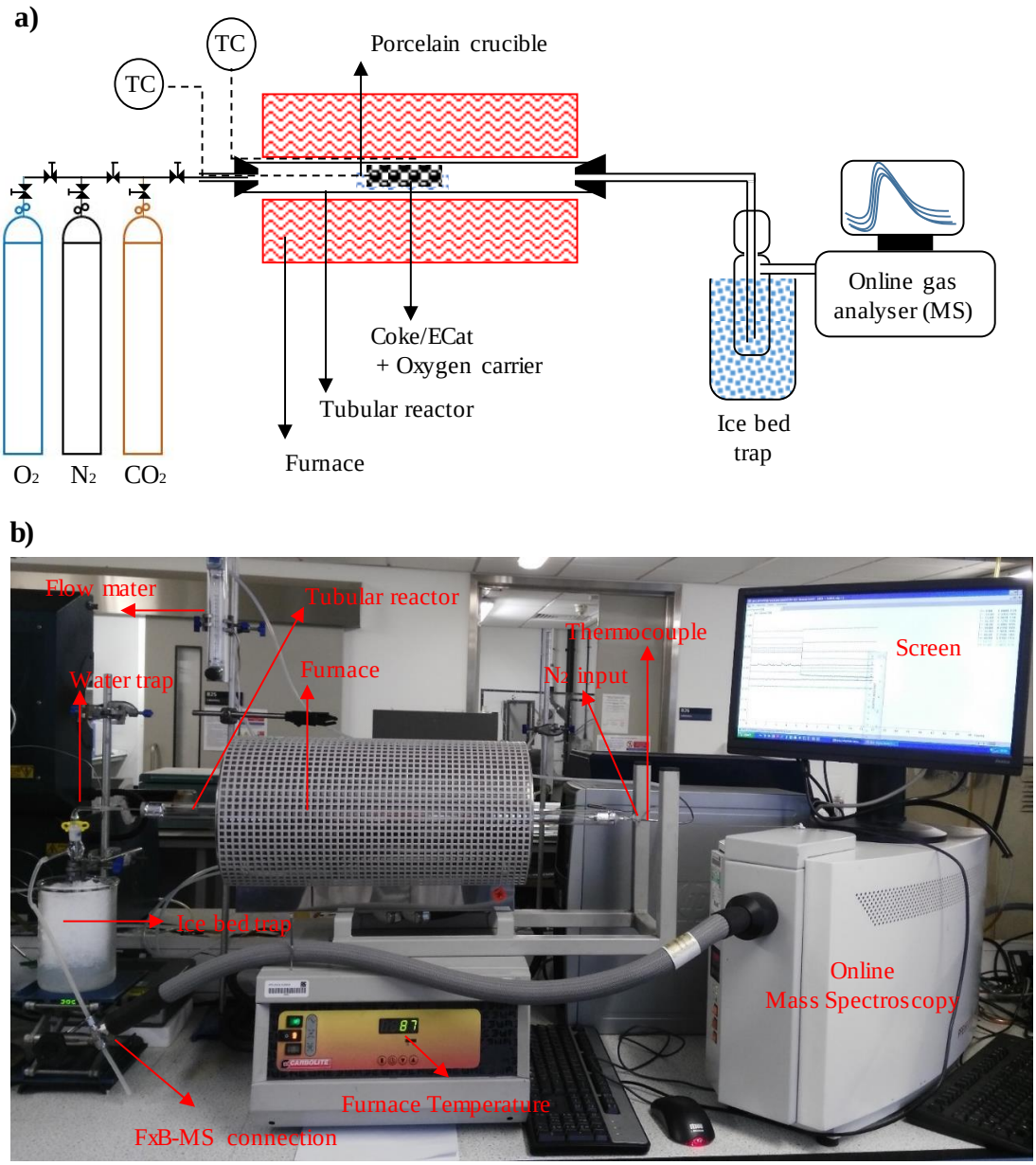


Figure 4.7. The experimental set-up of FxB-MS unit, a) Flowchart and b) Picture

4.3.2.3 Calibration graph for the converting of ion current to the percentage of CO_2 in combustion gases

A calibration graph was produced for ion current vs the volumetric ratio of CO_2. A group of gas mixtures having different volumetric ratios of CO_2 and N_2 were prepared and analysed in the online MS to get the specific ion current (A) values for the particular ratio of CO_2 mixtures. Then the calibration graph for the MS unit was produced.

4.3.2.4 Effects of the temperature on the combustion of MAT coke with bulk CuO

To investigate the effect of temperature on the combustion of coke deposited on ECat (MAT coke) with bulk CuO, stoichiometrically required amount of CuO (~1.32 g) and coke deposited ECat (~0.88 g) were mixed and placed in the quartz reactor in the FxB-MS unit. The mixture was then heated from ambient temperature to the combustion temperatures, 700, 750, 800 and 850 °C, with a heating rate of 20 °C/min under an N_2 flow rate of 35 ml/min and the temperature was kept at this level until the combustion completed. The combustion gases were simultaneously screened by an on-line MS as ion current and transformed to CO_2 flowrate using calibration graph.

4.3.2.5 Effects of the bulk oxygen carriers, CuO, Co_3O_4, and Mn_2O_3, on the combustion of MAT coke

To investigate the effects of oxygen carriers on the CLC of MAT coke, coke deposited ECat catalysts were mixed with the stoichiometrically required amount of oxidised oxygen carriers; CuO, Co_3O_4, and Mn_2O_3. ~0.92 g coke deposited ECat was mixed with ~1.38 g of CuO, ~0.89 g of coke deposited ECat was mixed with ~2.02 g of Co_3O_4, and ~0.93 g of coke deposited ECat was mixed with ~4.17 g of Mn_2O_3. Then, the combustion of coke deposited on ECat was investigated in the FxB-MS unit using the same experimental procedure (heating rate and flow rate of carrier gas) described above at a combustion temperature of 800 °C.

4.3.3 CLC test of coke deposited on reduced oxygen carriers impregnated ECat with oxidised oxygen carriers impregnated ECat in FxB-MS and FsB-MS units

The combustion of coke deposited on I-Cu/ECat and I-Mn_3O_4/ECat were investigated with stoichiometrically required amount of I-CuO/ECat and I-Mn_2O_3/ECat as proposed in the novel CLC-FCC concept. ~1.85 g coke deposited I-Cu/ECat (0.939 wt.% of C and 0.062 wt.% of H) was mixed with ~4.64 g of I-CuO/ECat (0.56 g of CuO) and ~1.85 g coke deposited I-Mn_3O_4/ECat (0.949 wt.% of C and 0.097 wt.% of H) was mixed with ~6.24 g of I-Mn_2O_3/ECat (1.81 g of Mn_2O_3). The samples placed into a quartz reactor

which located in FxB-MS unit and heated from ambient temperature to the combustion temperatures, (750 and 800 °C) with a heating rate of 20 °C/min under a N_2 flow rate of 35 ml/min.

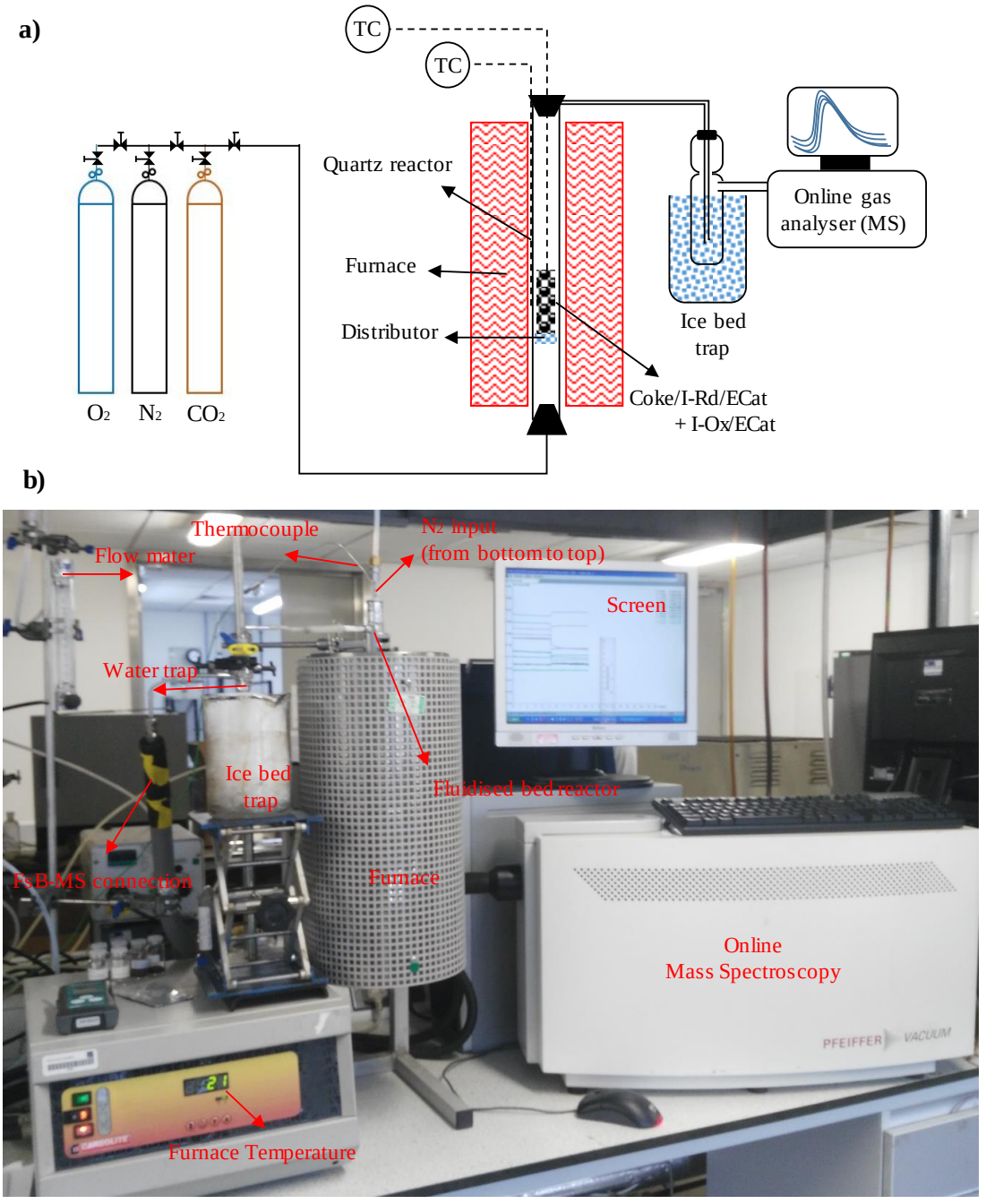


Figure 4.8. a) Schematic diagram and b) picture of FsB-MS experimental set-up (Rd: reduced oxygen carrier, Ox: Oxidised oxygen carrier)

Additionally, the combustion tests of coke deposited on I-Cu/ECat, and I-Mn_3O_4/ECat with I-CuO/ECat and I-Mn_2O_3/ECat were investigated in a lab-scale fluidised-bed reactor

(FsB-MS, Figure 4.8) using a minimum fluidising velocity (U/U_{mf} = 1.0). The mixture was placed in a quartz fluidised bed reactor, which was located into the tubular furnace as demonstrated in FsB-MS, the flow rate was set to the minimum fluidisation flow rate of N_2 (~280 ml of N_2/min). The reactor was then heated from room temperature to 750 °C, with a heating rate of 20 °C/min under an N_2 flow rate of minimum fluidising velocity and the temperature was kept at this level until the combustion finished. The combustion% for all these CLC tests in FxB-MS and FsB-MS was calculated using Equation 4.9.

$$\text{Combustion (of MAT coke) (vol.\%)} = \frac{V_{CO_{2,MS}}}{V_{CO_{2,Coke}}} * 100 \qquad (4.9)$$

$V_{CO_{2,MS}}$: Volume of CO_2 measured by MS after the combustion of coke with oxygen carrier (ml)

$V_{CO_{2,Coke}}$: Volume of CO_2 calculated on the basis of carbon in the coke (ml)

The minimum fluidising velocity (u_{mf}) was determined using the same procedure presented by Kunii and Levenspiel [203] and Yang [204]. If the particle Reynolds number at minimum fluidising conditions lower than 20, the minimum fluidising velocity can be determined using Equation 4.10.

$$u_{mf} = \frac{d_p^2(\rho_s - \rho_g)g}{150\mu} * \frac{\varepsilon_{mf}^3 \emptyset_s^2}{1-\varepsilon_{mf}} \qquad Re_{p,mf} < 20 \qquad (4.10)$$

$$Re_{p,mf} = \frac{d_p u_{mf} \rho_g}{\mu} \qquad (4.11)$$

u_{mf}: Minimum fluidisation velocity (cm/s)

d_p: Particle diameter (cm)

ρ_s: Density of solids (kg/cm^3)

ρ_g: Gas density (kg/cm^3)

g: Acceleration of gravity (980 cm/s^2)

μ: Viscosity of gas (kg/m.s)

ε_{mf}: Void fraction in a bed at minimum fluidising conditions

$\emptyset_s$: Sphericity of a particle (dimensionless)

$Re_{p,mf}$: Particle Reynolds number at minimum fluidising conditions (dimensionless)

The particle diameter of the ECat catalysts (d_p) was measured about 75 microns (0.0075 cm) by sieving method. Furthermore, it was assumed that the particle diameter was not dramatically changed after the impregnation of oxygen carriers neither coke deposition. The density of solid (ρ_s) for Cu-based experiments was assumed an average density of I-CuO/ECat (2.84 g/cm^3) and I-Cu/ECat (2.77 g/cm^3), which is 2.80 g/cm^3. Similarly, the density of solid for Mn-based experiments was assumed the average density of I-Mn_2O_3/ECat (3.11 g/cm^3) and I-Mn_3O_4/ECat (3.05 g/cm^3), which is 3.08 g/cm^3. The gas density (ρ_g) and viscosity (μ) for carrier N_2 were found as 0.001251 g/cm^3 and 0.000176 g/cm s, respectively. The catalyst pellets are spherical, thus, the sphericity of particle ($\emptyset_s$) must be 1.0 (the fragmentation of the catalyst particle after oxygen carrier impregnation was neglected). The void fraction in the bed can be read as 0.485 from the chart, "ε_{mf} as a function of d_p for fine particles" presented by Xu and Zhu [205].

From Equation 4.10, the minimum fluidisation velocity can be determined as;

u_{mf} =1.29 cm/s for the combustion of Coke/I-Cu/ECat with I-CuO/ECat

u_{mf} =1.42 cm/s for the combustion of Coke/I-Mn_3O_4/ECat with I-Mn_2O_3/ECat

From Equation 4.11, the particle Reynolds numbers can be found as;

$Re_{p,mf}$ = 0.069 for the minimum fluidising velocity of 1.29 cm/s

$Re_{p,mf}$ = 0.075 for the minimum fluidising velocity of 1.42 cm/s

Thus, both particle Reynolds numbers are lower than 20, the Equation 4.10 is suitable for the calculation of minimum fluidising velocity.

4.4 Characterisation of fresh and used oxygen carriers modified ECat

The crystalline phases of oxygen carrier modified ECat was identified by X-ray powder diffraction (XRD). The surface morphology and qualitative elemental composition of catalyst was investigated by Scanning electron microscope (SEM) and Energy-dispersive X-ray spectroscopy (EDS) mapping, respectively. The ratio of oxygen carrier impregnated on the ECat was quantitatively measured by X-ray fluorescence (XRF). The textural properties such as surface area and pore structure, were measured by N_2

adsorption-desorption method. The true densities of the oxygen carriers impregnated ECat catalysts were evaluated by Helium Pycnometer. The Brönsted and Lewis acidities of the catalysts were measured by Fourier-transform infrared spectroscopy (FTIR). Finally, the amount of carbon (coke) which was deposited on oxygen carrier modified ECat catalysts was measured by elemental analysis.

4.4.1 X-ray powder diffraction (XRD) analysis

XRD analysis can be used for the identification of crystalline phases presents in each oxygen carriers [128, 129, 146, 183, 206, 207]. The crystalline phases of the oxygen carriers modified ECat were measured by Siemens D500 X-ray powder diffractometer with Cu-Kα having a wavelength of 0.15406 nm radiation operating at 40 kV and 35 mA. Both fresh and used oxygen carrier modified ECat catalysts having a particle size of 53-150 µm were placed into a sample holder and using a press on the top of the sample side until a smooth surface was obtained. Subsequently, the samples were scanned over a 2θ range of 5° to 55° with a step size of 0.05° and a step time of 2 s. The XRD results were correlated with the references, Joint Committee on Powder Diffraction Standards (JCPDS).

4.4.2 Scanning electron microscope (SEM) and Energy-dispersive X-ray spectroscopy (EDS) analysis

SEM is used for the surface characterisation of oxygen carrier modified catalyst in terms of chemical and physical properties [127-129, 206, 208, 209]. The surface morphology, sintering and agglomeration of the oxygen carrier modified ECat catalysts were scanned using a JEOL JSM 6490LV instrument. The sample preparation technique of SEM-EDS analysis is explained as followed; both fresh and used catalysts having a diameter lower than 150 µm were sprinkled onto a carbon tape which was stick on an SEM holder. The samples were then coated using carbon for 10 min using QUORUM Q150R ES rotary pumped coater in order to enable the conductance of the catalysts. The carbon-coated fresh and used catalysts (ECat and oxygen carriers modified ECat) were located in JEOL JSM 6490LV microscope and imaged at different magnifications of 100, 20, 10 and 2 µm at 20 kV accelerated voltage using secondary electron imaging (SEI) modes.

Additionally, the elemental characterisation, especially the distribution of impregnated oxygen carriers on ECat catalysts have been identified by EDS mapping and spectrums using Oxford X-Max spectroscopy. The qualitative elemental analysis of the oxygen carrier impregnated ECat catalysts was performed in a spot mode where the beam is focused on a single area or point manually chosen in the field of view. The selected locations are presented on the SEM images with using a square (□) or a plus (+) signs.

4.4.3 Energy-dispersive X-ray fluorescence (XRF) analysis

In addition to qualitative elemental characterisation with EDS, the oxygen carrier impregnated on ECat has been measured by XRF using Panalytical Epsilon 3-XL. The samples, both fresh and used oxygen carrier impregnated ECat catalysts having a powder form, were filled in a pot having a diameter of 27 mm. Due to a thin Prolene film having a thickness of 4.0 µm placed at the bottom of the pot, the X-rays can quantitatively measure the elemental composition of the samples using a 40kV Ag-anode X-ray tube, calibrated by internal Omnion calibration programme.

4.4.4 Analysis of textural properties with N_2 sorption

The textural properties of prepared oxygen carrier impregnated ECat catalysts derived from nitrogen sorption measurements were conducted using a Micromeritics ASAP 2420 (Micromeritics) N_2 sorption instrument. Prior to analysis, approximately 0.2 g of catalyst was degassed under vacuum at 150 °C for 15 h to remove adsorbed gases and moisture on the samples. The nitrogen isotherms were measured a range of relative pressures (p/p°) from 0.01 to 0.99 at -195.85 °C in liquid nitrogen. The specific surface area of the samples was calculated according to the Brunauer, Emmett, and Teller (BET) method and the pore volume was determined using Barrett, Joyner, and Halenda (BJH) method using Microactive Software V3.0. Furthermore, the micro surface area and pore volume were calculated using the t-plot method, which is the most commonly used method to determine the external surface area and micropore volume of porous materials. Additionally, the average and neck diameters of the pores are measured by the BJH method.

4.4.5 True density analysis

The true density of fresh and used oxygen carrier impregnated ECat catalysts were measured by a Micromeritics AccuPyc II 1340 Gas Pycnometer. The equipment is a gas displacement pycnometer measuring the pore volume of the solid samples by differences of the volume of sample chamber and expansion chamber which was modified by the ratio of gauge pressure after fill and expansion. The volumes used in the calculation were measured with helium using a sample holder having a volume of 1 cm^3. The true density of the samples was calculated by the ratio of sample mass and sample volume. Instrument schematic diagram is presented in Figure 4.9.

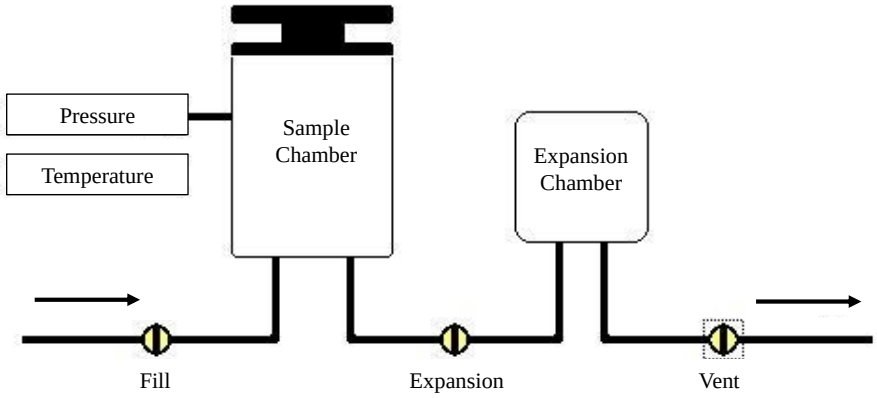


Figure 4.9. Schematic diagram of AccuPyc II 1340 pycnometer

4.4.6 Fourier-transform infrared spectroscopy-pyridine (IR-Py) analysis

The nature of acid sites (Brönsted and Lewis) of prepared catalysts were characterised using pyridine as a probe molecule and scanned using a Bruker Tensor 27 Fourier transform infrared spectroscopy (IR-Py). The sample preparation technique for the IR-Py analysis is explained as followed, before the pyridine adsorption on catalysts, approximately 0.5 g of catalyst was dried at 120 °C for 24 h. After samples cool down, pyridine was introduced to the sample using droplets until the catalysts are all covered by pyridine. The catalysts were then kept at room temperature for 16 h for the impregnation of pyridine molecules into the pores of the catalyst. Then the samples were degassed at 120 °C for 3-4 h. 16 mg of pyridine adsorbed catalysts were then physically mixed with 250 mg of KBr and palletised by pressing the sample powders at 10 kPa. The pelletised

sample was then scanned 64 times per analysis at a 4 cm^{-1} resolution within the 1400–1800 cm^{-1} infrared region.

4.4.7 Elemental analysis of coke deposited on prepared catalysts

The elemental analysis of coke (deposited on oxygen carrier modified ECat) and model coke were investigated by a Leco CHN-628 instrument. The basic principles of the elemental analysis of coke are the dry combustion where the accurately weighed aliquot of a sample is combusted to decompose it into gases; CO_2, N_2, H_2O [210]. The analysis principle of the equipment is presented in Figure 4.10.

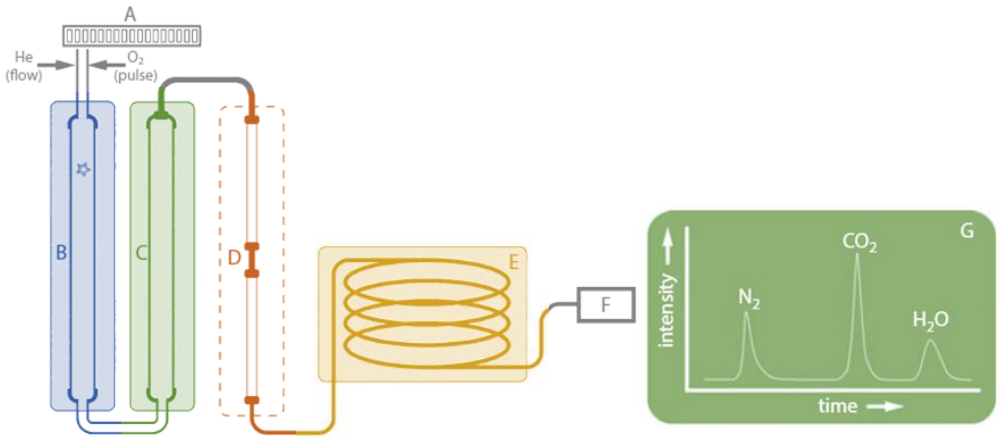


Figure 4.10. An elemental analysis instrument with vertical combustion furnace [210].

Approximately 0.15-0.20 g of used catalysts placed in tin foil cups are dropped from an automated sample carousel (A) to the combustion tube (B) where the combustion temperature held at ~1000 °C. The combustion gases, mainly CO_2, H_2O, and N_2, are swept to the reduction tube (C), where the temperature is kept at about 700 °C, with a constant helium flow. The gases are then passed through one or more chemical traps (D) to remove the unwanted contaminating gas species. The species of interest gases, CO_2, H_2O, and N_2, are chromatographically separated in a column (E) at 40-100 °C. The gases are then detected at different times by a detector (F), infrared cells where the amount of carbon and hydrogen were determined and the thermal conductivity cell where the amount of nitrogen was calculated. The peaks belonging separated species are presented at different times (G) that is the basis for estimating the abundance of the elements, C, H and N, in

each used oxygen carrier modified ECat [210]. The analyses were repeated five times to reduce any systematic error.

4.5 Chemical looping combustion of hydrocarbons with Cu- and Mn-Oxidises

4.5.1 Liquid fuels and oxygen carriers

In this study, n-hexadecane ($C_{16}H_{34}$, Purity: 99%, Alfa Aesar) and n-heptane (C_7H_{16}, Purity: 99%, Prolabo Chemicals) were selected as higher and lower hydrocarbon model liquid fuels. The combustion of model liquid fuels was carried out over two different oxygen carriers; namely, CuO (99%, Sigma Aldrich) and Mn_2O_3 (99%, Sigma Aldrich) in a fixed bed microactivity (MAT) reactor system, presented Figure 4.4.

4.5.2 Baseline thermal cracking tests of liquid fuels

Thermal cracking of the liquid hydrocarbons was carried out in the MAT fixed bed reactor using the following procedure. Although a fluidised bed reactor is the most common reactor type used for CLC tests, such experiments have also been conducted in fixed-bed reactors [211-214]. Firstly, a small amount of glass wool was placed inside the glass reactor, which was then located in the tubular furnace. The reactor temperature was set to 482 °C (since the potential of low temperature CLC of higher hydrocarbons became apparent during the cracking of n-hexadecane over FCC catalysts containing oxidised oxygen carriers at 482 °C while investigating whether CLC could be integrated with FCC for CO_2 capture). When this temperature was attained, the reactor was purged with N_2 for 10 min with a flow of 20 ml/min. Except where stated otherwise, approximately 0.60 ml of the hydrocarbon fuel, either n-hexadecane or n-heptane, was then introduced to the reactor at a rate of 0.03 ml/min for 20 min. During the injection period, the N_2 flow was set to 1 ml/min, and the fuel injection temperature was controlled by a vertically located thermocouple in contact with the glass wool bed. After injection, the reactor and product recovery systems were purged with an N_2 flow of 20 ml/min for 15 min.

The receiver, placed within a water-ice bath condensed the liquid products, and the gases were collected in a 1 L gas bag. The liquid products were analysed using a Clarus 580

GC (Perkin Elmer Elite-1 phase 60 m x 0.25 mm x 0.25 µm capillary column) fitted with an FID detector. An aliquot, 1 µl of the liquid sample (diluted in dichloromethane) was injected at 250 °C with helium as the carrier gas. The gas products collected in a gas bag were immediately analysed using a Clarus 580 GC fitted with FID and TCD detectors for the hydrocarbon and non-hydrocarbon gases respectively, operating at 200 °C. 5 ml of gas samples were injected (split ratio 10:1) at 250 °C with separation performed on an alumina plot fused silica 30 m x 0.32 mm x 10 µm column, with helium as the carrier gas. The oven temperature was programmed from 60 °C (13 min hold) to 160 °C (10 min hold) at 10 °C/min.

4.5.3 Combustion of model liquid fuels with oxygen carriers

The combustion tests of liquid fuels, n-hexadecane and n-heptane, with oxygen carriers (CuO and Mn_2O_3) were conducted in the same experimental set-up, using the same heating, N_2 flow and sample injection protocols as for thermal cracking baseline tests. The oxygen carriers; 3 g CuO or 6 g Mn_2O_3, with masses selected to give the same oxygen transfer capacity, were placed between two pieces of glass wool in the glass reactor. In addition to the liquid and gaseous products analysed as described above by GC, the coke deposited on the used oxygen carriers was quantified by elemental analysis using a Leco CHN628 instrument.

4.5.3.1 The effect of fuel to oxygen carrier equivalence ratio

The equivalence ratio is the ratio of the molar flow rate of fuel to that of oxygen, ϕ, [215, 216]. The definition of the equivalence ratio is asymmetrical relative to fuel-lean ($0<\phi<1$) and fuel-rich ($1<\phi<\infty$) conditions [216]. To demonstrate the effects of fuel to oxygen carrier equivalence ratio, the liquid fuels were introduced to the fixed-bed reactor at 0.03 ml/min for different fuel to oxygen carrier equivalence ratios (ϕ: 0.7, 1.0, 1.3, and 2.0), with all other experimental conditions unchanged. For the different equivalence ratios, while the amount of oxygen carriers were adjusted the same, 3 g of CuO and 6 g of Mn_2O_3, the amount of fuel injected was varied (n-hexadecane 0.158, 0.226, 0.293, and 0.452 mL; n-heptane 0.175, 0.251, 0.321, and 0.502 mL).

4.5.3.2 The effects of fuel feed rate and residence time

To investigate the effects of fuel residence time within the reactor, the CLC of n-hexadecane was carried out using 2 g of inert sand mixed with the 3 g of CuO (SaCuO; 40:60 wt.%) at different volumetric feed flow rates; 0.03, 0.1, 0.2, 1.4 ml/min for ϕ: 0.7 with the same experimental procedure. This has the effect of increasing the volume of the reactor bed by 70%, and so increasing the residence time that the liquid feed is in contact with the oxygen carrier by the same amount. In addition to the increase in the bed volume, the residence time of n-hexadecane in the reactor was also investigated with using different carrier gas volumetric flow rates of 0.5, 1.0, and 2.0 ml/min over CuO at 0.2 ml/min feed flow rate and for ϕ being 0.7.

4.5.3.3 The effect of temperature

To investigate the temperature effects on the performance of the combustion of model coke with oxygen carrier, the CLC of n-hexadecane were investigated with CuO for a fuel to oxygen carrier equivalence ratio of 0.7 at a feed flow rate of 0.2 ml/min at eight different temperatures of 320, 360, 380, 400, 440, 482, 520, 560 °C. The heating rate, N_2 flow, sample injection and product collection protocols were exactly the same as for thermal cracking baseline tests.

4.5.3.4 Multiple cycles tests of CuO with n-hexadecane combustion

The impact of repeated cycles of n-hexadecane combustion on the performance of the oxygen carriers was investigated with bulk CuO and fuel to oxygen carrier equivalence ratio of 1.3 at a feed flow rate of 0.03 ml/min over seven reduction and oxidation cycles. For the first five cycles, after each reduction of CuO with n-hexadecane, the reduced form Cu particles were oxidised at 700 °C for 20 min in a muffle furnace and then reused for the next combustion experiment. To ensure complete oxidation of the reduced form oxygen carrier for the 6th and 7th cycles it was re-oxidised at 700 °C and 900 °C for 60 min respectively. The multiple cycle tests were repeated using CuO/Al_2O_3 (80:20 wt.%), which was prepared by the co-precipitation method presented by Chuang et al. [178, 217, 218]. For the seven cycles, after each reduction of CuO/Al_2O_3 with n-hexadecane, the

reduced form Cu particles were re-oxidised at 700 °C for 20 min and then reused for the next cycle of combustion. These results were confirmed by measuring the CO_2 evolved during the seven multiple cycles of combustion via ThermoStar TM GSD 301T mass spectroscopy.

4.5.3.5 The combustion of methane over CuO at low temperature

In addition to the higher hydrocarbons, n-hexadecane and n-heptane, the reactivity and combustion of methane (in the form of a gas mixture: 20% CH_4 + 80% He) was investigated with CuO under similar experimental conditions using same experimental set-up. The stoichiometric amount of methane (approximately 210 ml methane) was introduced to 3 g of CuO placed in the microactivity reactor at 20 ml/min of 20% CH_4 and 80% He mixture at 482 °C. During this injection time, N_2 flow was switched off. After the injection, the reactor and product recovery systems were purged with an N_2 flow of 20 ml/min for 15 min, and the products collected in the gas bag were immediately analysed by using the Clarus 580 GC fitted with FID and TCD detectors.

4.5.4 Data evaluation

The equivalence ratio, ϕ, was calculated using Equation 4.12, which was modified from [215, 216]. The combustion% was defined as the ratio of the actual amount of CO_2 produced by combustion and the maximum amount of CO_2 that can be provided either full combustion of the liquid fuel (fuel-lean experiments) or full reduction of the oxygen carrier (fuel-rich experiments). It was calculated using Equation 4.13. The yield of the products; coke, $C_{1\text{-}6}$ (from methane to C_6 hydrocarbons) and un-combusted liquid fuel were calculated using the Equation 4.14 [169, 170, 172, 174]. Moreover, the oxygen carriers can show different oxygen transport capacities according to their combustion reaction. The oxygen transport capacities of oxygen carriers in CLC was calculated by Equation 4.15 [170].

$$\phi = \frac{b.n_F}{n_{OC}} \qquad (4.12)$$

ϕ: Equivalence ratio of fuel to oxygen carrier

n_{OC}, n_F: Molar mass of oxygen carrier and liquid fuel, respectively

b: Stoichiometric coefficient for each reaction.

$$\text{Combustion (of liquid fuels) wt.\%} = \frac{W_{CO_2}}{W_{CO_{2,max}}} * 100 \quad (4.13)$$

W_{CO_2}: Actual weight of CO_2 after combustion of liquid fuel with oxygen carrier (g)

$W_{CO_{2,max}}$: Maximum weight of CO_2 that can be produced either fully combustion of liquid fuel (fuel-lean experiments, $0<\phi<1$) or fully reduction of oxygen carrier (fuel-rich experiments, $1<\phi<\infty$), (g)

$$\gamma_i = \frac{W_{C,i}}{W_{C,feed}} * 100 \quad (4.14)$$

γ_i: Yield of *i* ($C_{1\text{-}6}$, and un-combusted liquid fuel, wt.%)

$W_{C,feed}$: Carbon based weight of liquid fuel (n-hexadecane or n-heptane), (g)

$W_{C,i}$: Carbon based weight of product i (CO, $C_{1\text{-}6}$, and un-combusted liquid fuel), (g)

$$R_0 = \frac{m_{ox} - m_{red}}{m_{ox}} \quad (4.15)$$

R_0: Oxygen transfer capacity

m_{ox} and m_{red}: Mass of oxygen carrier on the complete oxidation state and full reduction state, respectively.

4.5.5 Characterisation of used oxygen carriers

In order to characterise the used oxygen carriers (CuO, CuO/Al_2O_3, and Mn_2O_3), the true density of both the fresh and used carriers were measured by a Micromeritics AccuPyc II 1340 Gas Pycnometer. The particle size distributions of oxygen carriers were measured by sieving, ranging from 53 to 300 μm. The fragmentation and agglomeration of fresh and used CuO and CuO/Al_2O_3 were imaged by an SEM (JEOL JSM 6490LV) operated at 20 kV accelerated voltage, using secondary electron imaging (SEI) modes. The crystalline phases of the oxygen carriers were measured by a Siemens D500 X-ray powder diffractometer (XRD) with Cu-Kα having a wavelength of 0.15406 nm radiation

operating at 40 kV and 35 mA. The samples were scanned over a 2θ range of 20° to 80° with a step size of 0.02° and a step time of 2 s. The XRD results were correlated with the references, Joint Committee on Powder Diffraction Standards (JCPDS).

Chapter 5
Cracking Activity Test of Modified FCC Catalysts

5.1 Baseline cracking tests with commercial FCC catalysts

Prior to the cracking of the model feed (n-hexadecane) using the commercial FCC catalysts, thermal cracking experiments were firstly conducted at a temperature of 482 °C in an empty microactivity test (MAT) unit in order to understand the contribution of the thermal cracking on the conversion of the model cracking feed. These experiments resulted in minimal cracking with lower than 3.0 wt.% of the initial n-hexadecane converted to cracked products, with the remaining products composed of unaltered n-hexadecane. The low contribution of thermal cracking of n-hexadecane in the catalytic cracking is consistent with previous findings [219, 220] where the contribution of the thermal cracking of n-hexadecane was found to be lower than 5% of the whole conversion.

The catalytic activity of unmodified commercial FCC catalysts (FCC75, FCC76 and ECat) was investigated with n-hexadecane cracking in the same experimental set-up using the standard test method for testing FCC catalysts by the MAT unit (ASTM D3907) [76]. An example of the gas chromatogram for the liquid products is presented in Figure 5.1. The numbers on the chromatogram demonstrate the presence of n-alkanes and DCM, which represents dichloromethane, used as the solvent for the dilution of the liquid products before injecting them to gas chromatography (GC). The liquid products were identified using the library included within the GC-MS, and the peaks were also confirmed by comparison with a known model mixture of the standard hydrocarbons.

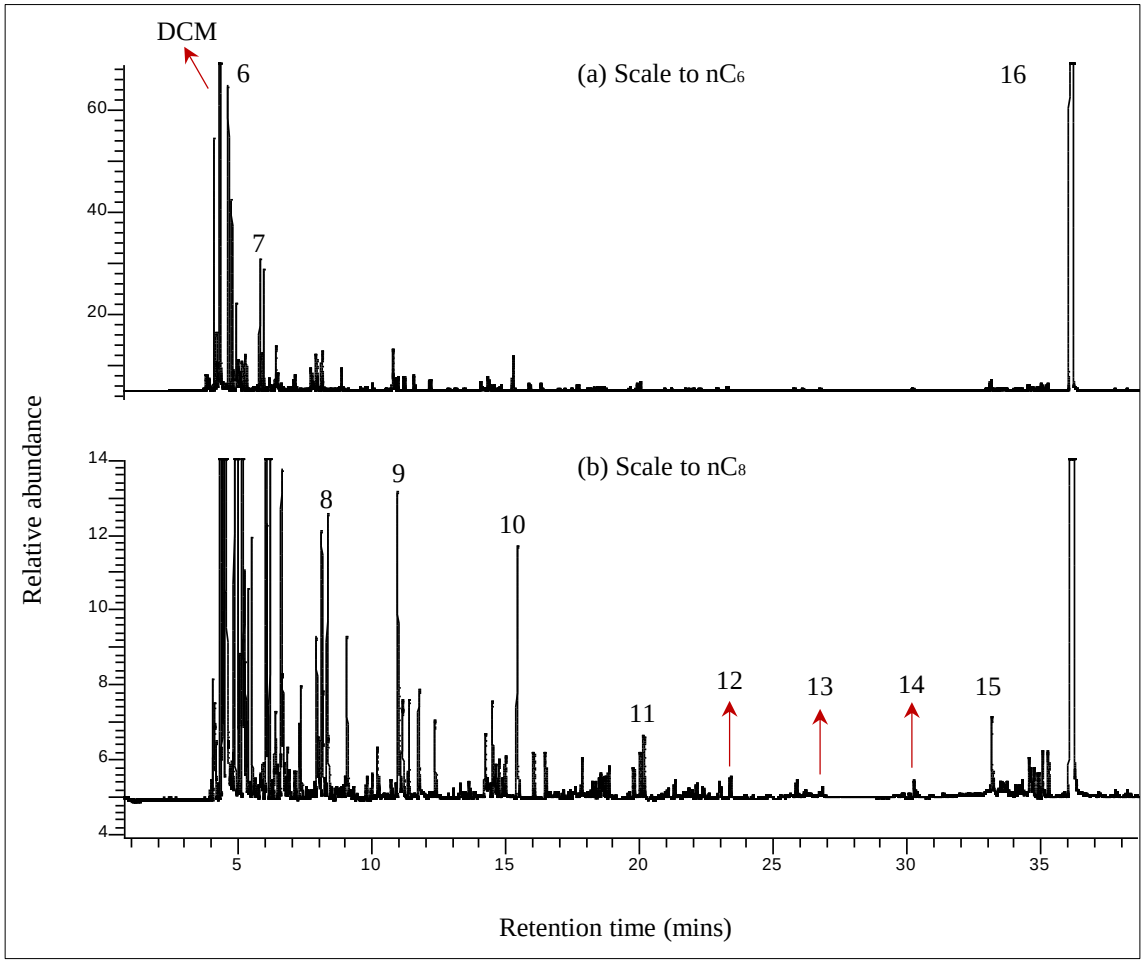


Figure 5.1. Gas chromatograms of the liquid products obtained from the cracking of n-hexadecane over ECat, a) scale to nC_6 b) scale to nC_8. The numbers on the chromatograms represent the presence of n-alkanes.

The chromatogram of liquid products in Figure 5.1. also shows that n-hexadecane cracked into lighter chemicals from C_{15} to C_6. Furthermore, the cracking of n-hexadecane into lighter hydrocarbons (lower than n-C_{11}) was much higher than the hydrocarbons between n-C_{12} and n-C_{15}. A group of reactions such as isomerisation, hydrogen transfer, transalkylation, cyclization of the olefins to naphthanes, dehydrogenation, and dealkylation, may occur in the FCC unit during the cracking reaction of FCC feeds [221]. As put forward by Betiha et al. [219], Christensen et al. [222], Hughes et al. [223] and Abbot and Wojciechowski [224] for cracking of n-hexadecane over various kind of catalysts, different products can be produced along with alkanes (paraffins). In addition to the alkanes (paraffins), alkenes (olefins) were also clearly seen in the cracked products on the chromatograms as it was mentioned that n-hexadecane is mainly cracked to not

only alkanes but also alkenes [219]. Additionally, the produced alkenes may have undergone dehydrocyclization (eliminate H^+ and H^-) to produce aromatic compounds [219]. Furthermore, small amounts of hydrocarbons, larger than n-C16, were produced by different combinations of cracked products.

Figure 5.2 shows that the gas products obtained from the cracking of n-hexadecane over ECat consisted of a small amount of light gases (C_{1-2}); methane, ethane and ethene. However, there were a large amount of liquefied petroleum gases (LPG); propane, propene, butanes, and butenes, and higher hydrocarbons such as pentanes, pentenes, and hexanes. In general, the quantity of alkanes was seen to be higher than the quantity of alkenes because of the model feedstock chemical structure. Similar cracking results have also been observed from the cracking of n-hexadecane over two zeolite catalysts; AISBA15 and AIMFA by Betiha et al. [219]. Additionally, the findings have some similarities with Christensen et al. [222] in which alkenes were not observed in the product mixtures from the cracking of n-hexadecane over platinum modified ZSM-5 catalysts since they were quickly converted to alkanes at the high hydrogen pressure.

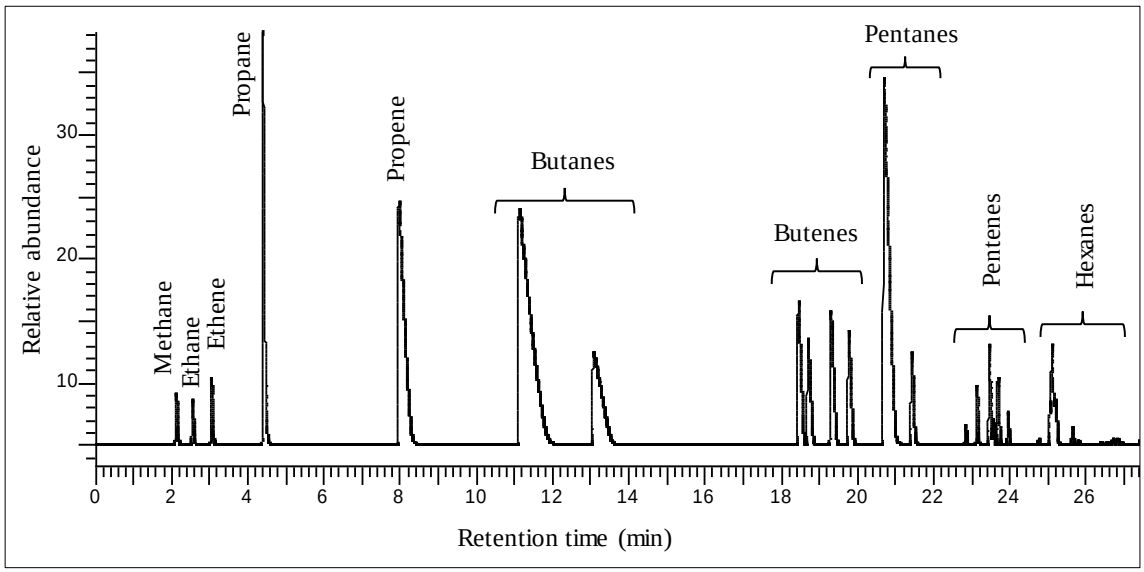


Figure 5.2. Gas chromatogram of the gas products obtained from the cracking of n-hexadecane over ECat at 482 ºC.

To find out the activity of commercial FCC catalysts, the conversion of n-hexadecane, coke, gas and liquid yields, and the selectivity of products such as C_{1-2} (light gases), C_{3-4} (LPG), C_{5-15} (gasoline), C_{16+} (higher hydrocarbons) and coke were determined and

compared for these commercial FCC catalysts. Although gasoline is described as C_5-C_{12} products in the literature [65], it was just adjusted from C_5 to C_{15} in this study because of the low amount cracked products of C_{13}-C_{15}. The conversion of n-hexadecane was calculated by Equation 4.1, and the results are given in Figure 5.3 for three different commercial catalysts (FCC76, FCC75, and ECat). The error bars on Figure 5.3-5.5 represent the standard deviation calculated from triplicate experiments.

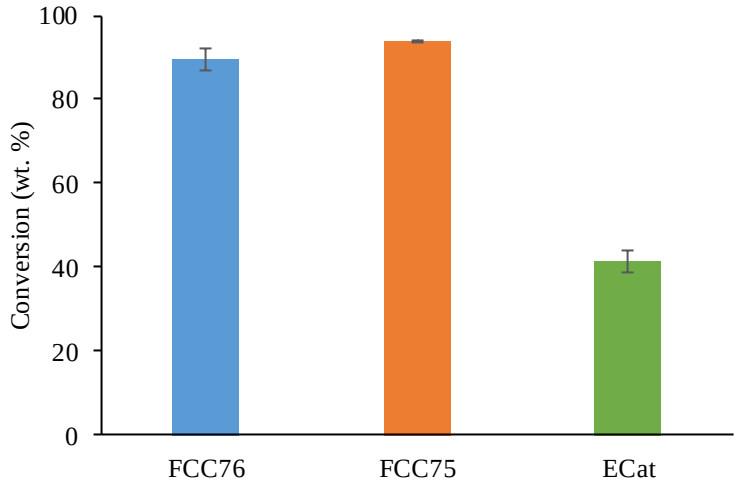


Figure 5.3. Overall conversion of n-hexadecane with the commercial FCC catalysts, FCC76, FCC75, and ECat.

Among these three commercial FCC catalysts, FCC75 and FCC76 demonstrate higher conversion (at about 94 wt.% and 90 wt.% respectively) compared with ECat (approximately 40 wt.%). This high conversion for the model cracking feed (n-hexadecane) may attributed to active sites, which were all accessible on the FCC75 and FCC76 catalysts as both were fresh commercial cracking catalysts supplied by BASF. As in the conventional FCC units, in an effort to reach desirable yield values, a suitable ratio of fresh and used cracking catalysts blends (which is called Equilibrium catalyst-ECat) was used as a cracking catalyst. The classification of catalyst, both fresh and equilibrium, allows for a targeted particle size distribution specific to a unit's design and operating conditions that improve overall catalyst circulation and decreases fresh catalyst additions. Furthermore, using both fresh and used catalyst mixture is economically more feasible than using only fresh catalyst. Although each ECat demonstrates different conversion and selectivity values, a previous research also reported similar n-hexadecane conversions

over ECat (approximately 40 wt.%) [225]. Although the conversion for ECat looks lower than that for FCC75 and FCC76, it can be adjusted with the blending ratio of fresh and used cracking catalysts.

Whereas FCC76 and FCC75 showed better results in terms of gas yield (approximately 67 wt.%), the liquid yields were similar (15 wt.% for FCC76, 13 wt.% for FCC75 and 17 wt.% for ECat) as demonstrated in Figure 5.4. For the coke yield, while the commercial ECat showed lower coke yield (about 1.5 wt.%), FCC76 and FCC75 were responsible for much higher coke yields (9 wt.% and 13 wt.% respectively). The higher coke yield on both FCC75 and FCC76 may be attributed to their fresh forms. Although the heat produced by the regenerator during the combustion of coke deposited on FCC catalysts is used for the heating of the riser, it is well known that the high amount of coke is undesirable in conventional FCC units. Since the coke is generally deposited on the catalyst and blocks the active sites and pores on the catalysts, which causes a decrease in the catalyst activity, a periodic regeneration is necessary [189, 191, 219, 226] for this catalyst.

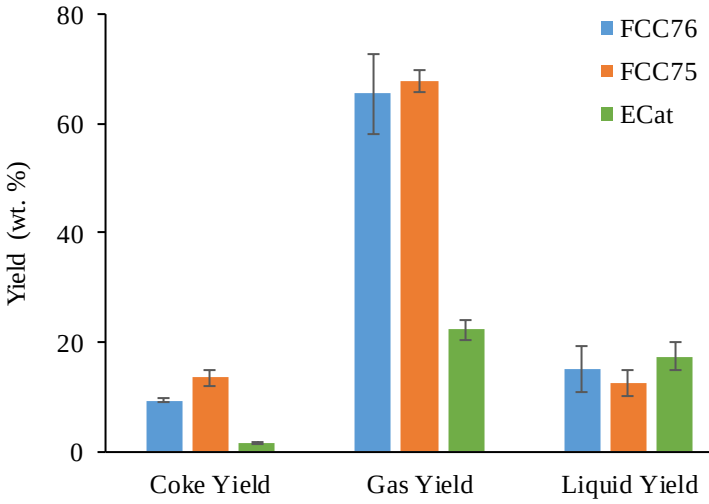


Figure 5.4. Coke, gas, and liquid yields from n-hexadecane cracking over FCC76, FCC75 and ECat.

The product selectivities for C_{1-2} (light gases), C_{3-4} (LPG), C_{5-15} (gasoline) and coke from the cracking of n-hexadecane were calculated by Equation 4.5, and the results are presented in Figure 5.5 for ECat, FCC75 and FCC76. The selectivity of C_{1-2} for ECat is

lower than that for the fresh commercial FCC catalysts. The high selectivity of C_{1-2} over fresh catalysts (FCC75 and FCC76) may be attributed to the micropores since further cracking may occur in the micro-pores, enabling the formation of light gases. This lends support to previous findings in the literature by Betiha et al. [219], who demonstrated that the catalyst having more micro-pores than mesopores gives the highest C_{1-2} distribution. The selectivity of C_{3-4} was estimated ~50 wt.% for FCC76, 53 wt.% for FCC75 and 34 wt.% for ECat, as shown in Figure 5.5. Additionally, the selectivity of C_{5-15} for ECat (61 wt.%), was higher than that for both FCC76 (about 38 wt.%) and FCC75 (nearly 31 wt.%). As for the coke selectivity, it is quite a similar trend for both FCC75 (14 wt.%) and FCC76 (10 wt.%), while it is higher compared with ECat, 3.6 wt.%. The selectivity of C_{16+} was not presented in Figure 5.5 as it was lower than 0.5 wt.% for all of these three catalysts. According to the selectivity results, it can be concluded that while the fresh FCC catalysts are selective for the formation of LPG, ECat is much more selective for gasoline production.

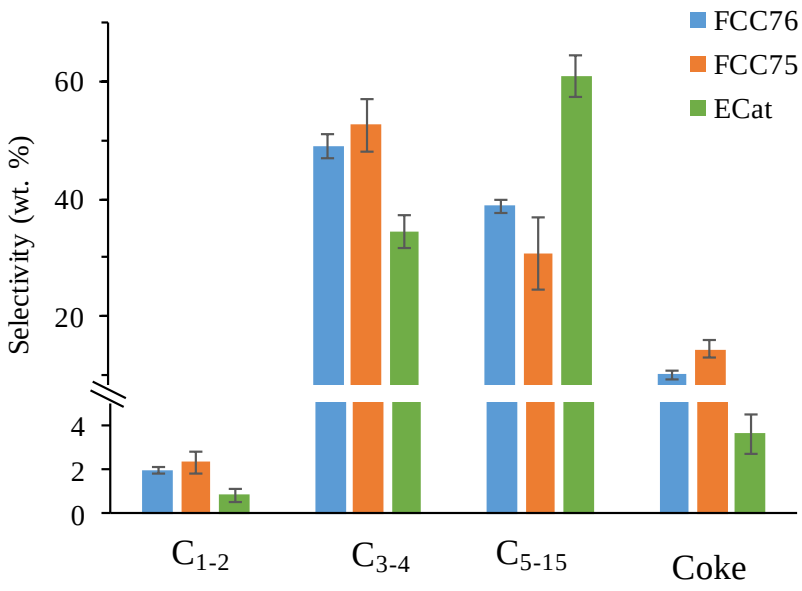


Figure 5.5. Product selectivity for C_{1-2} (light gases), C_{3-4} (LPG), C_{5-15} (gasoline) and coke from n-hexadecane cracking over FCC76, FCC75 and ECat.

Although the normalized elemental analysis demonstrated about 90 wt.% of carbon and approximately 10 wt.% of hydrogen for these catalysts, the amount of carbon on the commercial FCC76 (2.55 wt.%) and FCC75 (4.06 wt.%) were higher than that on the ECat (0.45 wt.%) as seen in Table 5.1. Besides, the hydrogen ratio in the coke was slightly

higher than previously published values where the hydrogen is about 2.0-4.0 wt.% [189]. The excess hydrogen was most likely resulting from the moisture content of the catalysts.

Table 5.1. Coke tests for fresh and used commercial catalysts, FCC76, FCC75 and ECat.

Catalyst	State	Coke on catalyst (wt.%)		Coke composition[a] (wt.%)	
		Carbon	Hydrogen	Carbon	Hydrogen
FCC76	Pure	-	0.16 ±0.01	-	100
	Used	2.55 ±0.28	0.30 ±0.02	89.4 ±1.0	10.5 ±1.0
FCC75	Pure	-	0.30 ±0.03	-	100
	Used	4.06 ±0.43	0.43 ±0.06	90.4 ±1.4	9.6 ±1.4
ECat	Pure	-	0.03 ±0.01	-	100
	Used	0.45 ±0.09	0.03 ±0.01	93.7 ±2.4	6.3 ±2.4

[a] Normalized coke composition was calculated by (weight of carbon/ weight of coke)*100, wt.%.

The coke percentages measured on FCC76 and FCC75 were not feasible compared with the coke on the catalysts using the conventional FCC unit, which is typically to be at about 1.0 wt.% coke [189, 190, 192, 226]. Additionally, the increase in the coke percentage would increase the amount of oxygen carrier required for the integration of CLC into the FCC unit. Hence, to keep the amount of oxygen carrier to a minimum, ECat seems more feasible for the modification of the oxygen carrier due to the realistic cracking results of n-hexadecane. Moreover, as previously discussed, ECat is a commercially used catalyst supplied by CPERI (Greece). Therefore, the results of oxygen carriers modified by ECat is likely to be more realistic compared with other commercial fresh cracking catalysts in terms of cracking reactions.

5.2 Cracking of n-hexadecane over oxygen carrier modified ECat prepared by mechanical mixing

After choosing the commercial FCC catalyst, ECat having more realistic cracking results, to demonstrate the effects of oxygen carriers modified ECat on the cracking reaction, stoichiometrically required amount of oxidised oxygen carriers such as CuO, Co_3O_4, and Mn_2O_3 and their possible reduced states such as Cu, Cu_2O, CoO and Mn_3O_4, were mechanically mixed with ECat and then tested in the cracking of n-hexadecane using MAT unit. Although the cracking reaction would be taken place over reduced oxygen carriers modified FCC catalyst (Me_nO_{m-1}/Cat) as mentioned on the proposed CLC-FCC process (Figure 3.1), the oxidised oxygen carrier modified FCC catalysts (Me_nO_m/Cat)

which come from the air reactor, and it may pass through the regenerator without full reduction. It is, therefore, possible to crack the cracking feed over oxidised oxygen carriers modified commercial FCC catalyst. Hence, testing of oxidised and reduced oxygen carriers modified ECat in the cracking reaction is highly important to investigate any detrimental effect of these oxygen carriers on the cracking reaction.

5.2.1 The effect of oxidised oxygen carriers mixed ECat

5.2.1.1 Characterisation of oxidised oxygen carriers mixed ECat

Because of the preparation method, mechanical mixing, the oxygen carriers should not have a detrimental effect on the surface or chemical structure of ECat as the oxidised oxygen carriers, and ECat were commercially supplied. However, it is exceptionally important to characterise the used oxidised oxygen carriers mixed ECat to identify the interaction of oxygen carriers and cracking feed at the experimental conditions. The oxidised oxygen carriers mixed ECat catalysts (M-Mn_2O_3/ECat, M-Co_3O_4/ECat, M-CuO/ECat) tested on cracking of n-hexadecane was characterised by XRD, and the coke deposited on the catalysts was quantified by elemental analysis.

XRD analysis: The XRD patterns of fresh ECat, and used M-Mn_2O_3/ECat, M-Co_3O_4/ECat, M-CuO/ECat proved that oxidised oxygen carriers; CuO, Co_3O_4, and Mn_2O_3 reduced to Cu, CoO and Mn_3O_4 during the cracking of n-hexadecane at 482 °C, demonstrated in Figure 5.6. The XRD pattern of used M-Mn_2O_3/ECat shown in Figure 5.6-b demonstrates that after cracking of n-hexadecane over M-Mn_2O_3/ECat, the characteristic XRD peaks of Mn_2O_3; 18.3°, 23.1°, 32.9°, 35.6°, 38.2°, 40.6°, 42.9°, 45.1°, 47.2°, 49.3°, 53.2° (JCPDS no: 01-071-0636), were not present. Instead, the characteristic XRD peaks of both Mn_3O_4; 18.1°, 28.9°, 30.9°, 32.3°, 36.08°, 50.8°9 (JCPDS no: 01-080-0382), and MnO; 40.5° (JCPDS no: 01-078-0424) were present. Similarly, Figure 5.6-c shows two main characteristic XRD peaks at 36.5°, and 42.4° belongs to CoO (JCPDS no:00-043-1004) in the place of characteristic XRD peaks of Co_3O_4; 19.0°, 31.2°, 36.8°, 38.5°, 44.8° (JCPDS no:00-042-1467). Additionally, two main characteristic XRD peaks of Cu; 43.3° and 50.4° (JCPDS no: 01-085-1326) were apparent instead of the XRD

peaks characteristic of CuO; 32.4°, 35.3°, 35.5°, 38.6°, 38.9°, 46.2°, 48.8°, 51.2°, 53.3° (JCPDS no:01-080-0076), as demonstrated in Figure 5.6-d.

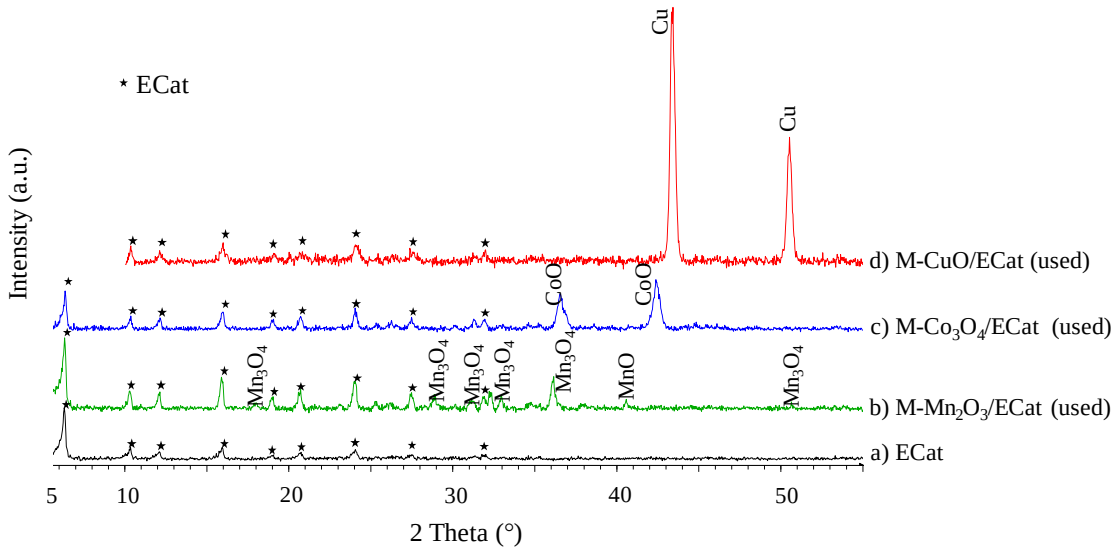


Figure 5.6. XRD patterns of a) fresh ECat and b) used M-Mn_2O_3/Cat, c) used M-Co_3O_4/ECat and d) used M-CuO/ECat.

The oxygen carriers do not show CLOU properties at temperatures of around 482 °C [23, 96, 97, 227, 228]. Therefore, the reduction of the oxygen carriers can be explained by the combustion reaction between the oxygen in the oxidised oxygen carriers and either hydrocarbon feed or cracked products. Such a reduction has never been previously reported in the literature. Another impressive result is that whereas full reduction from CuO to Cu was observed, the other oxygen carriers Co_3O_4 and Mn_2O_3 were only reduced to CoO and Mn_3O_4, respectively. The differences in the reduction stage can be attributed to the bonding energy between metal and oxygen in the oxygen carrier molecules. Further explanation about the combustion of higher hydrocarbons (alkanes) with oxygen carriers is presented in Chapter 7 under the title of "*Selective low temperature chemical looping combustion of higher alkanes with Cu- and Mn- oxides*".

Coke analysis: In order to investigate the coke deposition on the oxidised oxygen carriers mixed ECat during the cracking of n-hexadecane, the carbon and hydrogen (coke) percentage was measured by elemental analysis and presented in Table 5.2. The findings confirmed that the mixing of oxidised oxygen carriers with ECat had a negligible effect

on the amount of coke deposition, which was lower than 1.0 wt.% an acceptable range compared with the coke deposition typically encountered in conventional FCC unit [189, 190, 223, 226, 229].

Table 5.2. Coke percentage on the catalysts and normalized coke composition of fresh ECat, used ECat, M-CuOECat, M-Co_3O_4ECat, and M-Mn_2O_3ECat.

Catalyst	Coke on catalyst[a], wt.%		Coke composition[b], wt.%		H/C[c]
	Carbon	Hydrogen	Carbon	Hydrogen	
Fresh ECat	-	0.10	-	100	-
Used ECat	0.45 ±0.02	0.03 ±0.01	93.6 ±2.2	6.4 ±2.2	0.80
M-CuO/ECat	0.48 ±0.01	0.07 ±0.02	87.2 ±2.5	12.8 ±2.5	1.75
M-Co_3O_4/ECat	0.57 ±0.02	0.06 ±0.01	90.4 ±2.0	9.6 ±2.0	1.26
M-Mn_2O_3/ECat	0.53 ±0.01	0.05 ±0.01	91.2 ±1.7	8.8 ±1.7	1.13

[a] Based on g Coke / g ECat. [b] Normalized coke composition was calculated by (weight of carbon/ weight of coke)*100, wt.%. [c] The ratio of H/C was calculated by the weight of H*12/weight of C.

The coke level was estimated as 0.7% by Hughes et al. [229] for the cracking of n-hexadecane. In another study, Hughes et al. [223] presented realistic coke levels (0.5-1.0%) on the deactivated FCC catalysts tested under industrial operations. However, according to Michalakos et al. [230], the amount of carbon deposition on the catalysts is more significant once the commercial FCC feed used in the cracking reaction instead of n-hexadecane. As in the case of n-hexadecane cracking, coke is usually formed by the reactions subsequent to the cracking reaction, typically dehydrocarbonisation of olefins [230]. However, as for the cracking of commercial FCC feed, it consists of molecules with higher molecular weights, which increase the formation rate of olefins, and it also contains aromatics, naphthalenes, sulphur, and nitrogen heterocyclic compounds that are defined as strong coke precursors [230]. The initial carbon deposition rate and the final carbon level for the commercial FCC feed are, therefore, greater than n-hexadecane. Furthermore, coke deposition also depends on the catalyst type. Betiha et al. [219] found that the catalytic activity of the catalyst decreases as the rate of coke formation increases due to coke, covering acid sites and blocking the pores of the catalyst. The coke deposition was, therefore, measured between 1.39-2.4 for the cracking of n-hexadecane over the catalysts of SBA-15 and MFA type zeolites [219]. Similar findings were also presented by Eberly et al. [231] who reported 2.39% of carbon deposition after the cracking of n-hexadecane over the catalyst of Al_2O_3/SiO_2. Additionally, the ratio of H/C was similar to the values presented in the literature, about 0.46-1.74 [189]. However, the hydrogen

percentage (6.4-12.8 wt.%) in the coke composition was higher than the literature values of 2-4 wt.% [189], which may be attributed to the moisture content of the catalysts.

5.2.1.2 Cracking of n-hexadecane over oxidised oxygen carriers mixed ECat

To demonstrate the cracking activity of M-CuO/ECat, M-Co_3O_4/ECat, M-Mn_2O_3/ECat catalysts, n-hexadecane conversion (both overall and excluding-CLC), coke, liquid and gas yields and products selectivities were calculated by using Equations 4.1-4.6. The conversion of n-hexadecane from the cracking reaction occurred over M-Mn_2O_3/ECat, M-Co_3O_4/ECat, M-CuO/ECat catalysts are presented in Figure 5.7.

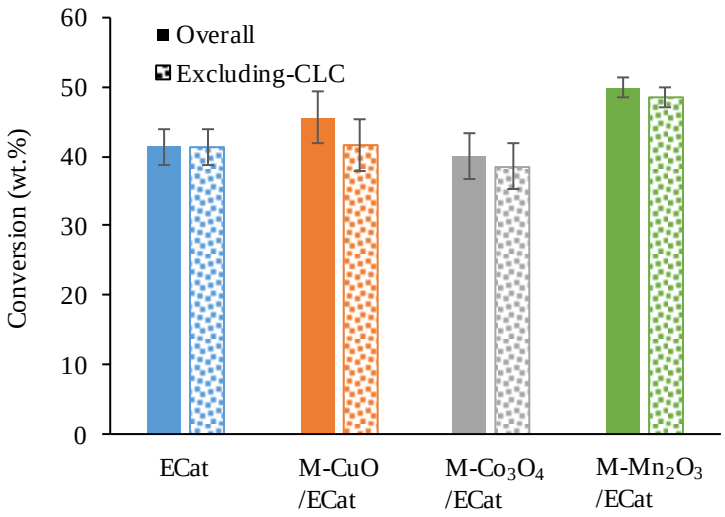


Figure 5.7. Conversion (overall and excluding CLC) of n-hexadecane over the commercial ECat and oxidised oxygen carriers mixed ECat; M-CuO/ECat, M-Co_3O_4/ECat, and M-Mn_2O_3/ECat.

The differences between the overall conversion, where CLC was included, and excluding CLC conversion may arise from the amount of C in the CO_2 produced with additional combustion during the cracking reaction. In terms of the conversion (excluding CLC), the mixing of both CuO and Co_3O_4 with ECat has an insignificant effect on conversion, which was about 40 wt.%, whereas the mixing of Mn_2O_3 with ECat slightly enhanced it from 40 wt.% to nearly 47 wt.% as illustrated in Figure 5.7. This increase may be attributed to the residence time of n-hexadecane in the oxygen carriers mixed catalyst bed. As the volume of the catalyst bed increased about 25 vol.% with the mixing of Mn_2O_3 due to the higher

amount of Mn_2O_3 required for the same oxygen capacity compare with Co_3O_4, and CuO (increased only about 3 wt.% of bed volume).

Moreover, the mixing of oxidised oxygen carriers increased the overall conversion due to the additional combustion. There was only one way to produce CO_2 on this system, which is the combustion of hydrocarbons with oxidised oxygen carriers. The differences between overall and excluding CLC conversions are about 4 wt.% for M-CuO/ECat and 1 wt.% for both M-Co_3O_4/ECat, M-Mn_2O_3/ECat. The higher overall conversion may explain the reduction from CuO to Cu, Co_3O_4 to CoO, and Mn_2O_3 to a mixture of Mn_3O_4-MnO as demonstrated in XRD patterns (Figure 5.6).

Although CuO decomposition is not thermodynamically favoured below 700 °C according to the Positive Gibbs free energy values, the reaction between CuO and C can be favoured between 200-1000 °C as described by Siriwardane et al. [175]. Furthermore, carbon can react with CuO at 482 °C and Cu_2O at 624 °C [175]. Additionally, according to the calculations and characterizations of this research, CuO can reduce to Cu with the combustion of liquid hydrocarbons at a low temperature such as 482 °C. The reduction of CuO to Cu at such a low temperature may be attributed to the minimal external mass transfer at low combustion temperatures. Chuang et al. [187, 218] clarified that the reduction of CuO with CO and H_2 followed the shrinking core mechanism, and proceeded via the intermediate, Cu_2O at high temperatures (~800 °C) when external mass transfer controlled the rate [187, 218]. However, at lower temperatures, the external mass transfer is minimal, and CuO can be reduced to Cu [187]. To identify the reduction of these oxygen carriers with liquid hydrocarbons at the cracking conditions, a group of combustion reactions of model hydrocarbon liquid fuels such as n-hexadecane and n-heptane with CuO and Mn_2O_3 were investigated and the results are presented under Chapter 7 with a title of "*Selective low temperature chemical looping combustion of higher alkanes with Cu- and Mn- oxides"*.

As illustrated in Figure 5.8, oxidised oxygen carriers mixed ECat, M-CuO/ECat, M-Co_3O_4/ECat, and M-Mn_2O_3/ECat, have a minimal effect on the coke yield, which is between 1.5-1.9 wt.%. Whereas the gas yield was enhanced from about 22 wt.% to 33 wt.%, the liquid yield was reduced from 17 wt.% to 10 wt.% by the mixing of CuO with

ECat. The increase in gas yield must be attributed to CO_2 production, thanks to the combustion of hydrocarbons with CuO. However, the mixing of both Co_3O_4 and Mn_2O_3 have a similar gas yield, approximately 22 wt.%. While the mixing of Co_3O_4 had an insignificant effect on the liquid yield, about 17 wt.%, the mixing of Mn_2O_3 increased the liquid yield from 17 wt.% to 26 wt.%.

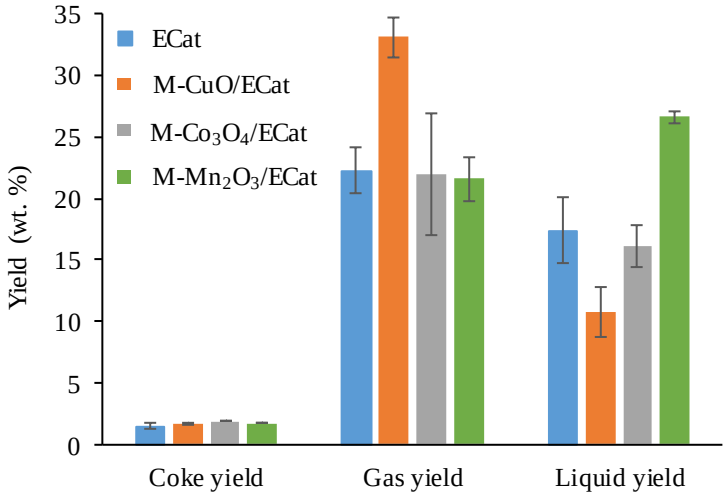


Figure 5.8. Coke, gas, and liquid yields from the cracking of n-hexadecane over commercial ECat and oxidised form oxygen carrier mixed ECat; M-CuO/ECat, M-Co_3O_4/ECat, and M-Mn_2O_3/ECat.

The effects of oxidised oxygen carriers mixing with ECat on the product selectivities are demonstrated in Figure 5.9. The product selectivity was described as the weight percentage of the product in the sum of cracked hydrocarbon products. For instance, the selectivity of $C_{1\text{-}2}$ is the weight percentage of $C_{1\text{-}2}$ in the sum of products; $C_{1\text{-}2}$, $C_{3\text{-}4}$, $C_{5\text{-}15}$, C_{16+}, and Coke. The selectivity of $C_{1\text{-}2}$ and $C_{3\text{-}4}$ demonstrated an increase from 0.8 wt.% to 1.5 wt.% and from 34 wt.% to about 48 wt.%, respectively, using M-CuO/ECat. However, the selectivity of gasoline decreased from 60 wt.% to about 46 wt.% for M-CuO/ECat. That is the reason for higher gas yield and lower liquid yield, shown in Figure 5.8 for M-CuO/ECat. The increase in the selectivity of LPG (about 14 wt.%) is almost equal to the decrease in the selectivity of gasoline for M-CuO/ECat. While the mixing of CuO had a positive effect on the selectivity of LPG, it has negatively affected the gasoline selectivity. On the other hand, the mixing of Co_3O_4 and Mn_2O_3 with ECat demonstrated a negligible difference on selectivity of hydrocarbons such as $C_{1\text{-}2}$, $C_{3\text{-}4}$, $C_{5\text{-}15}$, and C_{16+}, shown in Figure 5.9. The selectivity values are consistent with the previous studies [223,

224, 229, 232] in which the product distributions of n-hexadecane cracking over a standard FCC catalyst attain a maximum at the C_3, C_4 and C_5 region, following that there is a monotonic decrease in the product concentration to C_{15}. Christensen et al. [222] demonstrated the same monotonic decrease on the cracked products from the cracking of n-hexadecane catalysed by conventional and mesoporous ZSM-5 and Pt modified ZSM-5. This monotonic decrease can also be obtained in the GC chromatograms presented in Figure A1-2, Appendix A.

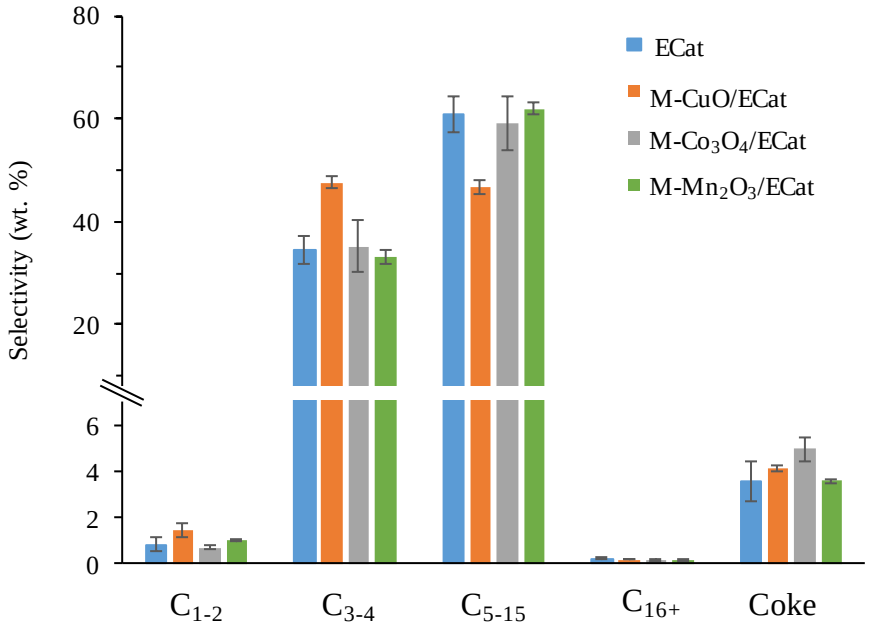


Figure 5.9. Product selectivity of C_{1-2} (light gases), C_{3-4} (LPG), C_{5-15} (gasoline), C_{16+} (higher hydrocarbons) and coke from the cracking of n-hexadecane over commercial ECat and reduced form oxygen carrier mixed ECat; M-CuO/ECat, M-Co_3O_4/ECat, and M-Mn_2O_3/ECat.

Whereas M-Co_3O_4/ECat slightly increased the coke selectivity from 3.6 wt.% to 4.9 wt.%, both M-CuO/ECat and M-Mn_2O_3/ECat demonstrated approximately the same level of coke selectivity (3.6 wt.%) with parent ECat. According to the results, the modification of oxidised oxygen carriers with ECat using mechanically mixing have an insignificant effect on the coke deposition at the cracking conditions thanks to the preparation method. There is no carbon deposition on oxygen carriers such as CuO, Co_3O_4, and Mn_2O_3, under the CLC conditions [97, 172-174, 233, 234] where the combustion of hydrocarbons (gas, liquid, and solid fuels) was investigated over oxygen carriers at relatively high temperatures (750-1000 °C).

5.2.2 The effects of reduced oxygen carriers mixed ECat

As mentioned in the proposed CLC-FCC process (Figure 3.1 in Chapter 3), the cracking reaction would expect to be over reduced oxygen carriers modified FCC catalyst (Me_nO_{m-1}/Cat). Therefore, to investigate the effects of reduced oxygen carriers on the cracking reaction, stoichiometrically required amount of oxidised oxygen carriers' reduced states such as Cu, Cu_2O, CoO and Mn_3O_4 were mechanically mixed with ECat, M-Cu/ECat, M-Cu_2O/ECat, M-CoO/ECat, M-Mn_3O_4/ECat and tested on the cracking of n-hexadecane. The 'M' used on the labelling demonstrates that ECat was modified with the oxygen carriers using mechanically mixing.

5.2.2.1 Reduction of oxidised oxygen carriers

Although oxidised oxygen carriers (CuO, Co_3O_4, and Mn_2O_3) were commercially supplied, the reduced states such as Cu_2O, CoO and Mn_3O_4 were prepared from their oxidised forms. The XRD patterns of prepared reduced oxygen carriers confirmed that the reduction from CuO to Cu_2O, from Co_3O_4 to CoO, and from Mn_2O_3 to Mn_3O_4, were successfully achieved, as shown in Figure 5.10. The peaks at 29.5°, 36.4°, 42.3°, 52.5°, 61.3°, 73.5°, and 77.2° on pattern-c were the characteristic peaks for Cu_2O (JCPDS no:01-075-1531), which reduction from CuO to Cu_2O was achieved as the characteristic peaks belonging to CuO (JCPDS no:01-080-0076) were absent. The peaks at 36.5°, 42.3°, 61.5°, 73.7°, and 77.5° on pattern-b indexed to the phase of CoO crystals (JCPDS no: 00-043-1004) which proves that Co_3O_4 was also successfully reduced to CoO. As for the reduction of Mn_2O_3 to Mn_3O_4, the peaks at 18.1°, 29.0°, 31.1°, 32.3°, 36.1°, 38.0°, 44.4°, 49.7°, 50.7°, 54.0°, 56.0°, 58.5°, 59.9°, 64.7°, 69.8°, 74.1°, and 76.5° on pattern-a prove that the reduction was successfully achieved. In addition to the XRD patterns, the reduction can be roughly understood by the colour changing as the colour of oxidised and reduced oxygen carriers are presented in Figure 5.11.

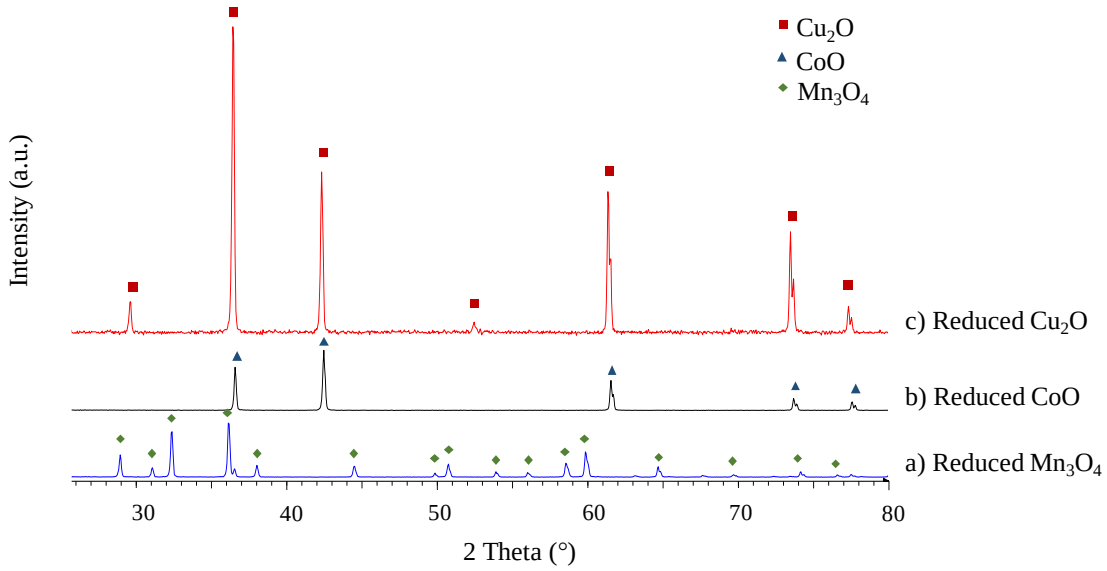


Figure 5.10. XRD patterns of the prepared reduced oxygen carriers; a) Mn_3O_4, b) CoO, c) Cu_2O.



Figure 5.11. Colour of both oxidised oxygen carriers (CuO, Co_3O_4, Mn_2O_3) and reduced oxygen carriers (Cu_2O, CoO, Mn_3O_4)

5.2.2.2 Characterisation of used reduced oxygen carriers mixed ECat

After the reduced oxygen carriers mixed ECat were tested with the cracking of n-hexadecane, XRD analysis of used catalysts was investigated to identify any crystalline deformation. Additionally, the coke percentage and coke composition deposited on M-Cu/ECat, M-Cu_2O/ECat, M-CoO/ECat, M-Mn_3O_4/ECat catalysts were quantified by elemental analysis.

XRD analysis: The characteristic ECat peaks (pointed with black stars) remain after the reduced oxygen carriers mixed ECat catalysts, M-Mn_3O_4/ECat, M-CoO/ECat, and M-Cu_2O/ECat, tested in cracking reaction, as seen Figure 5.12. Although the characteristic peaks for CoO remain for used M-CoO/ECat were seen in Figure 5.12-c, both M-Mn_3O_4/ECat and M-Cu_2O/ECat demonstrated a small reduction peak, belonging to MnO (Figure 5.12-b) and Cu (Figure 5.12-d).

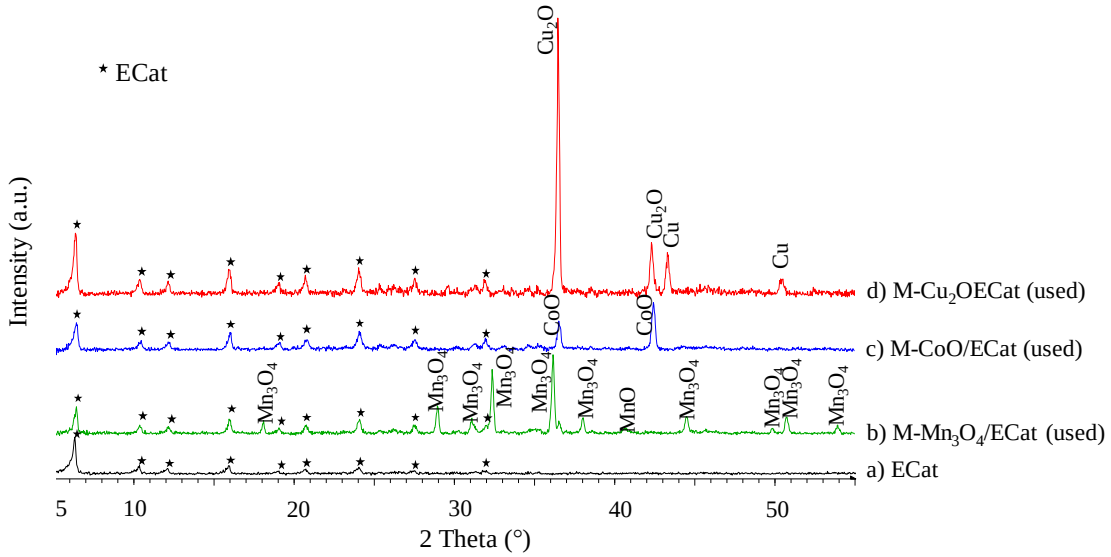


Figure 5.12. XRD patterns of a) fresh ECat and b) used M-Mn_3O_4/ECat c) used M-CoO/ECat d) used M-Cu_2O/ECat

These reductions might be attributed to the low amount of oxidised oxygen carriers, which were in the prepared reduced oxygen carriers. As the intensity of the first reduced states (Mn_3O_4 and Cu_2O) were much higher than that of the further reduced states (MnO and Cu). Although a low amount of reduction was observed after the cracking of n-hexadecane over reduced oxygen carriers mixed ECat, the catalysts were still mainly composed of their original reduced states (Cu_2O, CoO, Mn_3O_4) after the cracking reaction. In contrast, the reduced Cu may be attributed to the combustion of liquid fuels and/or OH/CO with relatively small amount of CuO. Since carbon can combust with CuO at 482 °C, while it needs a higher temperature, nearly 624 °C, for the combustion with Cu_2O, as mentioned by Siriwardane et al. [175].

Coke analysis: The coke deposition on the reduced oxygen carriers mixed ECat catalysts during the cracking of n-hexadecane were measured and presented in Table 5.3. The results confirmed that the coke percentage on ECat and reduced oxygen carriers mixed ECat (M-Cu/ECat, M-Cu_2O/ECat, M-CoO/ECat, and M-Mn_3O_4/ECat) are lower than 0.7 wt.%, which is lower than the ratio of coke formation presented in previous studies [189, 190, 226].

Table 5.3. Coke percentage on the catalysts and normalized coke composition of fresh ECat, used ECat, M-Mn_3O_4/ECat, M-CoO/ECat, and M-Cu_2O/ECat.

Catalyst	Coke on catalyst[a], wt.%		Coke composition[b], wt.%		H/C[c]
	Carbon	Hydrogen	Carbon	Hydrogen	
Fresh ECat	-	0.10	-	100	-
Used ECat	0.45 ±0.02	0.03 ±0.01	93.6 ±2.2	6.4 ±2.2	0.80
M-Cu/ECat	0.43 ±0.02	0.01 ±0.00	97.5 ±0.9	2.5 ±0.9	0.28
M-Cu_2O/ECat	0.39 ±0.02	0.03 ±0.00	93.2 ±0.8	6.8 ±0.8	0.92
M-CoO/ECat	0.42 ±0.01	0.02 ±0.01	95.0 ±2.4	5.0 ±2.4	0.57
M-Mn_3O_4/ECat	0.73 ±0.00	0.06 ±0.03	92.2 ±3.0	7.8 ±3.0	0.98

[a] Based on g Coke/ g ECat. [b] Normalized coke composition was calculated by (weight of carbon/ weight of coke)*100, wt.%. [c] The ratio of H/C was calculated the weight of H*12/weight of C.

For instance, the coke deposition was between 1.39-2.4 wt.% for the cracking of n-hexadecane over MFA and SBA-15 type zeolite catalysts by Betiha et al. [219], over a commercial FCC catalyst by Shi et al. [226] and over Al_2O_3/SiO_2 by Eberly et al. [231]. Furthermore, Voorhies [191] found an increase carbon formation on catalyst with increasing cracking time. Additionally, the ratio of H/C, 0.28-0.98, is quite similar to literature values of 0.46-1.74 [189]. However, the hydrogen percentage in the coke composition was slightly higher than the literature values [189] for the oxidised oxygen carriers mixed ECat catalysts. The high percentage of hydrogen in the coke compositions may be attributed to moisture content on the catalysts, as mentioned previously.

5.2.2.3 Cracking of n-hexadecane over reduced oxygen carriers mixed ECat

In order to investigate the effects of reduced oxygen carriers on the cracking, the prepared catalysts (M-Cu/ECat, M-Cu_2O/ECat, M-CoO/ECat, and M-Mn_3O_4/ECat) were tested on the cracking of n-hexadecane. The catalytic activity of these catalysts was identified with

the conversion of n-hexadecane, yields, and cracked products selectivities calculated by using the Equations 4.1-4.6.

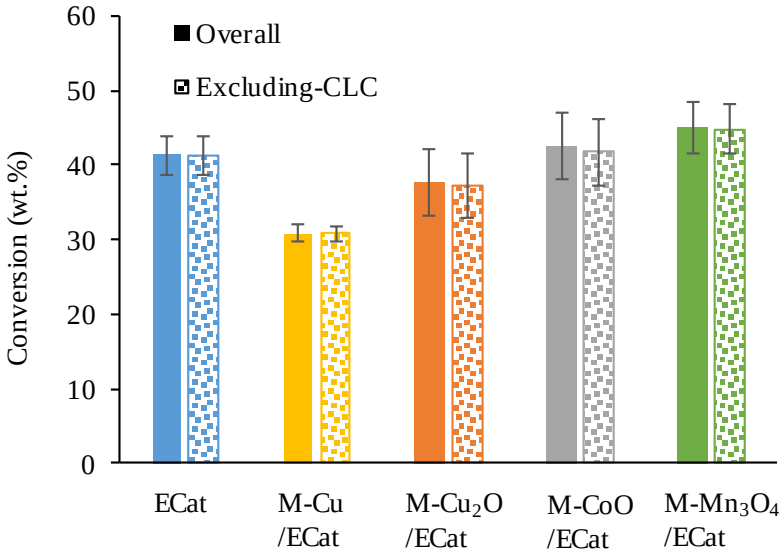


Figure 5.13. Conversion (both overall and excluding CLC) of n-hexadecane over ECat and reduced oxygen carriers mixed ECat, M-Cu/ECat, M-Cu_2O/ECat, M-CoO/ECat, and M-Mn_3O_4/ECat.

Figure 5.13 demonstrates that mixing of metallic Cu with ECat has remarkably detrimental effects on the conversion of n-hexadecane where the conversion decreased from 40 wt.% to 30 wt.%. The detrimental impact of Cu impregnation on the conversion of palm oil cracking over ZSM-5 zeolite catalysts has been mentioned by Siregar and Amin [235]. The decrease in the conversion with the impregnation of Cu was attributed to decreasing on the Brönsted acidity [235]. However, in this study, neither Brönsted nor Lewis acidities should be affected by mixing of metallic Cu as the preparation method does not change any surface properties. The decrease in the conversion may, therefore, be attributed to the negative interaction between model cracking feed and metallic Cu. On the other hand, the conversion was insignificantly affected by the mechanically mixing of Cu_2O, CoO, and Mn_3O_4.

There is no difference between the excluding CLC conversion and overall conversion, as seen in Figure 5.13. The reduced oxygen carries mixed ECat do not provide combustion with hydrocarbon feed (or cracked products) in contrast to oxidised oxygen carriers,

which reduced by the combustion of a hydrocarbon feed as demonstrated the previous section. These findings were also in line with the characterization results (XRD patterns) of tested reduced oxygen carriers mixed ECat where an insignificant further reduction, Cu and MnO, was observed for the reduced Cu_2O and Mn_3O_4, after cracking of n-hexadecane over M-Cu_2O/ECat and M-Mn_3O_4/ECat.

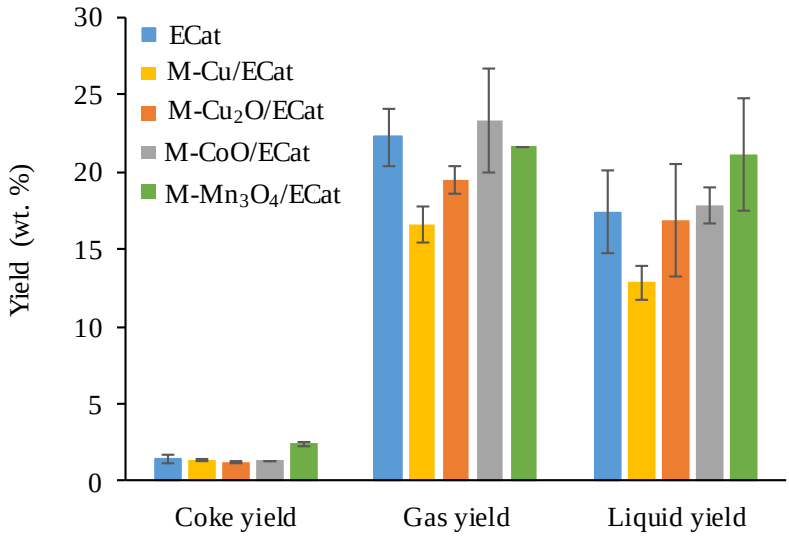


Figure 5.14. Coke, gas, and liquid yields from the cracking of n-hexadecane over ECat and reduced oxygen carriers mixed ECat; M-Cu/ECat, M-Cu_2O/ECat, M-CoO/ECat, and M-Mn_3O_4/ECat.

The coke, gas, and liquid yields after n-hexadecane cracking over commercial ECat and reduced oxygen carriers mixed ECat are presented in Figure 5.14. Cu, Cu_2O, and CoO mixed ECat have insignificant effects on the cracking reaction in terms of coke yield, approximately 1.4 wt.%, whereas it increased from 1.4 wt.% to 2.7 wt.% with the mixing of Mn_3O_4. While the gas yield decreased from 22 wt.% to 17 wt.% and 20 wt.% with the mixing of Cu and Cu_2O, respectively, it was not impacted by mixing with CoO and Mn_3O_4. As for the liquid yield, it also decreased from 18 wt.% to 13 wt.% with the mixing of Cu. However, it was not significantly affected by the mixing of other reduced oxygen carries; Cu_2O, CoO, and Mn_3O_4, as seen in Figure 5.14.

The product selectivities for ECat and reduced oxygen carriers mixed ECat are presented in Figure 5.15. Mixing of reduced oxygen carriers; Cu, Cu_2O. CoO and Mn_3O_4 with ECat, have a negligible effect on the product selectivities of $C_{1\text{-}2}$, $C_{3\text{-}4}$, $C_{5\text{-}15}$, and C_{16+}. The

selectivity of light gases and higher hydrocarbons were kept to minimum after mixing of reduced oxygen carriers as desired [65]. It is known that the formation of light gases takes place on active sites located in the micropores of the catalysts [219]. As the micropores of ECat was kept the same after the modification of reduced oxygen carriers due to the preparation method, mechanically mixing. Thus, the selectivity of light gases was maintained as steady even after modification. The low selectivity for light gases is in complete agreement with previous studies [219, 223, 224, 229, 232, 236], where the cracking of n-hexadecane was investigated over different kind of zeolite catalysts such as Beta, ZSM-5, SBA-15, MCM-41, Y and commercial FCC catalysts. Similarly, the low light gases yield were also presented for the cracking of industrial FCC feedstock [237], light diesel [238], 1,3,5-tri-isopropylbenzene [239], n-decane [240] over different kind of zeolite catalysts. The higher hydrocarbons may be formed by the polymerization of lower hydrocarbons. However, the catalyst, ECat, used in this study, was the commercially available cracking catalyst. Therefore, the minimal higher hydrocarbon selectivity was an expected result.

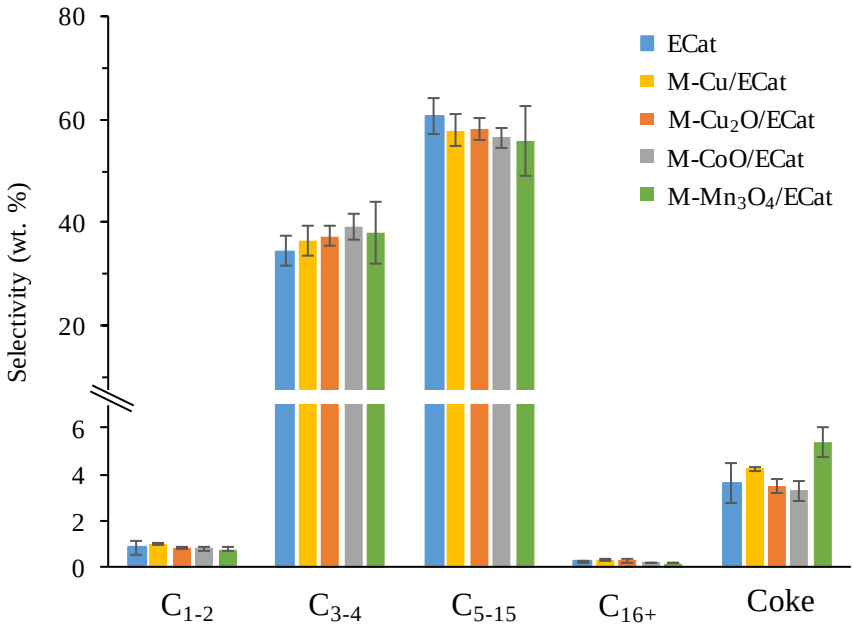


Figure 5.15. Product selectivity of C_{1-2} (light gases), C_{3-4} (LPG), C_{5-15} (gasoline), C_{16+} (higher hydrocarbons) and coke from the cracking of n-hexadecane over commercial ECat and reduced oxygen carriers mixed ECat; M-Cu/ECat, M-Cu_2O/ECat, M-CoO/ECat, and M-Mn_3O_4/ECat.

The selectivity of LPG is also consistent with the previous studies [223, 224, 229, 236] in which n-hexadecane cracking was investigated over a standard FCC catalyst attain a maximum at the C_3, C_4 and C_5 region, following that there is a monotonic decrease in the product concentration to C_{15} (Figure A1-2, Appendix A). Although mixing of Cu, Cu_2O and CoO with ECat have an insignificant effect on the coke selectivity (3.8 wt.%), Mn_3O_4 slightly increased it from 3.6 wt.% to 5.4 wt.%. This increase may be attributed to the residence time of cracking feed in the catalyst bed. As mentioned previously, the stoichiometrically required amount of Mn_3O_4 is higher than the other reduced oxygen carriers, Cu, Cu_2O and CoO due to its low oxygen carrier capacity [234]. The bed volume increase about 25 vol.% with the mixing of Mn_3O_4, which results in an increase the residence time of cracking feed in the catalyst bed, thus the conversion was slightly enhanced and coke selectivity increase due to the mixing of Mn_3O_4. However, it can be concluded that the mixing of reduced oxygen carriers, Cu_2O, CoO, Mn_3O_4, with ECat has negligible effects on the cracking in terms of conversion, yield and product selectivity.

5.3 Cracking of n-hexadecane over oxygen carrier modified ECat prepared by wet-impregnation

The catalysts prepared by mechanical mixing may show some disadvantages such as inhomogeneity in the fluidised bed due to the density differences between oxygen carriers and ECat. By using wet impregnation, it is possible to prepare a new catalyst consisting of an oxygen carrier and ECat having an average density [37, 38, 113, 127, 129, 158, 181-185]. In an effort to investigate the cracking activity of oxygen carriers impregnated ECat, the oxidised and reduced oxygen carriers were introduced into the matrix and fillers of ECat using this method.

5.3.1 The effects of oxidised oxygen carriers impregnated ECat

5.3.1.1 Characterisation of oxidised oxygen carriers impregnated ECat

XRD analysis: The sharp peaks at 35.5°, 38.6°, and 48.8° in Figure 5.16-b prove that CuO (JCPDS no: 01-080-0076) was successfully impregnated into the matrix and fillers of ECat. On the other hand, two new characteristic peaks of Cu at 43.3° and 50.4° (JCPDS

no: 01-085-1326) were obtained for the used I-CuO/ECat (Figure 5.16-c). The characteristic peaks belonging to ECat (demonstrated with black stars) was not affected by the impregnation of CuO.

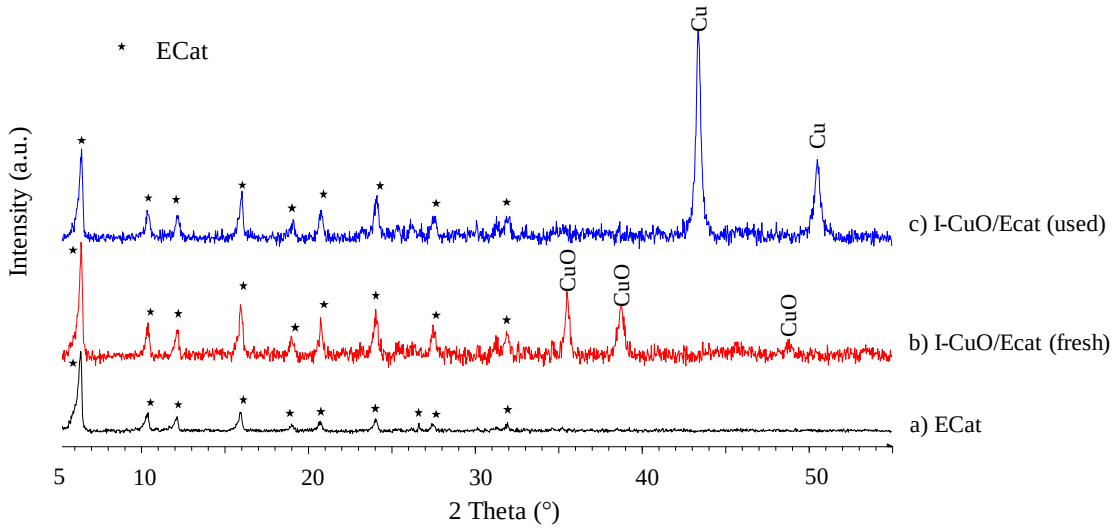


Figure 5.16. XRD patterns of a) ECat, b) fresh I-CuO/ECat, and c) used I-CuO/ECat.

The sharp peaks at 31.2°, 36.8°, 38.5°, and 44.8° in Figure 5.17-b demonstrate the successful Co_3O_4 impregnation (JCPDS no: 00-042-1467) on ECat. However, the characteristic peaks of Co_3O_4 were replaced with characteristic peaks of CoO; 36.5° and 42.4°, (see in Figure 5.17-c) for I-Co_3O_4/ECat tested in n-hexadecane cracking.

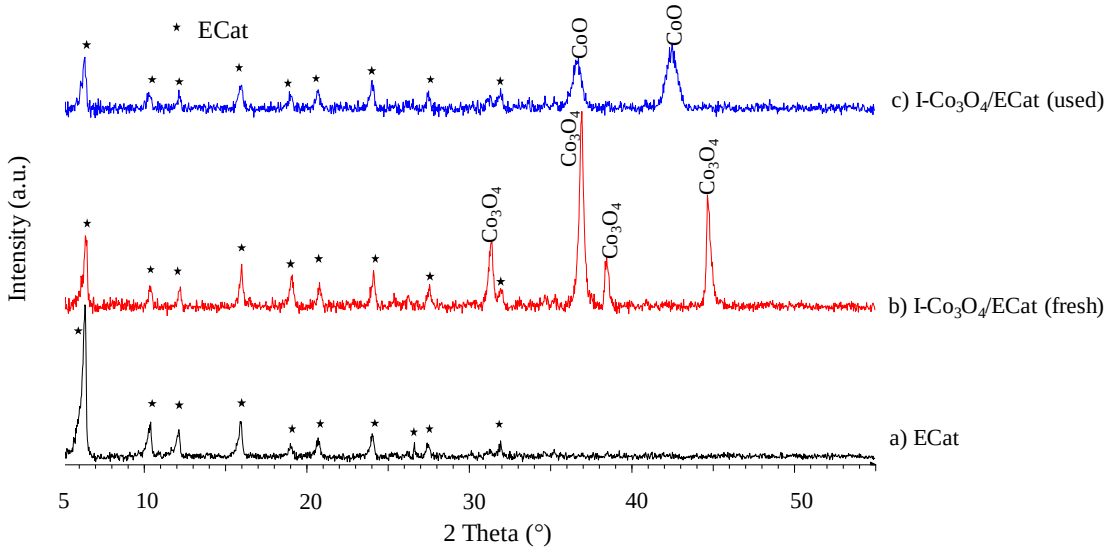


Figure 5.17. XRD patterns of a) ECat, b) fresh I-Co_3O_4/ECat, and c) used I-Co_3O_4/ECat.

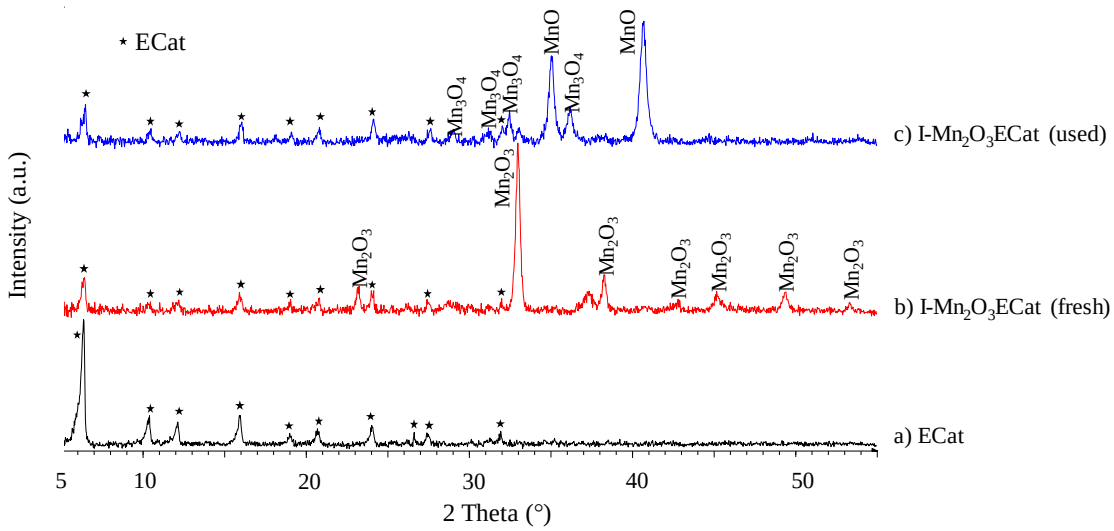


Figure 5.18. XRD patterns of a) ECat, b) fresh I-Mn_2O_3/ECat., and c) used I-Mn_2O_3/ECat.

Similarly, the characteristic peaks at 23.1°, 32.9°, 38.2°, 45.1°, 49.3°, and 53.2° (JCPDS no: 01-071-0636) on Figure 5.18-b identify the successful impregnation of Mn_2O_3 on ECat. However, after cracking of n-hexadecane over I-Mn_2O_3/ECat, the catalyst demonstrates the characteristic peaks of MnO (34.9°and 40.5°, JCPDS no: 01-078-0424) and Mn_3O_4 (28.9°, 30.1°, 32.3°, and 36.0°, JCPDS no: 01-080-0382), as shown in Figure 5.18-c.

The characteristic ECat peaks remain on the patterns for both fresh and used I-CuO/ECat, I-Co_3O_4/ECat, and I-Mn_2O_3/ECat, which proves the oxygen carrier impregnation does not affect the ECat structure. However, after the cracking reactions, the impregnated oxygen carriers (CuO, Co_3O_4, and Mn_2O_3) reduced to Cu, CoO, and Mn_3O_4 – MnO, respectively. As mentioned previously (in Section 5.2.1), these reductions may be attributed to the combustion of hydrocarbons (cracking feed and/or cracked products) with oxygen carriers during cracking reaction. In contrast to the mechanical mixing results, in which Mn_2O_3 mixed with ECat mainly reduced to Mn_3O_4, the Mn_2O_3 impregnated ECat demonstrated a further reduction from Mn_3O_4→MnO. The first step of the sequential reduction, Mn_2O_3→Mn_3O_4, seems faster than the second step, Mn_3O_4→MnO. This additional reduction can be ascribed to the dispersion of Mn_2O_3 on the surfaces of the catalyst. However, thanks to the low ratio of oxidised oxygen carriers impregnated on ECat, the amount of combusted cracking feed (or cracked products) is expected to be relatively low. Although a reduction on the oxygen carriers observed after

the cracking of n-hexadecane, Siregar and Amin [235] proved that the pore structure such as surface area, acidity and pore volume, have insignificantly affected by the reduction of CuO.

SEM analysis: SEM was employed to investigate any deformation on the surface morphology and physical structure of ECat particles after impregnation of oxygen carriers and testing in the cracking of n-hexadecane. Figure 5.19 demonstrates the surface morphology of fresh ECat having a spherical shape and smooth surface in four different zoom scalings, 100 µm, 20 µm, 10 µm, and 1 µm,

Figure 5.20 shows the SEM images of fresh and used I-CuO/ECat. There is no fragmentation nor physical deformation on ECat after the impregnation of CuO (Figure 5.20-a), neither after I-CuO/ECat was tested in the cracking of n-hexadecane (Figure 5.20-b). The CuO particles were dispersed on the surface of ECat catalysts. However, the bright points in Figure 5.20-a1 and -b1 correspond to the accumulation of CuO on ECat. Similarly, Chuang et al. [178] have also observed CuO accumulation on Al_2O_3 prepared by impregnation method. The increase in the content of CuO may increase surface accumulation [178, 183]. On top of that very little agglomeration between the spherical CuO impregnated ECat particles can be seen in Figure 5.20-b. The accumulated CuO on the single ECat particle is connected with another accumulated CuO on another ECat particle; this enables agglomeration.

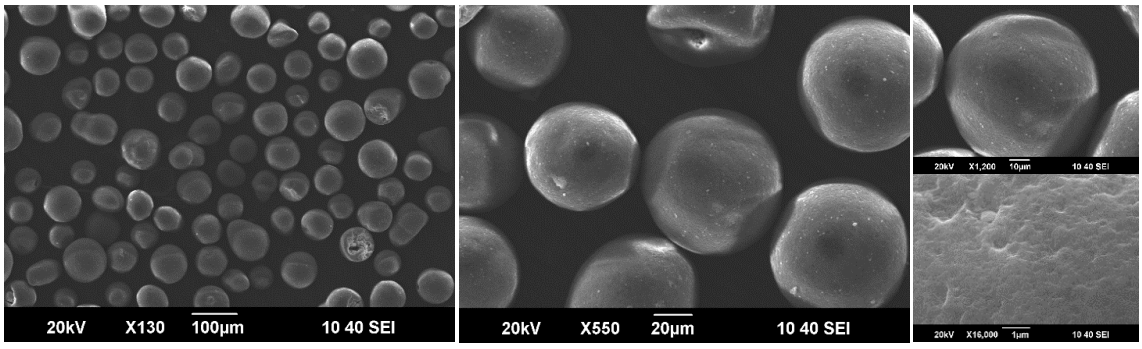


Figure 5.19. SEM images of fresh ECat surface.

The spherical ECat particles demonstrate fragmentation into smaller particles after the impregnation of Co_3O_4 (see in Figure 5.21-a and b). Additionally, a Co_3O_4 accumulation on prepared I-Co_3O_4/ECat has been observed in Figure 5.21-a3 and Figure 5.21-b3. This

accumulation may be attributed to the impregnated ratio of Co_3O_4 on the ECat. On the other hand, no significant differences on the surface of I-Co_3O_4/ECat were observed between fresh and used catalysts.

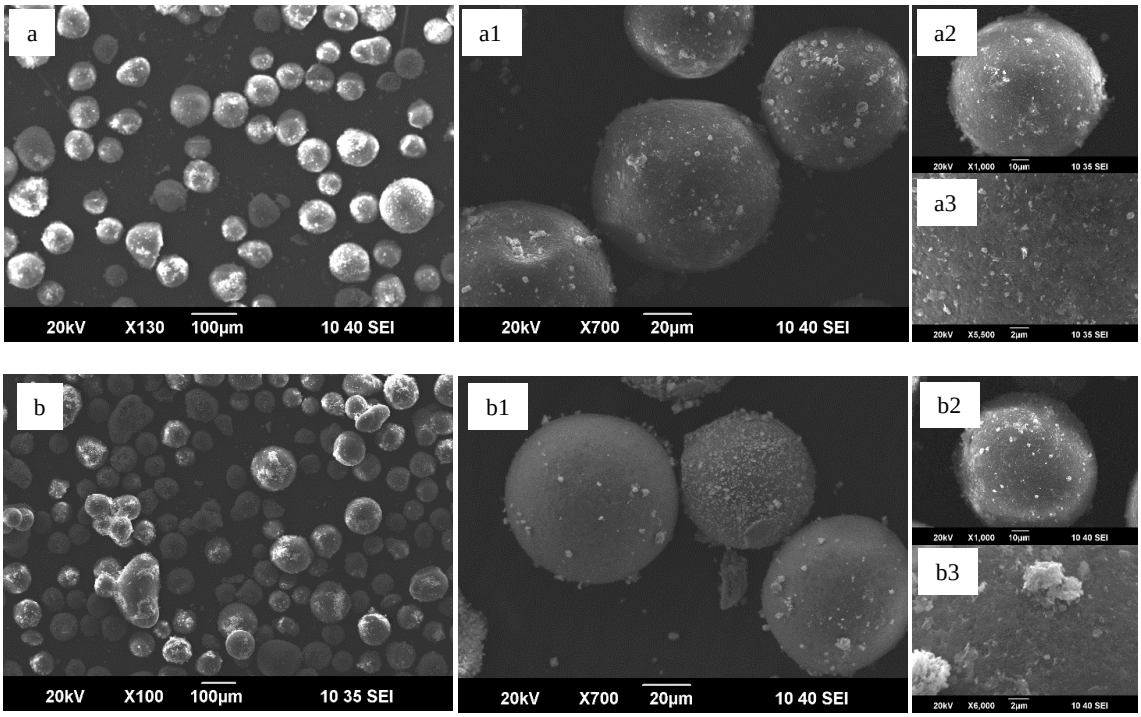


Figure 5.20. SEM images of a) fresh I-CuO/ECat and b) used I-CuO/ECat.

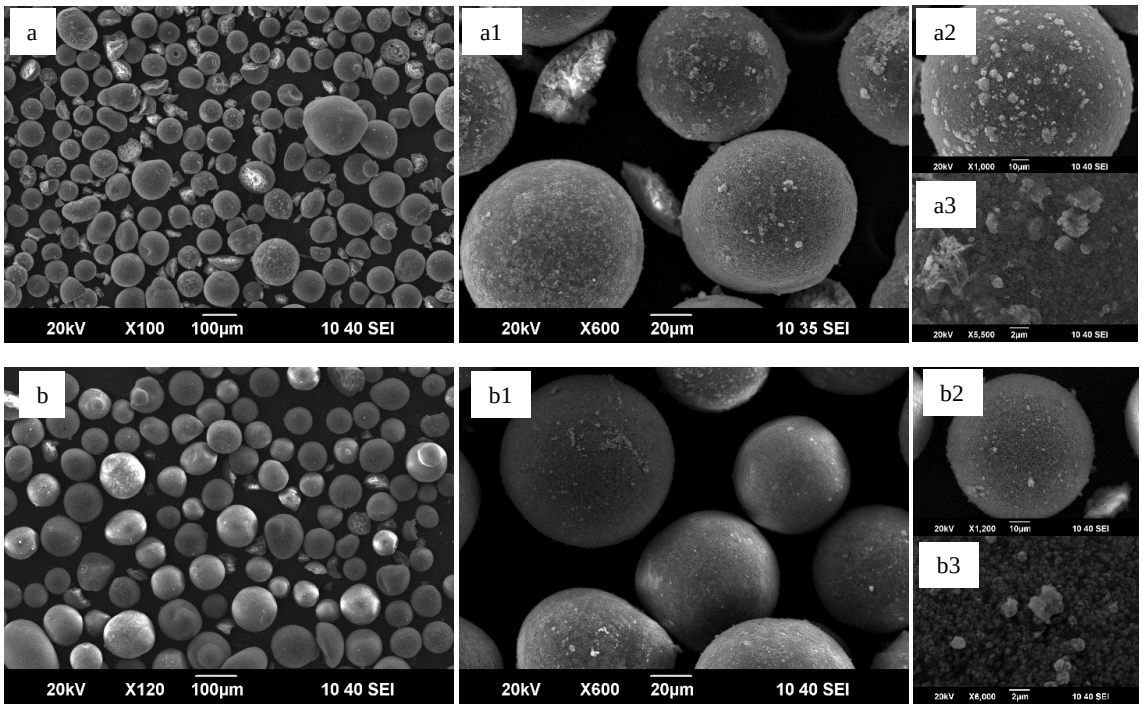


Figure 5.21. SEM images of a) fresh I-Co_3O_4/ECat and b) used I-Co_3O_4/ECat.

Figure 5.22 demonstrates that the spherical ECat particles were significantly fragmented into smaller particles following the impregnation of Mn_2O_3. Additionally, the smooth surface of the ECat was fully covered by Mn_2O_3 (see in Figures 5.22-a2 and -b2). Moreover, Figures 5.22-a and -b demonstrate a clear agglomeration between Mn_2O_3 impregnated ECat particles due to the high amount of Mn_2O_3 accumulation on the outer surface of ECat. However, similar to CuO and Co_3O_4 impregnated ECat catalysts, significant differences on the surface of fresh I-Mn_2O_3/ECat were not observed compared with the catalysts tested after the cracking of n-hexadecane.

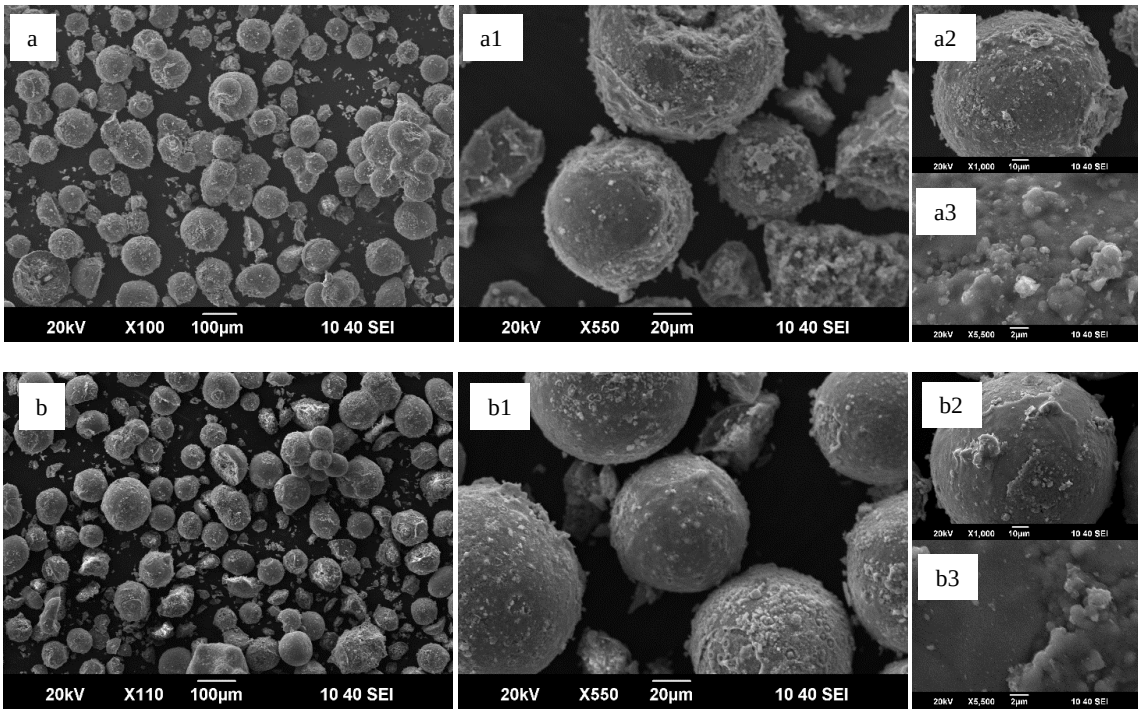


Figure 5.22. SEM images of a) fresh I-Mn_2O_3/ECat and b) used I-Mn_2O_3/ECat.

The oxygen carrier accumulation on ECat may be attributed to the impregnated metal's cation states as well as the quantity of oxygen carriers used for the impregnation. Bhan and Delgass [241] discovered that Me^{3+} cations are located preferentially on the outer surface of ZSM-5 zeolite catalyst, whereas Me^{2+} cations are found inside the zeolite structure. Similar findings have also been reported by Wang et al. [242] for the ZSM-5 zeolite catalyst modified by ZnO, CuO as Me^{2+} and Ga_2O_3 as Me^{3+}. One of the reasons for the less accumulation observed on the outer surface of Cu^{2+} impregnated ECat (Figure 5.24) may be attributed the cation state compared with Mn^{3+} impregnated ECat (Figure 5.26). Furthermore, the accumulation of Co_3O_4 impregnated ECat is more than I-

CuO/ECat while it is less than I-Mn_2O_3/ECat. This may be attributed to the cation states of Co_3O_4, which has both Co^{2+} and Co^{3+}. The Co^{2+} cations diffused into the pores while the Co^{3+} cations accumulated over the outer surface of the ECat.

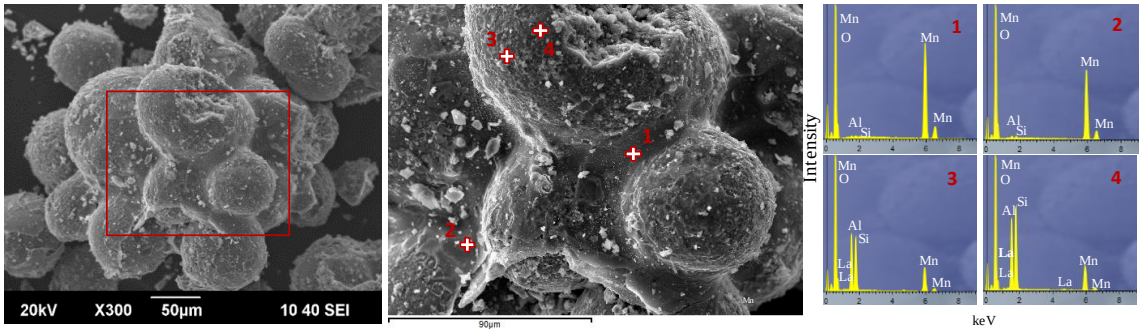


Figure 5.23. SEM image and EDS spectrum of agglomerated part of fresh I-Mn_2O_3/ECat.

The SEM image of the agglomerated part of I-Mn_2O_3/ECat (Figure 5.23) shows that the area between agglomerated ECat particles labelled 1 and 2 seem different than the surface of ECat labelled 3 and 4. EDS spectrums of the numbers 1 and 2 show that the oxygen carrier (Mn_2O_3) stuck together with the ECat particles, which causes the agglomeration. The EDS spectrums for 3 and 4 demonstrate that whilst the Mn_2O_3 covers the outer surface of ECat, the other elements such as Si, Al, and La, can still be detectable. The inner pores of ECat catalyst are still accessible, which is essential to maintain the cracking activity of the ECat the same. Further, the accumulation of oxygen carriers onto the outer surface of ECat is not crucial in this study, as these oxygen carriers are not used for the enhancement of the cracking activity of ECat. The cracking activity of the ECat would like to be maintained consistent after the modification of ECat with oxygen carrier.

XRF and EDS mapping: The true density and oxygen carrier ratio of I-CuO/ECat, I-Co_3O_4/ECat, and I- Mn_2O_3/ECat are presented in Table 5.4. The true density of ECat increased with the impregnation of oxidised oxygen carriers. Since the true density of oxygen carriers, CuO (6.22 g/cm^3), Co_3O_4 (6.11 g/cm^3), and Mn_2O_3 (4.84 g/cm^3) are higher than the density of ECat (2.70 g/cm^3). Thanks to the high ratio of ECat in the oxidised oxygen carrier impregnated ECat catalysts (13 wt.% of CuO, 18 wt.% of Co_3O_4, and 30 wt.% of Mn_2O_3), the densities are close to ECat's density.

Table 5.4. Amount of oxygen carrier impregnated on ECat.

Catalyst	True density[a] (g/cm^3)	Theoretical loading[b] (wt.%)	Actual loading[c] (wt.%)
ECat	2.70	n.a.	n.a.
I-CuO/ECat	2.84	12.5	12.2
I-Co_3O_4/ECat	2.95	17.8	16.6
I-Mn_2O_3/ECat	3.11	29.8	30.2

[a] Measured using Helium Pycnometer. [b] Determined the oxidised oxygen carriers based on the weight differences of ECat before and after oxygen carrier impregnation. [c] Measured oxidised oxygen carriers using XRF.

The ratio of oxidised oxygen carriers impregnated ECat were theoretically calculated using the weight differences of ECat before and after the impregnation process. According to these calculations, approximately 12.5 wt.% of CuO, 17.8 wt.% of Co_3O_4 and 29.8 wt.% of Mn_2O_3 were impregnated on the ECat catalysts. Additionally, the actual loading of oxidised oxygen carriers on ECat measured by XRF and the results demonstrate similarity with the theoretical calculations, as seen in Table 5.4.

EDS mappings and qualitative element spectrums for I-CuO/ECat, I-Co_3O_4/ECat, and I-Mn_2O_3/ECat are presented in Figure 5.24, 5.25 and 5.26, respectively. The locations for qualitative element analysis of fresh and used I-CuO/ECat catalysts are shown on the SEM images using a rectangular (□) and plus (+) signs and presented as EDS spectrums next to. Figure 5.24-a demonstrates that CuO particles were dispersed on the surface of the ECat as seen by the Cu mapping for fresh I-CuO/ECat. Furthermore, after testing of I-CuO/ECat in the cracking of n-hexadecane, dispersion of Cu on the ECat remains (see in Figure 5.24-b). However, the EDS spectrums show that the intensity of Cu was not the same everywhere on the external surface of ECat, which may be attributed to the agglomeration of CuO on external surface. As Chuang et al. [178] demonstrated CuO tends to concentrate on a particles exterior; further, the surface accumulation of CuO increases with an increase in the content of CuO. The EDS spectrums also demonstrate that fresh I-CuO/ECat consists of mainly Al, Si, O, and La in addition to Cu. The spectrums prove that the elements (Al, Si, La, O) creating ECat catalyst remain after cracking tests as it used to be on fresh I-CuO/ECat.

A Co_3O_4 accumulation was observed over fresh I-Co_3O_4/ECat (Figure 5.25-a), whereas the used catalyst demonstrated better Co dispersion on the ECat surface shown in Figure

5.25-b. The EDS spectrums clarify that in addition to Co, which was impregnated on ECat as a form of Co_3O_4, the other elements, Al, Si, O, and La, are observed.

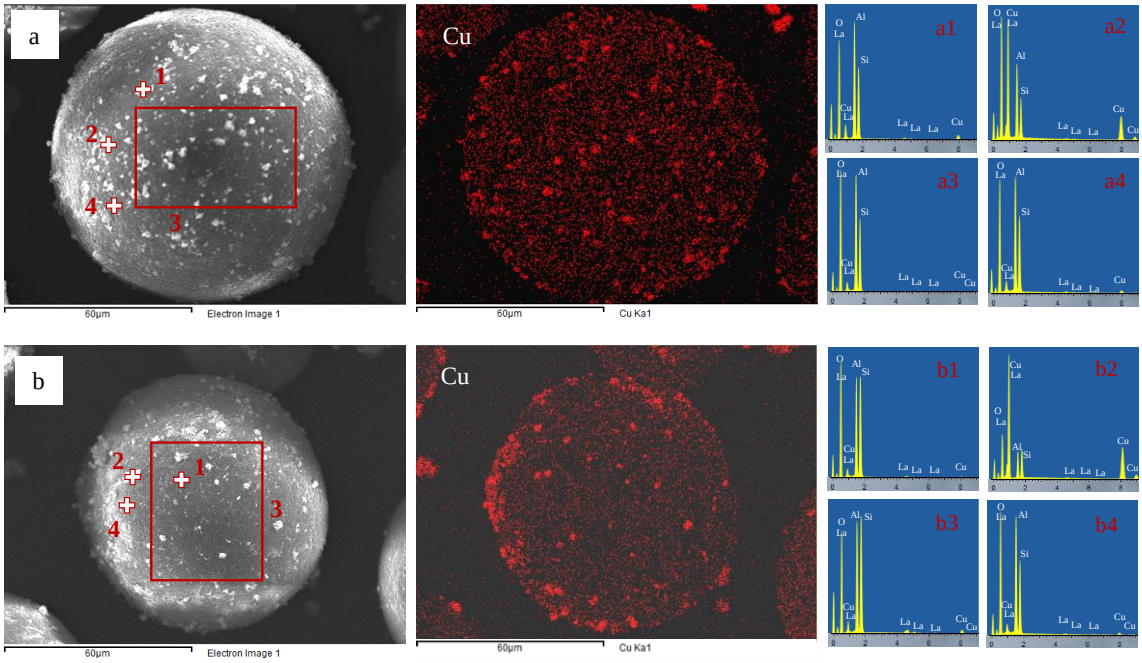


Figure 5.24. EDS mapping for Cu and element spectrums of a) fresh I-CuO/ECat and b) used I-CuO/ECat.

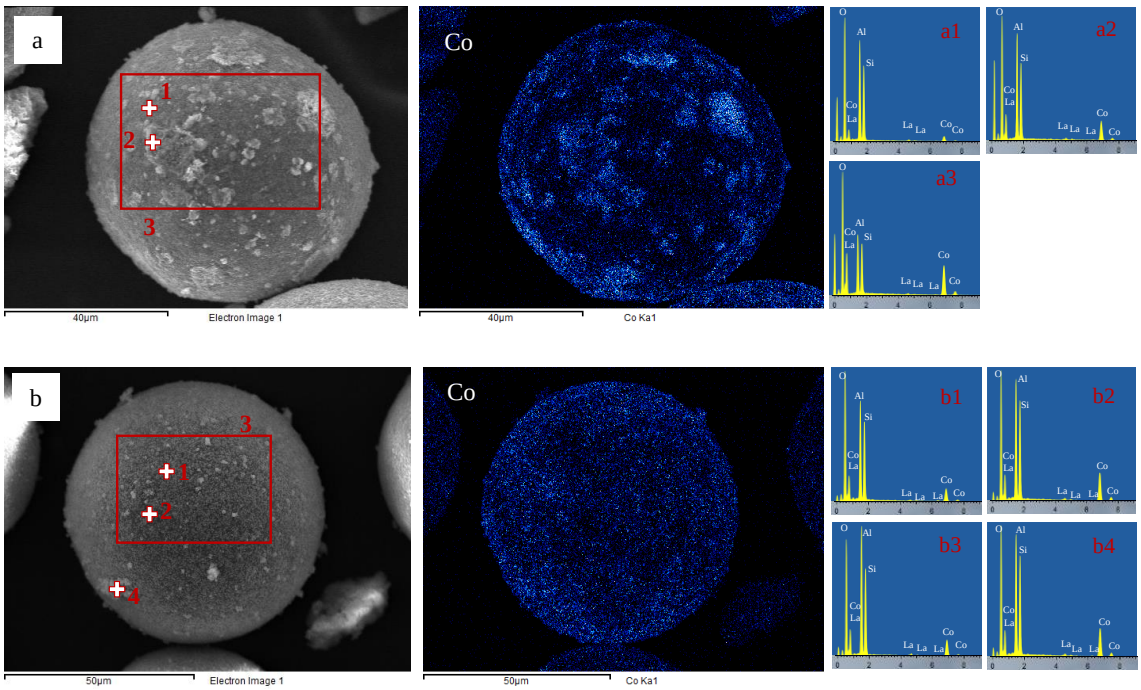


Figure 5.25. EDS mapping for Co and element spectrums of a) fresh I-Co_3O_4/ECat and b) used I-Co_3O_4/ECat.

Figure 5.26-a demonstrates that the impregnated Mn_2O_3 covers the whole surface of the ECat as a layer. It was same after the catalysts were tested in the cracking of n-hexadecane (Figure 5.26-b). Additionally, the EDS spectrums demonstrate the various intensity of Si and Al peaks on different spots (Figure 5.26), which also supported the intensive accumulation of Mn_2O_3 on the ECat surface. As mentioned previously, the accumulation of fresh oxygen carriers impregnated catalyst may be attributed to either cation states as Me^{3+} (such as Mn^{3+} and Co^{3+}) which may not be diffused into the pores of ECat. In contrast, Me^{2+} (such as Cu^{2+} and Co^{2+}) can be placed into the pores or the preparation procedure where a high amount of oxygen carriers were impregnated on ECat at once. The accumulation problem due to the cations Cu^{2+} and Co^{2+} may be decreased using multiple impregnation stages of CuO and Co_3O_4, as suggested by Chuang et al. [178] where the accumulation and agglomeration problems were not issues for the preparation of CuO/Al_2O_3.

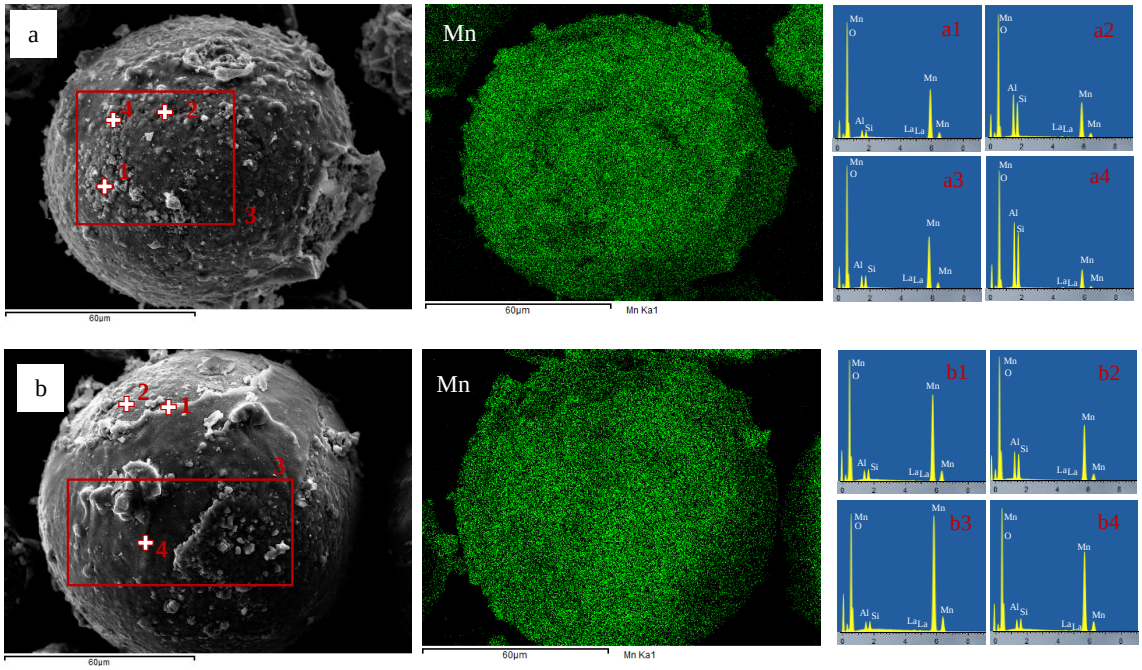


Figure 5.26. EDS mapping for Mn and element spectrums of a) fresh I-Mn_2O_3/ECat and b) used I-Mn_2O_3/ECat.

N_2 adsorption-desorption analysis: The N_2 sorption isotherms of I-CuO/ECat, I-Co_3O_4/ECat, I-Mn_2O_3/ECat are presented in Figure 5.27. Adsorption and desorption isotherms of the catalysts demonstrated different trends defined as hysteresis, starting from about $P/P_0 = 0.4$. According to the IUPAC classification [243, 244], the isotherm is

defined as “type IV”, which is a typical isotherm of mesoporous materials having a pore diameter of 2-50 nm. The adsorption-desorption isotherm of ECat was the same even after the impregnation of oxidised oxygen carriers. The isotherms consisted of two well-distinguished regions; adsorption of monolayer-multilayer and capillary condensation. The initiation part of the isotherms (P/P_0 = 0-0.4) are attributed to the former; monolayer-multilayer adsorption [243, 244]. On the other hand, the characteristic hysteresis is usually attributed to the latter (P/P_0 = 0.4-1.0), capillary condensation, taking place in mesopores [243].

Pore condensation is defined as a gas condensation to a liquid-like phase in the pore at a pressure, P, less than the saturation pressure, P_0, of a bulk liquid [243]. The hysteresis loops are mainly classified as four types, and the hysteresis drawn for the prepared catalysts (Figure 5.27) can be defined as “type H3” [243, 244]. The characteristic features of type H3 loop are the sharp step down off the desorption branch which is generally located in a narrow range P/P_0 (~ 0.4-0.5) for the particular adsorptive and temperature (nitrogen at temperatures of 77 K) [243].

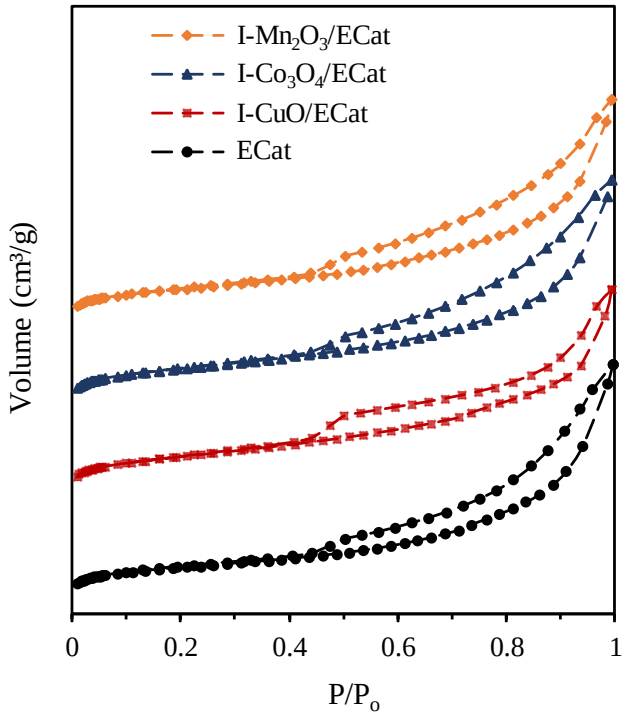


Figure 5.27. Nitrogen adsorption-desorption isotherms of fresh oxidised oxygen carriers impregnated ECat; ECat, I-CuO/ECat, I-Co_3O_4/ECat, I-Mn_2O_3/ECat.

Table 5.5. Surface properties of ECat, I-CuO/ECat, I-Co_3O_4/ECat, I-Mn_2O_3/ECat.

Catalysts	Surface area (m^2/g)		Pore volume (cm^3/g)			Pore diameter (nm)	
	S_{BET} [a]	S_{micro} [b]	V_{tot} [c]	V_{meso} [d]	V_{micro} [b]	d_{av} [e]	d_{neck} [e]
ECat	191	102	0.25	0.20	0.05	13.8	11.0
I-CuO/ECat	189	124	0.18	0.14	0.04	11.9	10.5
I-Co_3O_4/ECat	185	107	0.18	0.15	0.03	13.2	9.6
I-Mn_2O_3/ECat	177	84	0.17	0.15	0.02	12.5	10.0

[a] The BET surface area (S_{BET}) was calculated on the basis of g ECat. [b] Micro surface area (S_{micro}) and pore volume (V_{micro}) were calculated using the t-plot method. [c] Total pore volume (V_{tot}) was defined as sum of micro, meso and macro pore volumes. [d] Meso-pore volume (V_{meso}) was calculated by the BJH adsorption cumulative volume of pores (2.0-50.0 nm). [e] Pore diameters, average (d_{av}) and neck (d_{neck}), were calculated by the BJH method (4V/A).

The textural properties of these catalysts, such as surface area, pore volume and pore diameter, were calculated according to Brunauer-Emmett-Teller (BET) and Barrett-Joyner-Halenda (BJH) methods and presented in Table 5.5. The BET surface area slightly decreased by about 2, 6 and 14 m^2/g, after the impregnation of CuO, Co_3O_4 and Mn_2O_3, respectively. The decrease in the BET surface area is attributed to the concentration of oxidised oxygen carriers impregnated on ECat, and these oxygen carriers could have filled the pores of the catalyst and blocked some of the surfaces. As a decreasing trend was observed with the increase of the oxidised oxygen carriers concentrations, CuO < Co_3O_4 < Mn_2O_3. In terms of pore volume and average pore diameter, an apparent decrease can also be observed after the impregnation of oxidised oxygen carriers, as demonstrated in Table 5.5.

Similarly, the decreasing trend was also observed for the micropore volume with the increase in the concentration of impregnated oxidised oxygen carriers. Wang et al. [242], Li et al. [245], and Kubo et al. [246] described that a decreasing trend in BET surface area and pore volume were observed with the increasing of CuO ratio in modified ZSM-5 zeolite catalyst. Similarly, Awayssa et al. [247] showed that the BET surface area decreased with the impregnation of Mn, and that a further decrease was observed once the Mn concentration increased. In another study, Du et al. [248] demonstrated that impregnation of different metals such as Co, Cu, Fe, Ga, Mo and Ni on ZSM-5 zeolite catalyst caused different levels of decrease on the surface area.

Brönsted-Lewis acidities via Fourier-transform infrared spectroscopy (IR-Py): The positively charged atoms defined as carbocations (generic term for a positively charged

carbon ion) are formed where the cracking feed contact with the catalyst [221]. The carbonium ions ($R\text{-}CH_2^+$) are produced either transferring a proton (H^+) to olefins by Brönsted acid sites (B) or removing hydrogen (H^-) from paraffin by Lewis acid sites (L). The carbonium ions provide three main reactions; (i) the cracking of a carbon-carbon bond, (ii) isomerisation, (iii) hydrogen transfer. The Brönsted and Lewis acidities of parent ECat, I-CuO/ECat, I-Co_3O_4/ECat, and I-Mn_2O_3/ECat were, therefore, measured by pyridine adsorption. The interaction of both pyridine-Brönsted and pyridine-Lewis acid sites give a group of absorption bands in the IR spectrum ranging from 1400-1700 cm^{-1} [247, 249]. The IR spectrums of the pyridine adsorbed catalysts are presented in Figure 5.28, and the integrated area of defined IR peaks are summarized in Table 5.6. The bands around 1545 and 1640 cm^{-1} are indicative of pyridinium ions, which related to Brönsted acidity [235, 249], and the other bands about 1445, 1580 and 1620 cm^{-1} assign to pyridine coordinated to Lewis acid sites [235, 249, 250]. The last band at about 1490 cm^{-1} represents the pyridine molecule interacting with either Lewis or Brönsted acid site [235, 247, 249, 250].

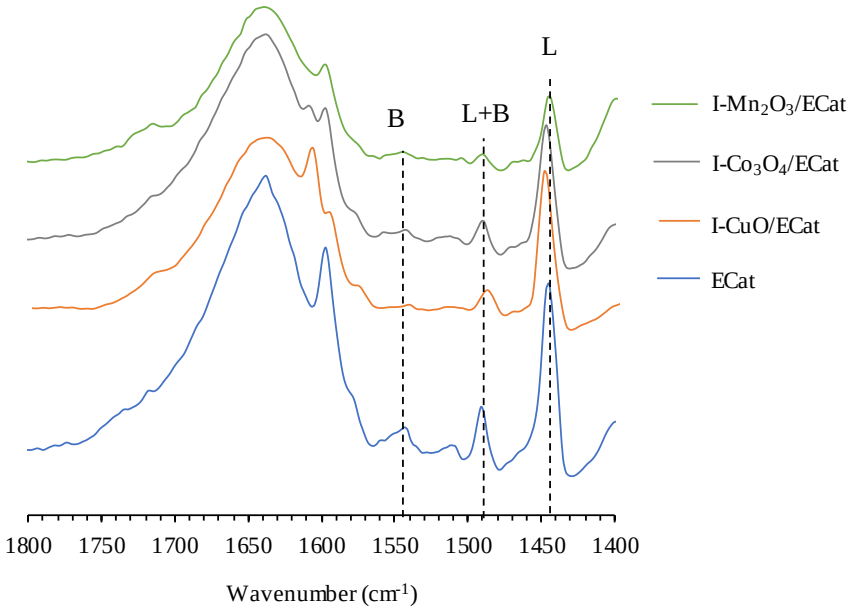


Figure 5.28. IR-Py spectra of parent and oxidised oxygen carriers impregnated ECat catalysts.

The acidity of an acidic catalyst is usually characterised using the adsorption bands at around 1445 and 1540 cm^{-1}. The intensity of Lewis acid site at around 1445 cm^{-1} was considerably higher than that of Brönsted acid site at about 1540 cm^{-1} for the parent, and

oxidised oxygen carriers impregnated ECat catalysts (see in Figure 5.28 and Table 5.6). Additionally, a decrease in the both Lewis and Brönsted acid sites (1445 and 1540 cm^{-1}) was observed with the impregnation of oxidised oxygen carriers, which are in line with the previous studies where lower Brönsted acidity was found both the Mn modified ECat [247] and Cu modified ZSM-5 [235, 242, 251]. The decrease in the Brönsted acidity was attributed to the increasing amount of non-framework aluminium or hydrogen cation that was replaced by the Cu^{2+} ion as the decrease in H^{+} ion decline the Brönsted acidity suggested by Siregar and Amin [235].

Table 5.6. Integrated area of IR-Py peaks for parent and oxidised oxygen carriers impregnated ECat.

Catalysts	L[a] (1445 cm^{-1})	L+B (1490 cm^{-1})	B[b] (1545 cm^{-1})
ECat	1.52	0.30	0.20
I-CuO/ECat	1.12	0.14	0.08
I-Co_3O_4/ECat	1.12	0.14	0.10
I-Mn_2O_3/ECat	0.58	0.06	0.08

[a] Lewis acidity area measured by IR peak at 1445 cm^{-1}. [b] Brönsted acidity area measured by IR peak at 1545 cm^{-1}.

The integrated area for both Brönsted and Lewis acid sites decreased after the impregnation of CuO, Co_3O_4 and Mn_2O_3, which may be attributed to the oxidised oxygen carriers impregnation, which fills the micropores and reduces both surface area and pore volume that could result in a decrease in the acidity of the catalyst. However, as stated by Wang et al. [242], although the IR-Py measurement indicated less Brönsted acidity for CuO impregnated ZSM-5 than that for parent ZSM-5, the relatively small amounts of Brönsted acid sites could still be sufficient for the cracking reaction.

Coke analysis: In general, being formed by the cracking reactions over the catalysts, coke also arises from thermal and metal-mediated reactions, which can contribute to the overall level of coke on the catalysts. Therefore, the increase in the coke yield for impregnation compared to mechanical mixing gives small reductions in surface area (Table 5.5) consistent with the relatively small increases in coke yield (Table 5.7).

In terms of the pore structure, an inverse relationship between average pore diameter (Table 5.5) and coke deposition was obtained for the oxidised oxygen carrier impregnated

ECat, as the average pore diameter followed the trends ECat > I-Co_3O_4/ECat > I-Mn_2O_3/ECat > I-CuO/ECat while the carbon percentage on catalysts displayed the opposite trend. The highest level of coke (1.68 wt.% C) was found on I-CuO/ECat, which had the lowest average pore diameter of 11.9 nm, once compared with other reduced oxygen carriers impregnated ECat.

Table 5.7. Coke percentage and normalized coke composition of used catalysts, ECat, I-CuO/ECat, I-Co_3O_4/ECat, I-Mn_2O_3/ECat.

Catalyst	Coke on catalyst[a] (wt.%)		Coke composition[b] (wt.%)		Coke type (wt.%)		H/C[e]
	Carbon	Hydrogen	Carbon	Hydrogen	SC[d]	HC[c]	
ECat	0.45 ±0.02	0.03 ±0.01	93.6 ±2.2	6.4 ±2.2	0.5	99.5	0.80
I-CuO/ECat	1.68 ±0.08	0.08 ±0.00	95.4 ±0.1	4.6 ±0.1	1.2	98.8	0.57
I-Co_3O_4/ECat	0.73 ±0.12	0.06 ±0.00	91.6 ±1.4	8.4 ±1.4	1.9	98.1	0.98
I-Mn_2O_3/ECat	1.15 ±0.00	0.05 ±0.00	96.2 ±0.0	3.8 ±0.0	13.3	86.7	0.52

[a] Based on g of total coke/ g of ECat. [b] Normalized coke composition was calculated by (weight of carbon (or hydrogen) / weight of coke)*100, wt.%. [c] Hard Coke, the remain coke % after solvent extraction. [d] Soft Coke, determined using the differences of (100-HC), wt.%. [e] The ratio of H/C was calculated weight of H*12/weight of C.

As mentioned previously, an apparent decrease in the surface area was observed due to the pore blockage after the impregnation of CuO, Co_3O_4 and Mn_2O_3, which slightly changed the matrix structure of ECat. Koon et al. [252] proved that after the extractable soft coke removed from the catalysts structure, a further pool of soft coke was found as physically entrapped within the catalyst pore structures and it was only released after demineralisation. Additionally, this second soft coke contains more aromatics, which ultimately controls the final coke yield. The further coke formation may be attributed to the decrease in the effective pore diameter and an increase in the diffusion resistance of reactants/products in the modified ECat catalysts.

Additionally, the differences in the soft and hard coke rations (Table 5.7) may be attributed to the metal-mediated coke formation reactions. As each type of metals impregnated on ECat differently promoted the coke formation reactions. For example, after Mn-based reduced oxygen carrier modification, a dramatic increase in the soft coke was observed (Table 5.7), which also arise the total coke ratio on the catalyst. However, the coke calculated for the oxidised oxygen carriers impregnated ECat was in the range reported in the literature where the FCC catalysts contain 0.46–1.74% of insoluble coke

[189] having a H/C ratio of 0.27–0.54. The expected coke was also about 0.8–1.0 wt% according to the figure drawn for the cracking time versus carbon deposition by Alexis Voorhies [191]. As for the hydrogen content, it was slightly higher due to the moisture content of the catalysts of 2–4 wt% [189].

5.3.1.2 Cracking of n-hexadecane over oxidised oxygen carriers impregnated ECat

The cracking activity of I-CuO/ECat, I-Co_3O_4/ECat, and I-Mn_2O_3/ECat was identified based on n-hexadecane conversion, yields, and product selectivities and the results are presented in Figures 5.29-5.31. The error bars in the figures represent the standard deviation calculated by the results of triplicate experiments.

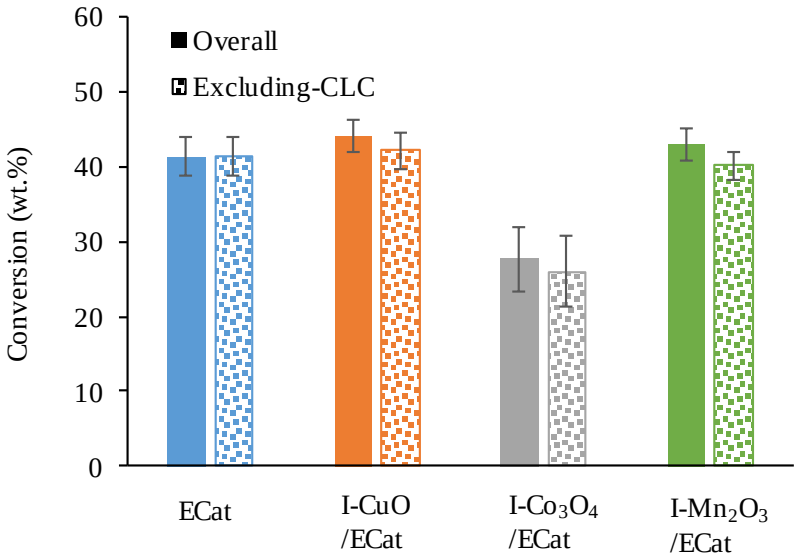


Figure 5.29. Conversion (overall and excluding CLC) of n-hexadecane over the control ECat and oxidised oxygen carriers impregnated ECat; I-CuO/ECat, I-Co_3O_4/ECat, and I-Mn_2O_3/ECat.

Figure 5.29 shows that the excluding-CLC conversion of I-CuO/ECat and I-Mn_2O_3/ECat were approximately 40 wt.%, which was similar to control ECat tests, while it decreased to about 26 wt.% for I-Co_3O_4/ECat. Additionally, the overall conversions were about 2-3 wt.% higher than the excluding-CLC conversions for I-CuO/ECat, I-Co_3O_4/ECat, and I-Mn_2O_3/ECat due to the combustion of hydrocarbons with oxidised oxygen carriers. The decrease in the neck diameter after the impregnation of Co_3O_4 can result in a decrease in the conversion as the bigger molecules cannot diffuse into the active sites in the pores.

This finding is consistent with previous results presented by Hosseinpour et al. [253], who demonstrated that Co modification decreased the conversion of cumene in the cracking reaction compared with the unmodified Y zeolite.

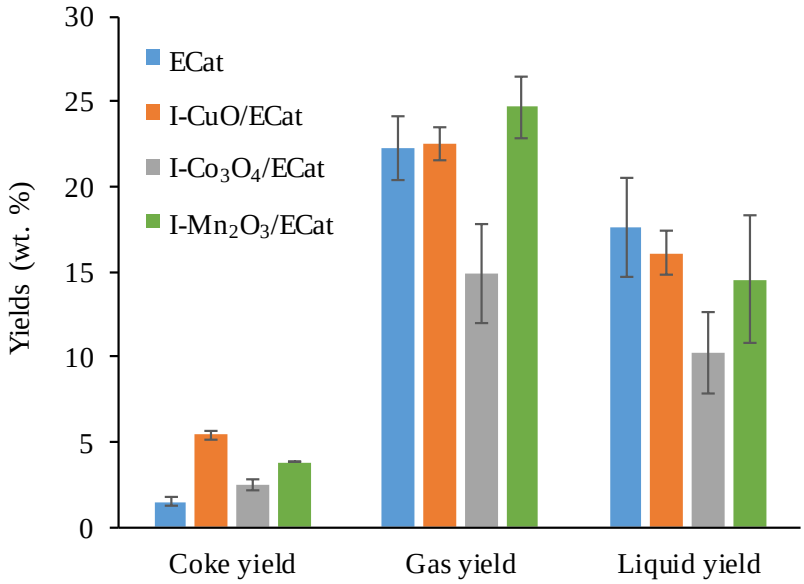


Figure 5.30. Coke, gas, and liquid yields from the cracking of n-hexadecane over control ECat and oxidise oxygen carriers impregnated ECat; I-CuO/ECat, I-Co_3O_4/ECat, and I-Mn_2O_3/ECat.

The coke yield increased from 1.4 wt.% to about 5.3 wt.%, 2.4 wt.% and 3.8 wt.% with the impregnation of CuO, Co_3O_4 and Mn_2O_3, respectively, as shown in Figure 5.30. The increase in the coke yield may be attributed to the new pore structure of catalyst after the modification of ECat with oxidised oxygen carriers. The larger molecules cannot diffuse outside from the inner pores due to the narrowing in the pores, which increase the coke accumulation in the pores. As mentioned previously, an inverse relationship between average pore diameter and formation of the coke can be seen as the average pore diameter is ECat > I-Co_3O_4/ECat > I-Mn_2O_3/ECat > I-CuO/ECat while the coke yield is the opposite, I-CuO/ECat > I-Mn_2O_3/ECat > I-Co_3O_4/ECat > ECat. Li et al. [245] demonstrated that the coke yield on the ZSM-5 catalyst decreased after the modification of CuO (having different ratios of 5-30 wt.%), while the coke accumulation increased using the regenerated catalyst in multiple tests. While gas and liquid yields demonstrated a decrease with the impregnation of Co_3O_4, they were not affected by the impregnation of CuO and Mn_2O_3, which are similar with the findings presented by Siregar and Amin [235].

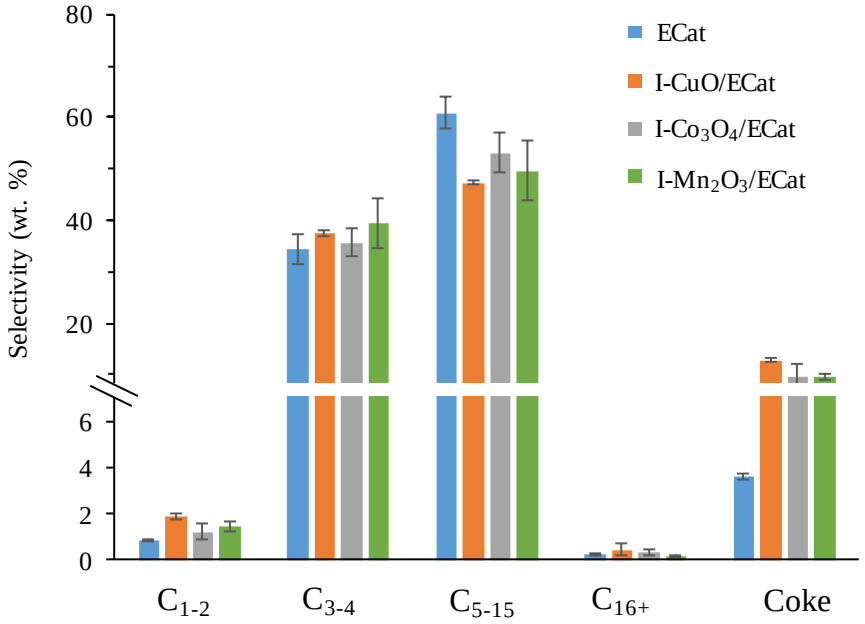


Figure 5.31. Product selectivity of C_{1-2} (light gases), C_{3-4} (LPG), C_{5-15} (gasoline), C_{16+} (higher hydrocarbons) and coke from the cracking of n-hexadecane over control ECat and oxidise oxygen carriers impregnated ECat; I-CuO/ECat, I-Co_3O_4/ECat, and I-Mn_2O_3/ECat.

Figure 5.31 shows that the selectivity of light gases (C_{1-2}) and higher hydrocarbons (C_{16+}) was kept as in the minimum as desired [65], after the oxidised oxygen carriers impregnated on ECat. Only the CuO modification slightly increased the generation of C_{1-2}, which is in line with the findings of Wang et al. [242]. The narrowing in the pores' neck can support further cracking in the pores, which resulted in increasing the selectivity of C_{1-2}. On the other side, the decrease in the micro-pores after the impregnation of oxidised oxygen carriers could decrease the formation of light gases. The selectivity of LPG was slightly enhanced by the impregnation of the oxidised oxygen carrier, whereas the selectivity of gasoline demonstrated a decrease with the impregnation of oxidised oxygen carriers. Moreover, coke accumulation considerably increased from about 3.6 wt.% to about 10 wt.% using these catalysts in the cracking of n-hexadecane due to the reason mentioned previously in the coke analysis section.

5.3.2 The effect of the reduced oxygen carriers impregnated ECat

5.3.2.1 Preparation of reduced oxygen carriers impregnated ECat

The oxidised oxygen carriers can be reduced by hydrogen [254-257]. The XRD patterns of I-CuO/ECat reduction states by hydrogen at 450, 250 and 200 °C are presented in Figure 5.32. The CuO impregnated on ECat can directly reduce to metallic Cu by the hydrogen, instead of a sequential reduction step $CuO \rightarrow Cu_4O_3 \rightarrow Cu_2O \rightarrow Cu$, which is line with the literature [254, 257]. However, a complete reduction from CuO to Cu_2O has been previously achieved using CO as a reduction gas at the isothermal reduction temperature of 250 °C [256].

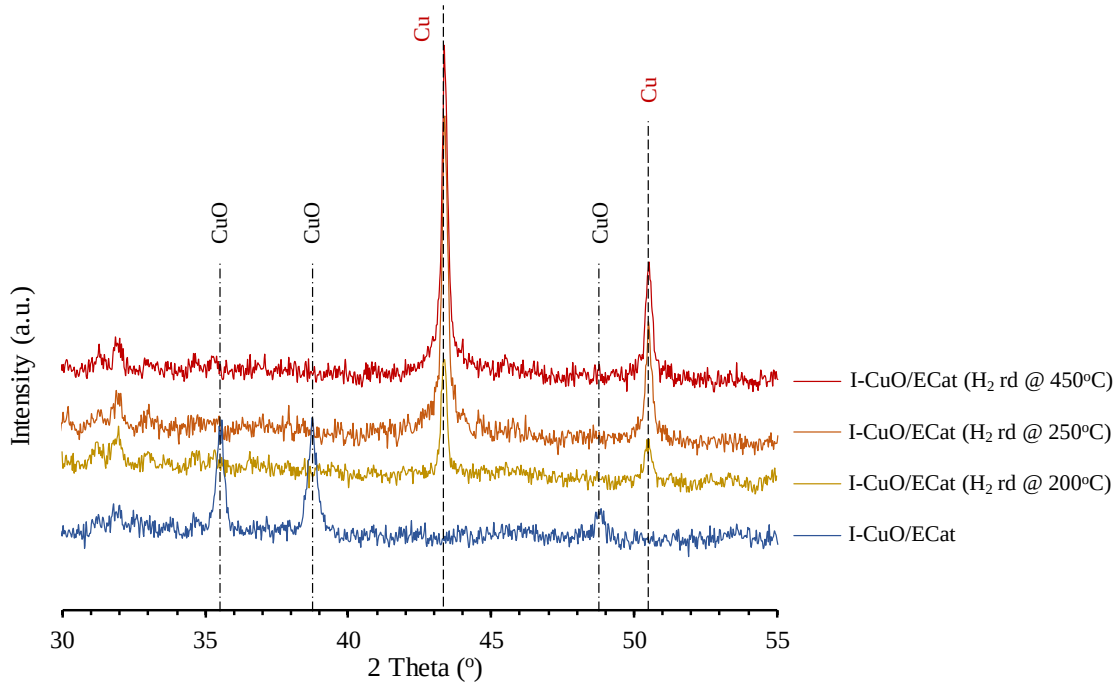


Figure 5.32. XRD patterns of the I-CuO/ECat and reduced I-CuO/ECat by hydrogen at 200, 300, 450 °C.

Figure 5.33 demonstrates the reduction states of Co_3O_4, which was impregnated on ECat depending on the temperatures. Co_3O_4 impregnated on ECat reduced to a mixture of CoO and Co at 450 °C, which may refer to a sequential reduction step $Co_3O_4 \rightarrow CoO \rightarrow Co$. The formation of Co was decreased, and so the formation of CoO was increased with a decrease in the reduction temperature from 450 °C to 350 °C. However, the Co_3O_4 was observed when the reduction temperature was under 300 °C. The further decrease in the

reduction temperature caused a decrease in the reduction. Ward et al. [255] observed that although the majority of the crystals are in the form of Co_3O_4, the formation of CoO has been beginning at the temperatures around 200 °C.

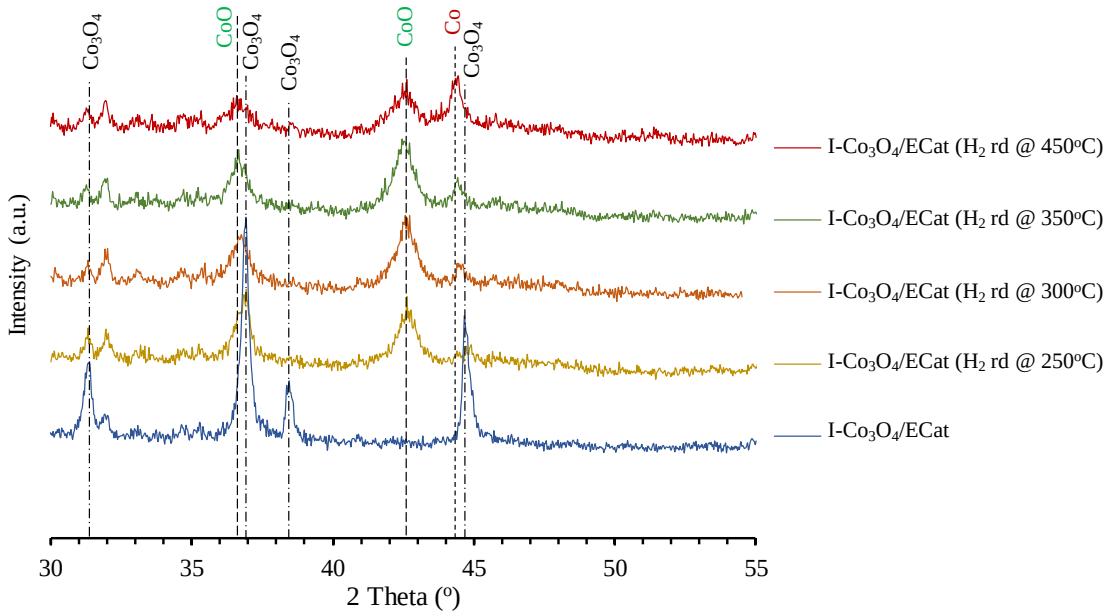


Figure 5.33. XRD patterns of I-Co_3O_4/ECat and reduced I-Co_3O_4/ECat by hydrogen at 250, 300, 350, 450 °C.

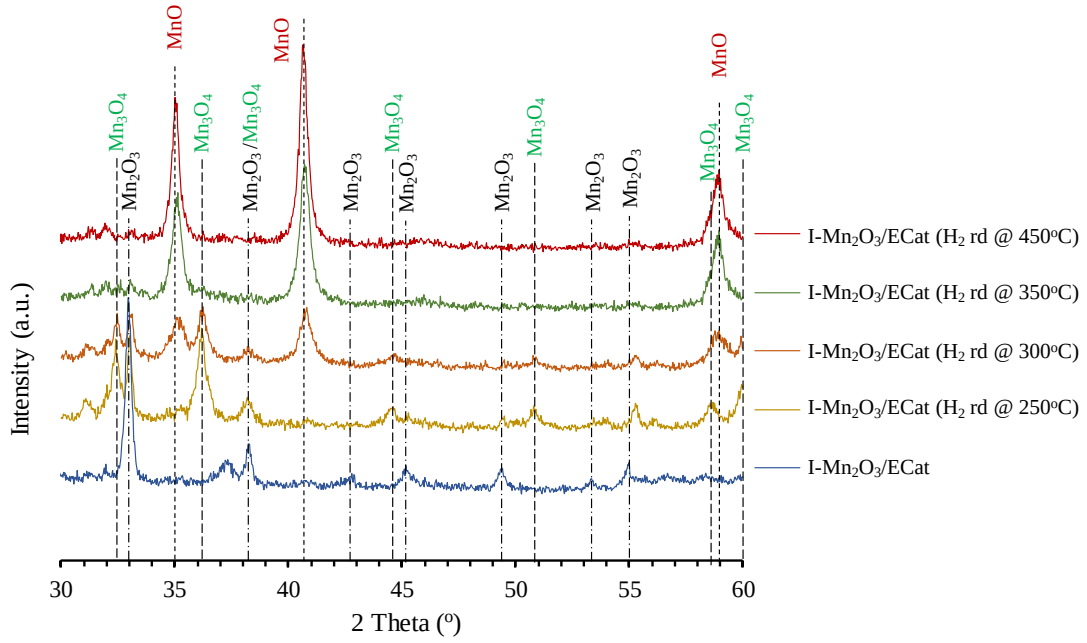


Figure 5.34. XRD patterns of I-Mn_2O_3/ECat and reduced I-Mn_2O_3/ECat by hydrogen at 250, 300, 350, 450 °C.

The same reduction process was performed for I-Mn_2O_3/ECat using hydrogen, and the results are presented in Figure 5.34. Mn_2O_3 can directly reduce to MnO at a temperature higher than 350 °C. However, once the temperature was between 250-300 °C, a sequential reduction step was observed as $Mn_2O_3 \rightarrow Mn_3O_4 \rightarrow MnO$. The reduction level of I-Mn_2O_3/ECat depends on the temperature as it was seen for I-Co_3O_4/ECat. The distribution of Cu-, Co- and Mn-states were determined using semi quantification method and presented in Table 5.8.

Table 5.8. Semi-quantification of Cu-, Co- and Mn-states after reduction of I-CuO/ECat, I-Co_3O_4/ECat, and I-Mn_2O_3/ECat at different temperatures by Hydrogen.

T_r[a] (°C)	Cu-states, wt.%			Co-states, wt.%			Mn-states, wt.%		
	CuO	Cu_2O	Cu	Co_3O_4	CoO	Co	Mn_2O_3	Mn_3O_4	MnO
450	-	-	100	-	14.9	85.1	-	-	100
350	-	-	100	-	80.2	19.8	6.3	8.9	84.8
300	n.a.	n.a.	n.a.	27.0	61.7	11.3	19.1	79.0	1.9
250	-	-	100	45.3	53.4	-	19.0	81.0	-

[a] Reduction temperature of oxidised oxygen carriers impregnated on ECat under H_2 atmosphere at 5 bar. "n.a." refers non-applicable, as the reduction of CuO with H_2 at 300 °C has not been investigated.

The oxidised CuO impregnated ECat can be reduced by hydrogen at any temperature between 200-450 °C to the synthesis of reduced Cu impregnated ECat, I-Cu/ECat. For the synthesis of I-CoO/ECat, the oxidised Co_3O_4 can be reduced by hydrogen at 350 °C (the percentage of CoO was approximately 80.2% with a small portion of Co, 19.8%). Additionally, the synthesis of I-Mn_3O_4/ECat and I-MnO/ECat were completed by the reduction of I-Mn_2O_3 /ECat with hydrogen at 250 °C and 450 °C, respectively.

5.3.2.2. Characterisation of reduced oxygen carriers impregnated ECat

XRD analysis: The XRD patterns of both fresh and used I-Cu/ECat, I-CoO/ECat, I-Mn_3O_4/ECat, and I-MnO/ECat are presented in Figure 5.35-5.38. The characteristic ECat peaks, indicated with black stars, remain after the reduction of oxidised oxygen carrier impregnated ECat by hydrogen (pattern b of these figures). Further, the characteristic ECat peaks also remain after the catalysts were tested following the cracking of n-hexadecane, presented on the pattern-c of these figures (Figures 5.35-5.38).

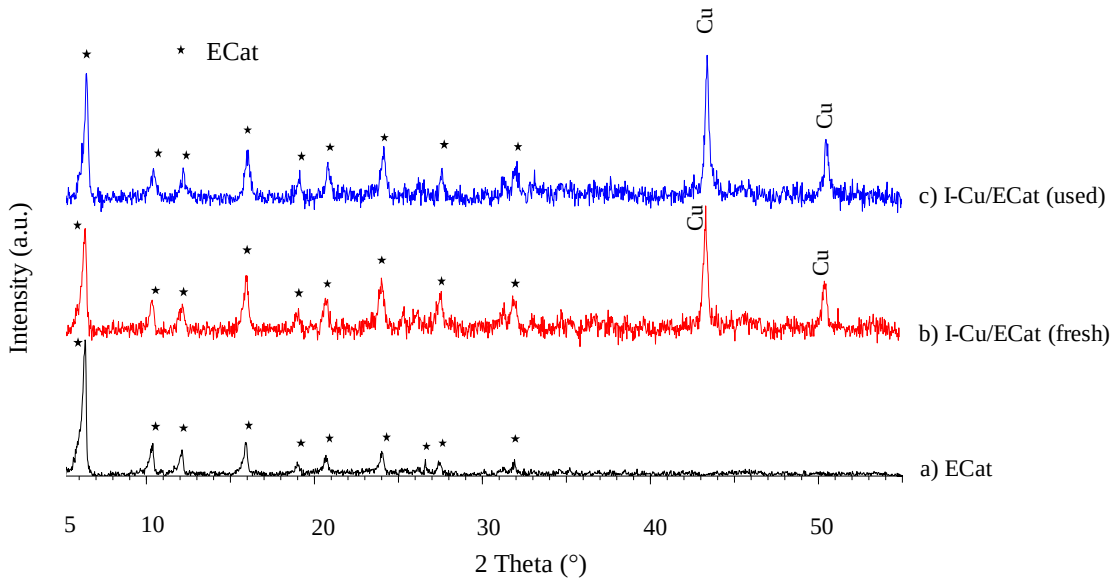


Figure 5.35. XRD patterns of a) ECat, b) fresh I-Cu/ECat, and c) used I-Cu/ECat.

The characteristic peaks of Cu at 43.3° and 50.4° (JCPDS no:01-085-1326) shown in Figure 5.35-b and -c prove that there is no deformation on the prepared I-Cu/ECat after testing in the cracking of n-hexadecane. Similar findings were observed for I-MnO/ECat catalyst as the characteristic peaks of MnO demonstrated at 34.9°, and 40.6° (JCPDS no:01-078-0424) in Figure 5.36-b and -c.

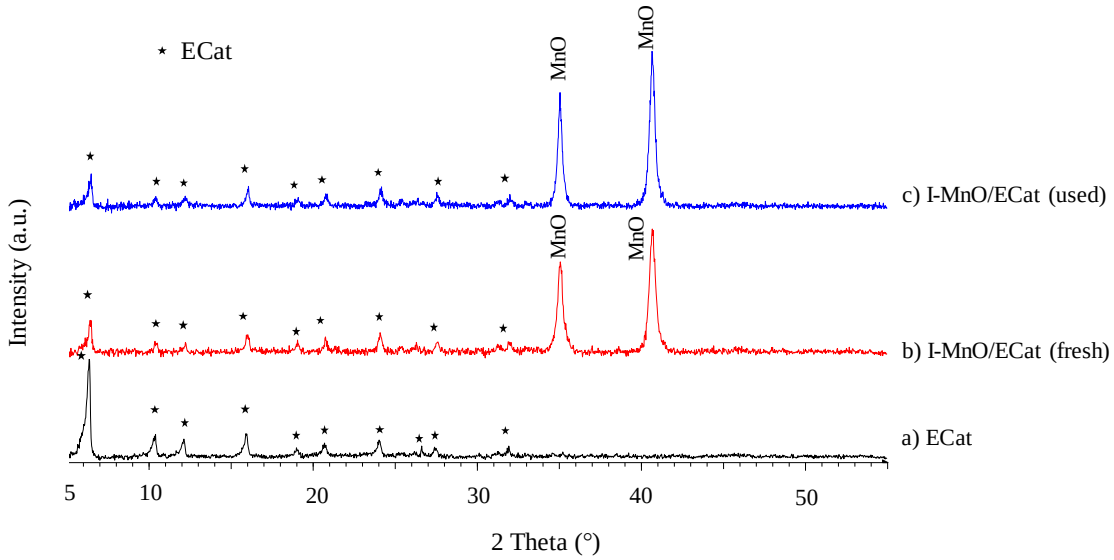


Figure 5.36. XRD patterns of a) ECat, b) fresh I-MnO/ECat, and c) used I-MnO/ECat.

However, as shown in Figure 5.37-b the fresh I-CoO/ECat contains ~20 wt.% of Co in addition to ~80 wt.% of CoO (see in Table 5.8), as it was synthesised by the reduction of I-Co_3O_4/ECat with hydrogen at 350 °C. After the cracking test over the I-CoO/ECat, the intensity of reduced CoO peaks decreased while the intensity of Co peaks increased as seen in Figure 5.37-c, which may be attributed to the reduction of CoO to Co in the sequential reduction step.

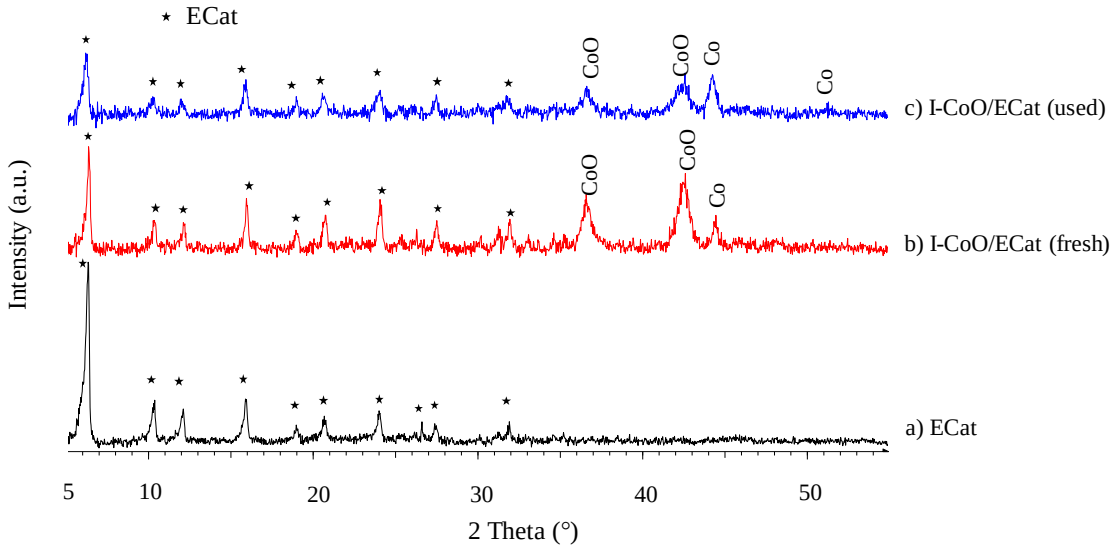


Figure 5.37. XRD patterns of a) ECat, b) fresh I-CoO/ECat, and c) used I-CoO/ECat.

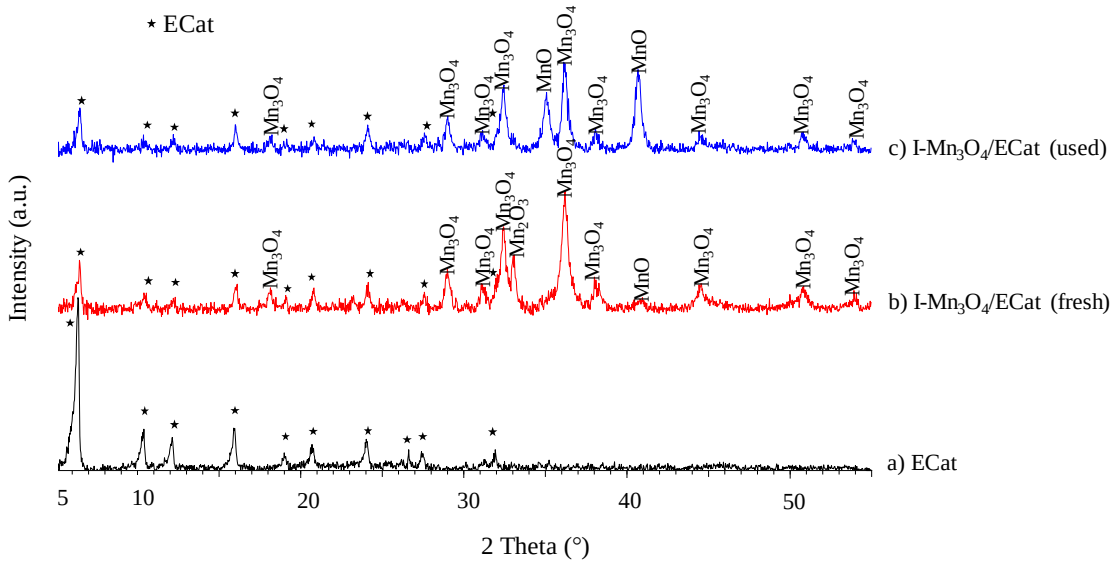


Figure 5.38. XRD patterns of a) ECat, b) fresh I-Mn_3O_4/ECat, and c) used I-Mn_3O_4/ECat.

Similarly, I-Mn_3O_4/ECat was successfully synthesised by the reduction of I-Mn_2O_3/ECat with hydrogen at 300 °C. However, the prepared catalysts include a small quantity of unreduced Mn_2O_3 (peak at 32.9°, JCPDS no:01-071-0636) and further reduced MnO (peak at 40.6°) as demonstrated in Figure 5.38-b. The unreduced Mn_2O_3 peak was not visible while the reduced MnO peaks (2θ= 34.9° and 40.6°, JCPDS no:01-078-0424) exists after the cracking of n-hexadecane over I-Mn_3O_4/ECat catalyst as seen in Figure 5.38-c, which prove the sequential reduction steps $Mn_2O_3 \rightarrow Mn_3O_4 \rightarrow MnO$.

The small quantity of oxidised oxygen carriers Co_3O_4 and Mn_2O_3 in the catalysts of I-CoO/ECat and I-Mn_3O_4/ECat can result in a further reduction to the CoO-Co and Mn_3O_4-MnO states, seen in Figure 5.37 and 5.38. However, it would be an insignificant effect on the cracking reaction thanks to the small portion. This further reduction may be eliminated with the prepare completely reduced oxygen carriers impregnated ECat as the reduced oxygen carriers, Cu, CoO, MnO, and Mn_3O_4, impregnated ECat did not show any further reduction.

SEM analysis: The SEM images of both fresh and used I-Cu/ECat, I-CoO/ECat, I-Mn_3O_4/ECat, and I-MnO/ECat were examined. Neither fragmentation nor agglomeration was observed on I-Cu/ECat as seen in Figure 5.39-a after the reduction of I-CuO/ECat with hydrogen. Furthermore, any deformation was not detected on the used I-Cu/ECat after testing in cracking of n-hexadecane as illustrated in Figure 5.39-b. However, Cu accumulation on both fresh and used I-Cu/ECat was observed in Figure 5.39-a1 and Figure 5.39-b1, respectively. Since I-Cu/ECat was prepared by the reduction of I-CuO/ECat with hydrogen, the accumulation of Cu would be expected as shown on CuO impregnated ECat, as demonstrated previously in Figure 5.20.

As for the I-CoO/ECat, although no agglomeration was observed on the SEM images, CoO accumulation and fragmentation were appointed on both fresh and used I-CoO/ECat catalyst demonstrated in Figure 5.40-a and b. However, neither the reduction process with hydrogen nor the cracking was the reason for these fragmentation nor metal accumulation. Instead, both were already observed during the preparation of I-Co_3O_4/ECat (Figure 5.21) and attributed to ion states of Co^{3+} and the impregnated amount of Co_3O_4.

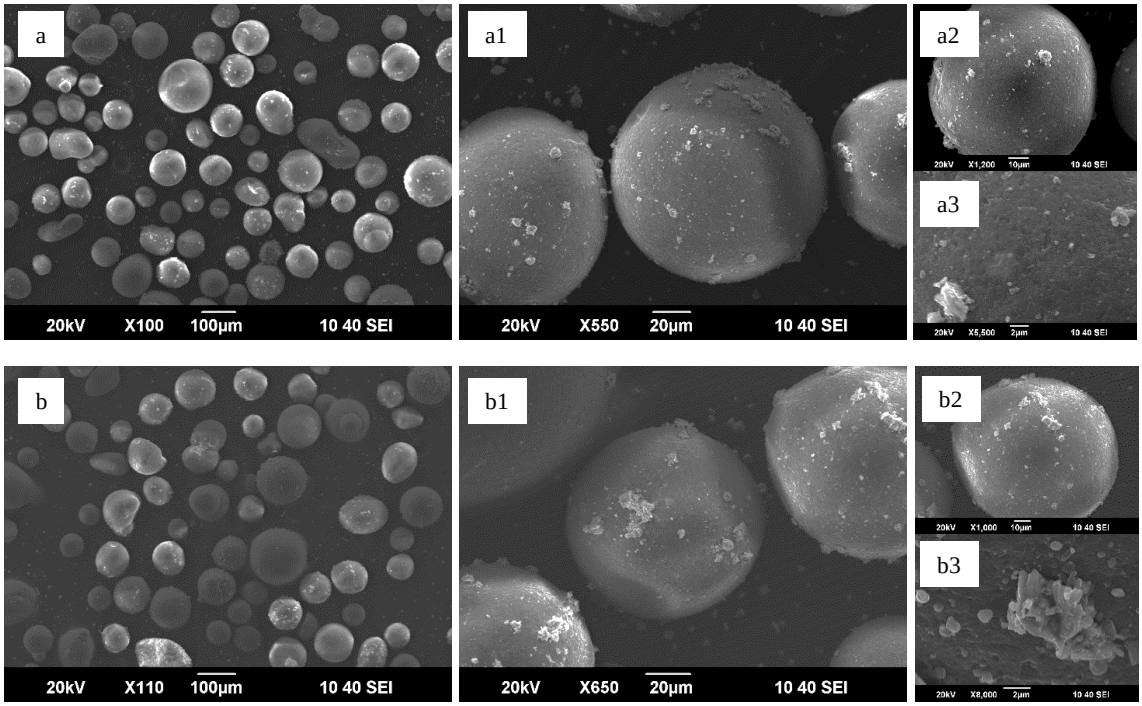


Figure 5.39. SEM images of a) fresh I-Cu/ECat and b) used I-Cu/ECat.

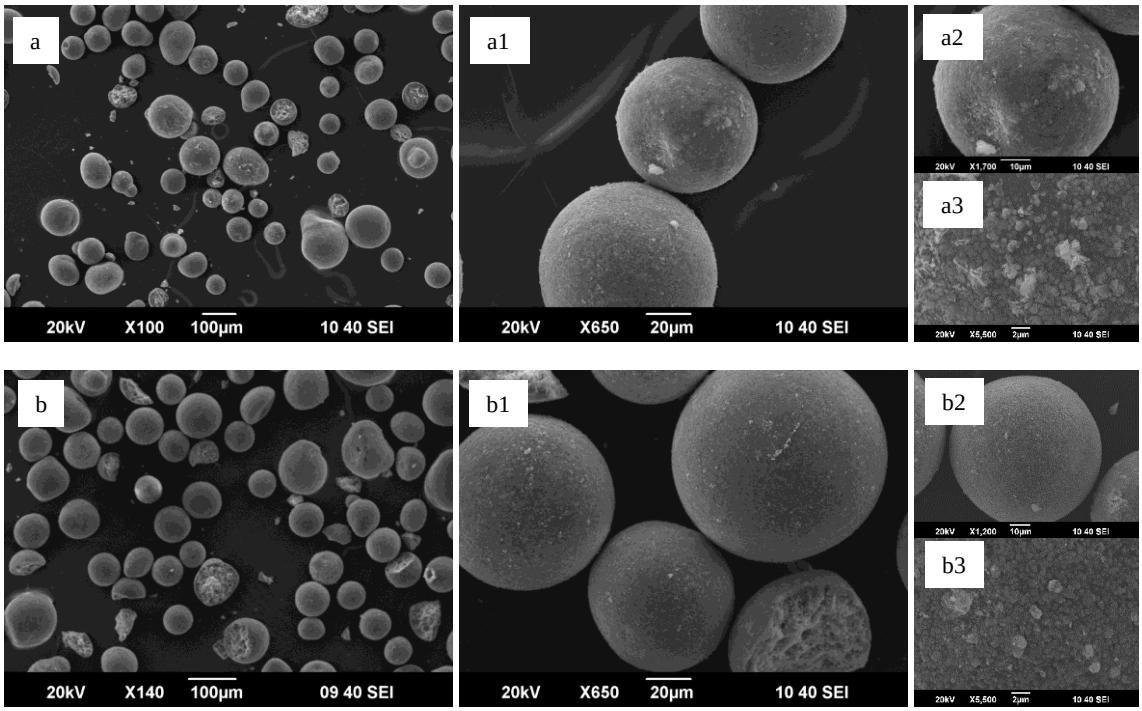


Figure 5.40. SEM images of a) fresh I-CoO/ECat and b) used I-CoO/ECat.

In terms of both I-MnO/ECat (Figure 5.41) and I-Mn_3O_4/ECat (Figure 5.42), the catalysts demonstrated similar properties such as fragmentation, agglomeration and Mn-based accumulation. As shown previously (Figure 5.22), ECat demonstrates fragmentation,

agglomeration and Mn- accumulation after the impregnation of Mn_2O_3. Thus, these deformations also came forward on its reduced forms, both I-MnO/ECat and I-Mn_3O_4/ECat.

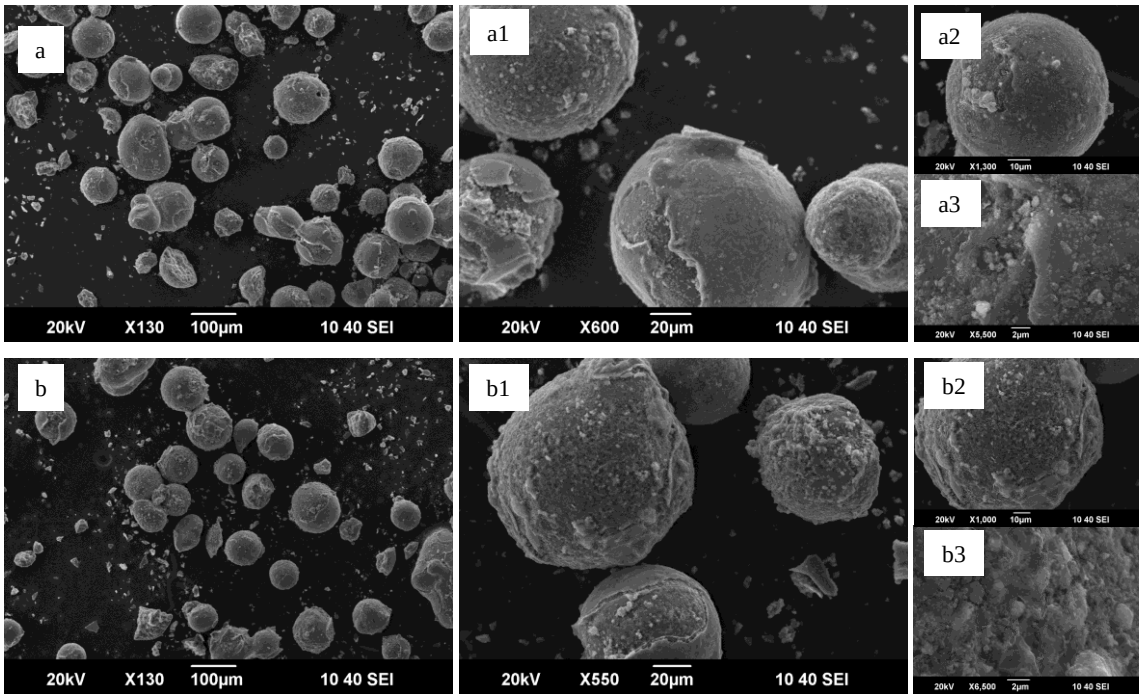


Figure 5.41. SEM images of a) fresh I-MnO/ECat and b) used I-MnO/ECat.

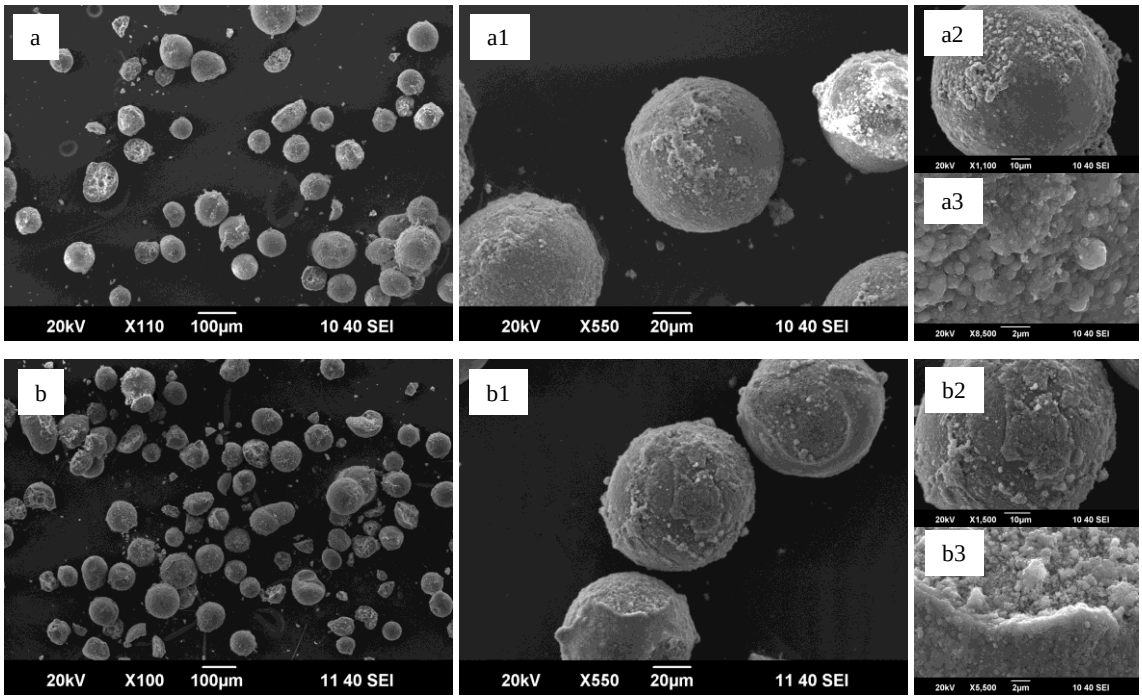


Figure 5.42. SEM images of a) fresh I-Mn_3O_4/ECat and b) used I- Mn_3O_4/ECat.

There is no clear suggestion that the deformations on the catalysts (I-Cu/ECat, I-CoO/ECat, I-Mn_3O_4/ECat, and I-MnO/ECat) were due to the reduction nor cracking reaction. The physical deformations such as fragmentation, agglomeration, and metal accumulation, on the prepared catalysts come to exist during the preparation of their oxidised states impregnated ECat. Suggestions to deal with these problems have already been mentioned previously, Section 5.3.1.1.

XRF and EDS mapping: The percentage of reduced oxygen carriers, Cu, CoO, Mn_3O_4 and MnO, impregnated on ECat, and the true densities of prepared catalysts are presented in Table 5.9. The true density of ECat slightly increased with the modification of reduced oxygen carriers. This may simply be attributed to the density differences of the ECat (2.70 g/cm^3) and the reduced oxygen carriers Cu (8.92 g/cm^3), CoO (6.44 g/cm^3), Mn_3O_4 (4.86 g/cm^3) and MnO (5.43 g/cm^3). The XRF results show that the required amount of reduced oxygen carriers were successfully impregnated on the ECat, which is about 5.5 wt.% of Cu, 16 wt.% of CoO, 29 wt.% of Mn_3O_4, and 27 wt.% of MnO.

Table 5.9. Proportion of reduced oxygen carriers impregnated with ECat.

Catalyst	True density[a] (g/cm^3)	Theoretical loading[b] (wt.%)	Actual loading[c] (wt.%)
ECat	2.70	n.a.	n.a.
I-Cu/ECat	2.77	5.4	6.6
I-CoO/ECat	2.94	16.8	16.3
I-Mn_3O_4/ECat	3.05	29.0	29.4
I-MnO/ECat	3.09	27.7	26.7

[a] Measured by Helium Pycnometer. [b] Determined the reduced oxygen carriers based on the weight differences of ECat before and after oxygen carrier impregnation. [c] Determined the reduced oxygen carriers using XRF.

Thanks to the preparation method of I-Cu/ECat, I-CoO/ECat, I-Mn_3O_4/ECat, and I-MnO/ECat, the dispersion of reduced oxygen carriers on the ECat surface was expected to be the same with their oxidised states impregnated. The qualitative element spectrums for catalysts are presented in Figure 5.43-5.46. As it can be detected on each elemental analysis, Cu was dispersed on the surface of ECat demonstrates in Figure 5.43-a. However, an accumulation of Cu on both fresh and used I-Cu/ECat was clearly observed on spot-2 in Figure 5.43-a2 and spot-1 in Figure 5.43-b1.

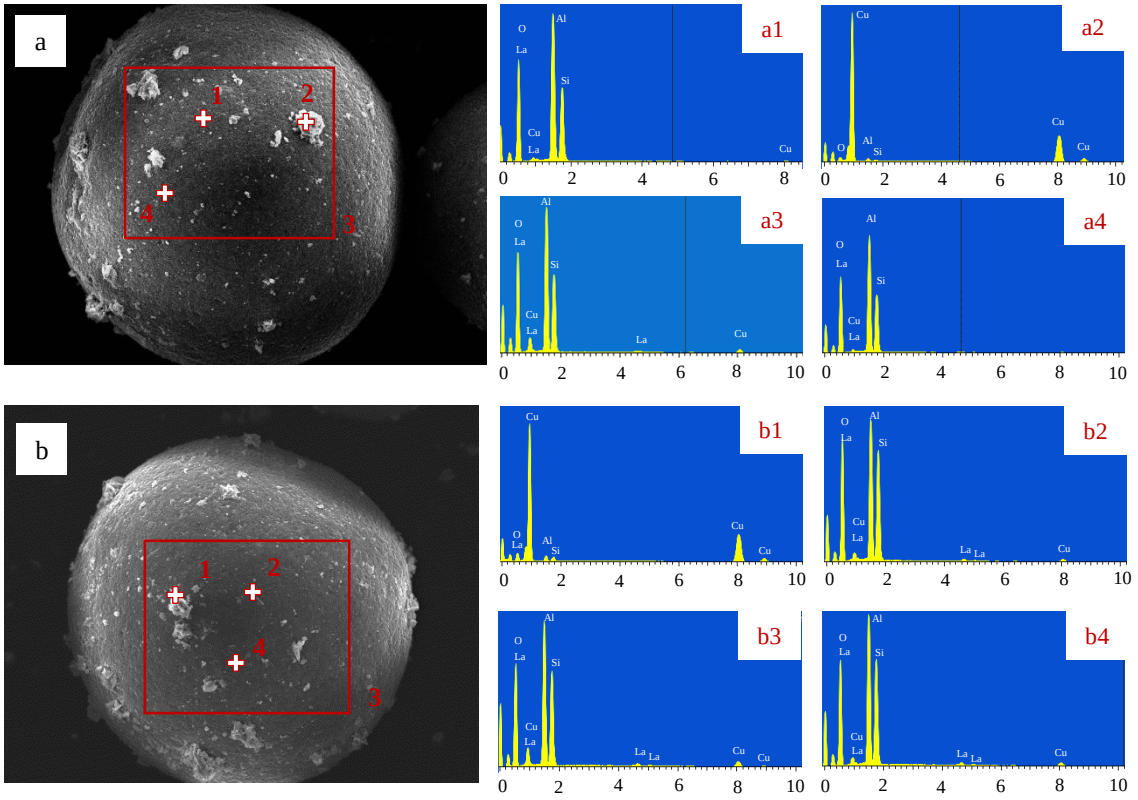


Figure 5.43. EDS element spectrums of a) fresh I-Cu/ECat and b) used I-Cu/ECat.

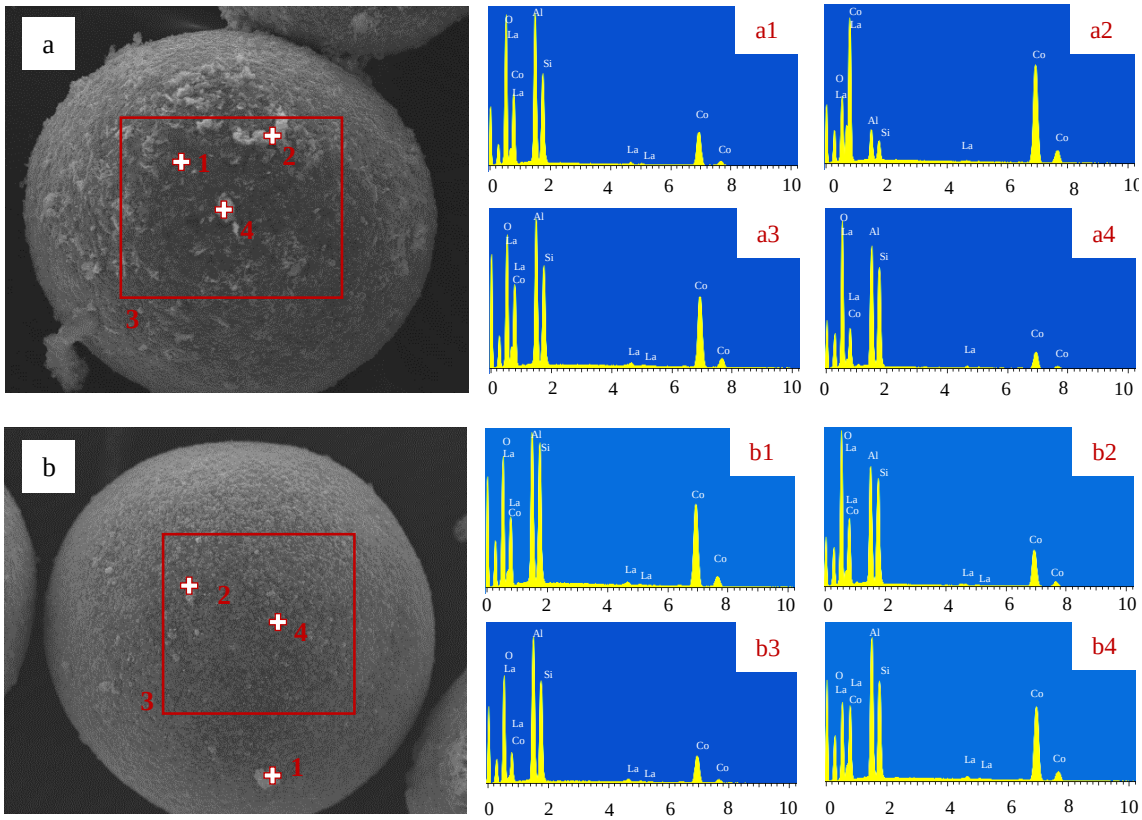


Figure 5.44. EDS element spectrums of a) fresh I-CoO/ECat and b) used I-CoO/ECat.

The similar accumulation can also be observed for CoO on both fresh and used I-CoO/ECat catalyst in Figure 5.44-a2 and Figure 5.44-b1. The intensity of the Co-accumulation on I-CoO/ECat was much higher than Cu accumulation on I-Cu/ECat as the ratio of impregnated CoO was higher than Cu. Furthermore, the catalysts were prepared by the reduction of their oxidised states, CuO and Co_3O_4, as mentioned previously. Thus, the more accumulation of Co on I-CoO/ECat may also be attributed to Co^{3+} ions, which may have a diffusion problem to the pores.

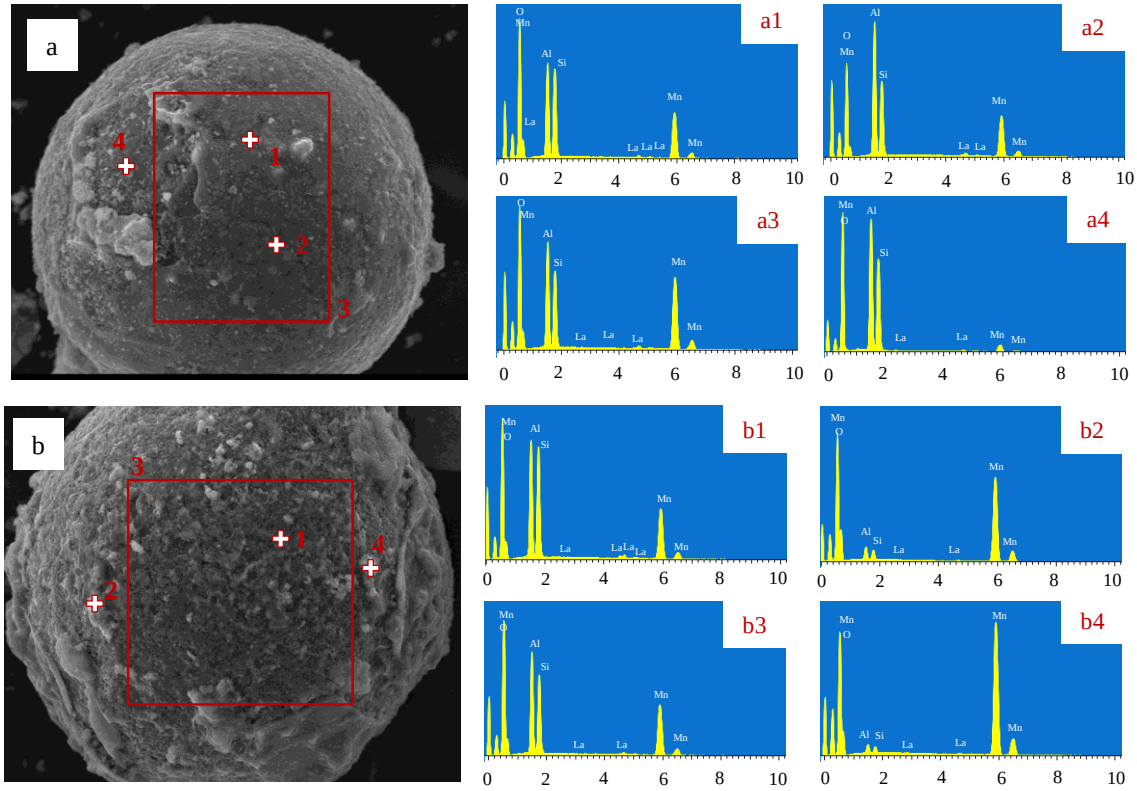


Figure 5.45. EDS element spectrums of a) fresh I-MnO/ECat and b) used I-MnO/ECat.

Similarly, an apparent accumulation of MnO and Mn_3O_4 can be obtained from the SEM images of I-MnO/ECat (Figure 5.45) and I-Mn_3O_4/ECat (Figure 5.46). The intensity of Mn on I-MnO/ECat and I-Mn_3O_4/ECat were higher than the intensity of Cu on I-Cu/ECat and Co on I-CoO/ECat. Additionally, even after using these catalysts for the cracking of n-hexadecane, the intensity of the metals was quite similar to their fresh forms.

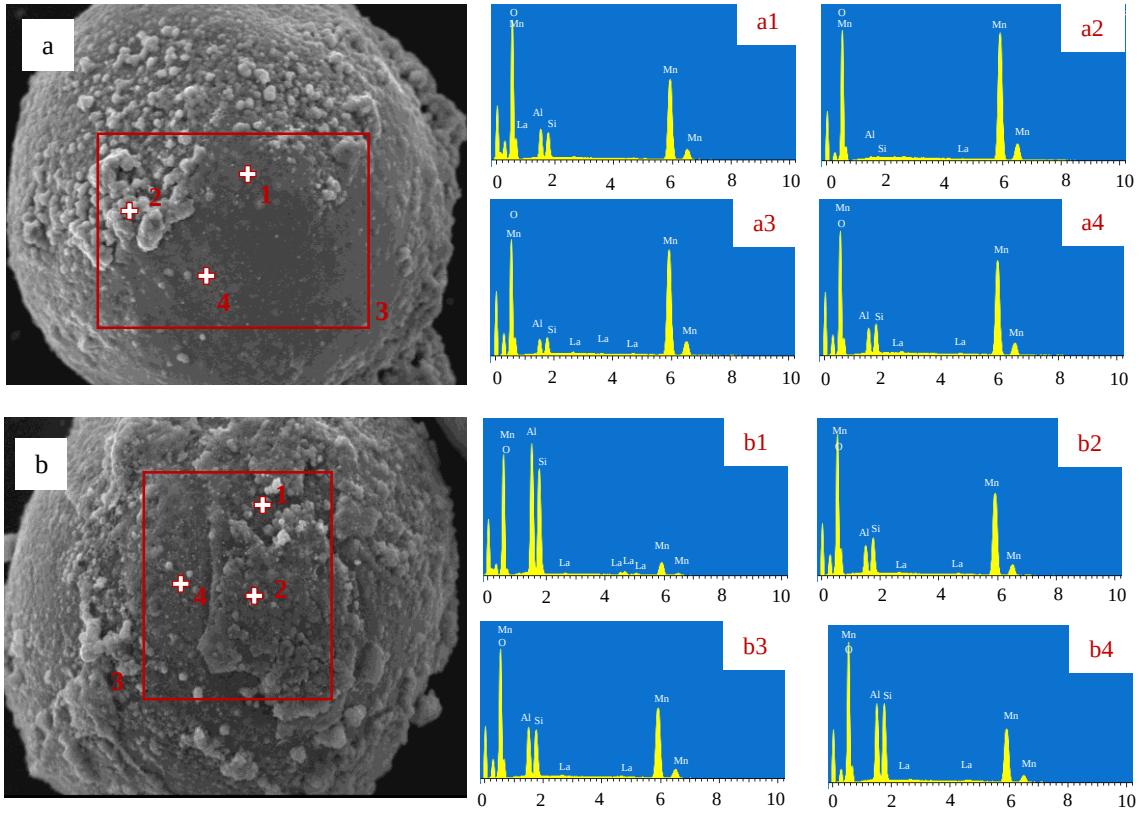


Figure 5.46. EDS element spectrums of a) fresh I-Mn_3O_4/ECat and b) used I- Mn_3O_4/ECat.

The other elements in the structure of ECat such as Si, Al, O and even La (trace amount) can still be detectable. Consequently, the reduced oxygen carriers Cu, CoO, MnO and Mn_3O_4 were not completely covered the surface of ECat, which means the pores were still accessible for the cracking feed. Although the accumulation is negative for the catalytic reactions where the impregnated metal needs to enhance the activity of the catalyst, it is not the case in terms of the proposed CLC-FCC concept. As the impregnated reduced (or oxidised) oxygen carriers should not affect the cracking reactions. To keep the pores and active sites accessible is, therefore, more important to get similar activity even after oxygen carrier modification.

N_2 adsorption-desorption analysis: The nitrogen sorption isotherms and textural properties of I-Cu/ECat, I-CoO/ECat, I-Mn_3O_4/ECat, and I-MnO/ECat are presented in Figure 5.47 and Table 5.10. Impregnation of reduced oxygen carriers did not change the form of the sorption isotherms of the ECats, which are defined as “type IV” according to IUPAC classification. Furthermore, the hysteresis loop shown in Figure 5.47 may also be

described as “type H3” as it was also represented on the oxidised oxygen carriers impregnated ECat catalysts.

After the impregnation of the reduced oxygen carriers, a decrease on BET surface area was observed approximately 12 m^2/g for the impregnation of Cu, CoO, MnO and about 22 m^2/g for the impregnation of Mn_3O_4. The decrease in the surface area by the impregnation of metals may be attributed to pore blocking by the metals impregnated pore mouths. However, as will be described, the fact that cracking activity remains high indicates that access to the zeolite micropores is not significantly affected. In terms of pore volume, the reduced oxygen carriers impregnated ECat demonstrated a similar total pore volume around 0.19 cm^3/g that was slightly lower than the parent ECat (0.25 cm^3/g). The reduction of oxidised oxygen carrier impregnated ECat using hydrogen had no significant effect on the total pore volume as it was ~0.18 cm^3/g.

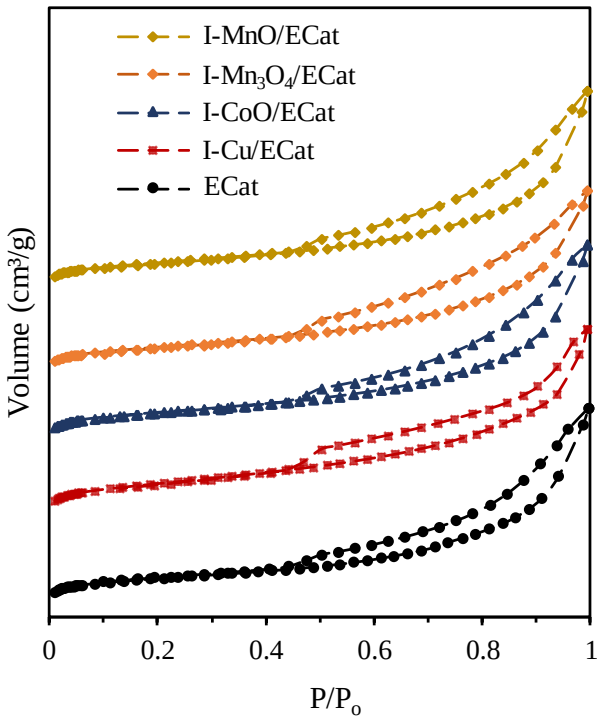


Figure 5.47. Nitrogen adsorption-desorption isotherms of fresh reduced oxygen carriers impregnated ECat; ECat, I-Cu/ECat, I-CoO/ECat, I-Mn_3O_4/ECat, I-MnO/ECat.

As for the average pore diameter, the impregnation of Cu and Mn_3O_4 slightly decreased it whereas the impregnation of MnO and CoO had no significant effect. Furthermore, the

neck diameter was not affected by the impregnation of Cu, CoO or MnO. The decrease in surface area, pore volume and pore diameter may be attributed to the diffusion of oxygen carriers into the ECat pores. As the decreasing trend in BET surface area and pore volume with the modification of transition metals on zeolite catalysts have been observed previously [242, 245-248].

Table 5.10. Surface properties of ECat, I-Cu/ECat, I-CoO/ECat, I-Mn_3O_4/ECat, I-MnO/ECat.

Catalyst	Surface area (m^2/g)		Pore volume (cm^3/g)			Pore diameter (nm)	
	S_{BET} [a]	S_{micro} [b]	V_{tot} [c]	V_{meso} [d]	V_{micro} [b]	d_{av} [e]	d_{neck} [e]
ECat	191	102	0.25	0.20	0.05	13.8	11.0
I-Cu/ECat	179	116	0.19	0.15	0.04	13.0	10.3
I-CoO/ECat	181	103	0.19	0.16	0.03	13.5	10.2
I-Mn_3O_4/ECat	169	74	0.17	0.15	0.02	12.8	8.8
I-MnO/ECat	177	87	0.18	0.17	0.01	13.7	10.0

[a] The BET surface area (S_{BET}) was calculated on the basis of g ECat. [b] Micro surface area (S_{micro}) and pore volume (V_{micro}) were calculated using the t-Plot method. [c] Total pore volume (V_{tot}) was defined as sum of micro, meso and macro pore volumes. [d] Meso-pore volume (V_{meso}) was calculated by the BJH adsorption cumulative volume of pores (2.0-50.0 nm). [e] Pore diameters, average (d_{av}) and neck (d_{neck}), were calculated by the BJH method (4V/A).

Brönsted-Lewis acidities via Fourier-transform infrared spectroscopy (IR-Py): The Brönsted (B) and Lewis (L) acidities measured by Py-IR of parent ECat, I-Cu/ECat, I-CoO/ECat, I-Mn_3O_4/ECat, and I-MnO/ECat, are presented in Figure 5.48, and the integrated area of the peaks are summarized in Table 5.11 using arbitrary units.

The interactions of pyridine-Brönsted and pyridine-Lewis acid sites are indicated with a group of adsorption bands on the IR spectrum, at 1540 and 1640 cm^{-1} (Brönsted acidity [249]), at 1445, 1580 and 1620 cm^{-1} (Lewis acidity [249, 250]) and the band about 1490 cm^{-1} (either Lewis or Brönsted acidity [247, 249, 250]). The intensity of the Lewis acid site at around 1445 cm^{-1} was considerably higher than that of Brönsted acid site at about 1540 cm^{-1} for the parent, and reduced oxygen carrier impregnated ECat. Additionally, both Lewis and Brönsted acid sites demonstrated a decrease with the impregnation of reduced oxygen carriers which are in line with previous studies [247, 251]. The integrated area of both Lewis and Brönsted acidities decreased after the impregnation of Cu, CoO, Mn_3O_4, and MnO, as seen in Table 5.11. Similar decreases in both Lewis and Brönsted acid sites were also obtained after the oxidised oxygen carriers impregnated on ECat. The

decrease in the acid sites may be attributed to the decrease in the surface area and pore volume due to the impregnation of oxygen carriers.

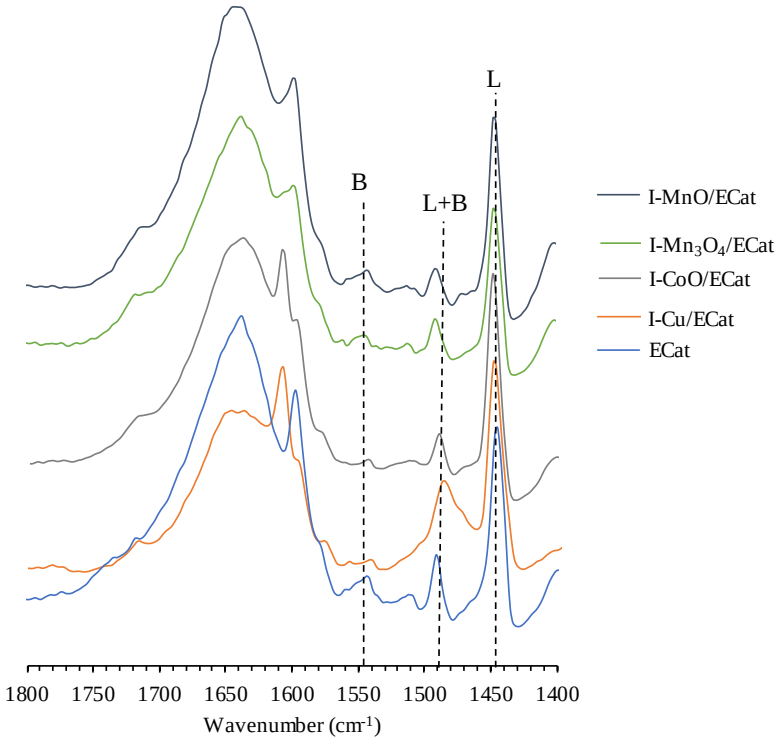


Figure 5.48. IR-Py spectra of parent and reduced oxygen carriers impregnated ECat catalysts.

Table 5.11. Integrated area of IR-Py peaks for parent and reduced oxygen carriers impregnated ECat.

Catalyst	L[a] (1445 cm^{-1})	L+B (1490 cm^{-1})	B[b] (1545 cm^{-1})
ECat	1.52	0.30	0.20
I-Cu/ECat	1.30	0.74	0.08
I-CoO/ECat	1.44	0.30	0.02
I-Mn_3O_4/ECat	1.14	0.20	0.08
I-MnO/ECat	1.36	0.16	0.16

[a] Lewis (L) acidity area measured by IR peak at 1445 cm^{-1}. [b] Brönsted (B) acidity area measured by IR peak at 1545 cm^{-1}.

Coke analysis: Table 5.12 shows that the carbon percentage increased from 0.45 wt.% to 1.09, 1.17, 1.22 and 0.77 wt.% with the impregnation of Cu, CoO, Mn_3O_4, and MnO, respectively. There were no differences on the coke deposition once the mechanical mixing method was used. Thus, as described previously, the increase in the coke must be attributed to the change in pore structures of the ECat with such modification. As observed previously for oxidised oxygen carrier impregnated ECat, an inverse

relationship between average pore diameter (Table 5.10) and coke deposition was obtained for the reduced oxygen carrier impregnated ECat, as the average pore diameter followed the trends ECat > I-MnO/ECat > I-CoO/ECat > I-Cu/ECat > I-Mn_3O_4/ECat while the carbon percentage on catalysts displayed the opposite trend. The highest level of coke (1.22 wt% C) was found on I-Mn_3O_4/ECat, which had the lowest average pore diameter of 12.8 nm and neck diameter of 8.8 nm once compared with other reduced oxygen carriers impregnated ECat.

Table 5.12. Coke percentage and normalized coke composition of used catalysts; ECat, I-Cu/ECat, I-CoO/ECat, I-Mn_3O_4/ECat, I-MnO/ECat.

Catalyst	Coke on catalyst[a] (wt.%)		Coke composition[b] (wt.%)		Coke type (wt.%)		H/C[e]
	Carbon	Hydrogen	Carbon	Hydrogen	SC[d]	HC[c]	
ECat	0.45 ±0.02	0.03 ±0.01	93.6 ±2.2	6.4 ±2.2	0.5	99.5	0.80
I-Cu/ECat	1.19 ±0.34	0.09 ±0.01	91.9 ±2.3	8.1 ±2.3	8.4	91.6	0.99
I-CoO/ECat	1.17 ±0.15	0.05 ±0.07	96.1 ±0.9	3.9 ±0.9	-	100	0.51
I-Mn_3O_4/ECat	1.22 ±0.16	0.09 ±0.05	93.6 ±2.7	6.4 ±2.7	32.8	67.2	0.88
I-MnO/ECat	0.77 ±0.01	0.05 ±0.01	93.1 ±0.9	6.9 ±0.9	19.5	80.5	0.78

[a] Based on g of total coke/ g of ECat. [b] Normalized coke composition was calculated by (weight of carbon (or hydrogen) / weight of coke)*100, wt.%. [c] Hard Coke, the remain coke % after solvent extraction. [d] Soft Coke was determined using the differences of (100-HC), wt.%. [e] The ratio of H/C was calculated the weight of H*12/weight of C.

Furthermore, the impregnation of both oxidised and reduced Mn on ECat increased the content of soft coke. As for the hydrogen content, it was slightly higher due to the moisture content on the catalysts as mentioned previously, the hydrogen composition in the coke should be 2-4 wt.% [189]. On the other side, the ratio of H/C calculated for the reduced oxygen carrier impregnated ECats was in the range presented in the literature, 0.46-1.74 [189].

5.3.2.3 Cracking of n-hexadecane over reduced oxygen carrier impregnated ECats

The cracking activity of reduced oxygen carrier impregnated ECat; I-Cu/ECat, I-CoO/ECat, I-Mn_3O_4/ECat, and I-MnO/ECat, was investigated using n-hexadecane, with the conversion, coke, gas, liquid yields, and product selectivities presented in Figures 5.49-5.51, respectively. The negligible increases in the overall conversion, where CLC

was included arise from the very small amounts of C in the CO_2 produced by the combustion reaction during the cracking reactions.

Figure 5.49 shows that there were no significant differences between the overall conversion and that excluding CLC for the reduced oxygen carrier impregnated ECat. It implies that there was no further reduction of reduced oxygen carriers due to the combustion of the cracking feed (n-hexadecane or cracked products) has occurred, which is confirmed by the XRD patterns of the used catalysts (Figures 5.35-38). In contrast to earlier studies demonstrating a negative impact of Cu impregnation on the effectiveness of ZSM-5 for the cracking of palm oil, attributed to a decrease of the Brönsted acidity [235], the conversion of n-hexadecane here was not affected by the impregnation of Cu or Mn_3O_4. Although the negative effect of Cu was attributed to the decrease on the Brönsted acidity by Siregar and Amin [235], the relatively small amounts of Brönsted acidity could still be sufficient for the cracking of n-hexadecane [242].

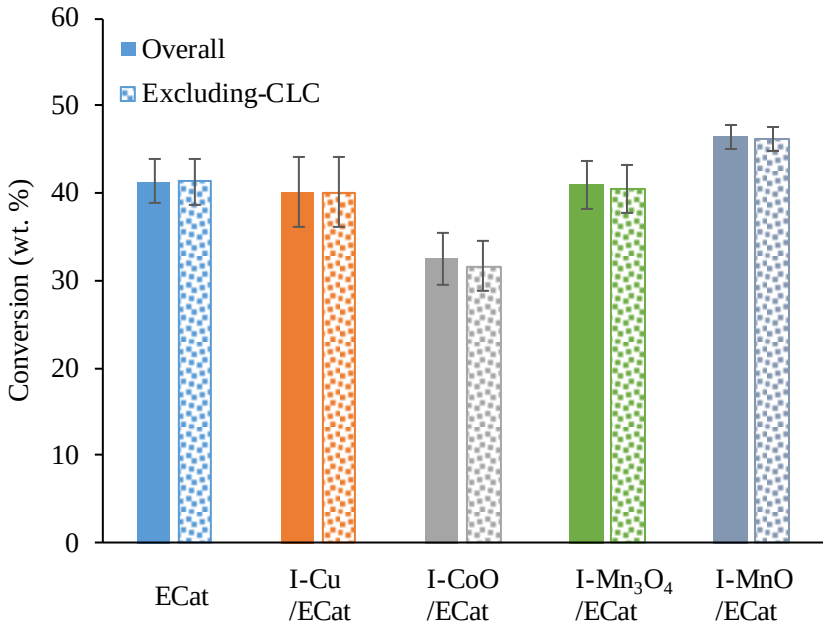


Figure 5.49. Conversion (overall and excluding CLC) of n-hexadecane over the control ECat and reduced form oxygen carrier impregnated ECat; I-Cu/ECat, I-CoO/ECat, I-Mn_3O_4/ECat, and I-MnO/ECat.

For CoO impregnation, which caused a dramatic reduction in the amount Brönsted acidity, the conversion of n-hexadecane was found to decrease to about 32 wt.%.

However, both the pore structure and acidity remained at a similar level after impregnation with MnO (Tables 5.10-11). On the other hand, the mechanically mixing of Co-based oxygen carriers (both reduced and oxidised) demonstrated no significant effect on the conversion of n-hexadecane. Therefore, the dramatic decrease in both pore structure and Brönsted acidity after the impregnation of CoO could reduce the cracking activity of ECat. Although the pore structure of I-CoO/ECat was lower than that of I-Co_3O_4/ECat, if the combustion of liquid fuels with oxidised Co_3O_4 takes place before the cracking reactions, both oxidised and reduced oxygen carriers would have demonstrated similar properties during the cracking reaction with a slightly different conversion result. As I-Co_3O_4/ECat demonstrated lower conversion (26 wt.%) than I-CoO/ECat (32 wt.%), due to the combustion of liquid feed with Co_3O_4. On the other hand, both the pore structure and acidity were kept quite similar after the impregnation of MnO.

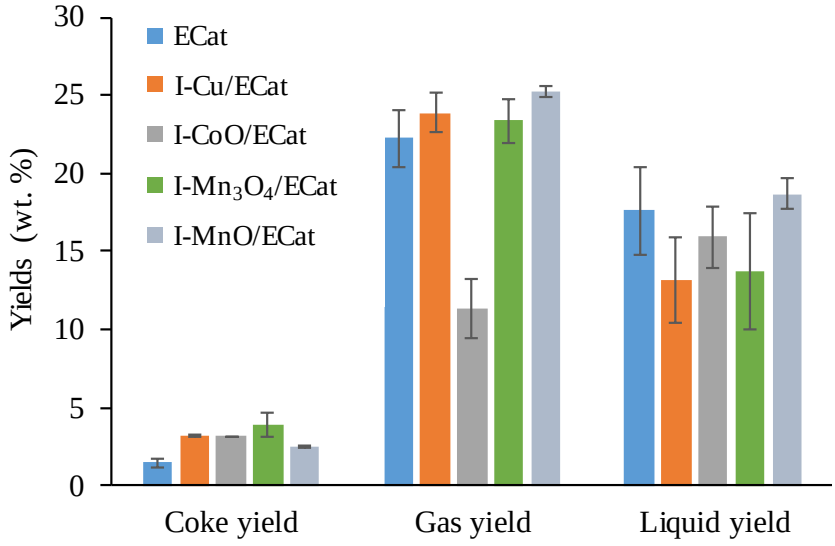


Figure 5.50. Coke, gas, and liquid yields from the cracking of n-hexadecane over control ECat and reduced form oxygen carrier impregnated ECat; I-Cu/ECat, I-CoO/ECat, I-Mn_3O_4/ECat, and I-MnO/ECat.

Figure 5.50 shows that the coke yield increase from 1.5 wt.% to about 3.0 wt.% with the impregnation of Cu and CoO, to 2.5 wt.% with the impregnation of MnO, whereas the impregnation of Mn_3O_4 almost trebled the coke yield, which may be attributed to the constriction of pore structure. Although the coke yields did increase with the impregnation of reduced oxygen carriers, the liquid to gas ratios was largely unaffected (except for the impregnation of CoO). Similarly, the increase in the coke deposition on

the FCC catalyst modified with MnO_3 after cracking of cumene was demonstrated by Hosseinpour et al. [253]. Although the impregnation of Cu decreased the coke deposition during the cracking of bio-oil, overloading of Cu increased the coke deposition [258]. The coke increase was attributed to the Lewis acid sites, which could promote the coking and results in deactivation due to the dehydrogenation reaction to the produce coke precursors [258].

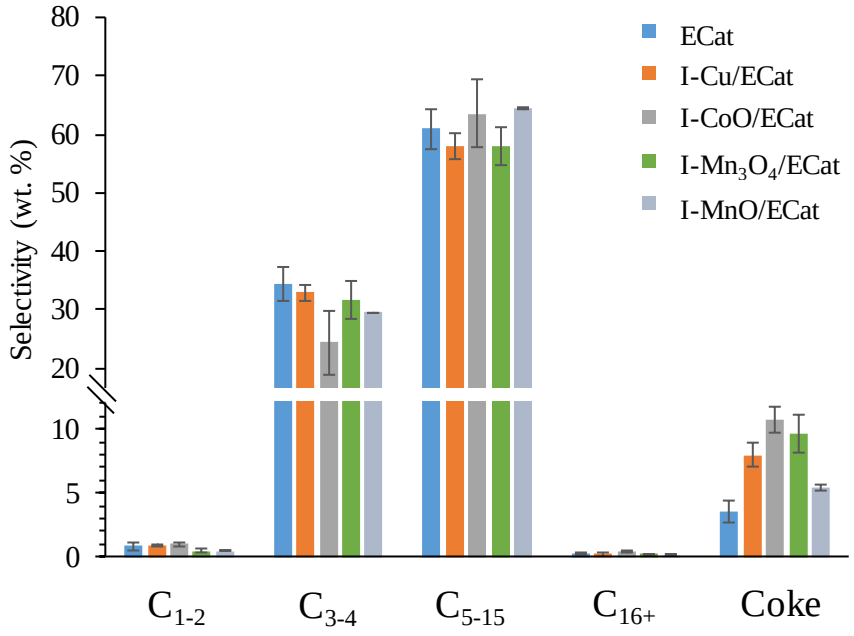


Figure 5.51. Product selectivity of C_{1-2} (light gases), C_{3-4} (LPG), C_{5-15} (gasoline), C_{16+} (higher hydrocarbons) and coke from the cracking of n-hexadecane over control ECat and reduced form oxygen carrier impregnated ECat; I-Cu/ECat, I-CoO/ECat, I-Mn_3O_4/ECat, and I-MnO/ECat.

Excluding coke formation, the use of reduced oxygen carrier modified ECat on the product selectivity was insignificant (Figure 5.51) except for the selectivity of LPG over CoO impregnated ECat, which may also explain the lower gas yield as presented in Figure 5.50. Given that the reduced oxygen carriers increased the coke yield on the catalyst, identification of the coke structure (soft coke and hard coke, Table-5.12) on the catalyst after the modification with the reduced oxygen carriers is, therefore, an essential issue for the proposed CLC-FCC concept.

However, the results may change based on the cracking feed. As Siregar and Amin [235] studied the cracking of palm oil over Cu modified ZSM-5 zeolite catalyst and reported

that the selectivity of gasoline decreased with the impregnation of copper. Further, a decreasing trend was observed once the ratio of impregnated copper was increased up to 8 wt.%, which was the highest ratio tested in their study. Although a decrease in coke deposition was observed with low Cu impregnation, the coke deposition increase with higher Cu impregnation on Beta zeolite catalysts in cracking of bio-oil [258].

Identification of the coke structure (soft coke and hard coke) on the catalyst after the modification with reduced oxygen carriers is important for the proposed CLC-FCC concept. If it is predominantly hard coke, a greater amount of oxidised oxygen carrier circulation from air reactor o regenerator would be required for the CLC-FCC concept. If the coke is predominantly soft, that will not affect the process dramatically, as the soft coke is stripped on the conventional system before the regeneration.

5.4 Summary

In summary, the cracking experiments over reduced oxygen carriers mixed ECat (M-Cu_2O/ECat, M-CoO/ECat, and M-Mn_3O_4/ECat) and reduced oxygen carrier impregnated ECat (I-Cu/ECat, I-Mn_3O_4/ECat, and I-MnO/ECat) demonstrate no significant effect on the cracking of n-hexadecane in terms of conversion, yields, and product selectivities. However, the mixing of metallic Cu (M-Cu/ECat) and impregnation of CoO (I-CoO/ECat) had a detrimental effect on the conversion of cracking reaction. In addition to the cracking reaction, a combustion reaction was discovered between oxidised oxygen carriers (CuO, Co_3O_4, and Mn_2O_3) modified with ECat and cracking feed (n-hexadecane) at a relatively low temperature of 482 °C. Due to the relatively small amount of oxidised oxygen carriers used in the modifications, the combustion reaction was minimized. Furthermore, it can be eliminated with the use of completely reduced oxygen carriers modified ECat on the cracking reaction, as suggested on the proposed CLC-FCC concept.

Chapter 6
Chemical Looping Combustion of FCC Coke

6.1 CLC of model coke with oxygen carriers in TA instrument

6.1.1 Oxygen carriers and model coke behaviours in TGA conditions

In CLC tests, a low volatile semi-anthracite Welsh coal was used as a model FCC coke due to its elemental similarities with FCC coke, and it was combusted with different oxygen carriers; CuO, Mn_2O_3, and Co_3O_4. A suitable oxygen excess number (which is defined as the molar ratio of oxygen to fuel) is one of the most crucial parameters to promote combustion of fuel (or model coke) [161]. Thus, the combustion of model coke with oxygen carriers was performed at different oxygen excess numbers (ratio of oxygen carrier/model coke; R=0.5, 1.0, 2.0).

Table 6.1. Ultimate and proximate analysis of the semi-anthracite model coke and normalized elemental analyses of the model and FCC cokes.

Ultimate analysis[a] (wt.%)					**Proximate analysis[c] (wt.%)**			
C	H	N	S	O[b]	TM[d]	VM	FC	Ash
86.3	4.3	1.5	2.2	5.7	0.5	16.2	70.3	13.5
Normalized element analysis (wt.%) of model coke and FCC cokes								
Coke type	**C %**	**H %**	**N %**	**S %**	**References**			
Model coke	91.6	4.6	1.6	2.3	-			
FCC coke-1	91.2	4.2	2.5	1.9	[189]			
FCC coke-2	93.0	2.9	3.8	0.4	[189]			
FCC coke-3	93.0	2.6	3.0	0.1	[189]			

TM: Total Moisture, VM: Volatile matter, FC: Fixed carbon. [a.] Dry basis, [b.] Determined by difference, [c.] On dry basis except for moisture which is as received basis, [d.] As received basis.

Before the CLC tests of model coke with oxygen carriers, baseline experiments of model coke and oxygen carriers were investigated in order to understand the composition of model coke and oxygen release capacity of oxygen carriers. The proximate and ultimate

analyses presented in Table 6.1 indicate that the semi-anthracite has a similar elemental composition to FCC coke, and, on this basis, was selected for the CLC experiments as a model coke.

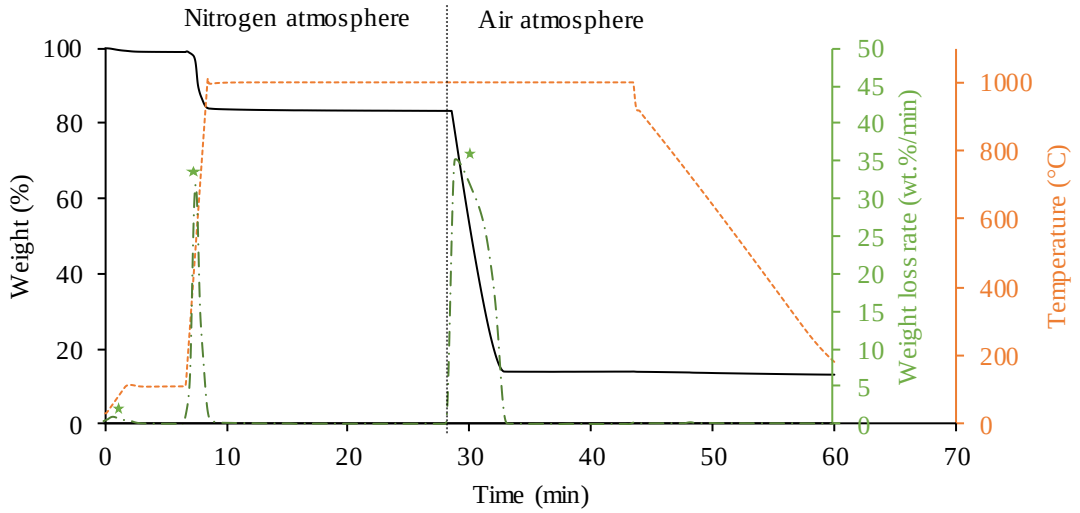


Figure 6.1. TGA profile of the model coke under nitrogen and air atmosphere at 1000 °C.

Figure 6.1 shows the TGA profile of the model coke under nitrogen and then air atmosphere. Model coke shows three weight loss stages; the first two stages were observed under nitrogen atmosphere at the temperatures of 35-110 °C and 200-600 °C. As soon as the air was switched on at the same conditions, the third weight decrease was obtained. The first one (0.5 wt.%) is the moisture content of model coke. The second one (approximately 16 wt.%) is probably due to the volatile matters of model coke, and the last one (70 wt.%) is the fixed carbon of the model coke. The remaining part (13 wt.%) is attributed to ash content (Figure 6.1).

In order to clarify the reduction steps of oxygen carriers, TGA profiles of oxygen carriers are demonstrated in Figure 6.2. The TGA results of the oxidised oxygen carriers shown that the weight loss percentages for the reductions from CuO to Cu_2O, Co_3O_4 to CoO and M_2O_3 to Mn_3O_4 are *ca*. 10.1, 6.4, and 3.6 wt.%, respectively, close to their theoretical values. The results proved that the oxygen carriers can release oxygen due to their CLOU properties as it has been demonstrated in the literature [23, 160, 175, 227]. The oxygen released from oxygen carriers can be therefore used to combust the coke on the FCC catalysts if mixed effectively with the model coke exists. Moreover, a good mixture of

FCC coke and oxygen carriers may give a solid-solid reaction between the coke and the oxygen carriers which has already been observed in TGA apparatus between char and Cu-, Co-, Mn- Ni- and Fe- based oxygen carriers [102, 153, 175, 259].

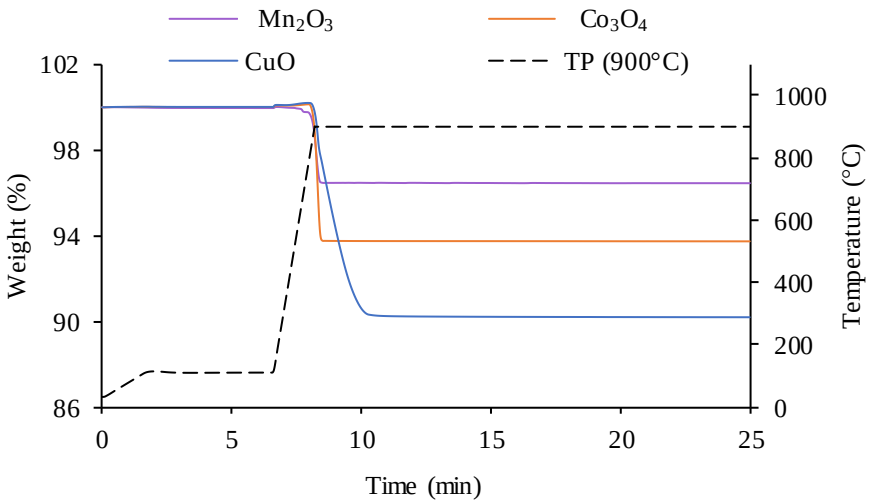


Figure 6.2. TGA profiles of oxygen carriers under N_2 atmosphere (TP: Temperature profile).

6.1.2 Chemical looping with oxygen uncoupling for the combustion of model coke with CuO

The effects of temperature and oxygen excess number (according to reaction 6.1) on the combustion of model coke with CuO are presented in Figure 6.3. It is possible to reach higher than 90 wt.% combustion with the minimum stoichiometrical requirement (R= 1.0) for CuO over the range 750 to 900 °C. Thus, increasing the oxygen excess number from 1.0 to 2.0 had no significant effects. Further, as expected, decreasing the oxygen carrier below the stoichiometric ratio decreased the extent of combustion (for R+0.5, 46, 31, 40 and 41 wt.% at 900, 850, 800, and 750 °C, respectively, Figure 6.3). The high degree of combustion was also reported for coal combustion with CuO by Siriwardane et al. [102]. However, although it is possible to reach full combustion at 750 °C, the combustion time dramatically increase at a temperature < 800 °C because of the fact that oxygen release at such temperatures is very low [23, 96, 160].

$$C_{71.9}H_{43.3} + 331CuO \rightarrow 165.5Cu_2O + 71.9CO_2 + 21.6H_2O \qquad (6.1)$$

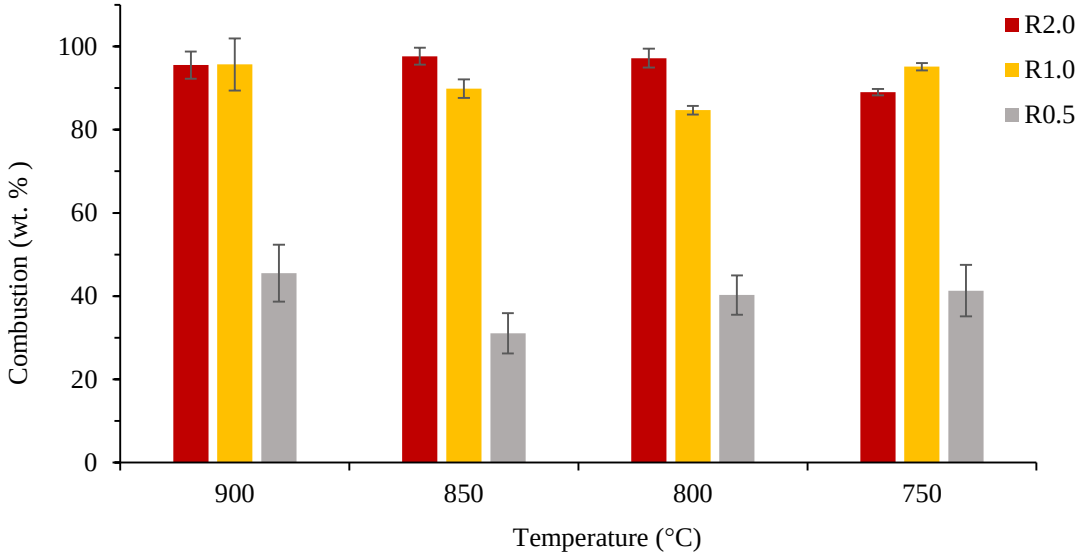


Figure 6.3. Combustion (wt.%) of model coke with CuO in various oxygen excess numbers (R = 0.5, 1.0, and 2.0) at various isothermal temperatures (750-900 °C).

The fractional reductions of the model coke with CuO for different oxygen excess numbers are presented in Figure 6.4, where WC refers to the model coke, Cu indicates CuO and R0.5, R1.0 and R2.0 refers to the oxygen excess numbers. As demonstrated in Figure 6.4, the fractional reduction tends to decrease with the isothermal combustion temperature as reported by Siriwardane et al. [102] for the combustion of solid fuels with oxygen carriers. For example, the required time for the 0.8 of fractional reduction was about 1, 3, 9, and 45 min at 900, 850, 800, and 750 °C, respectively, at the oxygen excess number of 1.0. These differences, especially below 800 °C, can possibly be attributed to the partial pressure of oxygen released from CuO at the isothermal temperatures being 15 times higher at 900 °C ($15*10^{-3}$) than that at 800 °C ($1.0*10^{-3}$) [23, 175]. This shows that the combustion reaction between gas phase oxygen and solid model coke is much faster than the solid oxygen carrier-solid model coke reactions, as expected.

Clearly, the oxygen excess number needs to be equal or higher than the stoichiometric level to achieve a fractional reduction of 1.0 and complete combustion [148], which was achieved here with a stoichiometric amount of CuO ($R \geq 1.0$) and allowing sufficient time (Figure 6.4). However, using excessive oxygen carrier sometimes negatively affects the fractional reduction. Figure 6.4 indicates that longer times were required to achieve high fractional reductions once the oxygen excess number was 2.0 (red-continuous line). This may be due to increasing inhomogeneity in the mixtures with the model coke, which will

be a negatively impact on solid-solid interactions. As expected, fractional reductions fell below the stoichiometrical requirement (R = 0.5). The high fractional reductions for CuO with the model coke when R= 1.0 is consistent with other reports for the combustion of coal with oxygen carriers [161, 175, 260].

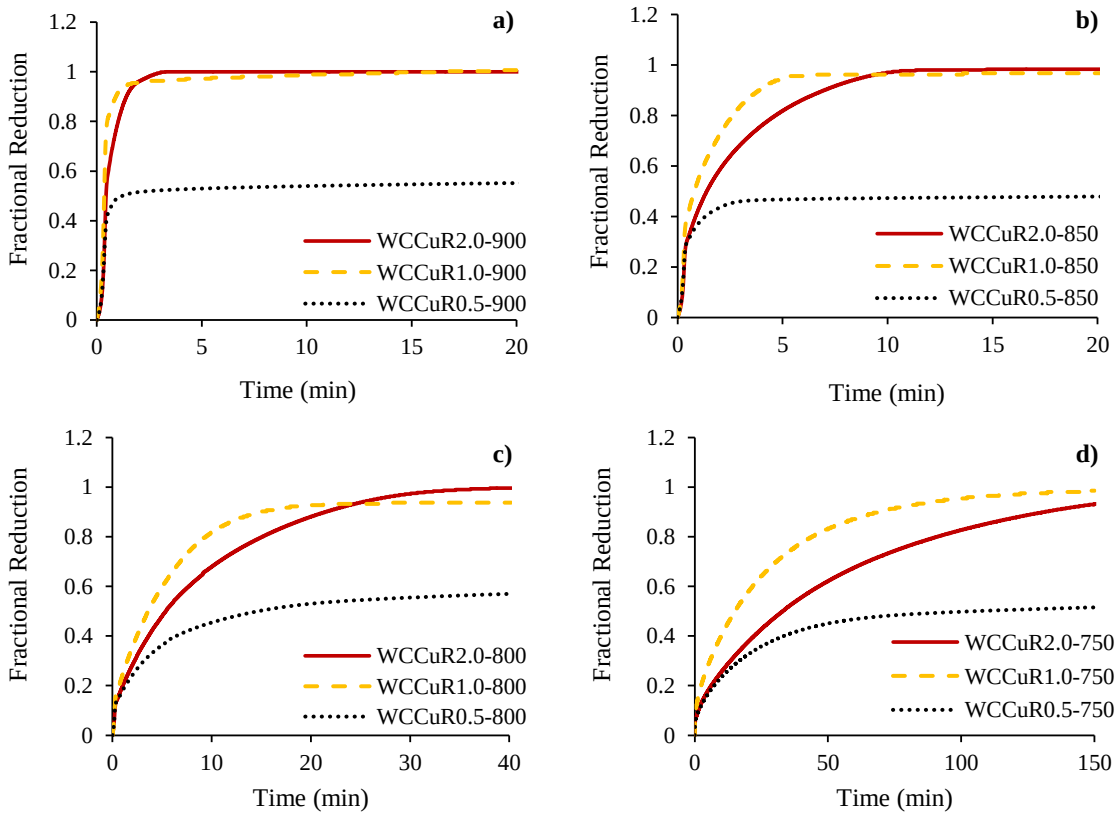


Figure 6.4. Fractional reduction of model coke with CuO for various oxygen excess numbers (R = 0.5, 1.0, and 2.0) at various isothermal temperatures a) 900 °C, b) 850 °C, c) 800 °C, d) 750 °C.

Figure 6.5 demonstrates the weight loss rates of model coke with CuO for different oxygen excess numbers and isothermal temperatures. The weight loss, related to fixed carbon of model coke, occurs between 660 °C - isotherm temperatures (750, 800, 850, and 900 °C), which was also reported in various CLC-solid fuel studies [102, 161, 261-263]. Additionally, the maximum weight loss occurs approximately in the isothermal region. The increase in the temperature dramatically increased the maximum weight loss rate to 34.1 wt.%/min for R=2.0, 43.2 wt.%/min for R=1.0, and 42.8 wt.%/min for R=0.5 at 900 °C (Figure 6.5-a).

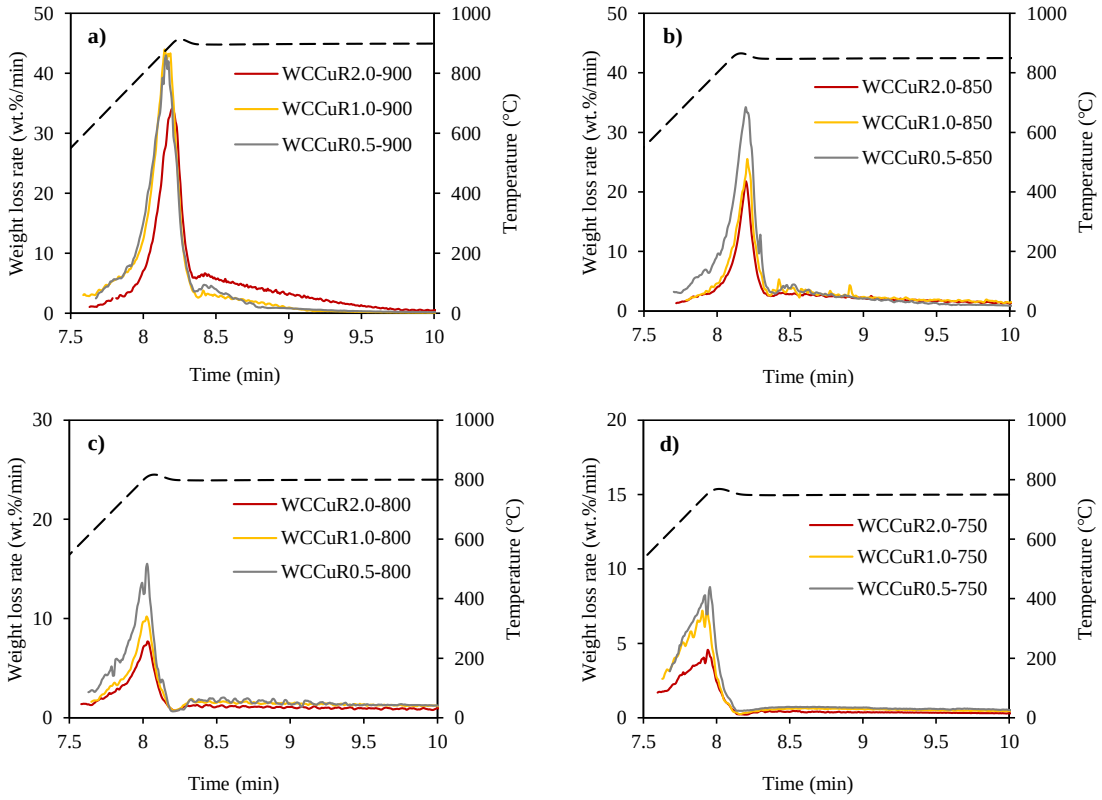


Figure 6.5. Weight loss rate of model coke (hard coke part) with CuO for various oxygen excess numbers (R=0.5, 1.0, and 2.0) at various isothermal temperatures a) 900 °C, b) 850 °C, c) 800 °C, d) 750 °C (line dashes represent the temperature profile).

The combustion between CuO and fixed carbon of model coke at high isothermal temperatures are much faster than that at low isothermal temperatures. The weight loss rates, which are found in these experiments, are high compared with the studies conducted by CuO-solid fuel [102, 150, 161, 261-265]. In the literature, the heating rate is generally used 20 - 100 °C/min for combustion. However, in this study, the heating rate was adjusted at 500 °C/min. As the regenerator of FCC unit is operated between 650-800 °C and the catalysts are generally faced with high temperatures once they drop into the regenerator. In order to obtain more accurate results, the regeneration of coke deposited FCC catalysts are therefore investigated with a rapid heating rate. The high weight loss rates in this study may be attributed to the rapid heating rate.

6.1.3 Chemical looping with oxygen uncoupling for the combustion of model coke with Co_3O_4

In addition to the CuO, the combustion results and fractional reduction of model coke with Co_3O_4 are presented in Figure 6.6 and 6.7, respectively. The combustion of model coke with Co_3O_4 being presented in reaction 6.2.

$$C_{71.9}H_{43.3} + 165.5Co_3O_4 \rightarrow 496.5CoO + 71.9CO_2 + 21.6H_2O \qquad (6.2)$$

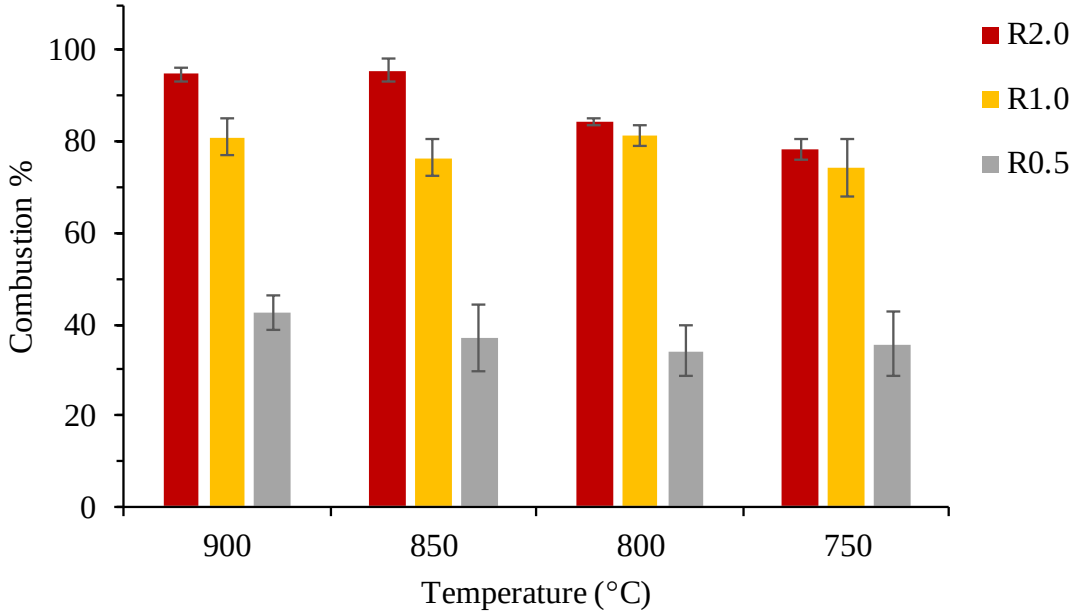


Figure 6.6. Combustion (wt.%) of model coke with Co_3O_4 in various oxygen excess numbers (R = 0.5, 1.0, and 2.0) at various isothermal temperatures (750-900 °C).

Figure 6.6 shows that the combustion increased with temperature and was over 80 wt.% using the stoichiometrically required amount of Co_3O_4 at the temperatures from 750 to 900 °C. However (as also observed for CuO) using higher than the stoichiometrically required amount of Co_3O_4, slightly increased the extent of combustion at all temperatures. On the other side, the extent of combustion of model coke with CuO was higher than that with Co_3O_4. For example, the combustion % was as approximately 90 wt.% for CuO compared to 80 wt.% for Co_3O_4 at 850 °C, as demonstrated in Figures 6.3 and 6.6, respectively.

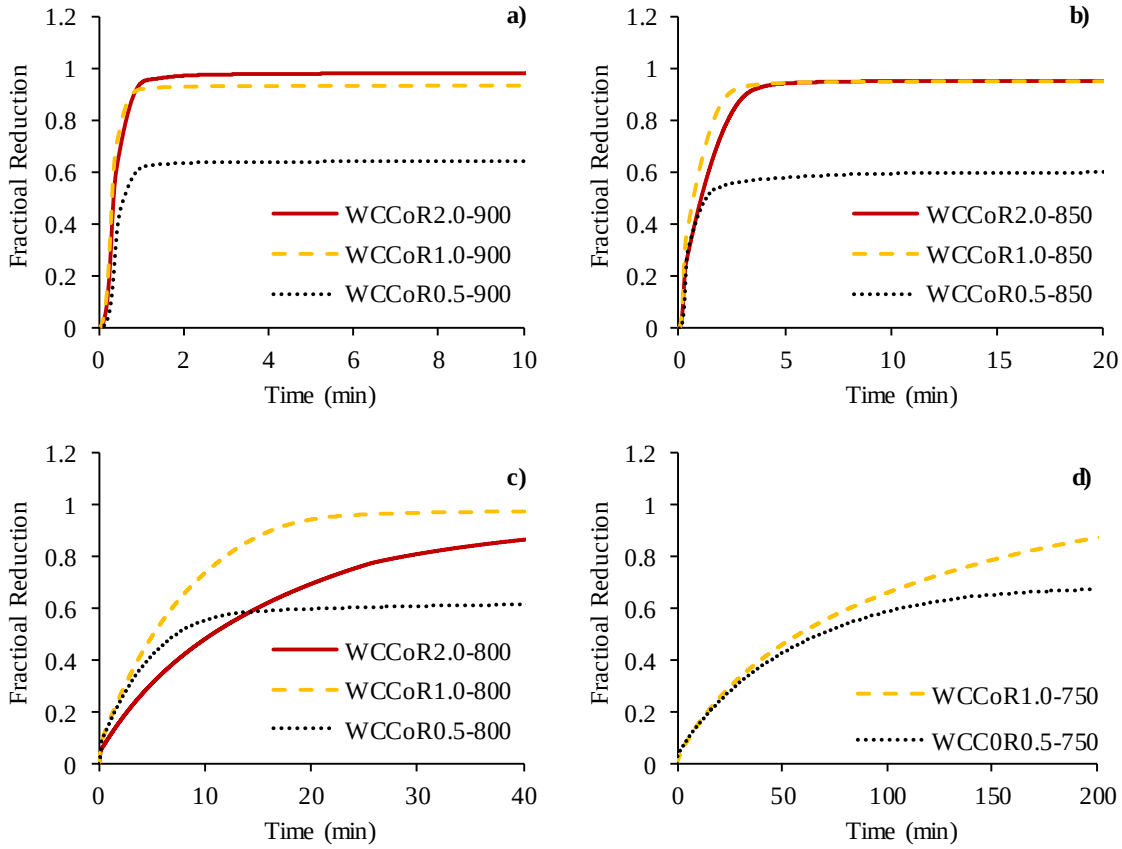


Figure 6.7. Fractional reduction of model coke with Co_3O_4 for various oxygen excess numbers (R = 0.5, 1.0, and 2.0) at various isothermal temperatures a) 900 °C, b) 850 °C, c) 800 °C, d) 750 °C.

A high fractional reduction at high isotherm temperatures in seconds is possible. However, for a fractional reduction of 0.9, 20 min is required 800 °C (R = 1.0 and 2.0). On the other hand, once the temperature decreased to 750 °C, the fractional reduction was only 0.8 after 200 min due to the low partial pressure of O_2 over Co_3O_4, about $1.0*10^{-3}$ at 750 °C, which is 6 times lower than that at 800 °C and 49 times lower than that at 850 °C [23]. As mentioned previously, a sufficient amount of Co_3O_4 is the utmost importance for the complete combustion. While there are no differences on the fractional reduction for the R = 1.0 and 2.0 at 850-900 °C, the fractional reduction has been negatively affected by using higher amount of oxygen excess number at 750 °C, seen Figure 6.7c.

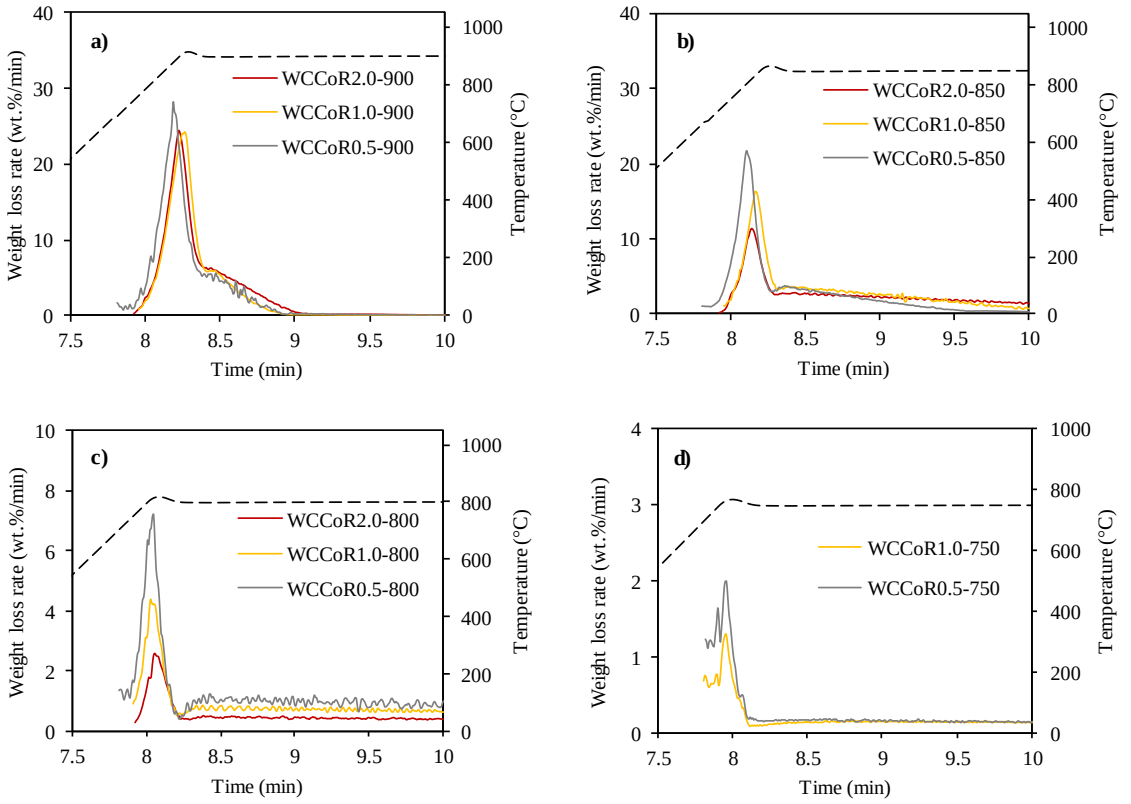


Figure 6.8. Weight loss rate of model coke (hard coke part) with Co_3O_4 for various oxygen excess numbers (R=0.5, 1.0, and 2.0) at various isothermal temperatures a) 900 °C, b) 850 °C, c) 800 °C, d)750 °C (line dashes represent the temperature profile).

Figure 6.8 shows that the maximum weight loss rate is observed at 900 °C as approximately 23 wt.%/min for the oxygen excess numbers of 1.0 and 2.0. However, the weight loss rates demonstrate a decreasing trend once the isotherm combustion temperature decreasing. Moreover, although the partial equilibrium pressure of O_2 over Co_3O_4 much higher than that over CuO at the same temperature [23, 175], the weight loss rates for Co_3O_4 are lower than that for CuO. While it is nearly about 25 wt.%/min for the combustion of model coke with CuO at 850 °C, it is only 15 wt.%/min for the combustion with Co_3O_4 at the same conditions. This differences may be attributed to the oxygen carrier capacity of oxygen carriers as each gram of model coke needs almost 23 g of CuO (for the reduction to Cu_2O) and 35 g of Co_3O_4 (for the reduction to CoO). Once the required amount of oxygen carrier increase, the interaction between model coke and the oxygen released from the oxygen carrier tends to take more time.

6.1.4 Chemical looping with oxygen uncoupling for the combustion of model coke with Mn_2O_3

The combustion of model coke was also investigated with Mn_2O_3, which can also show CLOU properties [23, 96, 266, 267] and the results are presented in Figure 6.9. Because of the relatively large amount of Mn_2O_3 requires, the experiments were investigated under 1.5 oxygen excess number instead of 2.0. The combustion of model coke with Mn_2O_3 is represented by the following reaction 6.3.

$$C_{71.9}H_{43.3} + 496.5Mn_2O_3 \rightarrow 331.0Mn_3O_4 + 71.9CO_2 + 21.6H_2O \qquad (6.3)$$

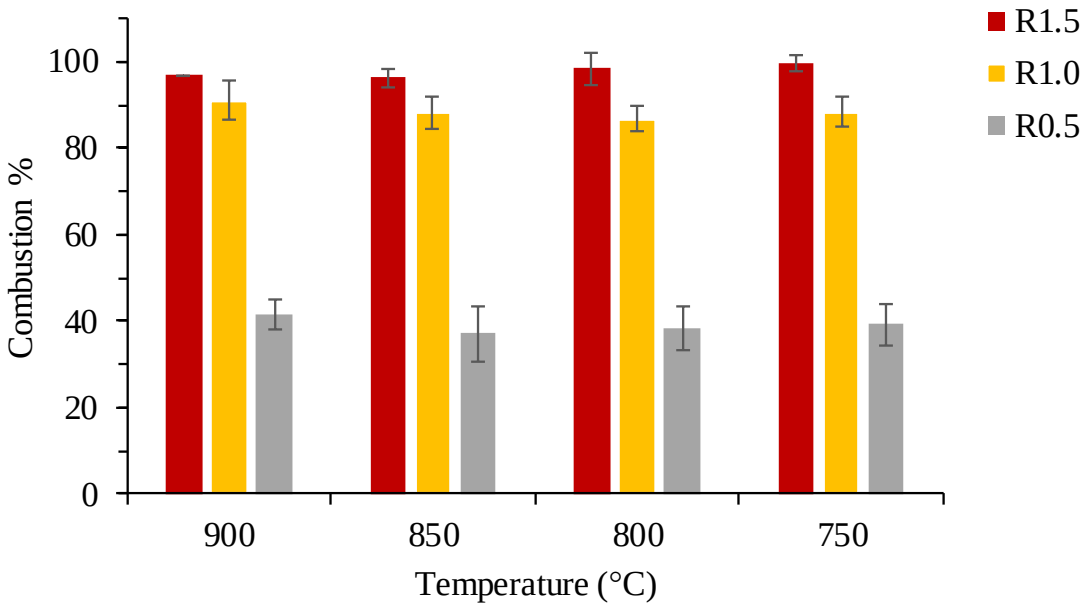


Figure 6.9. Combustion (wt.%) of model coke with Mn_2O_3 in various oxygen excess numbers (R = 0.5, 1.0, and 1.5) at various isothermal temperatures (750-900 °C).

It is possible to reach almost full combustion using the required amount of Mn_2O_3 from 750 °C to 900 °C, shown in Figure 6.9. The extent of combustion was almost 100 wt.% once the oxygen excess was number above 1.5. When the oxygen excess number was kept at the stoichiometrical amount, 1.0, the extent of combustion was in the range 87-92 wt.%. Again, as expected, when insufficient oxygen carrier was present, such as for an oxygen excess number of 0.5, the extent of combustion was below 50 wt.% (Figure 6.9).

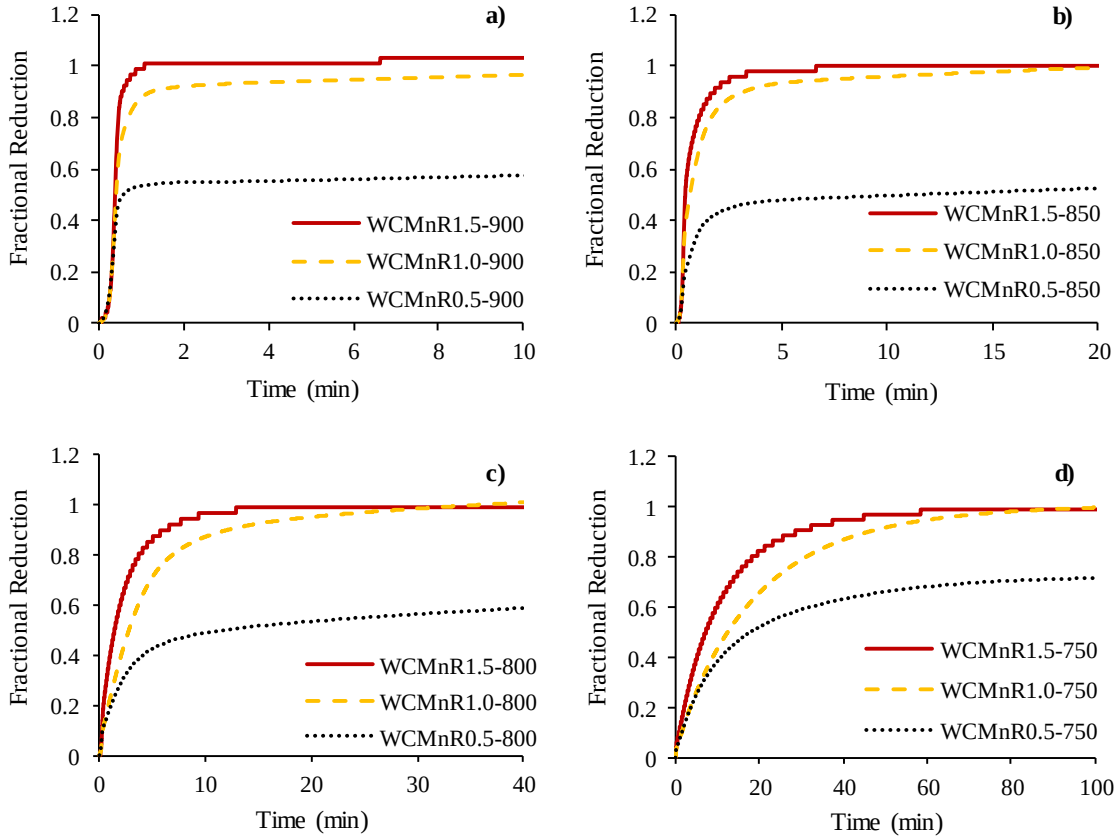


Figure 6.10. Fractional reduction of model coke with Mn_2O_3 for various oxygen excess numbers (R = 0.5, 1.0, and 1.5) at various isothermal temperatures a) 900 °C, b) 850 °C, c) 800 °C, d) 750 °C.

The fractional reductions of model coke with Mn_2O_3 for the different oxygen excess numbers and temperatures are presented in Figure 6.10. The fractional reductions reach 1.0 in less than 40 min, which is quite similar to the time for coke combustion in the conventional regenerator, approximately 30-60 min [268] at 750 °C with the stoichiometrically required amount of oxygen carrier, R = 1.0, or more, R = 1.5. Additionally, the required time to reach the fractional reduction of 1.0 with Mn_2O_3 (about 40 min) was lower than that with both CuO (about 60 min) and Co_3O_4 (about 200 min). This may be attributed to the partial pressure of oxygen over Mn_2O_3, which is much higher than that over both CuO and Co_3O_4 at the same temperature [23, 175]. The increase in combustion temperature enhanced the fractional reduction as for CuO and Co_3O_4. For instance, the fractional reduction reached 1.0 in seconds at 900 °C, in 5 min at 850 °C, and in 10 min at 800 °C (R = 1.0 and 1.5). In contrast to CuO and Co_3O_4, the increase in the oxygen excess number enhanced the fractional reduction of model coke with the

oxygen carrier, seen in Figure 6.10. This increase might be attributed to the amount of excess oxygen number.

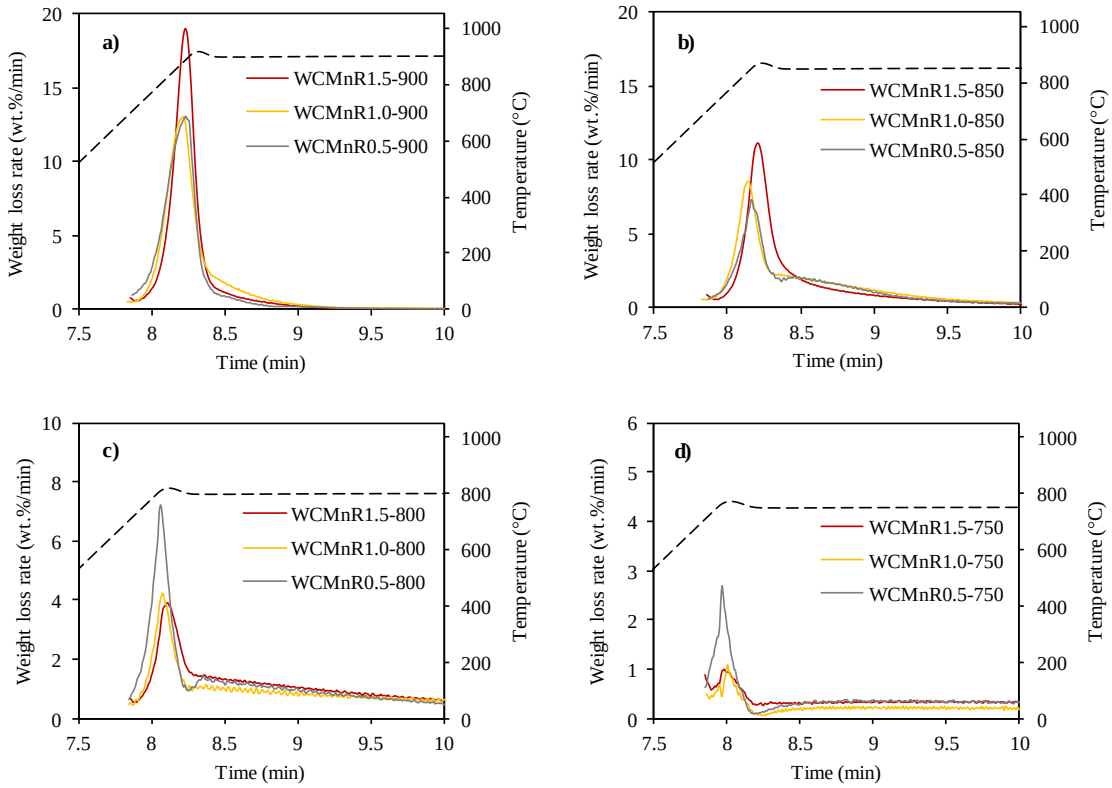


Figure 6.11. Weight loss rate of model coke (hard coke part) with Mn_2O_3 for various oxygen excess numbers (R=0.5, 1.0, and 1.5) at various isothermal temperatures a) 900 °C, b) 850 °C, c) 800 °C, d)750 °C (line dashes represent the temperature profile).

Figure 6.11 demonstrates the weight loss rate for the combustion of model coke with Mn_2O_3 at different isothermal combustion temperatures. The weight loss rate decrease with temperature decreasing from 15 wt.%/min at 900 °C to 1.0 wt.%/min at 750 °C for the oxygen excess number of 1.0. The weight loss rates demonstrate a long shoulder after the intensive initial weight decrease. The intensive peak may be attributed to the combustion of model coke with the gas phase oxygen released during the reduction of Mn_2O_3 to Mn_3O_4. The shoulder, after the sharp gas-solid combustion peak, may be attributed to the combustion reaction on the interface of solid model coke and solid Mn_3O_4 reducing to MnO obtained as a wide shoulder. The similar solid-solid reaction has already been observed for the combustion of char with Mn-based oxygen carriers [102, 153, 175, 259].

In summary, the TGA studies demonstrated that complete combustion is possible once the stoichiometrically required amounts of oxygen carriers (CuO, Co_3O_4, and Mn_2O_3) and sufficient time have been provided. Additionally, higher than 90 wt% combustion of model coke was achieved with CuO and Mn_2O_3 at 750 °C for 40–60 min, almost similar conditions used in the conventional regenerator of FCC units.

6.2 CLC of MAT coke with oxygen carriers in a fixed-bed mass spectroscopy (FxB-MS) unit

The combustion tests of model coke with oxygen carriers in the TGA equipment revealed productive results in terms of the optimum combustion temperature, oxygen excess number, and oxygen carriers. Using these optimum conditions the CLC tests were repeated with coke deposited on ECat (MC – derived from the cracking tests of n-hexadecane over ECat in MAT reactor) with oxygen carriers in a fixed-bed reactor equipped with online mass spectroscopy (FxB-MS).

6.2.1 Baseline experiments of the model and MAT coke in FxB-MS unit

6.2.1.1 Comparison of TGA and fixed-bed combustion profiles of model coke with CuO

In order to identify a relationship between TGA and FxB-MS results, the CLC test of model coke with CuO carried out in TGA was repeated using an FxB-MS unit under the same experimental conditions. As seen from Figure 6.12-a, the derivative weight (red line) consisted of three weight loss steps, the first one (S-1) had approximately 1.1 wt.% at the temperatures between 420-600 °C, which must be attributed to removing volatiles from coal and combustion with solid CuO. The low weight loss for the first step may explain the type of model coke, which is a low volatile semi-anthracite coal. As lower volatile matter contents produce lower CO_2 for the first stage as demonstrated by Wang et al. [262] who investigated the combustion of coals (LPS and YQ) having different ranks with $CuFe_2O_4$ as an oxygen carrier. The second one (S-2) had about 1.2 wt.% at the temperatures 600-780 °C, which may come to exist by solid-solid interaction of model coke and CuO. The final one (S-3) was approximately 10.4 wt.% at the temperatures 780-850 °C, which must be due to the combustion of fixed carbon with the gas phase oxygen

released from CuO due to auto-decomposition of it (from CuO to Cu_2O) at 790 °C [265], having a partial pressure of oxygen about $1.0*10^{-3}$ at 800 °C [23].

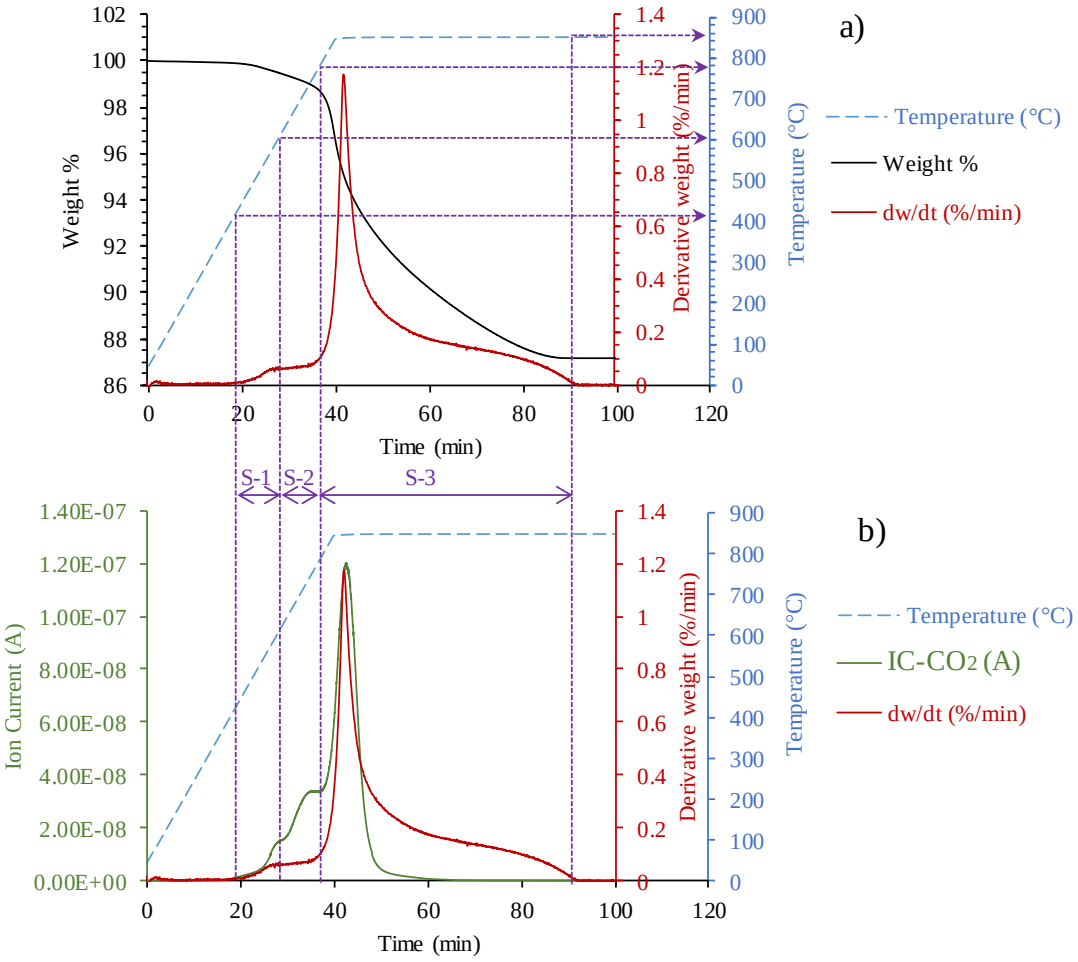


Figure 6.12. Comparison of TGA and FxB-MS combustion profiles of model coke with CuO at 850 °C under N_2 atmosphere, **a)** TGA results, **b)** comparison of TGA and FxB-MS results ("IC" refers to Ion Current measured by MS).

These findings are the same as Shabani et al. [265] who investigated the CLC of ash-free coal with CuO. According to Shabani et al. [265], CuO reduction induced by volatile matters released from the coal occurred at a temperature around 400 °C and char combustion induced by oxygen released from CuO at about 800 °C just after auto-decomposition of CuO. A slight loss in mass, observed from 450 to 790 °C, was attributed to solid-solid interaction of char and CuO particles [265]. Similarly, the three TGA reaction steps for the combustion of another coal, Illinois #6, with CuO were also presented by Siriwardane et al. [102], where the steps were defined at 300-460 °C, 460-

550 °C and 550-810 °C. Furthermore, the investigation of LPS coal combustion with Fe_2O_3 has occurred in three reaction stages, as presented by Baowen et al. [261].

In Figure 6.12-b, the weight derivative line (red line) obtained in TGA experiments were compared with the CO_2 evaluation (green line) obtained from the FxB-MS unit. The CO_2 recorded by MS demonstrates three different steps, which are in line with the steps measured by the TGA experiments. However, the derivative weight continued to decrease after 60 min, although no CO_2 released after that point. This further decrease may be attributed to excessive oxygen released from excess oxygen carriers due to the fact that some of the volatiles was removed from the mixture without combustion or adding a slightly higher oxygen carrier than required.

6.2.1.2 Identifying the products from the combustion of the model and MAT coke with CuO in FxB-MS unit

The CLC of both model and MAT coke with CuO were investigated at 850 °C under a N_2 atmosphere using the FxB-MS (Figure 6.13), with each combustion experiment repeated twice. The MS detected three main gases (a large amount of CO_2, and small amounts of CH_4 and H_2) released from the CLC of both model and MAT coke with CuO. Additionally, the intensity of the CO_2 peaks was about the same due to the fact that an equal amount of carbon was combusted in both experiments. The much lower ion current intensity derived from the uncombusted gases CH_4 and H_2 may be from either uncombusted volatiles removed from the MAT coke or the step where the solid-solid interaction occurs.

As mentioned previously, the combustion of model coke with CuO occurred in three steps at (i) 420-600 °C, (ii) 600-780 °C, and (iii) 780-850 °C (Figure 6.12 and 6.13-a), whilst the combustion of MAT coke with CuO occurred in one stage, which started from ~580 °C and accelerated after ~700 °C (Figure 6.13-b). The MAT coke deposited on the catalyst during the cracking reaction consisted of two main parts, soft coke (dichloromethane soluble) and hard coke (dichloromethane insoluble) [252, 269]. The former can be removed from the catalyst surface at low temperatures, but higher

temperatures and oxygen are required to remove the latter (hard coke) from the catalyst surface.

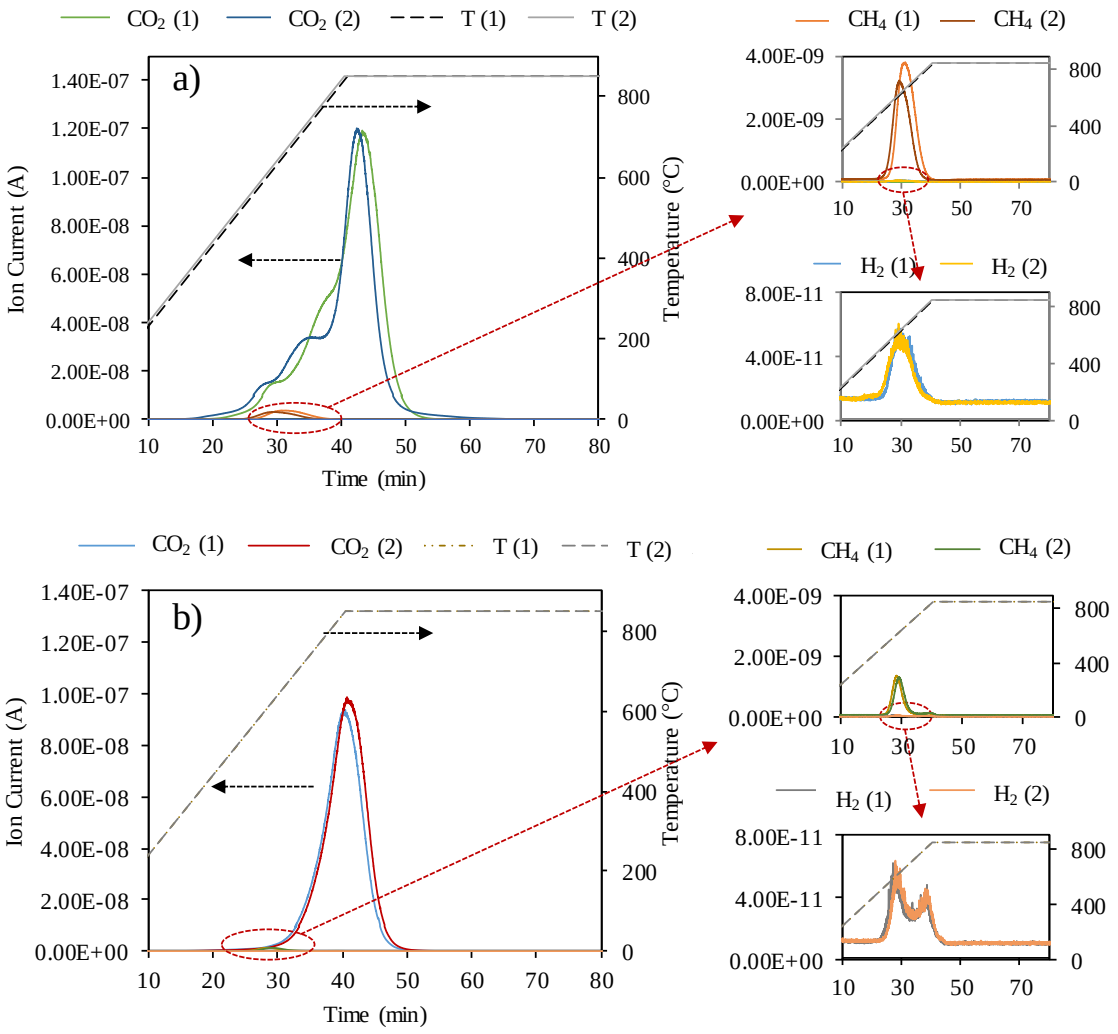


Figure 6.13. Comparison of the combustion products of a) model coke, which is a semi-anthracite, and b) MAT coke (MC), which was deposited on ECat during the cracking of n-hexadecane at 482 °C, using stoichiometrically required amount CuO in FxB-MS unit at 850 °C under N_2 atmosphere ("1 and 2" refers to repeating tests). The ratio of m/z was 44 for CO_2, 15 for CH_4, 2 for H_2 and 28 for N_2.

As presented in both Table 5.7 and Table 5.12 in Chapter 5, the amount of coke deposited on ECat was about 0.48 wt.% after the cracking of n-hexadecane, which was composed of 0.5 wt.% soft coke and 99.5 wt.% of hard coke. The combustion step for the soft coke was not, therefore, visible due to the low amount of soft coke. Furthermore, low-temperature combustion, (starting at ~580 °C and accelerating at ~700 °C) may be

attributed to the solid-solid interaction thanks to the dispersion of coke on the catalyst surface. Siriwardane et al. [175] noted that according to the positive Gibbs free energy analysis, the reaction between CuO and C can be favourable between 200-1000 °C even though CuO decomposition is not thermodynamically favourable below 713 °C. Therefore, the carbon in the coke may induce the Cu–O bond breaking process to initiate the combustion at a temperature of 580 °C. Similar findings, also presented by Siriwardane at al. [175] demonstrated the combustion of pure carbon with CuO occurred at 480 °C. Additionally, the shift on the CO_2 to the lower temperature for the combustion of MAT coke with CuO may also be attributed to the coke dispersion on the catalyst on the contrary of bulk model coke.

The combustion of model coke might have driven by the shrinking core model where the outer carbon combusts first and then the combustion continuous to inside [270]. Thus, a clear transition step due to the solid-solid interaction was observed for the combustion of model coke with CuO in Figure 6.13. In terms of MAT coke, the transition stage, however, connected with the combustion of hard coke with oxygen released from the oxygen carriers thanks to the coke dispersion on the catalyst surface, which enable high interaction surface of coke and CuO.

6.2.1.3 Calibration graph for converting of ion current (A) to the percentage of CO_2 (vol.%) in combustion flue gases

In order to present the combustion results in an understandable way, a calibration graph was drawn Ion Current vs volumetric ratio of CO_2. Each gas mixture having a specific CO_2 percentage demonstrated a specific Ion Current (A) value, as presented in Figure 6.14. When the ratio of CO_2 in the mixture kept same, the Ion Current measured by MS had a constant value. For example, the mixture having 6 vol.% of CO_2 gave an Ion Current of $1.61*10^{-8}$ A. Once the volumetric ratio of CO_2 increased to 10 vol.%, the Ion Current increased to $2.62*10^{-8}$ A. Thanks to the calibration graphs, the Ion Currents measured by MS with time could be converted to the volumetric CO_2 percentage in the output gas mixture. It is, therefore possible to calculate the volumetric flow rate of CO_2 in time using a constant carrier gas flow rate of N_2.

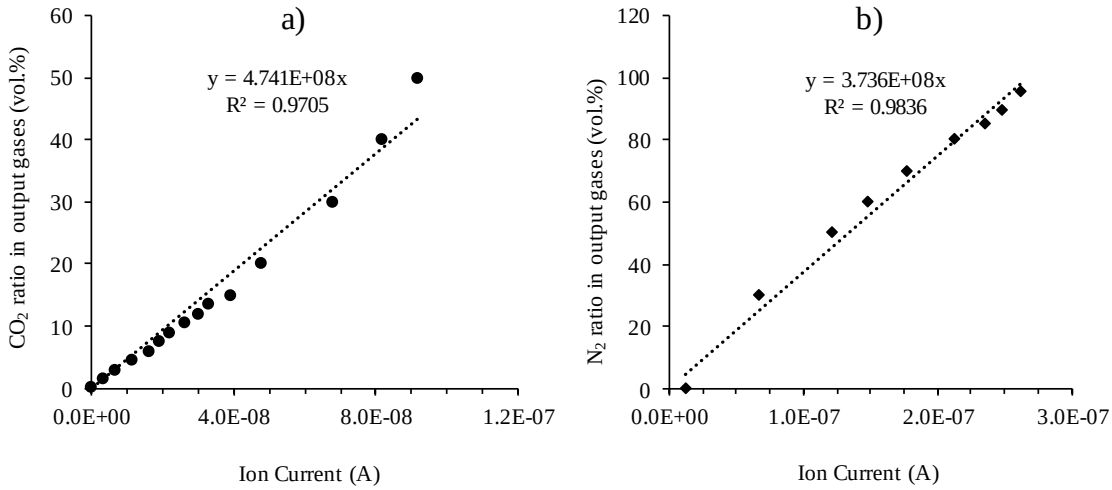


Figure 6.14. Calibration graph for the ion current to the a) percentage of CO_2 and b) percentage of N_2 in combustion gases.

6.2.1.4 Combustion behaviour of the model and MAT cokes with CuO in FxB-MS unit

It was important to compare the combustion behaviours of the cokes; (i) produced by the cracking of vacuum gas oil (VGO), which is a real feedstock, (ii) produced by cracking of model compound, n-hexadecane, and (iii) model coke, with CuO, as shown in Figure 6.15. The CO_2 release from the combustion of MAT coke (produced by the cracking of VGO) started at a temperature of 420 °C where the combustion of model coke (volatile matter) started. This first part of the combustion may, therefore, be attributed to the combustion of soft coke (in the MAT coke produced by VGO cracking) or volatiles (in model coke) with solid CuO. Furthermore, an apparent delay in the combustion of hard coke (produced by the cracking of VGO) can be observed compared with that of n-hexadecane, which may be attributed to different coke type produced by different cracking feeds, VGO and n-hexadecane. As the properties of coke such as location, nature and amount depend on the feed composition, catalyst type and reaction conditions [271]. Cerqueira et al. [272] noted that cokes deposited on the catalyst during the cracking reactions may be defined in five main groups; catalytic coke, catalyst to oil coke, thermal coke, additive coke, and contaminant coke.

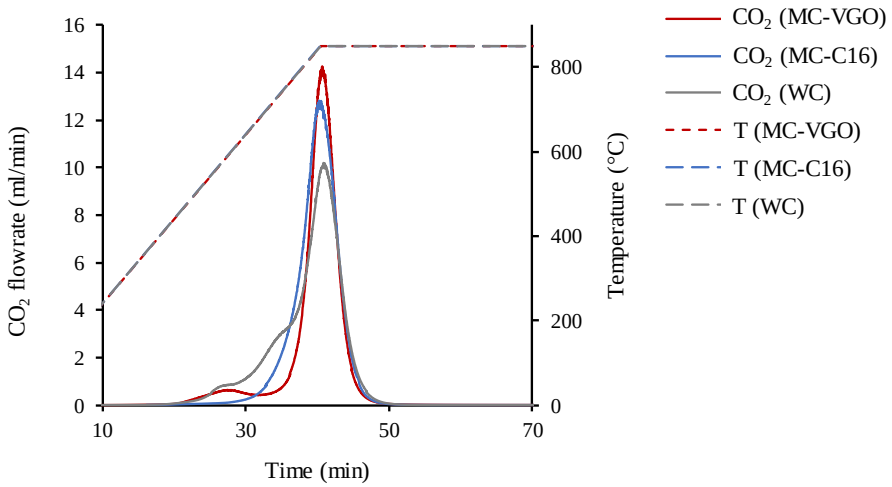


Figure 6.15. Comparison of the combustion behaviour of model and MAT coke with CuO in FxB-MS unit at 850 °C under N_2 atmosphere ("WC" refers to model coke, which is low volatile semi-anthracite Welsh coal, "MC-C16 and MC-VGO" refer to MAT coke which was deposited on ECat during the cracking of n-hexadecane (C16) and vacuum gas oil (VGO) at 482 °C).

Table 6.2. Combustion % of the model and MAT cokes with CuO in FxB-MS unit at 850 °C under N_2 atmosphere.

Coke source	Oxygen carrier	Temperature (°C)	$V_{CO2,Coke}$ [d] (ml)	$V_{CO2,MS}$ [e] (ml)	Combustion (vol.%)
WC [a]	CuO	850	80.5	77.5	96
MC-C16 [b]	CuO	850	78.6	78.2	99
MC-VGO [c]	CuO	850	71.9	71.1	99

[a] Model coke, low volatile semi-anthracite Welsh coal, [b] MAT coke deposited on ECat during the cracking of n-hexadecane (C16), [c] MAT coke deposited on ECat during the cracking of vacuum gas oil (VGO), [d] Volume of CO_2 calculated on the basis of carbon in coke, [e] Volume of CO_2 calculated by the integration of the lines presented in Figure 6.15.

Additionally, as demonstrated previously, the coke produced by the cracking of n-hexadecane contained a minimal amount of soft coke. However, complete combustion was achieved for the cokes provided by different kinds of feeds, VGO and n-hexadecane, using CuO as an oxygen supplier, as indicated in Table 6.2. Furthermore, high combustion (96 vol.%) was also achieved for the combustion of model coke with CuO under same conditions.

6.2.2 CLC of MAT coke deposited on ECat with bulk oxygen carriers in FxB-MS unit

6.2.2.1 Effect of the temperature on the CLC of MAT coke deposited on ECat

Although high temperatures (higher than 800 °C) are usually investigated for the combustion of solid fuels [153, 263-265, 273-275], it is preferable to 650-760 °C for the combustion of coke deposited on ECat [65, 272]. The CO_2 flowrates during the combustion of coke deposited on ECat with CuO for four different temperatures were presented in Figure 6.16, and the combustion % are indicated in Table 6.3.

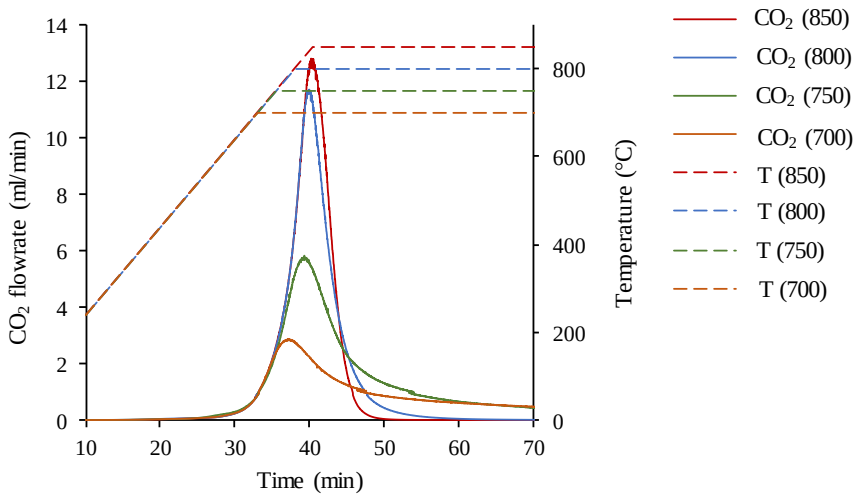


Figure 6.16. Effects of temperatures (700-850 °C) on the combustion of MAT coke with CuO in FxB-MS unit under N_2 atmosphere.

Figure 6.16 and Table 6.3 demonstrate that a decrease in the combustion temperature caused a decrease in combustion %. Whereas the combustion of coke with CuO reached a reasonably high value (higher than 90 vol.%) at the temperatures higher than 750 °C for 45 min, this was reduced to 59 vol.% at 700 °C. The required time to reach complete combustion at 700 °C is much higher than that at the temperatures higher than 750 °C. This decrease in the combustion may be attributed to the oxygen releasing rate of CuO being so much slower at lower temperatures [23, 97, 276, 277]. Due to the low partial pressure of oxygen at low temperatures, the CO_2 evolution demonstrated a long tail even after an hour. However, as clearly seen from Table 6.3, greater than 90 vol.% of coke deposited on ECat was be removed with bulk CuO at temperatures higher than 750 °C for

45 min which is within the range of standard regenerator conditions of conventional FCC units [65, 268, 272]. The identified products from the combustion of coke deposited on ECat with CuO at different temperatures are presented in Figure B1 in Appendix B.

Table 6.3. Combustion % of MAT coke with CuO in FxB-MS unit at a temperature ranges 850-700 °C under N_2 atmosphere.

Coke source	Oxygen carrier	Temperature (°C)	$V_{CO2,Coke}$ [a] (ml)	$V_{CO2,MS}$ [b] (ml)	Combustion (vol.%)
MC-C16	CuO	850	78.6	78.2	99
MC-C16	CuO	800	78.6	77.4	98
MC-C16	CuO	750	74.8	69.5	93
MC-C16	CuO	700	74.8	44.3	59

[a] volume of CO_2 calculated on the basis of carbon in the coke, [b] volume of CO_2 calculated by the integration of the graph for 45 min (25-70 min) presented in Figure 6.16.

6.2.2.2 Effect of the oxygen carriers on the CLC of MAT coke deposited on ECat

One of the temperatures (800 °C) tested in the previous section was selected to demonstrate the effect of different oxygen carriers, CuO, Co_3O_4, and Mn_2O_3, on the combustion of coke deposited on ECat under the same experimental conditions with the results presented in Figure 6.17 and Table 6.4.

Table 6.4. Combustion % of MAT coke with CuO, Co_3O_4, and Mn_2O_3 in FxB-MS unit at a temperature of 800 °C under N_2 atmosphere.

Coke source	Oxygen carrier	Temperature (°C)	$V_{CO2,Coke}$ [a] (ml)	$V_{CO2,MS}$ [b] (ml)	Combustion (vol.%)
MC-C16	CuO	800	78.6	77.4	98
MC-C16	Co_3O_4	800	75.6	68.7	91
MC-C16	Mn_2O_3	800	79.6	72.7	91

[a] volume of CO_2 calculated on the basis of carbon in the coke, [b] volume of CO_2 calculated by the integration of the graph for 70 min presented in Figure 6.17.

There was no, or minimal CO_2 observed due to the soft coke combustion with Co_3O_4 and CuO, was shown in Figure 6.17. On the other hand, the combustion of hard coke demonstrated variable times with the using of different oxygen carriers. The combustion of hard coke with Mn_2O_3 was slightly shifted to lower temperatures and completed earlier compared to the combustion with both CuO and Co_3O_4. The differences in the combustion

times and shifting on the CO_2 may be attributed to the oxygen releasing temperature and capacity of these oxygen carriers at the same conditions [23, 97, 276, 277].

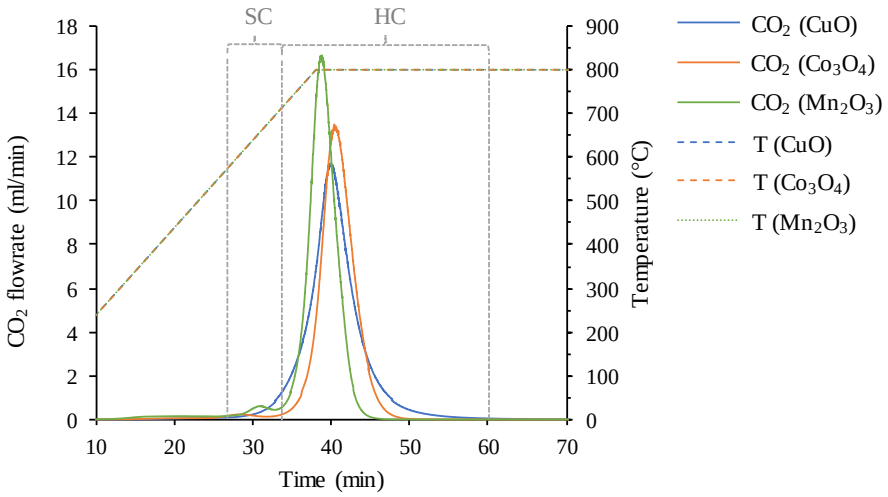


Figure 6.17. Effects of oxygen carriers, CuO, Co_3O_4, and Mn_2O_3, on the combustion of MAT coke in FxB-MS unit at 800 °C under N_2 atmosphere (SC: soft coke and HC: hard coke).

It was possible to reach higher than 90 vol.% coke combustion with CuO, Co_3O_4, and Mn_2O_3 for less than 30 min at a temperature of 800 °C, as shown in Table 6.4. These results are similar to the experimental results of model coke combustion with bulk oxygen carriers in a TGA presented in the previous section, in which approximately 12 min for the 90 wt.% combustion of model coke with Mn_2O_3, about 15 min for the 90 wt.% combustion of model coke with Co_3O_4, and roughly 19 min for the 100 wt.% combustion of model coke with CuO. The identified products from the coke combustion with CuO, Co_3O_4 and Mn_2O_3 at 800 °C are presented in Figure B2 in Appendix B.

6.3 CLC of coke deposited on reduced oxygen carrier impregnated ECat with oxidised oxygen carrier impregnated ECat in FxB-MS and FsB-MS units

In the previous section, the coke deposited on ECat was combusted with bulk oxygen carriers, CuO, Co_3O_4 and Mn_2O_3. However, as suggested in the proposed CLC-FCC unit, it is important to identify the combustion of coke deposited on reduced oxygen carriers impregnated ECat (coming from the FCC riser) with oxidised oxygen carriers impregnated ECat (coming from the air reactor). Therefore, the coke deposited on I-Cu/ECat and I-Mn_3O_4/ECat during the cracking of n-hexadecane was combusted using

their oxidised states impregnated ECat catalysts, I-CuO/ECat and I-Mn_2O_3/ECat, respectively. The coke deposited on I-CoO/ECat was not investigated due to its detrimental effect on cracking described above.

6.3.1 CLOU properties of oxidised oxygen carriers impregnated ECat

The CLOU properties of I-CuO/ECat and I-Mn_2O_3/ECat were investigated and compared with those of bulk CuO and Mn_2O_3, respectively. The m/z ratios (32 and16) were used for the determination of O_2 released by oxygen carriers. There was no other gas in the system, which can overlap with the O_2 line. Figure 6.18-a demonstrates that oxygen release started at ~510 °C, and linearly increased with temperature until ~750 °C, after that the rate of oxygen release increased rapidly. However, when the same amount of bulk CuO was tested, oxygen release started at ~780 °C (red line in Figure 6.18-a), and the rate was constant until 800 °C. These tests substantiate previous findings [23, 97, 265] in which the auto-decomposition of CuO to Cu_2O starts at ~790 °C with a partial pressure of oxygen of about $1.0*10^{-3}$.

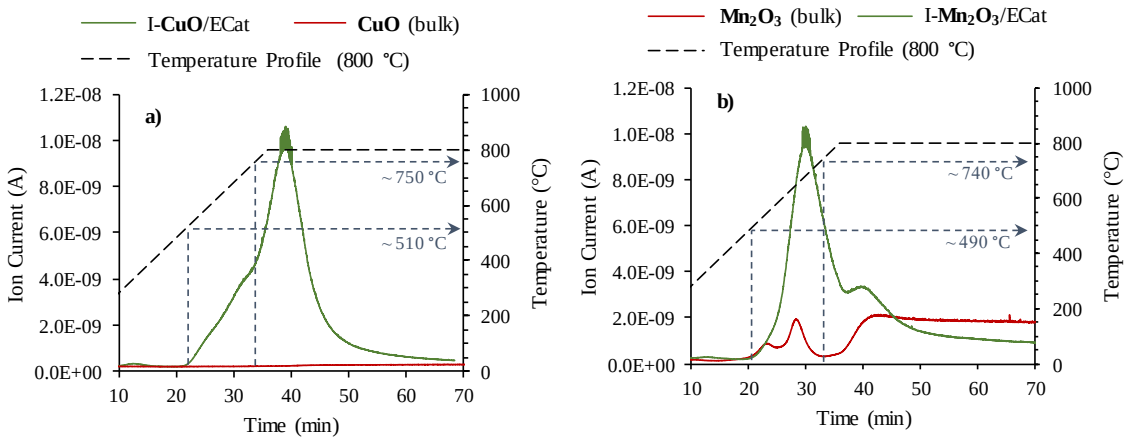


Figure 6.18. Comparison of chemical looping oxygen uncoupling (CLOU) properties of a) bulk CuO and I-CuO/ECat, b) bulk Mn_2O_3 and I- Mn_2O_3/ECat, at 800 °C under N_2 atmosphere in FxB-MS unit.

As with I-CuO/ECat, the impregnation of Mn_2O_3 on ECat clearly enhanced the CLOU properties of Mn_2O_3 at the lower temperatures (Figure 6.18-b). The impregnation of CuO and Mn_2O_3 onto ECat clearly enhanced the oxygen releasing features of oxygen carriers at lower temperatures, which may be attributed to the dispersion of CuO and Mn_2O_3 on

the catalyst surface. In this new catalyst formulation, ECat may act as a support for the oxidised oxygen carriers impregnated ECat in the regenerator.

6.3.2 CLC of MAT coke deposited on I-Cu/ECat with I-CuO/ECat

The CO_2 evolution for the combustion of coke deposited on I-Cu/ECat demonstrated three main parts, as shown in Figure 6.19. The first part (290-560 °C) may be attributed to the combustion of soft coke with solid CuO impregnated on ECat, while the second and third parts (560-740 °C and 740 °C <) are a consequence of the combustion of hard coke with gas phase oxygen released from I-CuO/ECat.

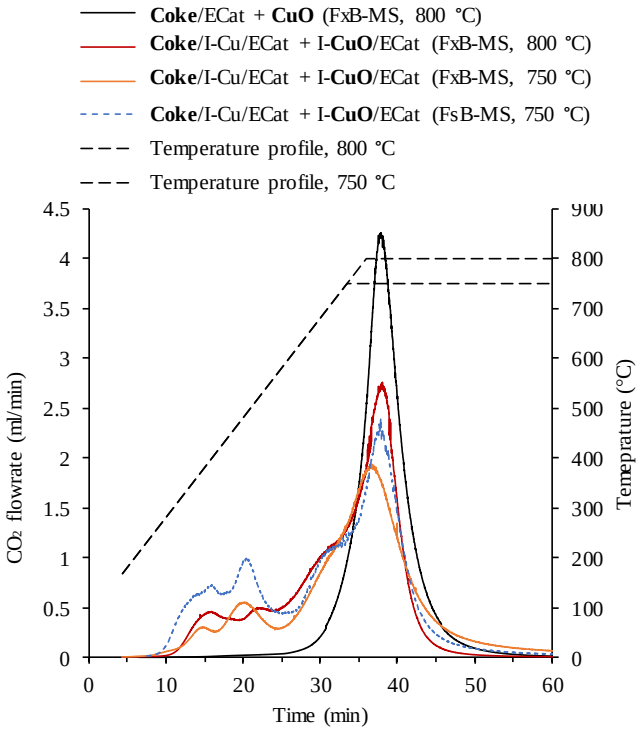


Figure 6.19. Combustion results of coke deposited on I-Cu/ECat with I-CuO/ECat at 800 and 750 °C under N_2 atmosphere in FxB-MS and FsB-MS units and the comparison with the combustion of coke deposited ECat with bulk CuO at 800 °C in FxB-MS unit (FxB: Fixed bed, FsB: Fluidised bed, MS: Mass spectroscopy).

Furthermore, once the test was investigated in the FsB-MS unit under a minimum fluidisation velocity, the CO_2 evolution shifted to lower temperatures where the soft coke combustion started at about 250 °C, but hard coke combustion started at 560 °C. Table 6.5 shows that the combustion of coke deposited on I-Cu/ECat with I-CuO/ECat reached

98 vol.% and 88 vol.% at the temperatures of 800 and 750 °C respectively in the FxB-MS unit for 45 min. Furthermore, the combustion was found to increase 96 vol.% at 750 °C for 45 min when the FsB-MS unit used instead of FxB-MS unit.

Table 6.5. Combustion % of coke deposited on I-Cu/ECat with I-CuO/ECat at 800 and 750 °C under N_2 atmosphere in FxB-MS and FsB-MS units, and the comparison with the combustion of coke deposited ECat with bulk CuO at 800 °C in FxB-MS unit.

Coke source	Oxygen carrier	Reactor	T^c (°C)	$V_{CO2,Coke}{}^d$ (ml)	$V_{CO2,MS}{}^e$ (ml)	Combustion (vol.%)
Coke/ECat [a]	**CuO** (bulk)	FxB-MS	800	27.7	27.2	98
Coke/I-Cu/ECat [b]	I-**CuO**/ECat	FxB-MS	800	29.9	29.2	98
Coke/I-Cu/ECat [b]	I-**CuO**/ECat	FxB-MS	750	30.1	26.4	88
Coke/I-Cu/ECat [b]	I-**CuO**/ECat	FsB-MS	750	33.1	31.8	96

[a] Coke deposited on ECat during cracking of n-hexadecane. [b] Coke deposited on Cu impregnated ECat during the cracking of n-hexadecane. [c] Combustion temperature. [d] Volume of CO_2 calculated on the basis of carbon in coke measured by LECO. [e] Volume of CO_2 calculated by the integration of the graph presented in Figure 6.19 for 45 min (between 5-50 min).

6.3.3 CLC of MAT coke deposited on I-Mn_3O_4/ECat with I-Mn_2O_3/ECat

Due to the combustion of soft coke (32.8 wt.% shown in Table 5.12, Section 5.3.2.2), the combustion of coke deposited on I-Mn_3O_4/ECat with I-Mn_2O_3/ECat started at about 290 °C in FxB-MS unit (Figure 6.20). The combustion of hard coke was initiated at about 510 °C thanks to the oxygen released from I-Mn_2O_3/ECat (demonstrated in Figure 6.18-b) and reached a maximum value at about 610 °C. When the test was repeated in FsB-MS, the CO_2 evolution was also shifted to lower temperatures, as shown in Figure 6.20.

Table 6.6. Combustion % of coke deposited on I-Mn_3O_4/ECat with I-Mn_2O_3/ECat at 800 and 750 °C under N_2 atmosphere in FxB-MS and FsB-MS units and the comparison with the combustion of coke deposited ECat with bulk Mn_2O_3 at 800 °C in FxB-MS unit.

Coke source	Oxygen carrier	Reactor	T^c (°C)	$V_{CO2,Coke}{}^d$ (ml)	$V_{CO2,MS}{}^e$ (ml)	Comb. (vol.%)
Coke/ECat [a]	**Mn_2O_3** (bulk)	FxB-MS	800	20.7	19.3	93
Coke/I-**Mn_3O_4**/ECat [b]	I- **Mn_2O_3**/ECat	FxB-MS	800	26.1	24.0	92
Coke/I-**Mn_3O_4**/ECat [b]	I- **Mn_2O_3**/ECat	FxB-MS	750	29.9	25.6	87
Coke/I-**Mn_3O_4**/ECat [b]	I- **Mn_2O_3**/ECat	FsB-MS	750	33.1	31.1	94

[a]Coke deposited on ECat during cracking of n-hexadecane. [b] Coke deposited on Cu impregnated ECat during the cracking of n-hexadecane. [c] Combustion temperature. [d] Volume of CO_2 calculated on the basis of carbon in coke measured by LECO. [e] Volume of CO_2 calculated by the integration of the graph presented in Figure 6.20 for 45 min (between 5-50 min).

The combustion % of coke deposited on I-Mn_3O_4/ECat with I-Mn_2O_3/ECat reached about 92 vol.% and 87 vol.% at the temperatures of 800 and 750 °C, for 45 min respectively in FxB-MS unit. Furthermore, it increased to 94 vol.% at 750 °C for 45 min once the combustion occurred in the FsB-MS unit, as shown in Table 6.6.

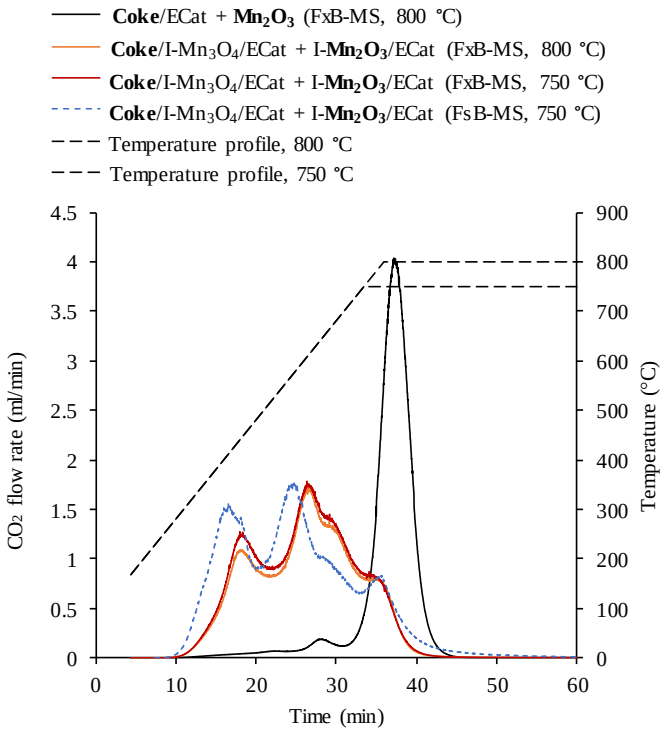


Figure 6.20. The combustion results of coke deposited I-Mn_3O_4/ECat with I-Mn_2O_3/ECat at 800 and 750 °C under N_2 atmosphere in FxB-MS and FsB-MS units, and the comparison with the combustion of coke deposited ECat with bulk Mn_2O_3 at 800 °C in FxB-MS unit (FxB: Fixed bed, FsB: Fluidised bed, MS: Mass spectroscopy).

As suggested in the proposed CLC-FCC concept, the coke deposited on I-Cu/ECat and I-Mn_3O_4/ECat was successfully regenerated using the stoichiometrically required amount of oxidised oxygen carrier impregnated ECat (I-CuO/ECat and I-Mn_2O_3/ECat) at temperatures of 750 and 800 °C for 45 min, which are the typical regenerator conditions in the conventional FCC units where the coke is cleaned with air [65, 268, 272]. Siriwardane et al. [102] noticed that there was no significant effect on the CLC reaction of coal with CuO under N_2 or CO_2 atmosphere which means that the results collected in this study may efficiently transfer for use in the proposed CLC-FCC concept where the fluidisation gas in the regenerator must be CO_2 instead of air or N_2. The CLC tests were investigated under a temperature profile having a heating rate of 20 °C/min although the

coke deposited on FCC catalyst is immediately faced with temperatures of 750 °C when it is circulated to the regenerator. The regeneration time for the coke (deposited on reduced oxygen carriers modified ECat) with oxygen carriers is, therefore, likely to be shorter than the value measured in this study.

6.3.4 Combustion behaviour of MAT coke with air, bulk-CuO and I-CuO/ECat

Combustion behaviours of MAT coke with air, bulk-CuO and CuO impregnated ECat (I-CuO/ECat) are compared in Figure 6.21. The combustion of coke with air started at about 350 °C, reached a maximum level at 700 °C and completed in 25 min. Additionally, the combustion of coke with bulk CuO reached a reasonably high value (93 vol.%) at the temperature of 750 °C for 45 min. However, the combustion with bulk CuO started much later temperature than that with air. On the other hand, using CuO impregnated ECat (I-CuO/ECat) as an oxygen supplier, the combustion of coke started earlier temperatures than bulk CuO as clarified before. The combustion value reached about 96 vol.% at 750 °C thanks to the enhancement on CLOU properties of CuO after impregnated on ECat. Furthermore, the combustion completed once the I-Cu/ECat used as an oxygen supplier compared with bulk CuO.

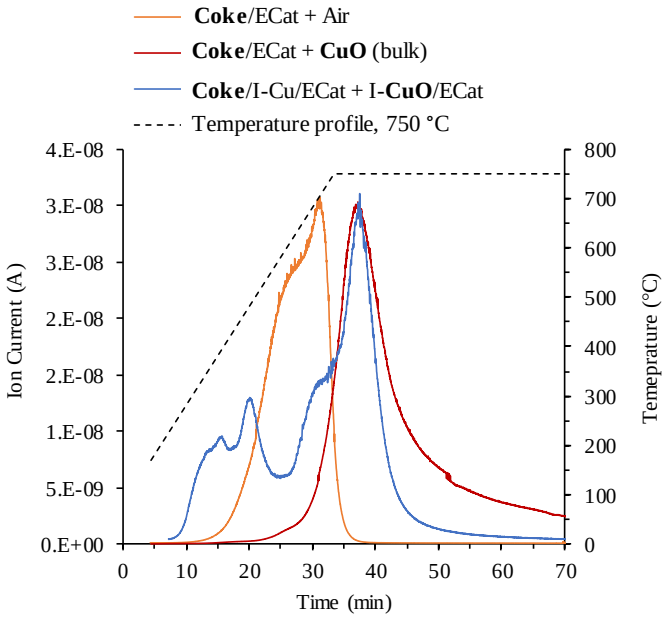


Figure 6.21. Combustion behaviour of coke using air, bulk-CuO, and CuO impregnated ECat (I-CuO/ECat) at 750 °C.

6.4 Summary

In summary, the TGA studies demonstrated that complete combustion of model coke (semi-anthracite coal) is possible once the stoichiometrically required amounts of oxygen carriers (CuO, Co_3O_4 and Mn_2O_3) and sufficient time have been provided. Additionally, a greater than 90 wt.% combustion of model coke was achieved with CuO and Mn_2O_3 at 750 °C for 40–60 min, which are the similar conditions used in the conventional regenerator of FCC units. Furthermore, the CLC tests of the coke deposited on ECat demonstrated higher than 90 wt.% combustion with bulk CuO, Co_3O_4 and Mn_2O_3, at a temperature of 800 °C for 30 min using FxB-MS unit.

The proposed CLC-FCC concept suggests that the coke deposited on reduced oxygen carriers impregnated catalyst must be regenerated by the oxidised oxygen carriers modified catalysts. As it was first demonstrated that with the impregnation of oxidised oxygen carriers on ECat, the oxygen releasing from the impregnated oxygen carriers were conducted at relatively low temperature when compared with the bulk oxygen carriers. Therefore, the CLC of coke deposited on I-Cu/ECat, and I-Mn_3O_4/ECat with the stoichiometrically required I-CuO/ECat and I-Mn_2O_3/ECat resulted in 90 vol.% combustion at 750 °C for 45 min in both FxB-MS and FsB-MS units. The conditions achieved for the 90 vol.% combustion in FsB-MS unit are similar to the conditions used in the conventional regenerator of FCC units.

Chapter 7

Selective Low Temperature CLC of Higher Alkanes with Cu- and Mn-Oxides

Oil refineries account for approximately 4% of the global CO_2 emissions and Fluid Catalytic Cracking (FCC) units are responsible for roughly a quarter of these, and so it was considered that CO_2 capture via CLC could potentially be applied to FCC. Combustion to remove coke in the regenerator proceeds at ca. 700-800 °C in the air and, for CLC, this can be accomplished by adding oxygen carriers to FCC catalysts. The oxygen carrier would need to be effectively inert with respect to cracking at temperatures close to 500 °C. However, in tests using the standard microactivity reactor (MAT) for FCC, CLC of n-hexadecane occurred with CuO mechanically mixed with an FCC catalyst. The preliminary cracking results of n-hexadecane over FCC catalyst and CuO mixed FCC catalyst are presented in Table 7.1. This observation provided the motivation to investigate the applicability of low temperature CLC as a process for removing organic contaminants from hot gas streams.

Table 7.1. Preliminary results for n-hexadecane cracking using a CuO mixed a FCC catalyst.

Product distribution (mol % carbon)**	**Catalyst***	**CuO + Catalyst**
CO	<0.2 ± 0	<0.2 ± 0
CO_2	**<0.2** ± 0	**12** ± 1
C_{1-2}	1 ± 0	5 ± 1
C_{3-4}	31 ± 2	32 ± 1
C_{5-12}	27 ± 1	23 ± 2
C_{13-15}	1 ± 0	0 ± 0
Coke	7 ± 1	10 ± 1
Unconverted C_{16}	**33** ± 1	**17** ± 2
Sum	**100**	**100**

*FCC catalyst supplied by BASF (FCC #7075). **The product distributions are on a carbon basis since, on a mass basis, the yield of CO_2 includes oxygen.

7.1 Baseline experiments

In order to understand the cracking behaviour of the model liquid feeds prior to the addition of the oxygen carriers, baseline thermal cracking experiments were conducted at 482 °C. These tests demonstrated minimal cracking of the feeds with just 5 wt.% of n-hexadecane found to be converted to light gases C_1-C_6 hydrocarbons, with the remaining of n-hexadecane, as demonstrated in Table 7.2. n-Heptane was even less reactive with only 2 wt.% of the gases obtained.

Table 7.2. Thermal cracking results for n-hexadecane and n-heptane.

Fuel	**Cracked products (C_1-C_6, wt.%)**
n-hexadecane ($C_{16}H_{34}$)	5.0 ±0.4
n-heptane (C_7H_{16})	2.0 ±0.1

To ascertain the extent of methane CLC at 482 °C, a stoichiometric quantity of methane was tested with CuO. This resulted in minimal combustion of methane, with the resultant products composed of only 0.9 wt.% CO_2 and over 99 wt.% of unconverted methane (Table 7.3). This finding was expected from literature reports of methane CLC using CuO occurring at around 800 °C [113, 127, 131, 278].

Table 7.3. Combustion products from methane with CuO at 482 °C

Fuel	**CO_2 (%)**	**CH_4 (%)**
Methane (CH_4)	0.9 ±0.004	99.1 ±0.004

7.2 The effects of fuel to oxygen carrier equivalence ratio (ϕ)

The extent of CLC for-hexadecane and n-heptane with CuO and Mn_2O_3 are presented in Figure 7.1 with respect to the different equivalence ratios of fuel to the oxygen carriers, which were calculated on the basis of the reduction of CuO to Cu and Mn_2O_3 to MnO. Figure 7.1 shows that it is possible to achieve almost complete combustion for both n-hexadecane and n-heptane using CuO as an oxygen carrier in fuel rich conditions at $\phi \geq$ 1.3. However, when the fuel/CuO equivalence ratio is stoichiometric at 1.0, the extent of

combustion fell to 80 wt.% for n-hexadecane and 90 wt.% for n-heptane. This can be explained by the uneven dispersion of the liquid fuels across the oxygen carrier bed.

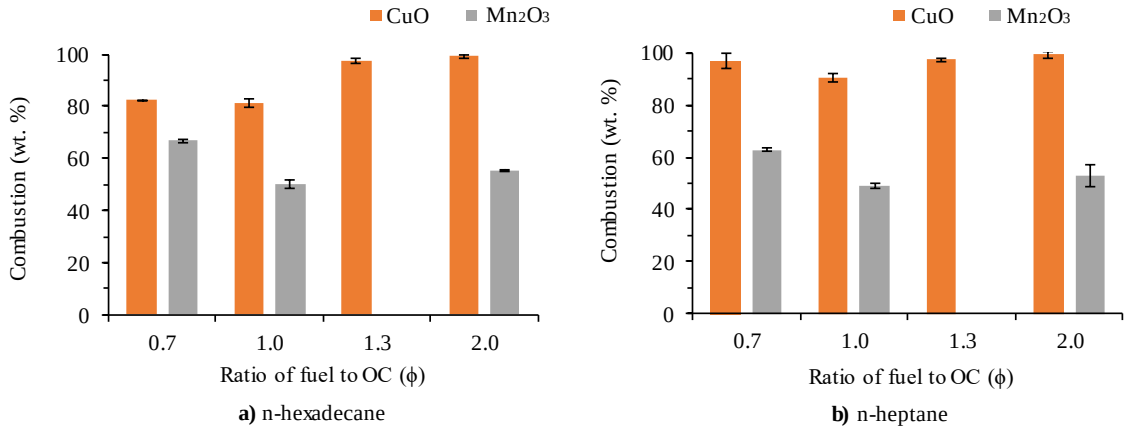


Figure 7.1. Combustion % of a) n-hexadecane; b) n-heptane over CuO and Mn_2O_3 for different fuel to oxygen carrier equivalence ratios (ϕ: 0.7, 1.0, 1.3, and 2.0) for 0.03 ml/min feed flow rate at 482 °C (the error bars represents the standard deviation calculated by triple experiments).

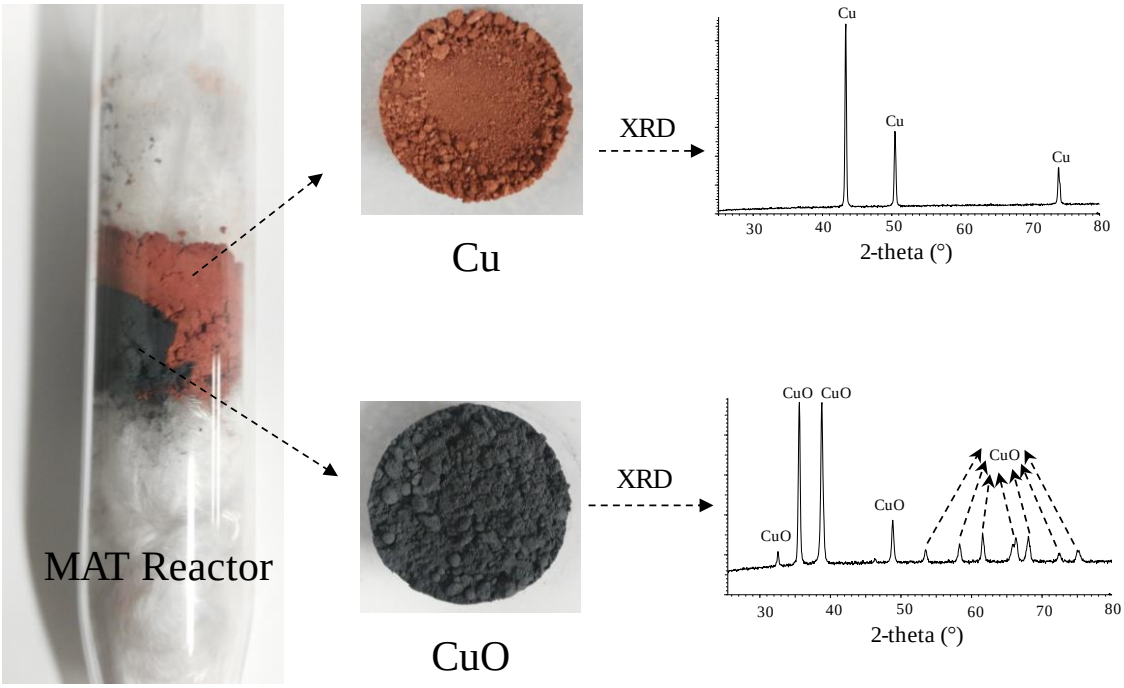


Figure 7.2. Oxygen carrier bed after the combustion of n-hexadecane at an oxygen carrier equivalence ratio of 1.0 for 0.03 ml/min feed flow rate at 482 °C.

Following the tests, the material on one side of the bed was observed to still be black in colour, along its whole length, indicating the presence of CuO, while the rest of the bed

was red, having clearly been reduced to Cu, as shown in Figure 7.2. This proves that some of the fuel may have passed through mainly the reduced part of the oxygen carrier bed instead of that containing oxidised oxygen carriers and consequently the theoretical extent of combustion is not attained. When the fuel to oxygen carrier equivalence ratio was decreased to 0.7 to give fuel lean conditions, the extent of combustion increased from 90 to 97 wt.% for n-heptane, but remained at close to 80 wt.% for n-hexadecane.

For Mn_2O_3, the extent of combustion fell from 56 to 50 wt.% as the equivalence ratio was decreased from 2.0 to 1.0 for both alkanes (Figure 7.1). Moving to fuel-lean conditions with an equivalence ratio of 0.7, the extent of combustion increased to 67 wt.% for n-hexadecane and 63 wt.% for n-heptane. The lower extent of combustion apparent with Mn_2O_3 can be attributed to the sequential reduction step of the oxygen carrier, $Mn_2O_3 \rightarrow Mn_3O_4 \rightarrow MnO$. Approximately one-third of the required oxygen comes from the first reduction step ($Mn_2O_3 \rightarrow Mn_3O_4$). The XRD results (Section 7.7) show that, while the Mn_2O_3 was almost entirely reduced, the recovered samples were composed of mixtures of Mn_3O_4 and MnO. Therefore, the lower combustion efficiencies compared to CuO arise from the slow second reduction step ($Mn_3O_4 \rightarrow MnO$). Furthermore, due to the similarity of the combustion at the equivalence ratio of 1.0-2.0, the combustion at the equivalence ratio of 1.3 was not investigated.

Moldenhauer et al. [169] mentioned that although the fuel conversion at the lowest temperatures (650-750 °C) is high enough, these temperatures are probably not very realistic, especially for commercial applications. Since oxygen release at such temperatures is so low that CLOU properties, which are an important benefit of this material, can be neglected [169]. However, although CuO decomposition is not thermodynamically favourable below 700 °C according to the Positive Gibbs free energy values, the reaction between CuO and C can be favourable between 200-1000 °C [175]. Furthermore, Siriwardane et al. [175] have noted that carbon can be reacted with CuO at 482 °C and with Cu_2O at 624 °C. Additionally, according to our calculations, CuO can reduce to Cu with the combustion of liquid fuels at a low temperature such as 482 °C. Although the CLOU properties are one of the most important features of oxygen carriers such as CuO and Mn_2O_3 for gas and solid fuels combustion, these properties may not be necessary for liquid fuels combustion.

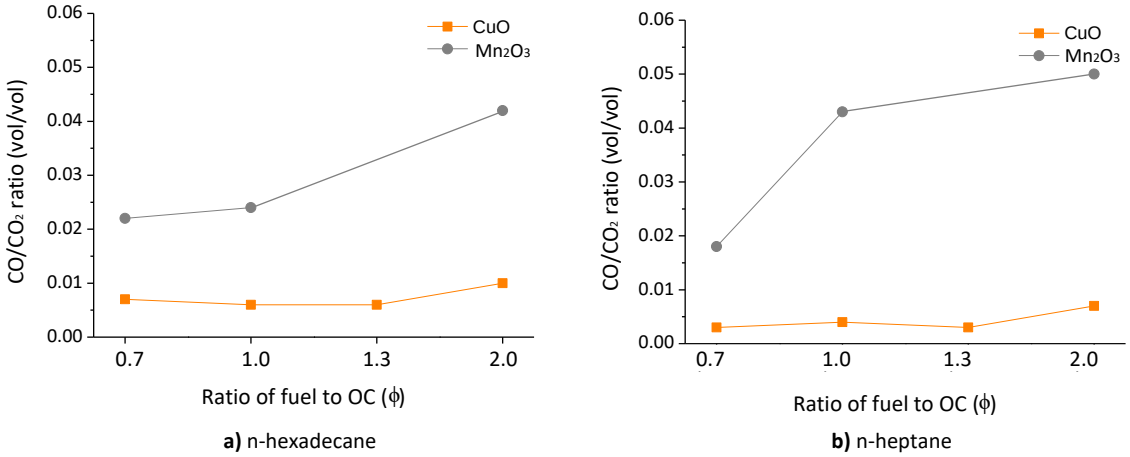


Figure 7.3. The volumetric ratio of CO/CO_2 for a) n–hexadecane; b) n-heptane combustion with CuO and Mn_2O_3 for 0.03 ml/min fuel feed flow rate at ϕ: 0.7, 1.0, 1.3, and 2.0 fuel to oxygen carrier equivalence ratios, 482 °C.

The low volumetric ratios of CO to CO_2 obtained from CLC are presented in Figure 7.3. However, the ratios are higher with Mn_2O_3 (<0.05) compared than for CuO (<0.01). Previous studies at higher temperatures have also observed low proportions of CO for diesel [279], kerosene [169], synthetic oil [168, 279], and asphalt-fuelled [155] combustion with oxygen carriers.

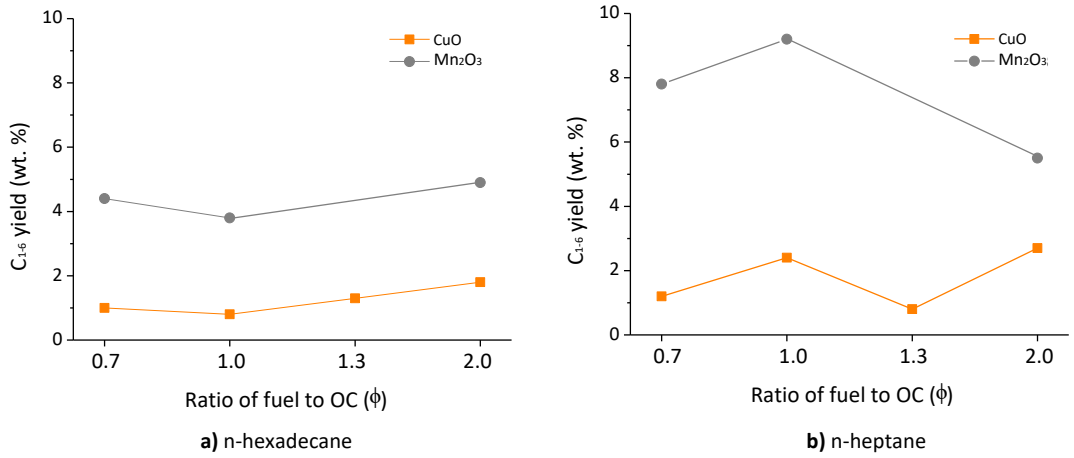


Figure 7.4. The yield of $C_{1\text{-}6}$ for a) n–hexadecane and b) n-heptane combustion, with CuO and Mn_2O_3 for 0.03 ml/min feed flow rate at ϕ: 0.7, 1.0, 1.3, and 2.0 fuel to oxygen carrier equivalence ratios, 482 °C.

Figure 7.4 shows that the yield of light gases, from methane to C_6 hydrocarbons, was around 1-2 wt.% for both n-hexadecane and n-heptane combustion with CuO. However,

it was about 4-6 wt.% for n-hexadecane and 6-9 wt.% for n-heptane combustion with Mn_2O_3. Based on the thermal cracking of n-hexadecane and n-heptane, whereas CuO has no significant effect on the cracking of n-heptane, it decreased the cracking of n-hexadecane, from 5 wt.% to 1 wt.%. On the other hand, while Mn_2O_3 increased the cracking of n-heptane, from 2 wt.% to 8 wt.%, it has no effect on the cracking of n-hexadecane.

7.3 Definition of gas and liquid products after combustion

At the fuel-rich experimental conditions (ϕ>1.0), even if the combustion is about 100%, it is possible to collect liquid fuel in the products due to the lean of oxygen supplied by oxygen carrier. As the excess amount of liquid fuel goes through the reactor without combustion after the oxygen consumed in the bed.

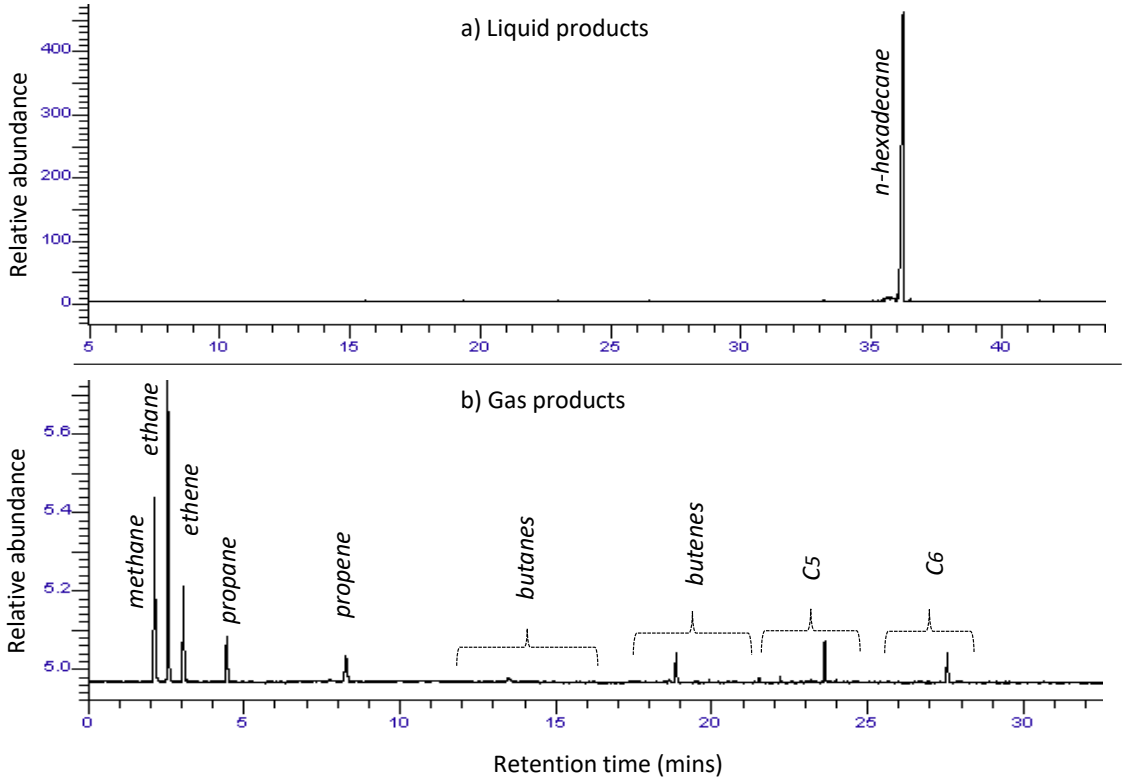


Figure 7.5. Gas chromatograms of the a) liquid products; b) hydrocarbon gas products obtained after n-hexadecane combustion with CuO for 0.03 ml/min at ϕ: 2.0 at 482 °C.

Figure 7.5 shows example chromatograms for both gas and liquid products from n-hexadecane combustion with CuO at fuel to oxygen carrier equivalence ratio of ϕ: 2.0 with a volumetric feed flow rate of 0.03 ml/min at 482 °C. The liquid products were clearly dominated by approximately 94 wt.% of unaltered n-hexadecane, with the products of thermal cracking composed of almost 6 wt.% of lower than C_{15}. The gaseous products consisted of small amounts of light hydrocarbon gases such as methane, ethane, ethene, and propane, lower than 2 wt.%, with the remaining products composed of CO_2 derived from the combustion of n-hexadecane with CuO.

7.4 Liquid fuel feed rate and residence time

The effects of fuel feed rate (residence time) were investigated using n-hexadecane with CuO and sand mixtures (SaCuO) at different volumetric feed and carrier gas (N_2) flow rates. The extent of combustion is presented in Figure 7.6 with respect to the volumetric feed flow rates (Figure 7.6a) and carrier gas flow rates (Figure 7.6b).

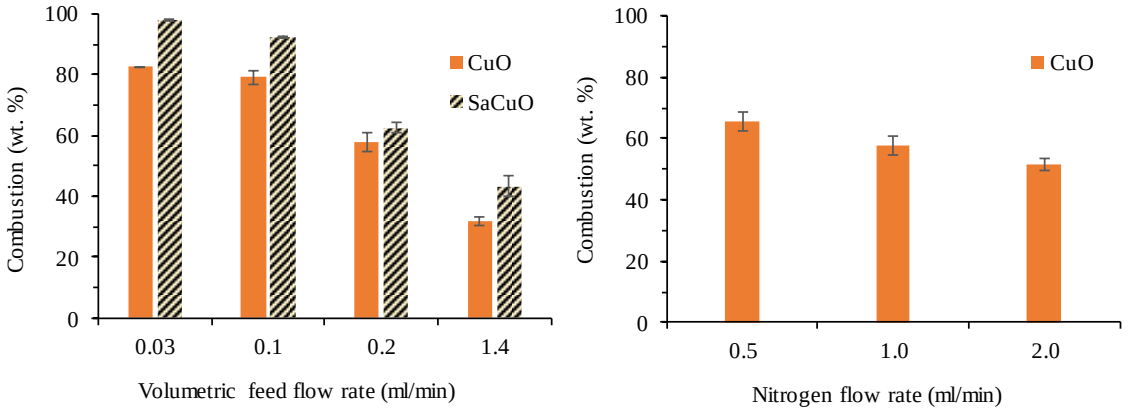


Figure 7.6. Combustion % of n-hexadecane over CuO and SaCuO a) at different volumetric feed flow rates (0.03, 0.1, 0.2, and 1.4 ml/min) for ϕ: 0.7 at 482 °C; b) Combustion % of n-hexadecane over CuO for ϕ: 0.7 at 0.2 ml/min, 482 °C using different carrier gas flow rates (0.5, 1.0, 2.0 ml/min).

As seen in Figure 7.6a, the extent of combustion was 80 and 99 wt.% with and without sand mixed CuO (SaCuO) at the lowest feed rate of 0.03 ml/min. Blending with sand increased the residence time and so dispersion of the liquid fuel within the oxygen carrier bed. The calculated vapour residence time of 13.1 s with a feed flow rate of 0.03 ml/min

was increased to 20.6 s by the dilution of the CuO in the sand. The same trend can be seen for the other volumetric flow rates. Increasing the feed rate from 0.03 ml/min gave lower conversions due to the residence time decreasing, but the effect was relatively minor until feed rates were higher than 0.1 ml/min. At higher rates, the decrease was greater, reflecting the decrease in residence time from 5.0 to 0.4 s with an increase in volumetric feed flow rate from 0.1 to 1.4 ml/min. A decrease in conversion was also brought about by increasing the carrier gas flow rate from 0.5 to 2 ml/min (Figure 7.6b). The relatively minor extent of this decrease is evidence that the injected n-hexadecane was completely vaporised, as in the vapour phase, increasing the carrier gas flow by this extent would only have increased the residence time from 2.5 to 2.8 s.

7.5 The effect of temperature

The effects of temperature were investigated to define the initiation combustion temperature of higher hydrocarbons with oxygen carriers, CuO. Figure 7.7 illustrates that the combustion of n-hexadecane with CuO fell from 80 to 40% as the temperature decreased from 560 to 380 °C, although the residence time increased from 2.4 to 3.0 s due to the temperature decreasing. The extent of combustion was negligible at 360 °C with a residence time of 3.2 s. Additional discussion about the dramatic decrease below 380 °C is presented in Section 7.8.

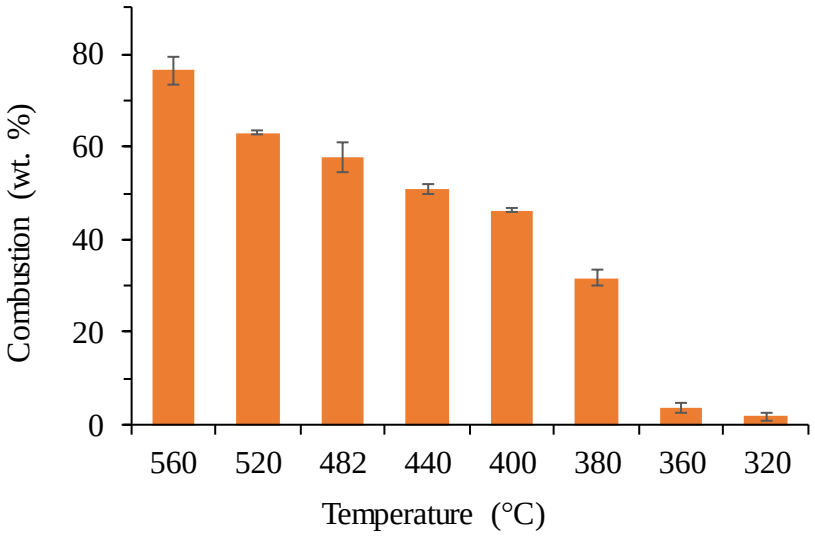


Figure 7.7. Combustion % of n-hexadecane over CuO for ϕ: 0.7 at 0.2 ml/min at eight different temperatures; 320, 360, 380, 400, 440, 480, 520, 560 °C.

7.6 Multiple cycles of n-hexadecane combustion with CuO

The results for the seven multi-cycle tests for n-hexadecane combustion at 482 °C, with re-oxidation after each step, both bulk oxygen carrier (CuO) and supported oxygen carrier (CuO/Al_2O_3) are shown in Figure 7.8. It was possible to achieve full combustion, clearly with complete reduction and re-oxidation being achieved for both bulk CuO and CuO/Al_2O_3 for the first three cycles. However, for bulk CuO, following the 4th and 5th cycles only 85 wt.% combustion occurred, probably due to the onset of sintering of the oxygen carrier (as shown in Figure 7.12 in the following section).

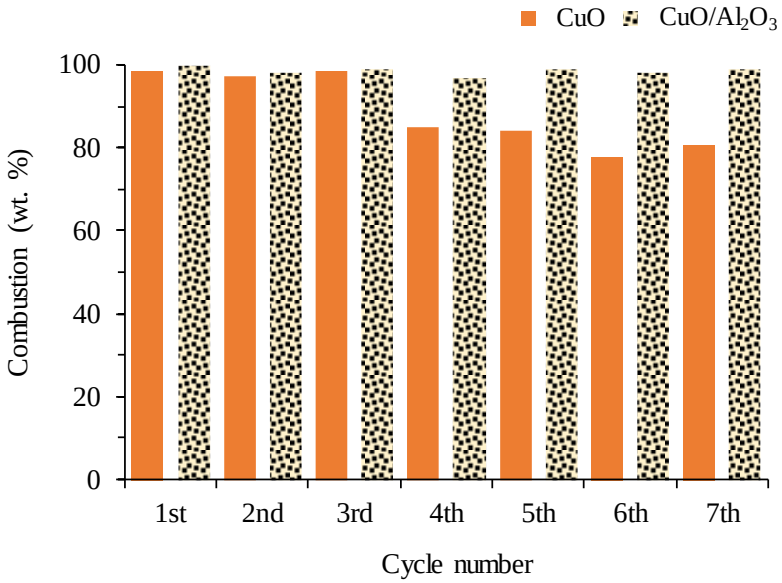


Figure 7.8. Combustion % of n-hexadecane over CuO for ϕ: 1.3 at 0.03 ml/min at 482 °C for seven cycles.

The extent of combustion reduced further to 78 wt.% after the 6th cycle as the extent of sintering increased. Even after increasing the oxidation temperature to 900 °C in the 7th cycle, only a small increase in combustion to 81 wt.% was observed, indicating that it was impossible to completely re-oxidise the oxygen carrier regardless of the temperature used. It is well-established that such sintering may be addressed using supports with suitable impregnation or co-precipitation preparation methods [102, 113, 183]. As seen in Figure 7.8, combustion efficiency of about 99 wt.% was achieved for all seven cycles once an Al_2O_3 supported CuO oxygen carrier was used in the combustion reaction instead

of bulk CuO. These results were confirmed by measuring the CO_2 evolved during the seven multiple cycles of combustion via mass spectroscopy, as presented in Figure 7.9.

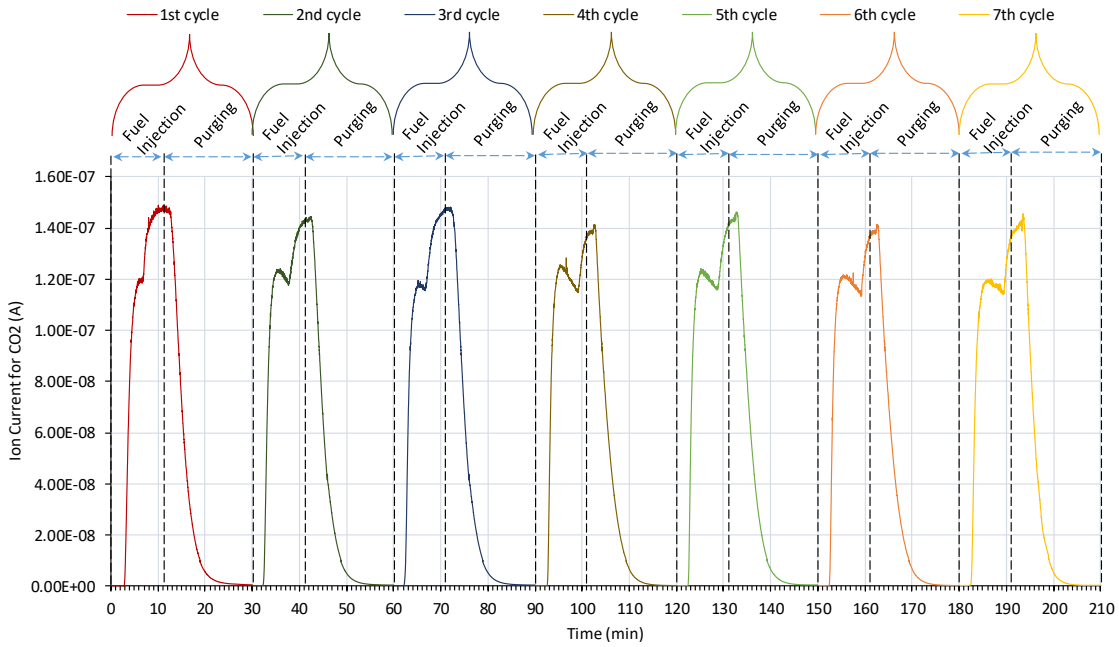


Figure 7.9. Ion Current for the CO_2 evolution by the combustion of n-hexadecane over CuO/Al_2O_3 for ϕ: 1.3 with an n-hexadecane flowrate of 0.03 ml/min at 482 °C for seven cycles.

7.7 Characterisation of fresh and used oxygen carriers

The density and particle size distributions of the oxygen carriers before and after combustion are presented in Table 7.4. The density of reduced form CuO is very close to the density of metallic Cu (8.9 g/cm^3). Moreover, the density of reduced form Mn_2O_3 is between those for Mn_3O_4 (4.86 g/cm^3) and MnO (5.37 g/cm^3), indicating a mixture of Mn_3O_4 and MnO is present. The elemental analysis confirmed that no carbon deposition had occurred on the oxygen carriers. The XRD patterns of fresh and used CuO (JCPDS no: 01-080-0076) and Mn_2O_3 (JCPDS no: 01-071-0636) are presented in Figure 7.10a and b, respectively. Figure 7.10a-2 confirms the high proportion of reduced Cu after CLC of n-hexadecane. Further, the characteristic Cu peaks (JCPDS no: 01-085-1326) seen in Figure 7.10a-3 demonstrate that full reduction from CuO to Cu occurred with fuel to oxygen carrier equivalence ratio, ϕ, of 2.0 at 482 °C. The reduction from CuO with higher hydrocarbons to Cu may be attributed to the minimal external mass transfer at the low combustion temperatures. Chuang et al. [187, 218] have described that the reduction of

CuO with either CO or H_2 followed the shrinking core mechanism, and proceeded via the intermediate, Cu_2O at higher temperatures when external mass transfer controlled the rate. However, at lower temperatures, the external mass transfer is minimal, and CuO can reduce directly to Cu.

Table 7.4. The main characteristics of the oxygen carriers before and after combustion tests.

Properties	**Before combustion**			**After combustion**		
	CuO	**CuO/Al_2O_3**	**Mn_2O_3**	**CuO[a]**	**CuO/Al_2O_3[b]**	**Mn_2O_3[c]**
Density (g/cm^3)	6.22	5.79	4.84	8.63	7.51	4.99
Particle size (%)						
<53 μm	n.a	n.a.	n.a.	6.1	76.9	5.9
53-150 μm	100	100	100	13.4	23.1	51.1
151-300 μm	n.a.	n.a.	n.a.	80.5	-	43.0

[a] Re-oxidised CuO after seven cycles. [b] Re-oxidised CuO/Al_2O_3 after seven cycles. [c] Re-oxidised Mn_2O_3 after one cycle.

The XRD patterns of the Mn_2O_3 oxygen carrier used in the combustion of n-hexadecane for ϕ: 1.0 and 2.0 at 482 °C, shown in Figure 7.10b-2 and 3, consist of mainly Mn_3O_4 and MnO (JCPDS no: 01-078-0424) in different ratios. These findings prove the sequential reduction steps of $Mn_2O_3 \rightarrow Mn_3O_4 \rightarrow MnO$ under the combustion of higher hydrocarbons at low temperatures. The percentage distribution of the reduced Mn states is presented in Table 7.5. As already described, the first reduction step ($Mn_2O_3 \rightarrow Mn_3O_4$) is much faster than the second one ($Mn_3O_4 \rightarrow MnO$).

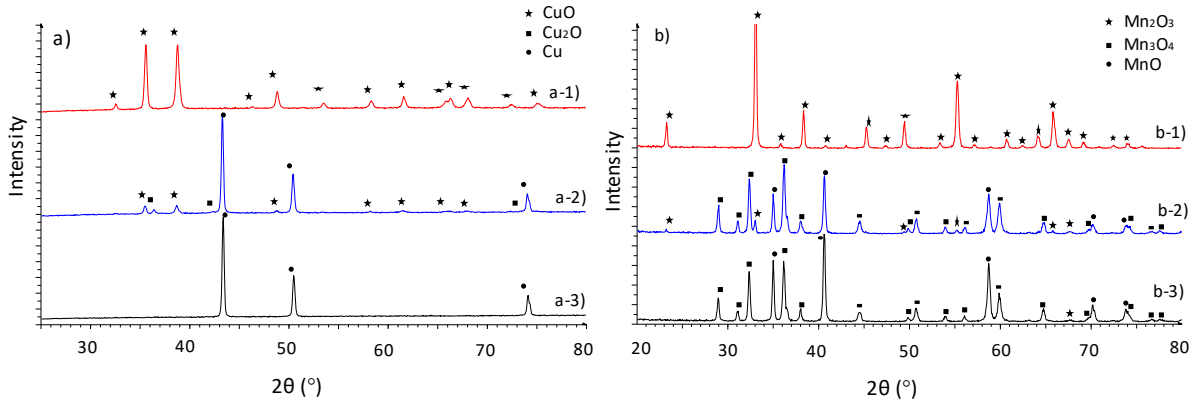


Figure 7.10. Wide-angle XRD patterns of a) CuO; b) Mn_2O_3 before and after n-hexadecane combustion experiments; a-1) fresh CuO, a-2) used CuO at ϕ: 1.0, a-3) used CuO at ϕ: 2.0, b-1) fresh Mn_2O_3, b-2) used Mn_2O_3 at ϕ: 1.0, b-3) used Mn_2O_3 at ϕ: 2.0 for 0.03 ml/min n-hexadecane feed flow rate at 482 °C.

Table 7.5. XRD results of fresh and used Mn_2O_3 in CLC for n-hexadecane at ϕ: 1.0-2.0 at 482 °C.

Sample	Mn_2O_3 (wt.%)	Mn_3O_4 (wt.%)	MnO (Wt.%)
Fresh Mn_2O_3	100	-	-
Used Mn_2O_3 at ϕ: 1.0	1	77	22
Used Mn_2O_3 at ϕ: 2.0	-	70	31

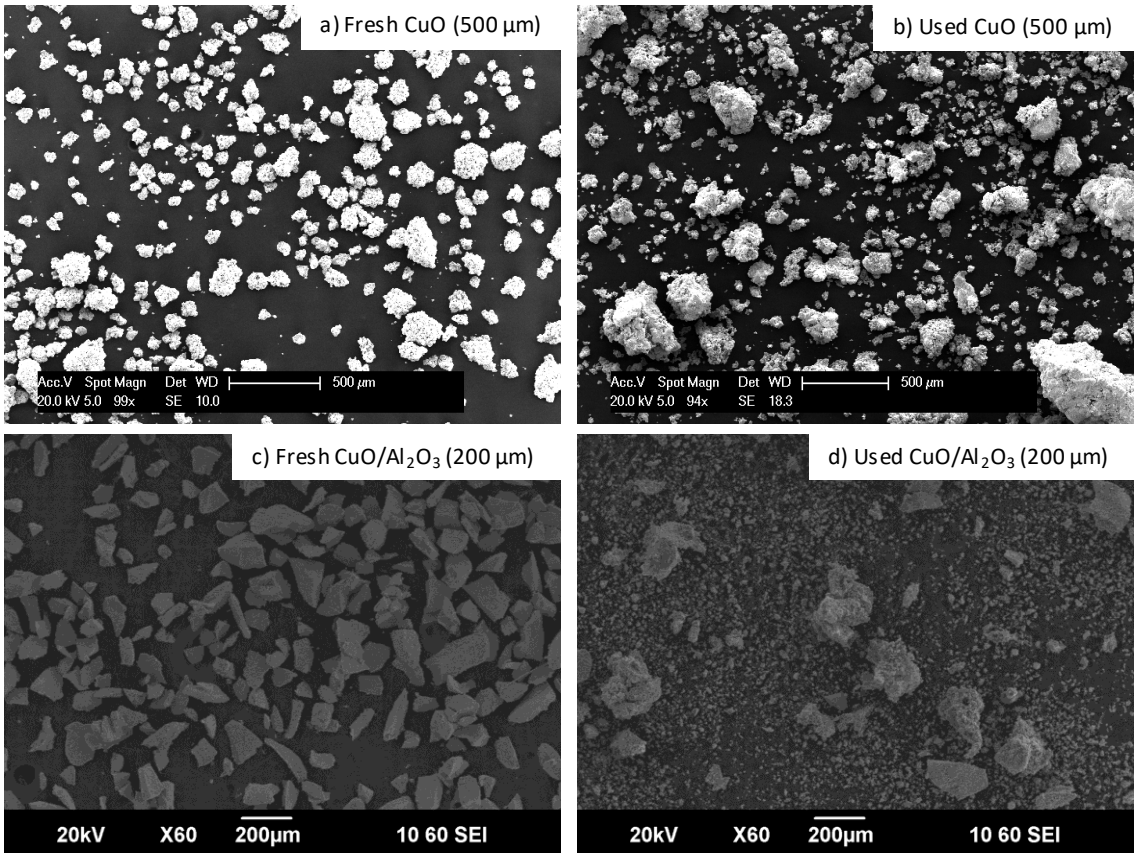
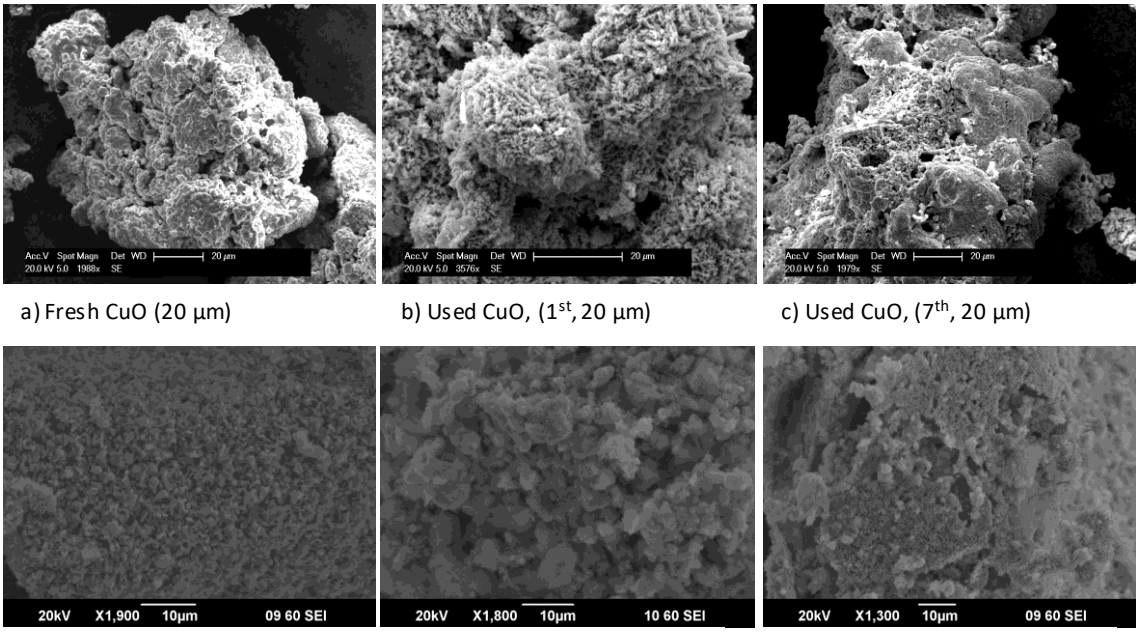


Figure 7.11. SEM images of fresh CuO (a), CuO/Al_2O_3 (c) and used CuO (b), CuO/Al_2O_3 (d) after 7 cycles at ϕ: 1.3 (7 cycles) under a 0.03 ml/min n-hexadecane feed flow rate at 482 °C.

The particle size distributions measured by sieving (Table 7.4) and SEM (Figure 7.11) for the fresh and used CuO and CuO/Al_2O_3 were compared after the 7 cycles. SEM results indicate that the particle size of bulk CuO has increased due to the sintering of reduced Cu. Sieving indicated 81 wt.% of the particles were in the range of 150-300 µm, with just 13 wt.% remaining in the size range of 53-150 µm and 6 wt.% reduced in size of lower than 53 µm (Table 7.4). On the other hand, both sintering and agglomeration problems of CuO can be solved using support [102, 113, 183]. For example, neither sintering nor agglomeration was demonstrated for CuO supported on Al_2O_3 prepared by

co-precipitation (Figure 7.12), which was also supported by Chuang et al. [178]. However, during this study particle attrition was observed after 7 cycles of combustion over CuO/Al_2O_3 as seen from both the SEM images and sieving measurements, with approximately 77 wt.% of the particles reduced in size from 53-150 μm to less than 53 μm (Table 7.4).



a) Fresh CuO (20 μm) b) Used CuO, (1st, 20 μm) c) Used CuO, (7th, 20 μm)

d) Fresh CuO/Al_2O_3, (10 μm) e) Used CuO/Al_2O_3, (1st, 10 μm) f) Used CuO/Al_2O_3, (7th, 10 μm)

Figure 7.12. SEM images of fresh CuO (a), CuO/Al_2O_3 (d) and used CuO (b, c), CuO/Al_2O_3 (e, f) after 1st and 7th cycles at ϕ: 1.3 under a 0.03 ml/min n-hexadecane feed flow rate at 482 °C.

7.8 Possible reaction pathways and potential applications

Depending upon the feed flow rate, the liquid fuels may enter the oxygen carrier bed in the form of both droplets and vapour phase. The former would be expected to be more prevalent for n-hexadecane due to its higher boiling point, but the results in Figure 7.6 suggest that n-hexadecane passed through the oxygen carrier bed in the form of vapour. According to the combustion tests of n-hexadecane and n-heptane with oxygen carriers, the reaction pathways can be drawn as presented in Figure 7.13. The possible reactions that can be occurred in the microactivity reactor are shown in Table 7.6.

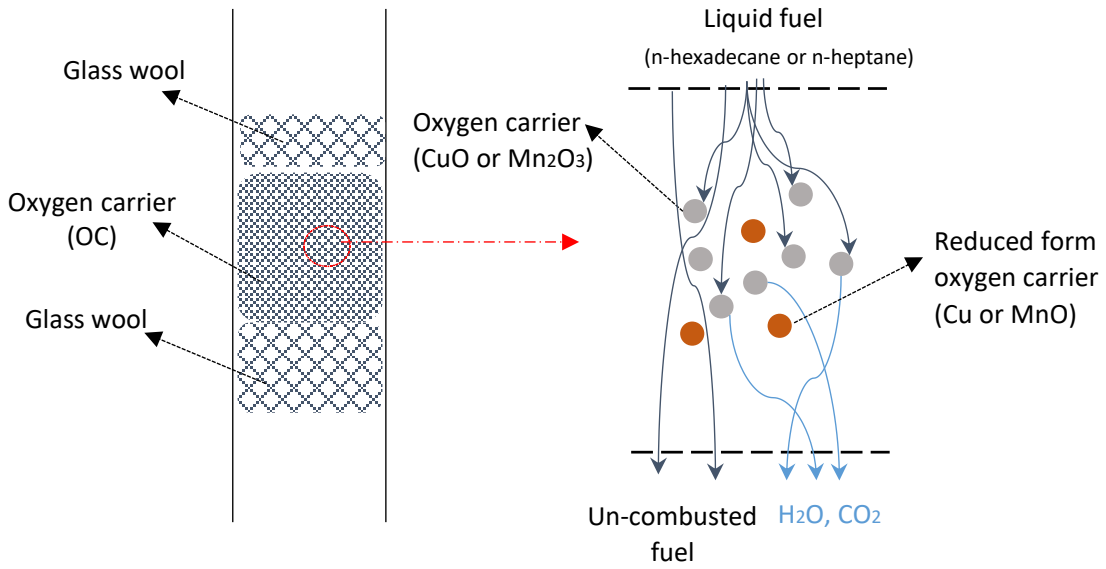


Figure 7.13. Possible reaction figure of CLC of liquid fuel with oxygen carriers at low temperature.

Table 7.6. Possible reactions of liquid fuels with and without oxygen carriers and oxygen transport capacities of CuO and Mn_2O_3.

Possible reactions with oxygen carriers		**R_0**	**b***
• *n-hexadecane complete combustion*			
$C_{16}H_{34} + 49CuO \rightarrow 16CO_2 + 17H_2O + 49Cu$	(R7.1)	0.201	49
$C_{16}H_{34} + 49Mn_2O_3 \rightarrow 16CO_2 + 17H_2O + 49MnO$	(R7.2)	0.101	49
• *n-hexadecane partial combustion*			
$C_{16}H_{34} + 16CuO \rightarrow 16CO + 17H_2 + 16Cu$	(R7.3)	0.201	16
$C_{16}H_{34} + 16Mn_2O_3 \rightarrow 16CO + 17H_2 + 32MnO$	(R7.4)	0.101	16
• *n-heptane complete combustion*			
$C_7H_{16} + 22CuO \rightarrow 7CO_2 + 8H_2O + 22Cu$	(R7.5)	0.201	22
$C_7H_{16} + 22Mn_2O_3 \rightarrow 7CO_2 + 8H_2O + 44MnO$	(R7.6)	0.101	22
• *n- heptane partial combustion*			
$C_7H_{16} + 7CuO \rightarrow 7CO + 8H_2 + 7Cu$	(R7.7)	0.201	7
$C_7H_{16} + 7Mn_2O_3 \rightarrow 7CO + 8H_2 + 14MnO$	(R7.8)	0.101	7
Other reactions without oxygen carriers			
• *Dehydrogenation* $C_nH_{2n+2} \rightarrow C_nH_{2n} + H_2$	(R7.9)		
• *Thermal cracking* $C_nH_{2n+2} \rightarrow C_{n-m}H_{2n-2m} + C_mH_{2m+2}$	(R7.10)		
• *Coking* $C_nH_{2n+2} \rightarrow nC + (n+1)H_2$	(R7.11)		

* Stoichiometric coefficient for oxygen carriers at the reactions from R1 to R8.

The highest combustion % and the yield of un-combusted fuel prove that the combustion reaction between liquid fuels (n-hexadecane and n-heptane) and oxygen carriers (CuO and Mn_2O_3) can explain complete combustions as described in R7.1 and R7.2 for n-

hexadecane combustion, R7.5 and R7.6 for n-heptane combustion. As suggested by Hoteit et al. [166], a large proportion of the fuels appeared to have oxidised almost immediately at injection, with the low CO/CO_2 ratios demonstrating that the partial combustion of both n-hexadecane and n-heptane is negligible. On the other hand, the low CO/CO_2 ratios show that partial combustion of both n-hexadecane (R7.3 and R7.4) and n-heptane (R7.7 and R7.8) with oxygen carriers are quite low. Similarly, Moldenhauer et al. [172] observed that once the temperature falls below 950 °C, the reaction from the fuel to $CO+H_2$ is slower than that from $CO+H_2$ to CO_2+H_2O. For CLC to be selective for n-heptane and n-hexadecane, this strongly suggested that the reactions initiated by bond cleavage are either thermolytic, leading to radicals, or catalytic, leading to carbocations. The sharp cut-off in combustion efficiency as the temperature falls below 380 °C probably represents the point where the extent of bond cleavage falling to a negligible level. Furthermore, dehydrogenation (R7.9), thermal cracking (R7.10), and coking (R7.11) reactions can be ignored due to the low amount of hydrogen, cracking products. Virtually complete CLC has been achieved with no evidence of coke formation, which is consistent with the studies at higher temperatures [113, 155].

The reported findings proved that CLC can potentially be used for hot gas clean-up, either to remove unburnt hydrocarbons and potentially other volatile organic species from flue gases or hot methane streams. Clearly, aromatic hydrocarbons and other compounds need to be tested to define the potential scope for these applications. The lighter n-alkanes, ethane, propane and butane, are expected to react slower than n-heptane and n-hexadecane due to their much stronger C-C bonds, as shown by the decrease in the cracking activity of alkanes with a decrease in their carbon number [280]. Low temperature CLC may not be applicable for the combustion of the polycyclic aromatic hydrocarbons to the strong aromatic C-C bonds.

7.9 A simple kinetic analysis of n-hexadecane combustion with CuO

To carry out kinetic analysis for n-hexadecane CLC with CuO, it was assumed that the liquid fuel entered the reactor in the form of droplets and went through the oxygen carrier bed in the vapour phase with the carrier gas, N_2. The **order of the reaction** (**n**) was determined using the steady state material balance for a plug flow reactor (Figure 7.14)

for four different volumetric feed flow rates; 0.03, 0.1, 0.2, and 1.4 ml/min, at 482 °C. Additionally, the **activation energy** (**E**) and **reaction rate coefficient** (**k**) were determined using an Arrhenius plot for n-hexadecane with CuO for 0.2 ml/min volumetric flowrate of n-hexadecane at different temperatures, 380, 400, 440, 482, 520, 560 °C (details of these calculations are presented in Appendix C).

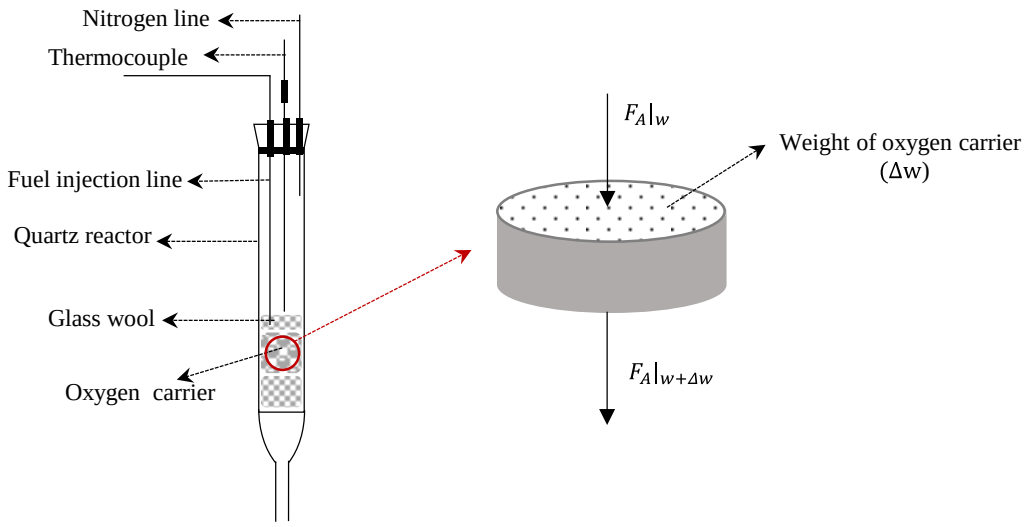


Figure 7.14. Elementary slice of solid oxygen carrier plug flow reactor (A represents n-hexadecane).

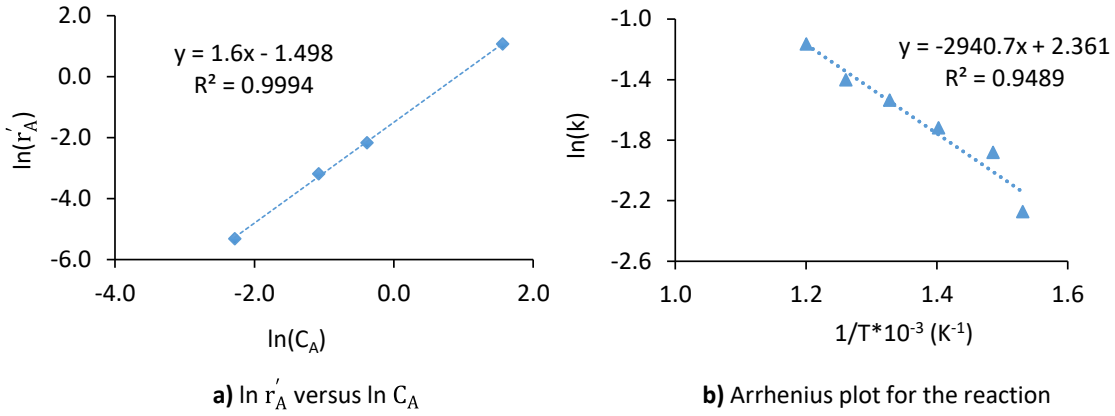


Figure 7.15. a) Reaction order (n) and reaction rate coefficient (k) calculation for n-hexadecane combustion with CuO at different volumetric feed flow rates (0.03, 0.1, 0.2, and 1.4 ml/min) for ϕ: 0.7 at 482 °C; **b)** Arrhenius plot for the combustion reaction rate constant of n-hexadecane with CuO for ϕ: 0.7 at 0.2 ml/min at different temperatures; 380, 400, 440, 482, 520, 560 °C.

The order of the reaction (n) (Figure 7.15-a) of 1.6 was determined using the steady state material balance for plug flow reactor (Figure 7.14) for four different volumetric feed flow rates; 0.03, 0.1, 0.2, and 1.4 ml/min, at 482 °C. The activation energy (E) of 24.5 kJ/mol was calculated using an Arrhenius plot (Figure 7.15-b) for n-hexadecane with CuO. A wide range of activation energies have been reported [118, 281, 282], 60, 33 and 14 kJ/mol for CLC of methane, hydrogen, and CO, respectively, with different oxygen carriers. Obviously, the activation energies for the combustion of methane, hydrogen, and CO cannot strictly be compared with those for the combustion of higher hydrocarbons. However, due to the lack of information for liquid fuel combustion with oxygen carriers, no comparisons can be made for preliminary empirical kinetic findings presented here.

7.10 Summary

Chemical looping combustion (CLC) of n-hexadecane and n-heptane with copper and manganese oxides (CuO and Mn_2O_3) has investigated in a fixed bed reactor to reveal the extent to which low temperature CLC can potentially be applicable to hydrocarbons. The effects of fuel to oxygen carrier ratio, fuel feed flow rate, and fuel residence time on the extent of combustion are reported. Methane did not combust, while near complete conversion was achieved for both n-hexadecane and n-heptane with excess oxygen carrier for CuO. For Mn_2O_3, complete reduction to Mn_3O_4 occurred, but the extent of combustion was controlled by the much slower reduction to MnO. Although the extent of cracking is relatively small in the absence of cracking catalysts, for the mechanism to be selective for higher hydrocarbons suggests that the reaction with oxygen involves radicals or carbocations arising from bond scission. Sintering of pure CuO occurred after repeated cycles, but this can easily be avoided using a support, such as alumina. The fact that higher hydrocarbons can be combusted selectively at 500 °C and below, offers the possibility of using CLC to remove these hydrocarbons and potentially other organics from hot gas streams.

Chapter 8
Conclusions and Future Work

8.1 Conclusions

The aim of this research was to investigate the applicability of CLC as a novel approach to CO_2 capture from FCC regenerator units. In this research, a novel CLC-FCC concept was proposed and then experimentally demonstrated that CLC is an alternative method for the next generation of FCC units to optimise CO_2 capture. A potential new generation of FCC catalysts modified by oxygen carriers were prepared using mechanical mixing and wet-impregnation methods. It was demonstrated that these oxygen carriers had no significant negative impacts on the performance of the novel catalysts in a model cracking reaction. Finally, the chemical looping combustion of coke deposited on the catalysts modified with oxygen carriers was demonstrated using both fixed-bed and fluidised-bed reactors.

8.1.1 Catalytic cracking tests over modified commercial FCC catalyst

In order to investigate the effect of both oxidised and reduced oxygen carriers modification on the cracking reaction, ECat was modified with both oxidised (CuO, Co_3O_4, Mn_2O_3) and reduced oxygen carriers (Cu, Cu_2O, CoO, Mn_3O_4) using mechanical mixing and wet-impregnation methods and tested with the cracking of n-hexadecane.

In terms of mechanical mixing, modification of Cu (M-Cu/ECat) was detrimental to the conversion of n-hexadecane. However, this was not the case for the mixing of Cu_2O, CoO, and Mn_3O_4 (M-Cu_2O/ECat, M-CoO/ECat, and M-Mn_3O_4/ECat) in terms of the conversion, yields, and product selectivities. The mixing of CoO with ECat seems to give the closest conversions, in terms of gas, liquid and coke yields to the reference ECat. The

other two reduced state oxygen carriers, Cu_2O and Mn_3O_4, were also shown to be promising, with relatively small differences in conversion.

The characterisation results of the oxygen carrier impregnated ECat demonstrated that it is possible to prepare a catalyst consisting of two structures; oxygen carrier and FCC catalyst. In the FCC riser, the cracking reaction occurs over the ECat part, while the reduced oxygen carriers act as inert material having no effect on reaction. In the regenerator, the coke deposited on modified catalyst is combust with oxygen carrier, while ECat part acts as a support for the oxygen carriers, which can decrease the agglomeration and carbon deposition during the combustion of coke.

The impregnation of Cu, MnO and Mn_3O_4 on ECat (I-Cu/ECat, I-MnO/ECat and I-Mn_3O_4/ECat) showed no negative impacts on the cracking of n-hexadecane in terms of the conversion, yields, and product selectivities when compared with the reference ECat, as required for the proposed CLC-FCC concept. However, the impregnation of CoO on ECat (I-CoO/ECat) caused a decrease in the conversion of n-hexadecane.

8.1.2 CLC tests of coke deposited on FCC catalyst

In order to investigate the combustion of FCC coke with oxidised oxygen carriers, CLC tests were firstly carried out using a TGA. Due to the weight limitation of TGA pans, a low volatile semi-anthracite Welsh coal having a similar chemical composition to FCC coke was selected as a model FCC coke for the CLC tests. The CLC tests of model coke with bulk oxygen carriers CuO, Co_3O_4 and Mn_2O_3, demonstrated that complete combustion is possible once the stoichiometrically required amounts of oxygen carriers and sufficient time were provided. Additionally, higher than 90 wt.% combustion of model coke was achieved with CuO and Mn_2O_3 at 750 °C for 40–60 min, which are similar conditions used in the conventional regenerator of FCC units.

In order to obtain more accurate and realistic data, the combustion behaviour of FCC coke deposited on ECat with the stoichiometrically required amount of oxidised oxygen carriers (CuO, Co_3O_4 and Mn_2O_3) was investigated in a lab scale fixed-bed reactor equipped with an online gas analyser. Relatively high combustion (about 90 vol.%) of the

coke deposited on ECat was achieved with the stoichiometrically required amount of bulk CuO, Co_3O_4 and Mn_2O_3 at 800 °C.

Furthermore, the combustion behaviour of the coke deposited on reduced oxygen carrier impregnated ECat (I-Cu/ECat and I-Mn_3O_4/ECat) with oxidised oxygen carrier impregnated ECat (I-CuO/ECat and I-Mn_2O_3/ECat) were repeated in both fixed-bed and fluidised-bed reactors. The decomposition of oxidised oxygen carriers through oxygen release at lower temperatures was enhanced using the impregnation on the commercial ECat. The CLC tests of coke deposited on I-Cu/ECat, and I-Mn_3O_4/ECat with the stoichiometrically required amount of I-CuO/ECat and I-Mn_2O_3/ECat demonstrated that it is possible to reach about 90 vol.% combustion in FxB-MS and greater than 94 vol.% in FsB-MS at 750 °C for 45 min. These findings have led us to conclude that CLC is a promising technology to incorporate into the next generation of FCC units to optimise CO_2 capture.

8.1.3 Low temperature CLC of hydrocarbons with Cu- and Mn- oxidises

The CLC of model liquid fuels; n-hexadecane and n-heptane, was investigated with oxygen carriers; CuO and Mn_2O_3, at low temperature, 482 °C, in a fixed-bed microactivity reactor. This study has established that selective CLC of higher alkanes over methane can be achieved with CuO and Mn_2O_3, at temperatures below 500 °C. Under fuel-lean ($0<\phi<1$) conditions, it is possible to achieve high levels of combustion of n-heptane and n-hexadecane over CuO at ϕ: 0.7. Additionally, in fuel-rich conditions ($1<\phi<\infty$), it is also possible to reach the maximum extent of combustion of n-hexadecane and n-heptane with CuO with ϕ >1.3 at 482 °C with a residence time of 13 s.

CuO can be fully reduced to Cu at low temperature CLC. However, the combustion efficiency for Mn_2O_3 was limited by the slow second reduction step (Mn_3O_4 to MnO). Sintering of CuO in a multi-cycle test was observed, but this was avoided by using an Al_2O_3 support. The combustion reaction pathways of model liquid fuels with oxygen carriers have been clarified as mainly complete combustion to CO_2 and H_2O. The partial combustion, dehydrogenation, and thermal cracking of liquid fuels are low enough to not be significant. Kinetic analysis for the combustion of n-hexadecane indicated a reaction

order of 1.6 and relatively high activation energy of 24.5 kJ/mol. The high selectivity achieved for higher hydrocarbons suggests the low temperature CLC can be used for hot gas clean-up to remove higher alkanes and potentially other volatile organic compounds.

8.2 Future work

8.2.1 Suggestions for the CLC-FCC concept

The laboratory scale experiments were demonstrated that the CLC-FCC concept is a promising technology to address the one quarter of CO_2 emissions from oil refineries. For future work, I firstly suggest that the FCC catalysts should be modified by reduced oxygen carriers using a co-precipitation method. Co-precipitation will probably decrease the structural problems such as oxygen carrier accumulation, fragmentation, pore distribution etc. identified due to the impregnation method. Secondly, the new type of oxygen carriers modified FCC catalysts should be tested in the cracking reaction of a refinery cracking feed (VGO) following a model compound using a fluidised bed reactor as in the conventional FCC riser. The impurities in the VGO may have a detrimental effect on the oxygen carriers. For the final part, the CLC tests of coke deposited on prepared catalysts with oxidised oxygen carrier modified catalysts should be investigated in a fluidised bed reactor using CO_2 as fluidisation gas instead of N_2. As the heating capacity of CO_2 is higher than the heating capacity of N_2, this will change the required flow rate for the regenerator.

Following the experimental studies in the laboratory, the suggested CLC-FCC concept can be simulated and modelled using computer programmes such as Aspen Plus, gPROMS. The models already applied to CLC may be helpful for the simulation, together with the catalyst regenerator and FCC reactor. The experimental data found in this study may also be helpful for the initial model validation.

Furthermore, for accurate prediction of the process performance, it is necessary to investigate the following aspects: (i) The heat and mass balance of the entire process should be evaluated to understand if it conforms to the requirement of a conventional FCC unit. (ii) To validate whether the assumptions made before are correct - coke can be

combusted at an acceptable rate in the regenerator. (iii) Other factors such feedstock variations, catalyst composition, space velocity, residence time and other operating parameters on the cracking efficiency and delta coke should be investigated. Based on this study, optimal process design and operation should be investigated in order to maximise the utilisation of the heat generated.

8.2.2 Suggestions for the applicability of CLC for other processes

Furthermore, the application of CLC for catalyst regeneration to other industrial processes may be investigated to decrease CO_2 emissions. For example, deactivated naphtha reforming catalysts (Pt/Re-alumina) can be modified in a similar manner to the FCC catalysts and the reduction of coke would be investigated to prove the concept that CLC can be adapted to catalyst regeneration. The CLC regenerated catalysts must be characterised and compared with those prepared by normal controlled combustion. The other processes are methane steam reforming and hydro-treating catalysts, which can be modified with CLC. The methane steam reforming and hydro-treating catalysts contains Ni and Ni/Mo, or Co/Mo, respectively, so they can only be physically mixed with oxygen carriers for regeneration. Although clearly Ni and Co are suitable oxygen carriers for CLC, these cannot be oxidised before regeneration to avoid normal combustion of the coke. Again, the characteristic of CLC-regenerated combustion must be compared with those by normal combustion.

8.2.3 Suggestions for the applicability of low temperature CLC

In order to define the potential scope of the application of low temperature CLC concept, higher hydrocarbons other than alkanes can be tested, for example, alkenes and aromatics. Furthermore, the utilisation of other oxygen carriers such as Ni-, Fe-, and Co-based may be investigated for the low temperature CLC concept. Additionally, while it is observed that using supported oxygen carriers eliminated sintering and agglomeration over a few cycles, this needs to be investigated in detail.

References

1 National Research Council (NRC). Advancing the science of climate chance. The National Academies Press, Washington, DC, USA, 2010. doi.org/10.17226/12782.

2 International Energy Agency (IEA). CO_2 emissions from fuel combustion. OECD Publishing, Paris, 2016. doi.org/10.1787/co2_fuel-2016-en.

3 Wang M, Lawal A, Stephenson P, Sidders J, Ramshaw C. Post-combustion CO_2 capture with chemical absorption: a state-of-the-art review. Chemical Engineering Research and Design 2011;89(9):1609-24.

4 Boden TA, Marland G, Andres RJ. Global, regional, and national fossil-fuel CO_2 emissions. Carbon Dioxide Information Analysis Center, Oak Ridge National Laboratory, U.S. Department of Energy, Oak Ridge, USA, 2017. doi.org/10.3334/CDIAC/00001_V2017

5 van Straelen J, Geuzebroek F, Goodchild N, Protopapas G, Mahony L. CO_2 capture for refineries, a practical approach. International Journal of Greenhouse Gas Control 2010;4(2):316-20.

6 Intergovernmental Panel on Climate Change (IPCC), IPCC Special Report on Carbon Dioxide Capture and Storage. Prepared by Working Group III of the Intergovernmental Panel on Climate Change [eds; Metz, B., O. Davidson, H. C. de Coninck, M. Loos, and L. A. Meyer]. Cambridge University Press, Cambridge, United Kingdom and New York, NY, USA, 2005.

7 Güleç F, Meredith W, Snape CE. Progress in the CO_2 Capture Technologies for Fluid Catalytic Cracking (FCC) Units—A Review. Frontiers in Energy Research. 2020, 8, 62.

8 Ali M, Saidur R, Hossain M. A review on emission analysis in cement industries. Renewable and Sustainable Energy Reviews 2011;15(5):2252-61.

9 Herzog H, Drake E, Adams E. CO_2 capture, reuse, and storage technologies for mitigating global climate change. A White Paper 1997; 1-70 (DOE Order No. DE-AF22-96PC01257).

10 Pérez-Fortes M, Moya JA, Vatopoulos K, Tzimas E. CO_2 capture and utilization in cement and iron and steel industries. Energy Procedia, 2014;63:6534-43.

11 International Energy Agency (IEA). Tracking clean energy progress, Industry-CCS annex. IEA Statistic; 2013.

12 van Straelen J, Geuzebroek F, Goodchild N, Protopapas G, Mahony L. CO_2 capture for refineries, a practical approach. Energy Procedia 2009;1(1):179-85.

13 US Environmental Protection Agency (EPA). Available and emerging technologies for reducing GHG emissions from petroleum refining. Washington, DC, September 2012.

14 Kheshgi H, de Coninck H, Kessels J. Carbon dioxide capture and storage: seven years after the IPCC special report. Mitigation and Adaptation Strategies for Global Change. 2012;17(6):563-7.

15 Peng P, Zhuang Y. The evaluation and comparison of carbon dioxide capture technologies applied to FCC flue gas in advanced materials research. Trans Tech Publications, 2012;347:1479-82.

16 Digne R, Feugnet F, Gomez A. A technical and economical evaluation of CO_2 capture from fluidized catalytic cracking (FCC) flue gas. Oil & Gas Science and Technology–Revue d'IFP Energies Nouvelles 2014;69(6):1081-9.

17 Melien T, Roijen SB. Economics. in Carbon dioxide capture for storage in deep geologic formations results from the CO2 capture project, in Advances in CO_2 Capture and Storage Technology Results, ed L. Eide (Newbury: CPL Press), 2009;3:237-64.

18 de Mello LF, Pimenta RD, Moure GT, Pravia OR, Gearhart L, Milios PB, Melien T. A technical and economical evaluation of CO_2 capture from FCC units. Energy Procedia 2009;1(1):117-24.

19 Miracca I, Butler D. CO_2 capture from a fluid catalytic cracking unit: Technical/Economical evaluation. in Carbon Dioxide Capture for Storage in Deep Geologic Formations–Results from the CO_2 Capture Project ed K. F. Gerdes (Gerdes: CPL Press) 2015;4:67-81.

20 Ksepko E, Siriwardane RV, Tian H, Simonyi T, Sciazko M. Effect of H_2S on chemical looping combustion of coal-derived synthesis gas over Fe–Mn oxides supported on sepiolite, ZrO_2, and Al_2O_3. Energy & Fuels 2012;26(4):2461-72.

21 Kerr HR. Capture and Separation Technology Gaps and Priority Research Needs. in Carbon dioxide capture for storage in deep geological formations-results from the CO_2 capture project Capture and Separation of Carbon Dioxide from Combustion Sources Ed D.C Thomas, Elsevier: Oxford, UK; 2005, 655-660.

22 Pröll T, Kolbitsch P, Bolhàr-Nordenkampf J, Hofbauer H. A novel dual circulating fluidized bed system for chemical looping processes. AICHE journal 2009;55(12):3255-66.

23 Mattisson T, Lyngfelt A, Leion H. Chemical-looping with oxygen uncoupling for combustion of solid fuels. International Journal of Greenhouse Gas Control 2009;3(1):11-9.

24 Drage TC, Arenillas A, Smith K, Snape CE. Comparison of pre and post-combustion CO_2 adsorbent technologies. 8th International Conference on Greenhouse Gas Control Technologies. Trondheim, Norway; 2006:1-6.

25 de Mello LF, Moure GT, Pravia OR, Gearhart L, Milios PB. Oxy-combustion for CO_2 capture from fluid catalytic crackers (FCC). in Carbon dioxide capture for storage in deep geologic formations results from the CO_2 capture project - advances in CO_2 capture and storage technology results, ed L. Eide (Newbury: CPL Press), 2009;3:31-42.

26 Güleç F, Meredith W, Snape EC. Progress in the CO_2 Capture Technologies for Fluid Catalytic Cracking (FCC) Units—A Review, Frontiers in Energy Research, 8 (2020).

27 Güleç F, Meredith W, Sun CG, Snape EC. Demonstrating the applicability of chemical looping combustion for the regeneration of fluid catalytic cracking catalysts, Chemical Engineering Journal, 2020: 389: 124492.

28 Güleç F, Meredith W, Sun CG, Snape EC. A novel approach to CO2 capture in Fluid Catalytic Cracking—Chemical Looping Combustion, Fuel, 2019; 244: 140-150.

29 Güleç F, Meredith W, Sun CG, Snape EC. Selective low temperature chemical looping combustion of higher alkanes with Cu-and Mn-oxides, Energy, 2019; 173: 658-666.

30 Dudley B. BP statistical review of world energy - 2018. London, UK. June 2018.

31 United Nations Framework Convention on Climate Change (UNFCCC). National Inventory Submissions; 2018. Available from: https://unfccc.int/process-and-meetings/transparency-and-reporting/reporting-and-review-under-the-convention/greenhouse-gas-inventories-annex-i-parties/national-inventory-submissions-2018. [Accessed 21.05.2019].

32 Global Carbon Atlas. Fossil Fuels Emissions, 2020. Available from: http://www.globalcarbonatlas.org/en/CO2-emissions [Accessed 13.09.2020].

33 International Energy Agency (IEA). CO_2 emissions from fuel combustion 2019. OECD Publishing, Paris, 2019, doi.org/10.1787/2a701673-en.

34 John G. Sources of CO_2. in PCC Special Report on Carbon Dioxide Capture and Storage. ed. Metz, B., O. Davidson, H. C. de Coninck, M. Loos, and L. A. Meyer, Cambridge University Press, Cambridge, United Kingdom and New York, NY, USA, 2005, 75-104.

35 Scott SA, Dennis JS, Hayhurst AN, Brown T. In situgasification of a solid fuel and CO_2 separation using chemical looping. AIChE Journal 2006;52(9):3325-8.

36 Figueroa JD, Fout T, Plasynski S, McIlvried H, Srivastava RD. Advances in CO_2 capture technology, the US Department of Energy's Carbon Sequestration Program. International Journal of Greenhouse Gas Control 2008;2(1):9-20.

37 Dennis JS, Müller CR, Scott SA. In situ gasification and CO_2 separation using chemical looping with a Cu-based oxygen carrier: Performance with bituminous coals. Fuel 2010;89(9):2353-64.

38 Dennis JS, Scott SA. In situ gasification of a lignite coal and CO_2 separation using chemical looping with a Cu-based oxygen carrier. Fuel 2010;89(7):1623-40.

39 National Mining Association. Carbon Capture and Storage: Clean coal technologies for carbon management. 2012.

40 Clarens F, Espí JJ, Giraldi MR, Rovira M, Vega LF. Life cycle assessment of CaO looping versus amine-based absorption for capturing CO_2 in a subcritical coal power plant. International Journal of Greenhouse Gas Control 2016;46:18-27.

41 Quader MA, Ahmed S, Raja Ghazilla RA, Ahmed S, Dahari M. Evaluation of criteria for CO_2 capture and storage in the iron and steel industry using the 2-tuple DEMATEL technique. Journal of Cleaner Production 2016;120:207-20.

42 Zhou W, Jiang D, Chen D, Griffy-Brown C, Jin Y, Zhu B. Capturing CO_2 from cement plants: A priority for reducing CO_2 emissions in China. Energy 2016;106:464-74.

43 Kohl Al, Nielsen R B. Gas Purification, Houston. TX; 1997. doi.org/10.1016/B978-0-88415-220-0.X5000-9

44 Pérez-Uriarte P, Ateka A, Gamero M, Aguayo AT, Bilbao J. Effect of the operating conditions in the transformation of DME to olefins over a HZSM-5 zeolite catalyst. Industrial & Engineering Chemistry Research 2016;55(23):6569-78.

45 Anthony JL, Maginn EJ, Brennecke JF. Solubilities and thermodynamic properties of gases in the ionic liquid 1-n-butyl-3-methylimidazolium hexafluorophosphate. The Journal of Physical Chemistry B 2002;106(29):7315-20.

46 Bonenfant D, Mimeault M, Hausler R. Determination of the structural features of distinct amines important for the absorption of CO_2 and regeneration in aqueous solution. Industrial & Engineering Chemistry Research 2003;42(14):3179-84.

47 Oyenekan BA, Rochelle GT. Alternative stripper configurations for CO_2 capture by aqueous amines. AIChE Journal 2007;53(12):3144-54.

48 Hicks JC, Drese JH, Fauth DJ, Gray ML, Qi G, Jones CW. Designing adsorbents for CO_2 capture from flue gas-hyperbranched aminosilicas capable of capturing CO_2 reversibly. Journal of the American Chemical Society 2008;130(10):2902-3.

49 Rodriguez N, Alonso M, Grasa G, Abanades JC. Heat requirements in a calciner of $CaCO_3$ integrated in a CO_2 capture system using CaO. Chemical Engineering Journal 2008;138(1):148-54.

50 Huang J, Zou J, Ho WW. Carbon dioxide capture using a CO_2-selective facilitated transport membrane. Industrial & Engineering Chemistry Research 2008;47(4):1261-7.

51 Amorino C PA, Larceri F. The Sotacarbo coal gasification pilot plant for hydrogen production and CO_2 removal. Proceedings, 24th Annual Pittsburgh Coal Conference. Pittsburgh, PA, USA; 2007: 11, 6-1.

52 Davison J. Electricity systems with near-zero emissions of CO_2 based on wind energy and coal gasification with CCS and hydrogen storage. International Journal of Greenhouse Gas Control 2009;3(6):683-92.

53 Siriwardane R. CO_2 capture utilizing solid sorbents. 5th Annual Conference on Carbon Capture & Sequestration. Alexandria, VA, USA; 2006:30.

54 da Costa JD, Reed GP, Thambimuthu K. High temperature gas separation membranes in coal gasification. Energy Procedia, 2009;1(1):295-302.

55 Tomizaki K-y, Kanakubo M, Nanjo H, Shimizu S, Onoda M, Fujioka Y. 13C NMR studies on the dissolution mechanisms of carbon dioxide in amine-containing aqueous solvents at high pressures toward an integrated coal gasification combined cycle− carbon capture and storage process. Industrial & Engineering Chemistry Research 2009;49(3):1222-8.

56 Habib M, Badr H, Ahmed S, Ben-Mansour R, Mezghani K, Imashuku S, La O GJ, Shao-horn Y, Mancini ND, Mitsos A, Kirchen P, Ghoneim AF. A review of recent developments in carbon capture utilizing oxy-fuel combustion in conventional and ion transport membrane systems. International Journal of Energy Research 2011;35(9):741-64.

57 Stadler H, Beggel F, Habermehl M, Persigehl B, Kneer R, Modigell M, Jeschke P. Oxyfuel coal combustion by efficient integration of oxygen transport membranes. International Journal of Greenhouse Gas Control 2011;5(1):7-15.

58 Manovic V, Anthony EJ. Thermal activation of CaO-based sorbent and self-reactivation during CO_2 capture looping cycles. Environmental Science & Technology 2008;42(11):4170-4.

59 Ogbuka CP. Development of solid adsorbent materials for CO_2 capture. PhD thesis, University of Nottingham; 2013.

60 Global CCS Institute. The global status of CCS 2019 - Targeting Climate Change. Global CCS Institute; 2019.

61 International Energy Agency (IEA). Technology Roadmap - Carbon Capture and Storage in Industrial Applications. International Energy Agency, Paris, 2011. www.iea.org/reports/technology-roadmap-carbon-capture-and-storage-in-industrial-applications

62 International Energy Agency (IEA). Technology Roadmap - Carbon Capture and Storage. International Energy Agency, Paris, 2013. https://webstore.iea.org/technology-roadmap-carbon-capture-and-storage-2013

63 US Environmental Protection Agency (EPA). Available and emerging technologies for reducing GHG emissions from petroleum refining. Washington, DC, October 2010.

64 Kuramochi T, Ramírez A, Turkenburg W, Faaij A. Comparative assessment of CO_2 capture technologies for carbon-intensive industrial processes. Progress in Energy and Combustion Science 2012;38(1):87-112.

65 Rawlence DJ, Gosling K. FCC catalyst performance evaluation. Applied Catalysis 1988;43(2):213-37.

66 Sadeghbeigi R. Fluid Catalytic Cracking Handbook. Houston: Gulf Publishing Company; 2000. doi.org/10.1016/C2010-0-67291-9

67 Jones DS, Pujadó PP. Handbook of petroleum processing. Springer Science & Business Media; 2006. doi.org/10.1007/1-4020-2820-2

68 Vogt E, Weckhuysen B. Fluid catalytic cracking: recent developments on the grand old lady of zeolite catalysis. Chemical Society Reviews 2015;44(20):7342-70.

69 Cheng W-C, Kim G, Peters AW, Zhao X, Rajagopalan K, Ziebarth M, Pereira CJ. Environmental fluid catalytic cracking technology. Catalysis Reviews 1998;40(1-2):39-79.

70 Otterstedt J-E, Zhu Y-M, Sterte J. Catalytic cracking of heavy oil over catalysts containing different types of zeolite Y in active and inactive matrices. Applied Catalysis 1988;38(1):143-55.

71 Gianetto A, Farag HI, Blasetti AP, de Lasa HI. Fluid catalytic cracking catalyst for reformulated gasolines. Kinetic modeling. Industrial & Engineering Chemistry Research 1994;33(12):3053-62.

72 Al-Khattaf S, De Lasa H. Activity and selectivity of fluidized catalytic cracking catalysts in a riser simulator: the role of Y-zeolite crystal size. I Industrial & Engineering Chemistry Research 1999;38(4):1350-6.

73 Manos G, Yusof IY, Papayannakos N, Gangas NH. Catalytic cracking of polyethylene over clay catalysts. Comparison with an ultrastable Y zeolite. Industrial & Engineering Chemistry Research 2001;40(10):2220-5.

74 Occelli ML. Fluid Catalytic Cracking VII: Materials, Methods and Process Innovations. Studies in Surface Science and Catalysis series, Elsevier, 2007, 166.

75 Ng SH, Dabros T, Humphries A. Fluid catalytic cracking quality improvement of bitumen after paraffinic Froth treatment. Energy and Fuels 2007;21(3):1432-41.

76 International ASTM. Standard Test Method for Testing Fluid Catalytic Cracking (FCC) Catalysts by Microactivity Test. ASTM International ASTM D3907-13; 2013:1-6.

77 Miracca I. Introduction to the CCP3 Capture Technology Portfolio. in Carbon Dioxide Capture for Storage in Deep Geologic Formations–Results from the CO_2 Capture Project, ed K. F. Gerdes (Gerdes: CPL Press) 2015:9-16.

78 de Mello LF, Gobbo R, Moure GT, Miracca I. FCC Oxy-Fuel Demonstration at Petrobras Shale Industrial Business Unit. in Carbon Dioxide Capture for Storage in Deep Geologic Formations–Results from the CO_2 Capture Project, ed K. F. Gerdes (CPL Press), 2015;4:51-65.

79 Mace EJ, Blume AM, Yeung TW. New roles for FCCU: carbon capture unit and coke gasifier. Petroleum Technology Quarterly 2009;14(1):59-64.

80 Miracca I. Introduction to the CCP3 Capture Technology Portfolio. in Carbon Dioxide Capture for Storage in Deep Geologic Formations–Results from the CO_2 Capture Project, ed K. F. Gerdes (Gerdes: CPL Press) 2015:9-16.

81 Chan WN, Walter A, Sugiyama MI, Borges GC. Assessment of CO_2 emission mitigation for a Brazilian oil refinery. Brazilian Journal of Chemical Engineering. 2016;33(4):835-50.

82 Ho M T and Wiley DE. Liquid absorbent-based post-combustion CO_2 capture in industrial processes.In Absorption-based post-combustion capture of carbon dioxide, Woodhead Publishing, 2016, 711-756.

83 Crombie M, Imbus S, Miracca I. CO_2 capture project phase 3 - Demonstration phase. Energy Procedia 2011;4:6104-8.

84 Johansson D, Rootzén J, Berntsson T, Johnsson F. Assessment of strategies for CO_2 abatement in the European petroleum refining industry. Energy 2012;42(1):375-86.

85 de Mello LF, Gobbo R, Moure GT, Miracca I. Oxy-combustion technology development for Fluid Catalytic Crackers (FCC)–large pilot scale demonstration. Energy Procedia 2013;37:7815-24.

86 de Mello LF, Gobbo R, Moure GT, Miracca I. FCC Oxy-Fuel Demonstration at Petrobras Shale Industrial Business Unit. in Carbon Dioxide Capture for Storage in Deep Geologic Formations–Results from the CO_2 Capture Project, ed K. F. Gerdes (CPL Press), 2015;4:51-65.

87 de Mello LFG, R.; Moure, G. T.; Miracca, I. CO_2 Capture From A Fluid Catalytic Cracking Unit. in Carbon Dioxide Capture for Storage in Deep Geologic Formations, ed K. F. Gerdes (CPL Press) 2015, p. 47-9.

88 Lemaire E, Bouillon PA, Gomez A, Kittel J, Gonzalez S, Carrette PL, et al. New IFP optimized first generation process for post-combustion carbon capture: HiCapt+^{TM}. Energy Procedia 2011;4:1361-8.

89 Wei M, Qian F, Du W, Hu J, Wang M, Luo X, et al. Study on the integration of fluid catalytic cracking unit in refinery with solvent-based carbon capture through process simulation. Fuel 2018;219:364-74.

90 de Mello LFG, R.; Moure, G. T.; Miracca, I. CO_2 Capture From A Fluid Catalytic Cracking Unit. in Carbon Dioxide Capture for Storage in Deep Geologic Formations, ed K. F. Gerdes (CPL Press) 2015, p. 47-9.

91 dos Santos LT, Santos FM, Silva RS, Gomes TS, Esteves PM, Pimenta RD, Menezes SMC, Chamberlain OR, Lam YL, Pereira MM. Mechanistic insights of CO_2-coke reaction during the regeneration step of the fluid cracking catalyst. Applied Catalysis A: General 2008;336(1):40-7.

92 da Silva TC, Pinto JF, Santos FM, dos Santos LT, Aranda DA, Ribeiro F, et al. Vanadium and alumina modified with groups I and II elements for CO_2 and coke reaction under fluid catalytic cracking process. Applied Catalysis B: Environmental 2015;164:225-33.

93 Abu-Zahra MR, Schneiders LH, Niederer JP, Feron PH, Versteeg GF. CO_2 capture from power plants: Part I. A parametric study of the technical performance based on monoethanolamine. International Journal of Greenhouse Gas Control 2007;1(1):37-46.

94 de Mello LF, Moure GT, Pravia OR, Gearhart L, Milios PB. Oxy-combustion for CO_2 capture from fluid catalytic crackers (FCC). in Carbon dioxide capture for storage in deep geologic formations results from the CO_2 capture project - advances in CO_2 capture and storage technology results, ed L. Eide (Newbury: CPL Press), 2009;3:31-42.

95 Richter HJ, Knoche KF. Reversibility of combustion processes. ACS Publications; 1983, 71-85 (doi: 10.1021/bk-1983-0235.ch003).

96 Wang P, Means N, Shekhawat D, Berry D, Massoudi M. Chemical-looping combustion and gasification of coals and oxygen carrier development: a brief review. Energies 2015;8(10):10605-35.

97 Adanez J, Abad A, Garcia-Labiano F, Gayan P, Luis F. Progress in chemical-looping combustion and reforming technologies. Progress in Energy and Combustion Science 2012;38(2):215-82.

98 Cho P, Mattisson T, Lyngfelt A. Comparison of iron-, nickel-, copper-and manganese-based oxygen carriers for chemical-looping combustion. Fuel 2004;83(9):1215-25.

99 Chiu P-C, Ku Y. Chemical looping process-a novel technology for inherent CO_2 capture. Aerosol Air Qual Res 2012;12:1421-32.

100 Mattisson T, Lyngfelt A. Applications of chemical-looping combustion with capture of CO_2. Second Nordic Minisymposium on CO_2 Capture and Storage, Göteborg, Sweden 2001.

101 Wang S, Wang G, Jiang F, Luo M, Li H. Chemical looping combustion of coke oven gas by using Fe_2O_3/CuO with $MgAl_2O_4$ as oxygen carrier. Energy & Environmental Science 2010;3(9):1353.

102 Siriwardane R, Tian H, Richards G, Simonyi T, Poston J. Chemical-looping combustion of coal with metal oxide oxygen carriers. Energy & Fuels 2009;23(8):3885-92.

103 Tian H, Chaudhari K, Simonyi T, Poston J, Liu T, Sanders T, et al. Chemical-looping combustion of coal-derived synthesis gas over copper oxide oxygen carriers. Energy & Fuels 2008;22(6):3744-55.

104 Mattisson T, Lyngfelt A, Cho P. The use of iron oxide as an oxygen carrier in chemical-looping combustion of methane with inherent separation of CO_2. Fuel 2001;80(13):1953-62.

105 Mattisson T, Johansson, M., and Lyngfelt, A. CO_2 capture from coal combustion using chemical-looping combustion Reactivity investigation of Fe, Ni and Mn based oxygen carriers using syngas, The Clearwater Coal Conference. 2006.

106 Bhavsar S, Najera M, Solunke R, Veser G. Chemical looping: To combustion and beyond. Catalysis Today 2014;228:96-105.

107 Rydén M, Lyngfelt A. Using steam reforming to produce hydrogen with carbon dioxide capture by chemical-looping combustion. International Journal of Hydrogen Energy 2006;31(10):1271-83.

108 Adánez J, de Diego LF, García-Labiano F, Gayán P, Abad A, Palacios J. Selection of oxygen carriers for chemical-looping combustion. Energy & Fuels 2004;18(2):371-7.

109 Adánez J, García-Labiano F, Abad A, de Diego L, Gayán P, Dueso C. NiO-based oxygen carriers impregnated on Al_2O_3-based materials for chemical-looping combustion. in Carbon dioxide capture for storage in deep geologic formations results from the CO_2 capture project - advances in CO_2 capture and storage technology results, ed L. Eide (Newbury: CPL Press), 2009;3:85-94.

110 Wang X, Liu H, Jin B, Zhao J, Sun C, Snape CE. Experimental Evaluation of a Chinese Sulfur-Containing Lean Iron Ore as the Oxygen Carrier for Chemical-Looping Combustion. Industrial & Engineering Chemistry Research 2016;55(2):428-35.

111 Mendiara T, Pérez R, Abad A, de Diego L, García-Labiano F, Gayan P, et al. Low-cost Fe-based oxygen carrier materials for the iG-CLC process with coal. Industrial & Engineering Chemistry Research 2012;51(50):16216-29.

112 Tian H, Siriwardane R, Simonyi T, Poston J. Natural ores as oxygen carriers in chemical looping combustion. Energy & Fuels 2013;27(8):4108-18.

113 Adánez J, Gayán P, Celaya J, de Diego LF, García-Labiano F, Abad A. Chemical looping combustion in a 10 kWth prototype using a CuO/Al_2O_3 oxygen carrier: Effect of operating conditions on methane combustion. Industrial & Engineering Chemistry Research 2006;45(17):6075-80.

114 Mendiara T, Abad A, de Diego L, García-Labiano F, Gayán P, Adánez J. Reduction and oxidation kinetics of Tierga iron ore for Chemical Looping Combustion with diverse fuels. Chemical Engineering Journal 2019;359:37-46.

115 Cabello A, Abad A, García-Labiano F, Gayán P, de Diego L, Adánez J. Kinetic determination of a highly reactive impregnated Fe2O3/Al2O3 oxygen carrier for use in gas-fueled chemical looping combustion. Chemical Engineering Journal 2014;258:265-80.

116 Ahmed I, de Lasa H. 110th Anniversary: Kinetic Model for Syngas Chemical Looping Combustion Using a Nickel-Based Highly Performing Fluidizable Oxygen Carrier. Industrial & Engineering Chemistry Research. 2019;58(8):2801-11.

117 Mattisson T, García-Labiano F, Kronberger B, Lyngfelt A, Adánez J, Hofbauer H. Chemical-looping combustion using syngas as fuel. International Journal of Greenhouse Gas Control 2007;1(2):158-69.

118 Abad A, García-Labiano F, de Diego LF, Gayán P, Adánez J. Reduction kinetics of Cu-, Ni-, and Fe-based oxygen carriers using syngas ($CO+ H_2$) for chemical-looping combustion. Energy & Fuels 2007;21(4):1843-53.

119 Siriwardane R, Poston J, Chaudhari K, Zinn A, Simonyi T, Robinson C. Chemical-looping combustion of simulated synthesis gas using nickel oxide oxygen carrier supported on bentonite. Energy & Fuels 2007;21(3):1582-91.

120 Jin H, Ishida M. A new type of coal gas fueled chemical-looping combustion. Fuel 2004;83(17):2411-7.

121 Adánez J, Dueso C, de Diego LF, Garcia-Labiano F, Gayán P, Abad A. Methane combustion in a 500 Wth chemical-looping combustion system using an impregnated Ni-based oxygen carrier. Energy & Fuels 2008;23(1):130-42.

122 Forero C, Gayán P, De Diego L, Abad A, García-Labiano F, Adánez J. Syngas combustion in a 500 Wth chemical-looping combustion system using an impregnated Cu-based oxygen carrier. Fuel Processing Technology 2009;90(12):1471-9.

123 Kolbitsch P, Bolhàr-Nordenkampf J, Pröll T, Hofbauer H. Operating experience with chemical looping combustion in a 120 kW dual circulating fluidized bed (DCFB) unit. International Journal of Greenhouse Gas Control 2010;4(2):180-5.

124 Kolbitsch P, Pröll T, Bolhar-Nordenkampf J, Hofbauer H. Characterization of chemical looping pilot plant performance via experimental determination of solids conversion. Energy & Fuels 2009;23(3):1450-5.

125 Son SR, Kim SD. Chemical-looping combustion with NiO and Fe_2O_3 in a thermobalance and circulating fluidized bed reactor with double loops. Industrial & Engineering Chemistry Research 2006;45(8):2689-96.

126 Ryu H-J, Jin G-T, Yi C-K. Demonstration of inherent CO_2 separation and no NOx emission in a 50kW chemical-looping combustor: continuous reduction and oxidation experiment. Greenhouse Gas Control Technologies 7. Elsevier; 2005, p. 1907-10.

127 Gayán P, Forero CR, Abad A, de Diego LF, García-Labiano F, Adánez J. Effect of Support on the Behavior of Cu-Based Oxygen Carriers during Long-Term CLC Operation at Temperatures above 1073 K. Energy & Fuels 2011;25(3):1316-26.

128 Luis F, Garcı F, Gayán P, Celaya J, Palacios JM, Adánez J. Operation of a 10kWth chemical-looping combustor during 200h with a $CuO–Al_2O_3$ oxygen carrier. Fuel 2007;86(7):1036-45.

129 García-Labiano F, Gayán P, Adánez J, De Diego LF, Forero CR. Solid waste management of a chemical-looping combustion plant using Cu-based oxygen carriers. Environmental Science & Technology 2007;41(16):5882-7.

130 Abad A, Adánez J, García-Labiano F, Luis F, Gayán P. Modeling of the chemical-looping combustion of methane using a Cu-based oxygen-carrier. Combustion and Flame 2010;157(3):602-15.

131 Forero C, Gayán P, García-Labiano F, De Diego L, Abad A, Adánez J. High temperature behaviour of a $CuO/\gamma Al_2O_3$ oxygen carrier for chemical-looping combustion. International Journal of Greenhouse Gas Control 2011;5(4):659-67.

132 Dueso C, García-Labiano F, Adánez J, Luis F, Gayán P, Abad A. Syngas combustion in a chemical-looping combustion system using an impregnated Ni-based oxygen carrier. Fuel 2009;88(12):2357-64.

133 Johansson E, Mattisson T, Lyngfelt A, Thunman H. Combustion of syngas and natural gas in a 300 W chemical-looping combustor. Chemical Engineering Research and Design 2006;84(9):819-27.

134 Forero C, Gayán P, De Diego L, Abad A, García-Labiano F, Adánez J. Syngas combustion in a 500 Wth Chemical-Looping Combustion system using an impregnated Cu-based oxygen carrier. Fuel Processing Technology 2009;90(12):1471-9.

135 Abad A, Mattisson T, Lyngfelt A, Johansson M. The use of iron oxide as oxygen carrier in a chemical-looping reactor. Fuel 2007;86(7-8):1021-35.

136 Abad A, Mattisson T, Lyngfelt A, Rydén M. Chemical-looping combustion in a 300 W continuously operating reactor system using a manganese-based oxygen carrier. Fuel 2006;85(9):1174-85.

137 García-Labiano F, de Diego LF, Gayán P, Adánez J, Abad A, Dueso C. Effect of fuel gas composition in chemical-looping combustion with Ni-based oxygen carriers. 1. Fate of sulfur. Industrial & Engineering Chemistry Research 2009;48(5):2499-508.

138 Forero C, Gayán P, García-Labiano F, De Diego L, Abad A, Adánez J. Effect of gas composition in chemical-looping combustion with copper-based oxygen carriers: fate of sulphur. International Journal of Greenhouse Gas Control 2010;4(5):762-70.

139 Shen L, Gao Z, Wu J, Xiao J. Sulfur behavior in chemical looping combustion with NiO/Al_2O_3 oxygen carrier. Combustion and Flame 2010;157(5):853-63.

140 Adánez J, Dueso C, de Diego LF, García-Labiano F, Gayán P, Abad A. Effect of fuel gas composition in chemical-looping combustion with Ni-based oxygen carriers. 2. Fate of light hydrocarbons. Industrial & Engineering Chemistry Research 2009;48(5):2509-18.

141 Noor M, Wandel AP, Yusaf T. The modelling of the effect of air fuel ratio on unburned hydrocarbons for MILD combustion. Proceedings of the 2nd Malaysian Postgraduate Conference. Education Malaysia, Sydney (EMAS); 2012:159-63.

142 Lefebvre AH, Ballal DR. Gas turbine combustion: alternative fuels and emissions. CRC Press, Taylor and Francis Group, New York, NY, 2010. (ISSN: 978-1-4200-8604-1).

143 Wei W, Wang S, Chatani S, Klimont Z, Cofala J, Hao J. Emission and speciation of non-methane volatile organic compounds from anthropogenic sources in China. Atmospheric Environment 2008;42(20):4976-88.

144 Koppmann R, Czapiewski Kv, Reid J. A review of biomass burning emissions, part I: gaseous emissions of carbon monoxide, methane, volatile organic compounds, and nitrogen containing compounds. Atmospheric Chemistry and Physics Discussions 2005(5):10455-516.

145 Atimtay AT, Kaynak B. Co-combustion of peach and apricot stone with coal in a bubbling fluidized bed. Fuel Processing Technology 2008;89(2):183-97.

146 Xu L, Li Z, Sun H, Bao J, Cai N. Low-temperature chemical looping combustion for removing unburnt gaseous components with a cement-supported CuO oxygen carrier. Energy & Fuels 2013;27(11):6872-9.

147 Medrano JA, Hamers H, Williams G, van Sint Annaland M, Gallucci F. $NiO/CaAl_2O_4$ as active oxygen carrier for low temperature chemical looping applications. Applied Energy 2015;158:86-96.

148 Leion H, Mattisson T, Lyngfelt A. The use of petroleum coke as fuel in chemical-looping combustion. Fuel 2007;86(12-13):1947-58.

149 Wang C, Cui H, Di H, Guo Q, Huang F. Experimental Investigation on the Multi-cycle Performance of Coal/Straw Chemical Loop Combustion with α-Fe_2O_3 as the Oxygen Carrier. Energy & Fuels 2014;28(6):4162-6.

150 Yu Z, Li C, Fang Y, Huang J, Wang Z. Reduction rate enhancements for coal direct chemical looping combustion with an iron oxide oxygen carrier. Energy & Fuels 2012;26(4):2505-11.

151 Cho P, Mattisson T, Lyngfelt A. Carbon formation on nickel and iron oxide-containing oxygen carriers for chemical-looping combustion. Industrial & Engineering Chemistry Research 2005;44(4):668-76.

152 Brown T, Dennis J, Scott S, Davidson J, Hayhurst A. Gasification and chemical-looping combustion of a lignite char in a fluidized bed of iron oxide. Energy & Fuels 2010;24(5):3034-48.

153 Rubel A, Liu K, Neathery J, Taulbee D. Oxygen carriers for chemical looping combustion of solid fuels. Fuel 2009;88(5):876-84.

154 D. Yamaguchi, L. Tang, N. Burke, K. Chiang, L. Rye, T. Hadley, S. Lim, Small scale hydrogen production from metal-metal oxide redox cycles, D. Minic (Ed.), Hydrogen energy - challenges and perspectives, InTech, Rijeka 2012, Chp2.

155 Cao Y, Casenas B, Pan W-P. Investigation of chemical looping combustion by solid fuels. 2. Redox reaction kinetics and product characterization with coal, biomass, and solid waste as solid fuels and CuO as an oxygen carrier. Energy & Fuels 2006;20(5):1845-54.

156 Cao Y, Pan W-P. Investigation of chemical looping combustion by solid fuels. 1. Process analysis. Energy & Fuels 2006;20(5):1836-44.

157 Leion H, Lyngfelt A, Mattisson T. Solid fuels in chemical-looping combustion using a NiO-based oxygen carrier. Chemical Engineering Research and Design 2009;87(11):1543-50.

158 Mattisson T, Järdnäs A, Lyngfelt A. Reactivity of some metal oxides supported on alumina with alternating methane and oxygen application for chemical-looping combustion. Energy & Fuels 2003;17(3):643-51.

159 Sedor KE, Hossain MM, de Lasa HI. Reduction kinetics of a fluidizable nickel–alumina oxygen carrier for chemical-looping combustion. The Canadian Journal of Chemical Engineering 2008;86(3):323-34.

160 Aghabararnejad M, Patience GS, Chaouki J. TGA and kinetic modelling of Co, Mn and Cu oxides for chemical looping gasification (CLG). The Canadian Journal of Chemical Engineering 2014;92(11):1903-10.

161 Wang B, Zhao H, Zheng Y, Liu Z, Zheng C. Chemical looping combustion of petroleum coke with $CuFe_2O_4$ as oxygen carrier. Chemical Engineering & Technology 2013;36(9):1488-95.

162 Lyngfelt A. Chemical-looping combustion of solid fuels–status of development. Applied Energy 2014;113:1869-73.

163 Adanez J. Chemical looping combustion of gaseous fuels. in Calcium and Chemical Looping Technology for Power Generation and Carbon Dioxide (CO_2) Capture Ed Fennell P, Anthony B, Elsevier; 2015, p. 256-85.

164 Adanez J, Abad A, Garcia-Labiano F, Gayan P, de Diego LF. Progress in chemical-looping combustion and reforming technologies. Progress in Energy and Combustion Science 2012;38(2):215-82.

165 Cao Y, Li B, Zhao H-Y, Lin C-W, Sit SP, Pan W-P. Investigation of asphalt (bitumen)-fuelled chemical looping combustion using durable copper-based oxygen carrier. Energy Procedia 2011;4:457-64.

166 Hoteit A, Forret A, Pelletant W, Roesler J, Gauthier T. Chemical Looping Combustion with Different Types of Liquid Fuels. Oil & Gas Science and Technology – Revue d'IFP Energies Nouvelles 2011;66(2):193-9.

167 Bao J, Liu W, Cleeton JPE, Scott SA, Dennis JS, Li Z, et al. Interaction between Fe-based oxygen carriers and n-heptane during chemical looping combustion. Proceedings of the Combustion Institute 2013;34(2):2839-46.

168 Serrano A, García-Labiano F, de Diego LF, Gayán P, Abad A, Adánez J. Chemical looping combustion of liquid fossil fuels in a 1 kW th unit using a Fe-based oxygen carrier. Fuel Processing Technology 2017;160:47-54.

169 Moldenhauer P, Rydén M, Mattisson T, Lyngfelt A. Chemical-looping combustion and chemical-looping with oxygen uncoupling of kerosene with Mn- and Cu-based oxygen carriers in a circulating fluidized-bed 300W laboratory reactor. Fuel Processing Technology 2012;104:378-89.

170 Moldenhauer P, Rydén M, Mattisson T, Lyngfelt A. Chemical-looping combustion and chemical-looping reforming of kerosene in a circulating fluidized-bed 300W laboratory reactor. International Journal of Greenhouse Gas Control 2012;9:1-9.

171 Moldenhauer P. Thesis Chemical-Looping Combustion Liquid Fuel. Department of Energy and Environment. PhD. Chalmers University of Technology; 2014.

172 Moldenhauer P, Rydén M, Mattisson T, Hoteit A, Jamal A, Lyngfelt A. Chemical-looping combustion with fuel oil in a 10 kW pilot plant. Energy & Fuels 2014;28(9):5978-87.

173 Moldenhauer P, Rydén M, Mattisson T, Younes M, Lyngfelt A. The use of ilmenite as oxygen carrier with kerosene in a 300W CLC laboratory reactor with continuous circulation. Applied Energy 2014;113:1846-54.

174 Moldenhauer P, Rydén M, Mattisson T, Jamal A, Lyngfelt A. Chemical-looping combustion with heavy liquid fuels in a 10 kW pilot plant. Fuel Processing Technology 2017;156:124-37.

175 Siriwardane R, Tian H, Miller D, Richards G, Simonyi T, Poston J. Evaluation of reaction mechanism of coal–metal oxide interactions in chemical-looping combustion. Combustion and Flame 2010;157(11):2198-208.

176 Roux S, Bensakhria A, Antonini G. Study and improvement of the regeneration of metallic oxides used as oxygen carriers for a new combustion process. International Journal of Chemical Reactor Engineering 2006;4(1).

177 de Diego LF, García-Labiano F, Adánez J, Gayán P, Abad A, Corbella BM, et al. Development of Cu-based oxygen carriers for chemical-looping combustion. Fuel 2004;83(13):1749-57.

178 Chuang S, Dennis J, Hayhurst A, Scott S. Development and performance of Cu-based oxygen carriers for chemical-looping combustion. Combustion and Flame 2008;154(1-2):109-21.

179 Ishida M, Jin H. A novel combustor based on chemical-looping reactions and its reaction kinetics. Journal of Chemical Engineering of Japan 1994;27(3):296-301.

180 Tian H, Simonyi T, Poston J, Siriwardane R. Effect of hydrogen sulfide on chemical looping combustion of coal-derived synthesis gas over bentonite-supported metal− oxide oxygen carriers. Industrial & Engineering Chemistry Research 2009;48(18):8418-30.

181 Aghabararnejad M, Chaouki J, Patience GS. The development of a novel Cu-Mn oxygen carrier for the chemical looping gasification of biomass. in 10th International conference on circulating fluidized beds and fluidization technology, Ed T. Knowlton, ECI Symposium Series, 2013. http://dc.engconfintl.org/cfb10/31

182 Lambert A, Briault P, Comte E. Spinel mixed oxides as oxygen carriers for chemical looping combustion. Energy Procedia 2011;4:318-23.

183 De Diego LF, Gayán P, García-Labiano F, Celaya J, Abad A, Adánez J. Impregnated CuO/Al_2O_3 oxygen carriers for chemical-looping combustion: avoiding fluidized bed agglomeration. Energy & Fuels 2005;19(5):1850-6.

184 Güleç F, Şimşek EH, Karaduman A. Zr/ZSM5 zeolit katalizörleri varlığında 2-metil naftalinin disproporsiyon kinetiği. Journal of the Faculty of Engineering and Architecture of Gazi University 2016;31(3):609-19.

185 Niftaliyeva A, Güleç F, Şimşek EH, Gullu M, Karaduman A. The Methylation Kinetics of 2-Methyl Naphthalene over Cu and La Modified Y Zeolite. Anadolu University Journal of Science and Technology A- Applied Sciences and Engineering 2015;16(2):167-78.

186 Chuang S, Dennis J, Hayhurst A, Scott S. Kinetics of the Oxidation of a Co-precipitated Mixture of Cu and Al2O3 by O2 for Chemical-Looping Combustion. Energy & Fuels 2010;24(7):3917-27.

187 Chuang S, Dennis J, Hayhurst A, Scott S. Kinetics of the chemical looping oxidation of CO by a co-precipitated mixture of CuO and Al_2O_3. Proceedings of the Combustion Institute 2009;32(2):2633-40.

188 Shi J, Guan J, Guo D, Zhang J, France LJ, Wang L, et al. Nitrogen Chemistry and Coke Transformation of FCC Coked Catalyst during the Regeneration Process. Sci Rep 2016;6:27309.

189 Behera B, Gupta P, Ray SS. Structure and composition of hard coke deposited on industrial fluid catalytic cracking catalysts by solid state 13 C nuclear magnetic resonance. Applied Catalysis A: General 2013;466:123-30.

190 Behera B, Ray SS. Structural changes of FCC catalyst from fresh to regeneration stages and associated coke in a FCC refining unit: A multinuclear solid state NMR approach. Catalysis Today 2009;141(1):195-204.

191 Voorhies A. Carbon formation in catalytic cracking. Industrial & Engineering Chemistry 1945;37(4):318-22.

192 Qian K, Tomczak DC, Rakiewicz EF, Harding RH, Yaluris G, Cheng W-C, et al. Coke formation in the fluid catalytic cracking process by combined analytical techniques. Energy & Fuels 1997;11(3):596-601.

193 Wear C C. Coke Selectivity Fundamentals. Catalagram 106; 2009, 1-9. Available from; https://grace.com/catalysts-and-fuels/en-us/Documents/106-oke%20Selectivity%20Fundamentals.pdf. [Accessed 10.05.2019].

194 Güleç F, Niftaliyeva A, Karaduman A. Selective synthesis of 2,6-triad dimethylnaphthalene isomers by disproportionation of 2-methylnaphthalene over mesoporous MCM-41, Research on Chemical Intermediates, 2018; 44: 7205-7218.

195 Güleç F, Özen A, Niftaliyeva A, Aydın A, Şimşek EH, Karaduman A. A kinetic study on methylation of naphthalene over Fe/ZSM-5 zeolite catalysts, Research on Chemical Intermediates, 2018; 44: 55-67.

196 Güleç F, Sher F, Karaduman A. Catalytic performance of Cu-and Zr-modified beta zeolite catalysts in the methylation of 2-methylnaphthalene, Petroleum Science, 2019; 16: 161-172.

197 Barker J, Richards P, Snape C, Meredith W. A novel technique for investigating the nature and origins of deposits formed in high pressure fuel injection equipment. SAE International Journal of Fuels and Lubricants 2010;2(2):38-44.

198 Lovás P, Hudec P, Hadvinová M, Ház A. Use of ZSM-5 catalyst in deoxygenation of waste cooking oil. Chemical Papers 2015;69(11).

199 Bari Siddiqui MA, Aitani AM, Saeed MR, Al-Khattaf S. Enhancing the Production of Light Olefins by Catalytic Cracking of FCC Naphtha over Mesoporous ZSM-5 Catalyst. Topics in Catalysis 2010;53(19-20):1387-93.

200 Shimada I, Takizawa K, Fukunaga H, Takahashi N, Takatsuka T. Catalytic cracking of polycyclic aromatic hydrocarbons with hydrogen transfer reaction. Fuel 2015;161:207-14.

201 Mikulec J, Vrbova M. Catalytic and thermal cracking of selected polyolefins. Clean Technologies and Environmental Policy 2008;10(2):121-30.

202 International ASTM. Standard Test Method for Testing Fluid Catalytic Cracking (FCC) Catalysts by Microactivity Test. ASTM International ASTM D3907-92; 2001:1-6.

203 Kunii D, Levenspiel O. Fluidization engineering. 2nd edition, Elsevier; 2013. (ISBN 0-409-90233-0) doi.org/10.1016/C2009-0-24190-0.

204 Yang WC. Handbook of fluidization and fluid-particle systems. CRC press; 2003. (ISBN 9780824702595) doi.org/10.1201/9780203912744.

205 Xu CC, Zhu J. Prediction of the minimum fluidization velocity for fine particles of various degrees of cohesiveness. Chemical Engineering Communications 2008;196(4):499-517.

206 Gayán P, Dueso C, Abad A, Adanez J, Luis F, García-Labiano F. NiO/Al_2O_3 oxygen carriers for chemical-looping combustion prepared by impregnation and deposition–precipitation methods. Fuel 2009;88(6):1016-23.

207 Hossain MM, Lopez D, Herrera J, de Lasa HI. Nickel on lanthanum-modified γ-Al_2O_3 oxygen carrier for CLC: reactivity and stability. Catalysis Today 2009;143(1-2):179-86.

208 Gao Z, Shen L, Xiao J, Qing C, Song Q. Use of coal as fuel for chemical-looping combustion with Ni-based oxygen carrier. Industrial & Engineering Chemistry Research 2008;47(23):9279-87.

209 Zafar Q, Mattisson T, Gevert B. Redox investigation of some oxides of transition-state metals Ni, Cu, Fe, and Mn supported on SiO_2 and $MgAl_2O_4$. Energy & Fuels 2006;20(1):34-44.

210 Bird M, Keitel C, Meredith W. Analysis of biochars for C, H, N, O and S by elemental analyser. Biochar: A Guide to Analytical Methods 2017:39.

211 Han L, Bollas GM. Chemical-looping combustion in a reverse-flow fixed bed reactor. Energy 2016;102:669-81.

212 Han L, Bollas GM. Dynamic optimization of fixed bed chemical-looping combustion processes. Energy 2016;112:1107-19.

213 Jin H, Ishida M. Reactivity study on natural-gas-fueled chemical-looping combustion by a fixed-bed reactor. Industrial & Engineering Chemistry Research 2002;41(16):4004-7.

214 Corbella BM, De Diego L, García F, Adánez J, Palacios JM. The performance in a fixed bed reactor of copper-based oxides on titania as oxygen carriers for chemical looping combustion of methane. Energy & Fuels 2005;19(2):433-41.

215 Flagan RC, Seinfeld JH. Fundamentals of air pollution engineering. Dover Publication Inc, Courier Corporation; 2012. (ISBN 9780486488721)

216 Law CK. Combustion physics. Cambridge: Cambridge University Press. (doi:10.1017/CBO9780511754517)

217 Chuang S, Dennis J, Hayhurst A, Scott S. Kinetics of the chemical looping oxidation of CO by a co-precipitated mixture of CuO and Al_2O_3. Proceedings of the Combustion Institute 2009;32(2):2633-40.

218 Chuang S, Dennis J, Hayhurst A, Scott S. Kinetics of the chemical looping oxidation of H_2 by a co-precipitated mixture of CuO and Al_2O_3. Chemical Engineering Research and Design 2011;89(9):1511-23.

219 Betiha MA, Menoufy MF, Al-Sabagh AM, Hassan HM, Mahmoud SA. Acidic mesostructured aluminosilicates assembled from economic acidic template characterized by catalytic cracking reactions. Microporous and Mesoporous Materials 2015;204:15-24.

220 Greensfelder B, Voge H, Good G. Catalytic cracking of pure hydrocarbons. Industrial & Engineering Chemistry 1945;37(12):1168-76.

221 Sadeghbeigi R. Fluid catalytic cracking handbook: An expert guide to the practical operation, design, and optimization of FCC units. Elsevier; 2012.

222 Christensen CH, Schmidt I, Christensen CH. Improved performance of mesoporous zeolite single crystals in catalytic cracking and isomerization of n-hexadecane. Catalysis Communications 2004;5(9):543-6.

223 Hughes R, Hutchings G, Koon C, McGhee B, Snape C. A fundamental study of the deactivation of FCC catalysts: a comparison of quinoline and phenanthrene as catalysts poisons. Studies in Surface Science and Catalysis. Elsevier; 1994, p. 377-84.

224 Abbot J, Wojciechowski B. The effect of temperature on the product distribution and kinetics of reactions of n-hexadecane on HY zeolite. Journal of Catalysis 1988;109(2):274-83.

225 Galiano MC, Sedran UA. Light alkene selectivity on Y zeolite FCC catalysts. Industrial & Engineering Chemistry Research 1997;36(10):4207-11.

226 Shi J, Guan J, Guo D, Zhang J, France LJ, Wang L, et al. Nitrogen chemistry and coke transformation of FCC coked catalyst during the regeneration process. Scientific Reports 2016;6:27309.

227 Adánez-Rubio I, Gayán P, García-Labiano F, Luis F, Adánez J, Abad A. Development of CuO-based oxygen-carrier materials suitable for chemical-looping with oxygen uncoupling (CLOU) process. Energy Procedia 2011;4:417-24.

228 Arjmand M, Keller M, Leion H, Mattisson T, Lyngfelt A. Oxygen release and oxidation rates of MgAl2O4-supported CuO oxygen carrier for chemical-looping combustion with oxygen uncoupling (CLOU). Energy & Fuels 2012;26(11):6528-39.

229 Hughes R, Hutchings G, Koon C, McGhee B, Snape C. The influence of feedstocks and catalyst formulation on thedeactivation of FCC catalysts. Studies in Surface Science and Catalysis. Elsevier; 1996, p. 313-22.

230 Michalakos P, Robinson R, Tang Y. Catalyst deactivation in the cracking of hexadecane and commercial FCC feed as studied by microactivity test–multiple cold trap (MAT–MCT) technique. Catalysis Today 1998;46(1):13-26.

231 Eberly P, Kimberlin C, Miller W, Drushel H. Coke formation on silica-alumina cracking catalysts. Industrial & Engineering Chemistry Process Design and Development 1966;5(2):193-8.

232 Wang Y, Tao Z, Wu B, Chen H, Xu J, Yang Y. Shape-controlled synthesis of Pt particles and their catalytic performances in the n-hexadecane hydroconversion. Catalysis Today 2016;259:331-9.

233 Gayán P, Adánez-Rubio I, Abad A, Luis F, García-Labiano F, Adánez J. Development of Cu-based oxygen carriers for Chemical-Looping with Oxygen Uncoupling (CLOU) process. Fuel 2012;96:226-38.

234 Imtiaz Q, Hosseini D, Müller CR. Review of oxygen carriers for chemical looping with oxygen uncoupling (CLOU): thermodynamics, material development, and synthesis. Energy Technology 2013;1(11):633-47.

235 Siregar TB, Amin N. Catalytic cracking of palm oil to gasoline over pretreated Cu-ZSM-5. Jurnal Teknologi 2006;44(1).

236 Wang Y, Wang R, Xu D, Sun C, Ni L, Fu W, et al. Synthesis and properties of MFI zeolites with microporous, mesoporous and macroporous hierarchical structures by a gel-casting technique. New Journal of Chemistry 2016;40(5):4398-405.

237 Sertić-Bionda K, Gomzi Z, Fabulić-Ruszkowski M, Mužic M. Study of nonisothermal gas-oil catalytic cracking applying the microactivity test. Petroleum Chemistry 2008;48(1):6-14.

238 Meng Q, Liu B, Piao J, Liu Q. Synthesis of the composite material Y/ASA and its catalytic performance for the cracking of n-decane. Journal of Catalysis 2012;290:55-64.

239 Tarach K, Góra-Marek K, Tekla J, Brylewska K, Datka J, Mlekodaj K, et al. Catalytic cracking performance of alkaline-treated zeolite Beta in the terms of acid sites properties and their accessibility. Journal of Catalysis 2014;312:46-57.

240 Blasco T, Corma A, Martínez-Triguero J. Hydrothermal stabilization of ZSM-5 catalytic-cracking additives by phosphorus addition. Journal of Catalysis 2006;237(2):267-77.

241 Bhan A, Nicholas Delgass W. Propane aromatization over HZSM-5 and Ga/HZSM-5 catalysts. Catalysis Reviews 2008;50(1):19-151.

242 Wang S, Cai Q, Chen J, Zhang L, Zhu L, Luo Z. Co-cracking of bio-oil model compound mixtures and ethanol over different metal oxide-modified HZSM-5 catalysts. Fuel 2015;160:534-43.

243 Thommes M, Kaneko K, Neimark AV, Olivier JP, Rodriguez-Reinoso F, Rouquerol J, et al. Physisorption of gases, with special reference to the evaluation of surface area and pore size distribution (IUPAC Technical Report). Pure and Applied Chemistry 2015;87(9-10):1051-69.

244 Sing K. Reporting physisorption data for gas/solid systems with special reference to the determination of surface area and porosity (Provisional). Pure and applied chemistry 1982;54(11):2201-18.

245 Li C, Ma J, Xiao Z, Hector SB, Liu R, Zuo S, et al. Catalytic cracking of Swida wilsoniana oil for hydrocarbon biofuel over Cu-modified ZSM-5 zeolite. Fuel 2018;218:59-66.

246 Kubo K, Iida H, Namba S, Igarashi A. Comparison of steaming stability of Cu-ZSM-5 with those of Ag-ZSM-5, P/H-ZSM-5, and H-ZSM-5 zeolites as naphtha cracking catalysts to produce light olefin at high temperatures. Applied Catalysis A: General 2015;489:272-9.

247 Awayssa O, Al-Yassir N, Aitani A, Al-Khattaf S. Modified HZSM-5 as FCC additive for enhancing light olefins yield from catalytic cracking of VGO. Applied Catalysis A: General 2014;477:172-83.

248 Du Z, Ma X, Li Y, Chen P, Liu Y, Lin X, et al. Production of aromatic hydrocarbons by catalytic pyrolysis of microalgae with zeolites: Catalyst screening in a pyroprobe. Bioresource Technology 2013;139:397-401.

249 Hernández-Beltrán F, Quintana-Solórzano R, Sánchez-Valente J, Pedraza-Archila F, Figueras F. Effect of highly reactive sulfur species on sulfur reduction in cracking gasoline. Applied Catalysis B: Environmental 2003;42(2):145-54.

250 Marakatti VS, Shanbhag GV, Halgeri A. Sulfated zirconia; an efficient and reusable acid catalyst for the selective synthesis of 4-phenyl-1, 3-dioxane by Prins cyclization of styrene. Applied Catalysis A: General 2013;451:71-8.

251 Kubo K, Iida H, Namba S, Igarashi A. Ultra-high steaming stability of Cu-ZSM-5 zeolite as naphtha cracking catalyst to produce light olefin. Catalysis Communications 2012;29:162-5.

252 Koon C, Akbar F, Hughes R, Tyagi Y, Diaz MC, Martin S, et al. Development of an experimental protocol to evaluate FCC stripper performance in terms of coke yield and composition. Chemical Engineering Research and Design 2000;78(5):738-44.

253 Hosseinpour N, Mortazavi Y, Khodadadi AA. Cumene cracking activity and enhanced regeneration of FCC catalysts comprising HY-zeolite and $LaBO_3$ (B= Co, Mn, and Fe) perovskites. Applied Catalysis A: General 2014;487:26-35.

254 Rodriguez JA, Kim JY, Hanson JC, Pérez M, Frenkel AI. Reduction of CuO in H_2: in situ time-resolved XRD studies. Catalysis Letters 2003;85(3-4):247-54.

255 Ward M, Boyes E, Gai P. In-situ Reduction of Co_3O_4 in H_2 using Environmental HRTEM. Journal of Physics: Conference Series. 522. IOP Publishing; 2014:012009.

256 Pike J, Chan S-W, Zhang F, Wang X, Hanson J. Formation of stable Cu_2O from reduction of CuO nanoparticles. Applied Catalysis A: General 2006;303(2):273-7.

257 Kim JY, Hanson JC, Frenkel AI, Lee PL, Rodriguez JA. Reaction of CuO with hydrogen studied by using synchrotron-based x-ray diffraction. Journal of Physics: Condensed Matter 2004;16(33):S3479.

258 Widayatno WB, Guan G, Rizkiana J, Yang J, Hao X, Tsutsumi A, et al. Upgrading of bio-oil from biomass pyrolysis over Cu-modified β-zeolite catalyst with high selectivity and stability. Applied Catalysis B: Environmental 2016;186:166-72.

259 Zhao H, Liu L, Wang B, Xu D, Jiang L, Zheng C. Sol–gel-derived $NiO/NiAl_2O_4$ oxygen carriers for chemical-looping combustion by coal char. Energy & Fuels 2008;22(2):898-905.

260 Piekiel NW, Egan GC, Sullivan KT, Zachariah MR. Evidence for the predominance of condensed phase reaction in chemical looping reactions between carbon and oxygen carriers. The Journal of Physical Chemistry C 2012;116(46):24496-502.

261 Baowen W, Wei-shu W, Chuan-chang G, Hai-bo Z, Ying Z, Chu-guang Z. TGA-FTIR investigation of the chemical looping combustion by coal with a $CuO-Fe_2O_3$ combined oxygen carrier. Electric Information and Control Engineering (ICEICE), 2011 International Conference on. IEEE; 2011:2724-7.

262 Wang B, Yan R, Zhao H, Zheng Y, Liu Z, Zheng C. Investigation of chemical looping combustion of coal with $CuFe_2O_4$ oxygen carrier. Energy & Fuels 2011;25(7):3344-54.

263 Wang L, Qin W, Wu LN, Hu XQ, Gao MZ, Zhang JJ, et al. Experimental Study on Coal Chemical Looping Combustion Using $CuFe_2O_4$ as Oxygen Carrier. Advanced Materials Research. 805. Trans Tech Publ; 2013:1387-90.

264 Wang B, Gao C, Wang W, Kong F, Zheng C. TGA-FTIR investigation of chemical looping combustion by coal with CoFe2O4 combined oxygen carrier. Journal of Analytical and Applied Pyrolysis 2014;105:369-78.

265 Shabani A, Rahman M, Pudasainee D, Samanta A, Sarkar P, Gupta R. Evaluation of ash-free coal for chemical looping combustion-part I: Thermogravimetric single cycle study and the reaction mechanism. The Canadian Journal of Chemical Engineering 2017;95(4):623-33.

266 Rydén M, Leion H, Mattisson T, Lyngfelt A. Combined oxides as oxygen-carrier material for chemical-looping with oxygen uncoupling. Applied Energy 2014;113:1924-32.

267 Zhang X, Banerjee S, Agarwal RK. Validation of chemical-looping with oxygen uncoupling (CLOU) using Cu-based oxygen carrier and comparative study of Cu, Mn and Co based oxygen carriers using ASPEN plus. International Journal of Energy and Environment 2015;6(3):247.

268 Arbel A, Huang Z, Rinard IH, Shinnar R, Sapre AV. Dynamic and control of fluidized catalytic crackers. 1. Modeling of the current generation of FCC's. Industrial & Engineering Chemistry Research 1995;34(4):1228-43.

269 Sahoo SK, Ray SS, Singh I. Structural characterization of coke on spent hydroprocessing catalysts used for processing of vacuum gas oils. Applied Catalysis A: General 2004;278(1):83-91.

270 Chejne F, Hernandez J, Florez W, Hill A. Modelling and simulation of time-dependent coal combustion processes in stacks. Fuel 2000;79(8):987-97.

271 Bayraktar O, Kugler E. Coke content of spent commercial fluid catalytic cracking (FCC) catalysts. Journal of Thermal Analysis and Calorimetry 2003;71(3):867-74.

272 Cerqueira H, Caeiro G, Costa L, Ribeiro FR. Deactivation of FCC catalysts. Journal of Molecular Catalysis A: Chemical 2008;292(1-2):1-13.

273 Abián M, Abad A, Izquierdo MT, Gayán P, Luis F, García-Labiano F, et al. Titanium substituted manganese-ferrite as an oxygen carrier with permanent magnetic properties for chemical looping combustion of solid fuels. Fuel 2017;195:38-48.

274 Sun X, Xiang W, Wang S, Tian W, Xu X, Xu Y, Xio Y. Investigation of coal fueled chemical looping combustion using Fe_3O_4 as oxygen carrier: Influence of variables. Journal of Thermal Science 2010;19(3):266-75.

275 Fan Y, Siriwardane R. Novel new oxygen carriers for chemical looping combustion of solid fuels. Energy & Fuels 2014;28(3):2248-57.

276 Adánez-Rubio I, Gayán P, Abad A, García-Labiano F, de Diego L, Adánez J. Kinetic analysis of a Cu-based oxygen carrier: relevance of temperature and oxygen partial pressure on reduction and oxidation reactions rates in chemical looping with oxygen uncoupling (CLOU). Chemical Engineering Journal 2014;256:69-84.

277 Rydén M, Lyngfelt A, Mattisson T. Combined manganese/iron oxides as oxygen carrier for chemical looping combustion with oxygen uncoupling (CLOU) in a circulating fluidized bed reactor system. Energy Procedia 2011;4:341-8.

278 Luis F, Garcı F, Gayán P, Celaya J, Palacios JM, Adánez J. Operation of a 10kWth chemical-looping combustor during 200h with a $CuO–Al_2O_3$ oxygen carrier. Fuel 2007;86(7):1036-45.

279 García-Labiano F, de Diego LF, García-Díez E, Serrano A, Abad A, Gayán P, et al. Combustion and reforming of liquid fossil fuels through chemical looping processes: Integration of chemical looping processes in a refinery. Energy Procedia 2017;114:325-33.

280 Kissin YV. Chemical mechanisms of catalytic cracking over solid acidic catalysts: alkanes and alkenes. Catalysis Reviews 2001;43(1-2):85-146.

281 García-Labiano F, de DIEGO LF, Adánez J, Abad A, Gayán P. Reduction and oxidation kinetics of a copper-based oxygen carrier prepared by impregnation for chemical-looping combustion. Industrial & Engineering Chemistry Research 2004;43(26):8168-77.

282 Garcia-Labiano F, Adánez J, de Diego LF, Gayán P, Abad A. Effect of pressure on the behavior of copper-, iron-, and nickel-based oxygen carriers for chemical-looping combustion. Energy & Fuels 2006;20(1):26-33.

Appendix A — GC chromatograms for the liquid and gas products

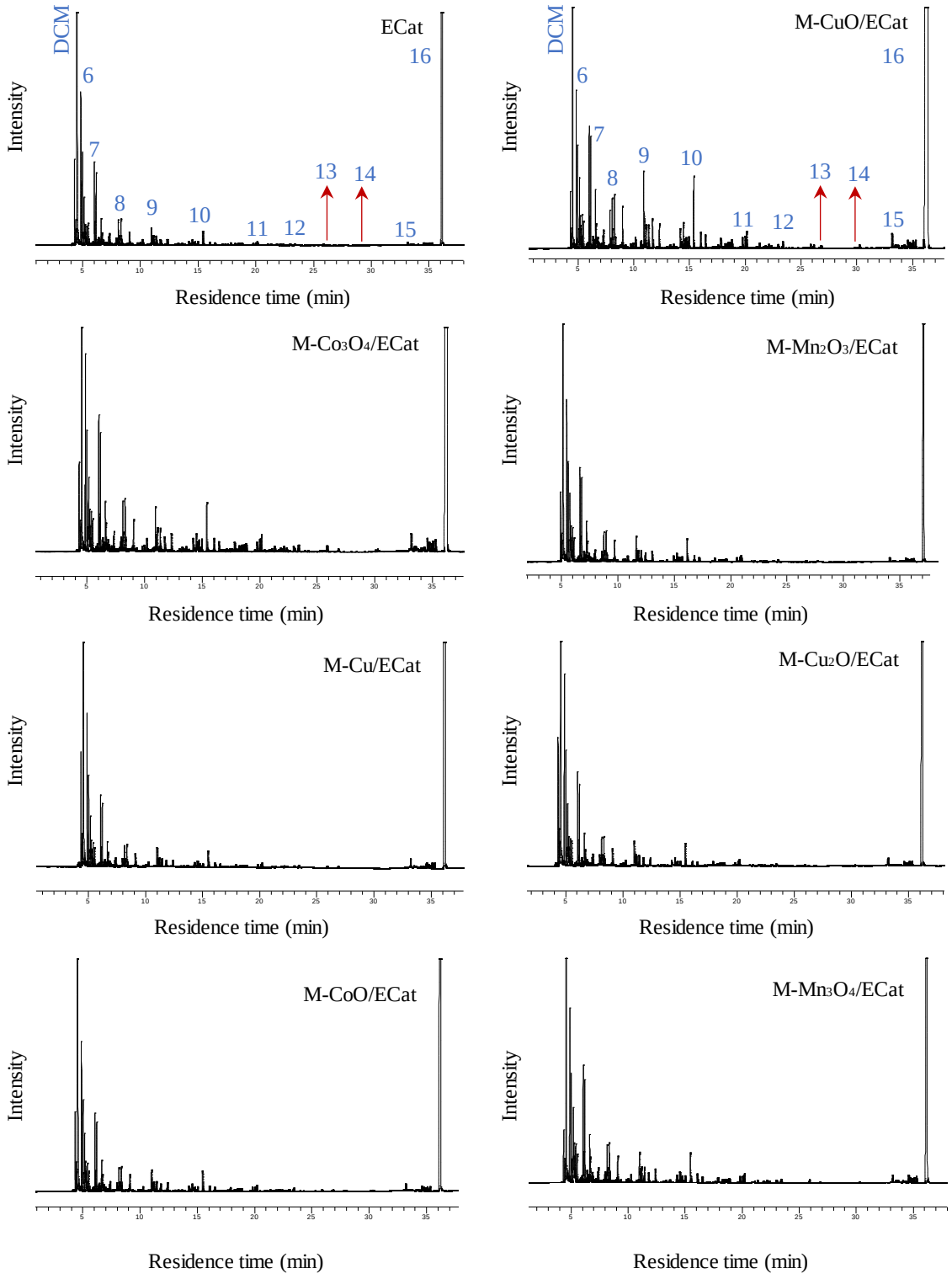


Figure A.1. GC chromatogram of the liquid products obtained from the cracking of n-hexadecane over oxidised and reduced oxygen carriers modified ECat by mechanically mixing. The numbers on the chromatograms represent the presence of n-alkanes.

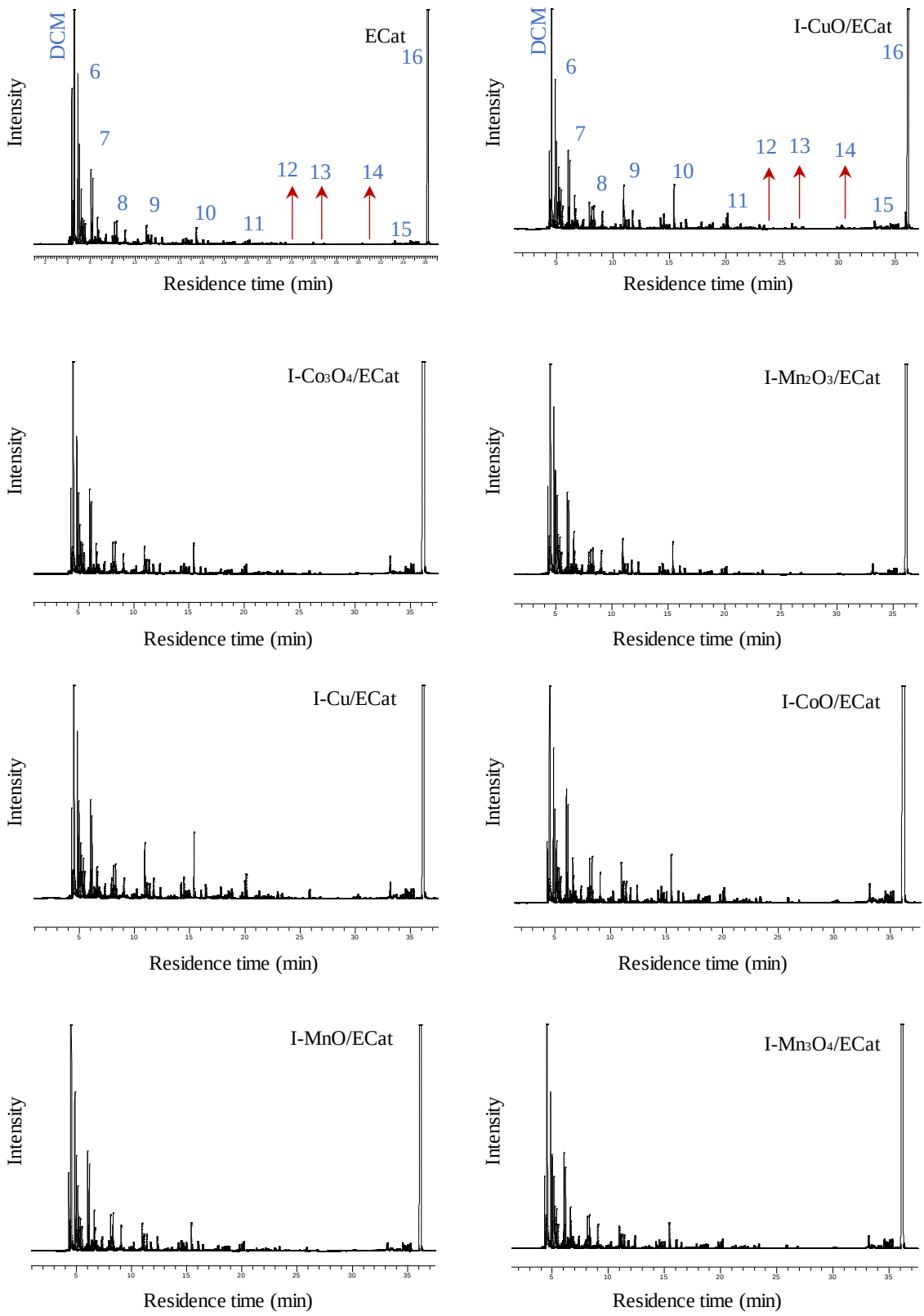


Figure A.2. GC chromatogram of the liquid products obtained from the cracking of n-hexadecane over oxidised and reduced oxygen carriers modified ECat by impregnation. The numbers on the chromatograms represent the presence of n-alkanes.

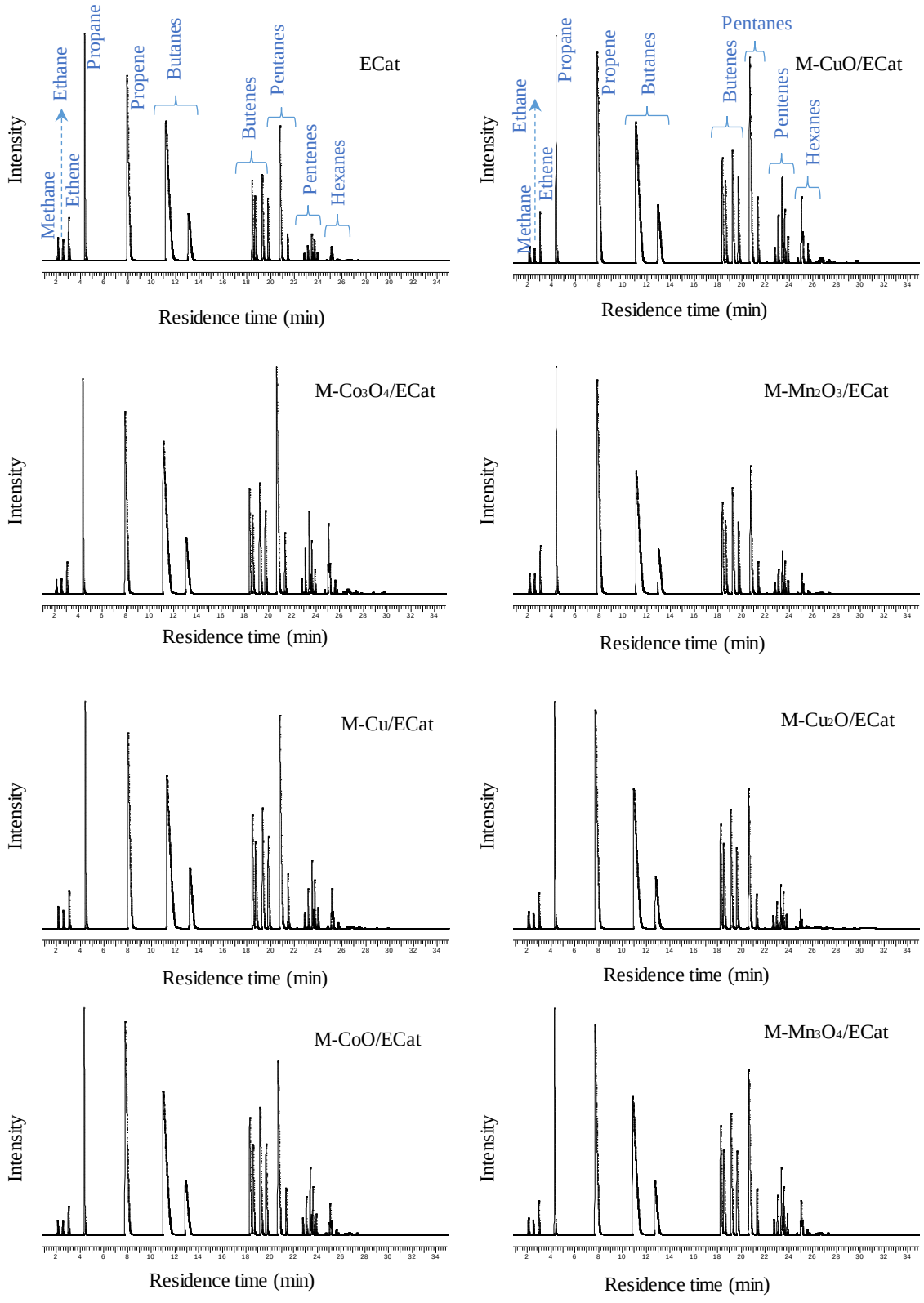


Figure A.3. GC chromatogram of the gas products obtained from the cracking of n-hexadecane over oxidised and reduced oxygen carriers modified ECat by mechanically mixing.

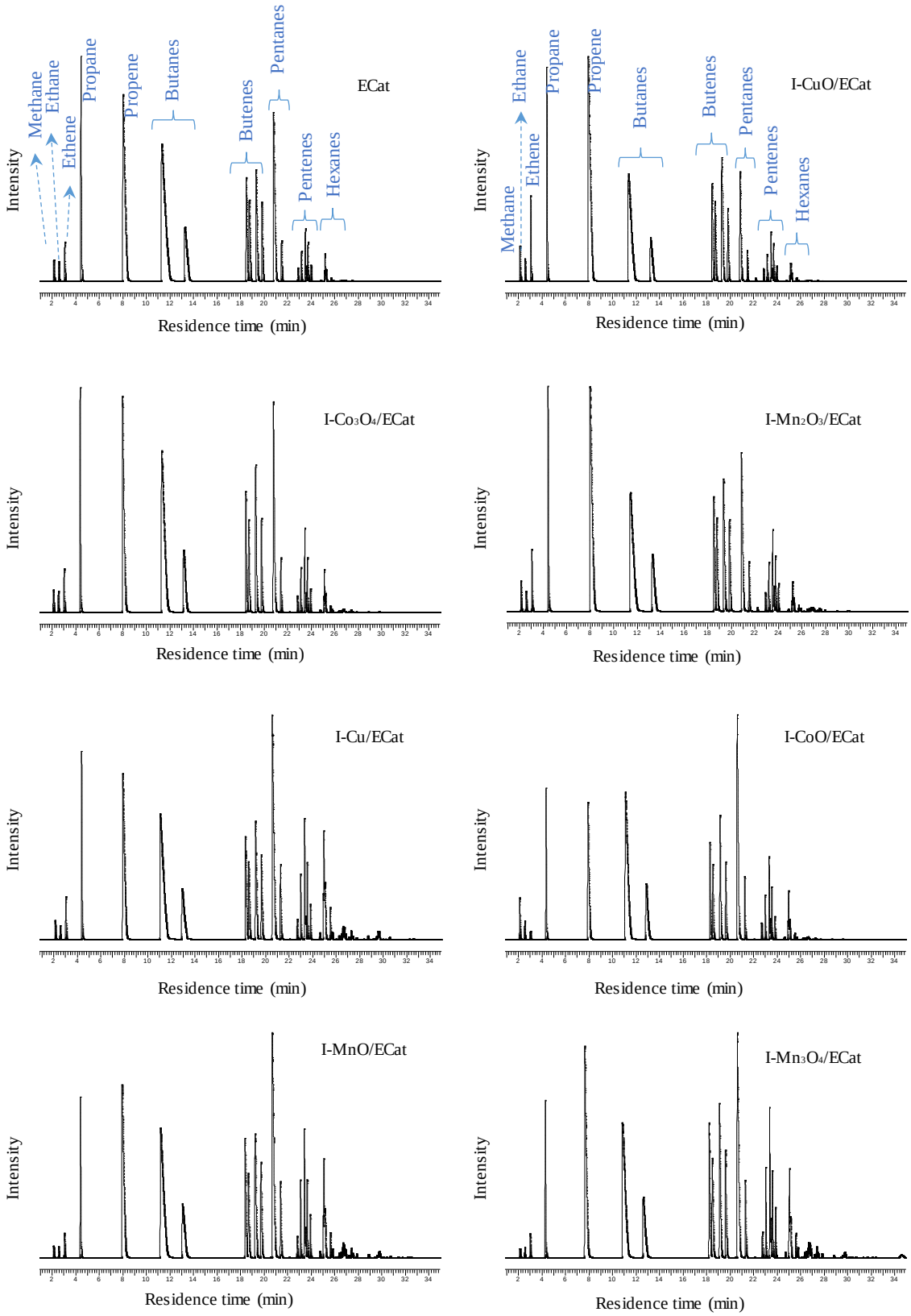


Figure A.4. GC chromatogram of the gas products obtained from the cracking of n-hexadecane over oxidised and reduced oxygen carriers modified ECat by impregnation.

Appendix B — Effects of temperature and oxygen carriers on the CLC products of coke

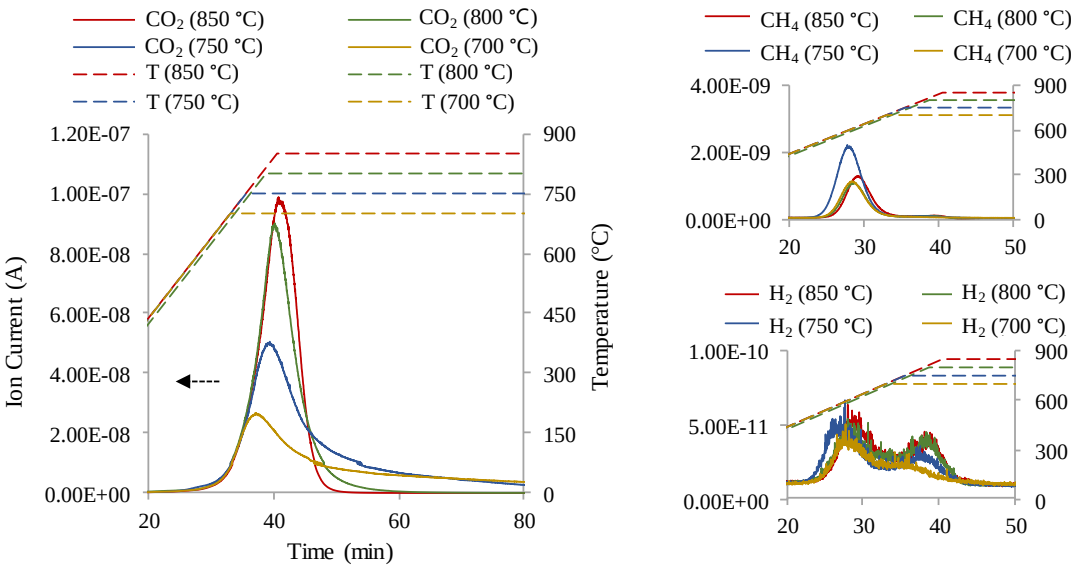


Figure B.1. CLC products from the combustion of coke deposited on ECat with CuO at 700-850 °C in FxB-MS unit.

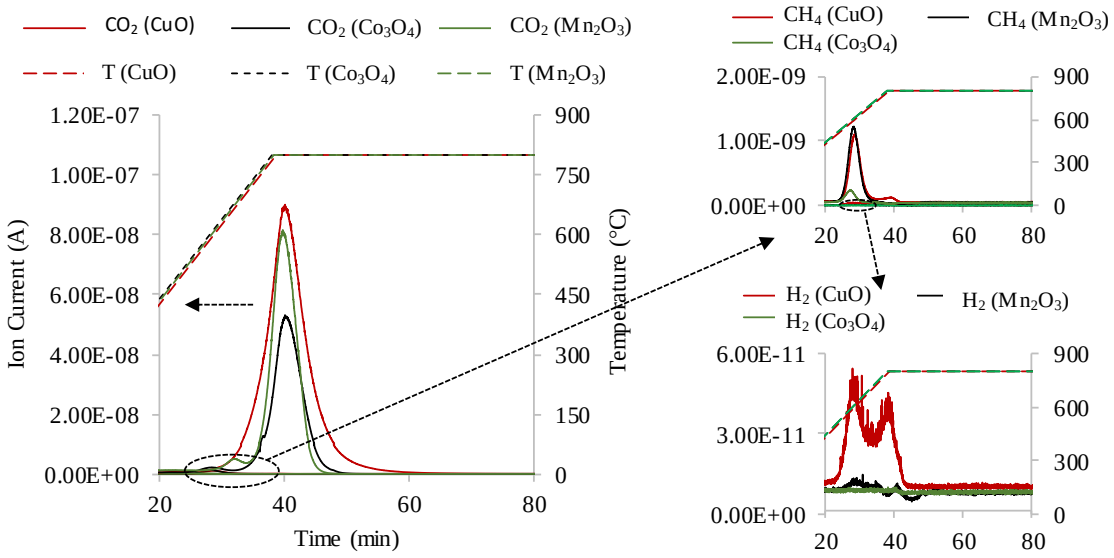


Figure B.2. CLC products from the combustion of coke deposited on ECat with CuO, Co_3O_4 and Mn_2O_3 at 800 °C in FxB-MS unit.

Appendix C — Kinetic analysis of n-hexadecane combustion with CuO

C.1. Determination of reaction order (n)

The steady state material balance for n-hexadecane;

$$F_A|_w - F_A|_{w+\Delta w} \pm r_A^{'}.\Delta w = 0 \quad \text{(C.1)}$$

$F_A|_w$; Molar flow rate of A before reaction (mol/min), $F_A|_{w+\Delta w}$; Molar flow rate of A after reaction (mol/min), r_A'; Reaction rate of A (mol A*g OC^{-1}*s^{-1}), Δw; differential weight of oxygen carrier (g OC).

$$F_A = Q * C_A$$

$$r_A^{'} = Q * \frac{(C_{A0} - C_A)}{w_{OC}}$$

$$r_A^{'} = \frac{(C_{A0} - C_A)}{\rho_{OC} * \tau} \quad \text{(C.2)}$$

C_{A0}; Droplet concentration of A before reactor (mol/L), C_A; Concentration of A after reactor (mol/L), ρ_{oc}; Bulk density of oxygen carrier (g OC/ml), τ; Residence time (s).

An example calculation was demonstrated below for n-hexadecane flowrate of 0.03 ml/min at 480 °C.

❖ ***C_{A0} in droplet condition***

$$F_{A0} = \frac{Q_{A0} * \rho_A}{M_A} \quad \text{(C.3)}$$

$$F_{A0} = 0.03\frac{mlA}{min} * 0.77\frac{g\,A}{ml\,A} * \frac{1}{226.41\frac{g\,A}{mol\,A}} = 1.02 * 10^{-4}\frac{molA}{\min}$$

$$n_{A0} = F_{A0} * t_{feed} = 1.02 * 10^{-4}\frac{mol\,A}{\min} * 6.67\,\min = 6.80 * 10^{-4} molA \quad \text{(C.4)}$$

$$V_{N_2} = Q_{N_2} * t_{feed} = 1.0\frac{ml}{\min} * \frac{1L}{1000ml} * 6.67\,\min = 6.67 * 10^{-3} L \quad \text{(C.5)}$$

$$C_{A0} = \frac{n_{A0}}{V_{N_2}} = \frac{6.80 * 10^{-4} molA}{6.67 * 10^{-3} L} = 0.102\frac{molA}{L} \quad \text{(C.6)}$$

❖ ***Determination of C_A***

$$C_A = C_{A0}(1-X) \tag{C.7}$$

$$C_A = C_{A0}(1-X) = 0.102\frac{mol\ A}{L} * (1-0.82) = 0.02\frac{mol\ A}{L}$$

The further results of n-hexadecane concentrations for four different flow rates and conversions are presented in Table C.1.

Table C.1. Concentration of n-hexadecane (A) in reactor inlet (C_{A0}) and outlet (C_A)

Q_A (ml/min)	t_{feed} (min)	F_{A0} (mol/min)	n_{A0} (mol)	V_{N2} (L)	C_{A0} (mol/L)	Conv.	C_A (mol/L)
0.03**	6.67	1.02E-04	$6.80*10^{-4}$	$6.67*10^{-3}$	0.10	0.82	0.02
0.10	2.12	3.40E-04	$7.20*10^{-4}$	$2.12*10^{-3}$	0.34	0.79	0.07
0.20	1.03	6.80E-04	$7.03*10^{-4}$	$1.03*10^{-3}$	0.68	0.58	0.29
1.40	0.15	4.76E-03	$7.14*10^{-4}$	$0.15*10^{-3}$	4.76	0.32	3.24

**Calculations demonstrated above were done for the flow rate of 0.03 ml/min and repeat for the other flow rates.

❖ ***Residence time (τ)***

$$\tau = \frac{Void\ volume}{Q_{N_2} + Q_A} \tag{C.8}$$

Q_{N_2}; Nitrogen flowrate trough the reactor (ml/s), Q_A; Vapour phase n-hexadecane flowrate trough the reactor (ml/s).

$$Q_{N_2} = 1\frac{ml}{\min} * \frac{1\min}{60s} = 0.0166\frac{ml}{s}$$

$$Q_A = 1.02*10^{-4}\frac{mol\ A}{min} * \frac{22400ml}{1mol\ A} * \frac{1min}{60s} = 0.038\frac{ml}{s}$$

The flow rate through the reactor at reactor temperature,

$$Q_{tot} = 0.054\frac{ml}{s} * \frac{T_{reactor}}{T_{ambient}} = 0.054 * \frac{273+480}{25+273} = 0.136\frac{ml}{s}$$

$$Void\ volume = V_{empty\ reactor} - \frac{w_{oc}}{\rho_{oc}} \tag{C.9}$$

$$Void\ volume = 2.294ml - \frac{3g\ CuO}{6.31\frac{gCuO}{ml\ CuO}} = 1.81ml$$

$$\tau = \frac{Void\ volume}{Q_{tot}} = \frac{1.81ml}{0.136\frac{ml}{s}} = 13.15s$$

❖ ***For reaction rates***

$$r_A^{'} = \frac{(C_{A0} - C_A)}{\rho_{OC,bulk} * \tau} = \frac{0.10\frac{mol}{L} - 0.02\frac{mol}{L}}{1.30\frac{gOC}{ml} * 13.30s} = 4.89 * 10^{-3}\frac{mol\ A}{gOC * s}$$

Table C.2. Reaction rate values for four different flowrates of n-hexadecane (Q_A).

Q_A (ml/min)	**C_{A0}** (mol/L)	**C_A** (mol/L)	**τ** (s)	**r_A'** (mol A/gOC*s)	**ln(r_A')**	**ln(C_{A0})**
0.03**	0.10	0.02	13.15	$4.89*10^{-3}$	-5.3200	-2.2825
0.1	0.34	0.07	5.01	$4.12*10^{-2}$	-3.1890	-1.0785
0.2	0.68	0.29	2.66	$1.14*10^{-1}$	-2.1715	-0.3854
1.4	4.76	3.24	0.40	$2.92*10^{0}$	1.0714	1.5605

**Calculations demonstrated above were done for the flow rate of 0.03 ml/min and repeat for the other flow rates.

The other reaction rate (r_A') values for the flowrates of 0.1, 0.2, and 1.4 ml/min are presented in Table C.2.

If the combustion reaction of n-hexadecane with CuO was assumed n^{th} order as $r_A^{'} = k * C_A^{\ n}$, the slope of the graph ln(r_A') versus ln(C_{A0}), Figure 7.15-a, should give the order of the reaction (**n**). The reaction order for n-hexadecane combustion with CuO was found as about n=1.6 and the reaction rate coefficient was about k= 0.223 $L^{1.6}/(mol\ A^{0.6} * g\ OC * s)$.

C.2. Determination of activation energy (E)

When the order of the reaction is assumed constant (1.6) at different temperatures, the activation energy can be calculated by Arrhenius plot for a constant flow rate of n-hexadecane at different temperatures, 380, 400, 440, 480, 520, 560 °C. An example calculation was demonstrated below for n-hexadecane flowrate of 0.2 ml/min at 480 °C.

❖ ***Concentration of n-hexadecane***

From equation C.3-C.7,

$$F_{A0} = \frac{0.2\frac{mL\,A}{min} * 0.77\frac{g\,A}{ml\,A}}{226.41\frac{g\,A}{mol\,A}} = 6.80 * 10^{-4}\frac{mol\,A}{min}$$

$$n_{A0} = F_{A0} * t_{feed} = 6.80 * 10^{-4}\frac{mol\,A}{\min} * 1.03\min = 7.03 * 10^{-4} molA$$

$$V_{N_2} = Q_{N_2} * t_{feed} = 1.0\frac{ml}{\min} * \frac{1L}{1000ml} * 1.03\min = 1.03 * 10^{-3} L$$

$$C_{A0} = \frac{n_{A0}}{V_{N_2}} = \frac{6.80 * 10^{-4} molA}{1.03 * 10^{-3} L} = 0.680\frac{molA}{L}$$

$$C_A = C_{A0}(1 - X) = 0.480\frac{mol\,A}{L} * (1 - 0.58) = 0.286\frac{mol\,A}{L}$$

- ***Residence time (τ)***

From equation C.8 and C.9;

$$Q_{N_2} = 1\frac{ml}{\min} * \frac{1\min}{60s} = 0.0166\frac{ml}{s}$$

$$Q_A = 6.80 * 10^{-4}\frac{mol\,A}{min} * \frac{22400ml}{1mol\,A} * \frac{1min}{60s} = 0.254\frac{ml}{s}$$

The flow rate through the reactor at ambient temperature,

$$Q_{tot} = 0.0166 + 0.254 = 0.2706\frac{ml}{s}$$

The flow rate through the reactor at reactor temperature,

$$Q_{tot} = 0.2706\frac{ml}{s} * \frac{T_{reactor}}{T_{ambient}} = 0.2706 * \frac{273 + 480}{25 + 273} = 0.684\frac{ml}{s}$$

$$Void\ volume = 2.294ml - \frac{3g\,CuO}{6.31\frac{gCuO}{ml\,CuO}} = 1.81ml$$

$$\tau = \frac{Void\ volume}{Q} = \frac{1.81ml}{0.684\frac{ml}{s}} = 2.647s \text{ at } 480\ ^\circ\text{C}$$

- ***Reaction rate at 480 °C***

Using the equation C.2,

$$r_A^{'} = \frac{(C_{A0} - C_A)}{\rho_{OC,bulk} * \tau} = \frac{0.680\frac{mol}{L} - 0.286\frac{mol}{L}}{1.30\frac{gOC}{ml} * 2.647s} = 0.114\frac{mol\ A}{gOC * s}$$

$$r_A^{'} = k * C_{A0}^{1.6} \qquad \text{(C.10)}$$

$$k = \frac{r_A^{'}}{C_A^{1.6}} = \frac{0.114\frac{mol\ A}{gOC * s}}{\left(0.680\frac{mol\ A}{L}\right)^{1.6}} = 0.211\frac{L^{1.6}}{mol\ A^{0.6} * gOC * s}$$

The further results at the temperatures from 380 to 560 °C are presented in Table C.3.

Table C.3. Reaction rate values at different temperatures from 380 to 560 °C.

T (°C)	**Conv.**	**C_{A0}** (mol/L)	**C_A** (mol/L)	**τ** (s)	**r_A'** (mol A/gOC*s)	**k**	**ln(k)**	**1/T** (1/K)
560	0.76	$6.80*10^{-1}$	$1.63*10^{-1}$	2.41	$1.65*10^{-1}$	$3.06*10^{-1}$	-1.18	0.0012
520	0.63	$6.80*10^{-1}$	$2.52*10^{-1}$	2.53	$1.30*10^{-1}$	$2.42*10^{-1}$	-1.42	0.0013
480⁂	0.58	$6.80*10^{-1}$	$2.86*10^{-1}$	2.66	$1.14*10^{-1}$	$2.11*10^{-1}$	-1.55	0.0013
440	0.51	$6.80*10^{-1}$	$3.33*10^{-1}$	2.81	$9.49*10^{-2}$	$1.76*10^{-1}$	-1.74	0.0014
400	0.46	$6.80*10^{-1}$	$3.67*10^{-1}$	2.98	$8.08*10^{-2}$	$1.50*10^{-1}$	-1.90	0.0015
380	0.32	$6.80*10^{-1}$	$4.63*10^{-1}$	3.07	$5.45*10^{-2}$	$1.01*10^{-1}$	-2.29	0.0015

⁂Calculations demonstrated above were done at 480 °C and repeat for the other temperatures.